

IMAGING OF TISSUE INJURY-REPAIR ADDRESSING THE SIGNIFICANCE
OF OXYGEN AND ITS DERIVATIVES

DISSERTATION

Presented in Partial Fulfillment of the Requirements for
the Degree Doctor of Philosophy in the
Graduate School of The Ohio State University

By

Navdeep Ojha, M.S.

The Ohio State University

2007

Dissertation Committee:

Dr. Chandan Sen, Adviser

Dr. Sashwati Roy

Dr. Periannan Kuppusamy

Dr. Orlando Simonetti

Approved by:

Adviser

Biomedical Engineering Graduate Program

ABSTRACT

The biomedical imaging field actively engages several areas of translational research and is a perfect example of successful collaboration between traditionally diametrically-opposite fields of biology and engineering. In line with this philosophy, the purpose of this work was to study tissue injury-repair using non-invasive biomedical imaging techniques of Magnetic Resonance Imaging (MRI) and Electron Paramagnetic Resonance (EPR).

Objective: This dissertation had three major objectives: to characterize oxygen and oxidant damage in tissue using MRI and EPR spectroscopy techniques; to develop an MRI based cardiac imaging technique for analysis of murine cardiac function, structure and infarct volume after Ischemia-Reperfusion in an attempt to characterize the effects of secondary myocyte death processes on LV remodeling; and to establish the functional significance of oxygen as a modulator of perceived hyperoxia during ischemia-reperfusion.

Experimental Approach and Results: MRI was employed to evaluate the effect of focal ischemic insult to brain and heart in rodent models whereas EPR Spectroscopy was used to study dermal wound healing in mouse models of excisional wounds. We established a robust Middle Cerebral Artery Occlusion model of focal cerebral ischemia in rodents with verification from MRI. Serial

evaluation of ischemic damage showed that MRI characteristics of ischemic regions change dynamically in the reperfusion period. We concluded that the prevention of subacute vasogenic edema after ischemia appeared to be a valuable therapeutic target, and treatment efficacy may be evaluated with serial MRI.

As part of this dissertation, a novel and effective EPR based approach was standardized to assess the redox environment of dermal wound site in vivo. Non-invasive measurements of metabolism of topically applied nitroxide ¹⁵N-perdeuterated tempone in murine excisional dermal wounds demonstrated that the wound site is rich in oxidants, the level of which peaked two day post-wounding in the inflammatory phase. Using Rac2-deficient mice we investigated the significance of Rac2 in wound site redox environment and healing responses. We concluded that Rac2 significantly contributes to oxidant production at the wound site and supports the healing process.

High resolution (11.7T) cardiac MRI and histological approaches were employed in tandem to characterize the progressive secondary damage suffered by the murine myocardium following the initial insult caused by ischemia-reperfusion (IR). IR induced changes in the myocardium were examined at specific time-points post reperfusion. A progressive loss of myocardial function associated with increased infarct volume and worsened regional wall motion was observed both with MRI and histological approaches. It was concluded that

myocardial remodeling following IR includes progressive myocardial tissue damage which is tightly associated with loss of cardiac function.

The final objective of this dissertation was to test the functional significance of tissue remodeling process induced by hyperoxic shock in the heart in a mouse IR model. It was hypothesized that tissue remodeling induced by 'perceived hyperoxia' in the heart post-reperfusion has a detrimental effect on cardiac function, and this diminished function can be circumvented by a lower oxygen shock suffered by the reperfused tissue. The worst cardiac function post IR was observed in animals that suffered highest hyperoxic shock, and lowest loss of function in animals with least shock. The p21 pathway was implicated as a major player in the induction of perceived hyperoxic shock and its functional effects.

Conclusions: In this dissertation, biomedical imaging techniques for evaluation of tissue injury-repair are described. Application of these imaging modalities to small animal disease models holds immense promise for study of tissue repair mechanisms.

This dissertation is dedicated to my loving family

ACKNOWLEDGMENTS

I would like to thank my family for their love and support all throughout my graduate school years. They have always been a source of endless support and good advice. I would not be in this position today if not for their continued encouragement.

I am grateful to my PhD advisers Dr. Chandan Sen, Dr. Sashwati Roy, Dr. Periannan Kuppusamy and Dr. Lon Simonetti for introducing me to the wonderful world of scientific research. I have enjoyed long and fulfilling conversations with them on topics that range from science and industry, to sports and philosophy. I acknowledge special thanks to Dr. Sen for spending countless hours with me in an attempt to make me the person and the scientist I am today.

This work would be incomplete without support from members of the molecular biology team. I am indebted to Dr. Savita Khanna, Cameron Rink, Jared Radtke and Dr. Sabyasachi Biswas for their prompt and generous assistance in various projects.

My sincere thanks go to the hardware team members, Dr. Petra Schmalbrock and Dr. Amir Abduljalil, who made sure that the imaging equipment

was always at its best performance. I am thankful to Dr. Jay Zweier for his insightful comments on cardiac MRI study design.

I greatly appreciate the support provided by Biomedical Engineering Department faculty and staff that helped me through various academic hurdles. This thesis was executed in the Department of Surgery. I thank the Chairman Dr. Christopher Ellison for his support of our program.

Finally, I acknowledge NIH grants NIGMS R01GM069589, NIGMS R01GM077185, NHLBI R01HL073087 and NINDS R01NS042617 awarded to Dr. Sen for sponsoring and supporting my PhD thesis in Biomedical Engineering.

VITA

June 7, 1982.....	Born – Khanna, India
1999- 2003.....	B.E. Electronics (Instrumentation and Control), India
May 2007.....	M.S. Biomedical Engineering, The Ohio State University
2004 – Present	Graduate Research Associate, The Ohio State University

PUBLICATIONS

1. Ojha N, Roy S, He G, Biswas S, Velayutham M, Khanna S, Kuppusamy P, Zweier JL and Sen CK. Assessment of wound-site redox environment and the significance of Rac2 in cutaneous healing. *Free Radical Biology and Medicine*, 2007.
2. Bagchi D, Roy S, Patel V, He G, Khanna S, Ojha N, Phillips C, Ghosh S, Bagchi M and Sen CK. Safety and whole-body antioxidant potential of a novel anthocyanin-rich formulation of edible berries. *Mol Cell Biochem.* 281: 197-209., 2006.
3. Patel V, Chivukula IV, Roy S, Khanna S, He G, Ojha N, Mehrotra A, Dias LM, Hunt TK and Sen CK. Oxygen: from the benefits of inducing VEGF expression to managing the risk of hyperbaric stress. *Antioxid Redox Signal.* 7: 1377-1387., 2005.

FIELDS OF STUDY

Major Field: Biomedical Engineering

Emphasis: Biomedical Imaging

TABLE OF CONTENTS

	Page
Abstract.....	ii
Dedication.....	v
Acknowledgments	vi
Vita.....	viii
List of Figures.....	xii
List of Tables.....	xvi
Introduction to the degree of Doctorate of Philosophy.....	1
Chapters:	
1. Exposure to Biomedical Imaging Techniques.....	14
1.1 Introduction.....	14
1.2 Magnetic Resonance Imaging of brain stroke in rodents.....	18
1.3 Redox Measurement using Electron Paramagnetic Resonance....	38
1.4 Figures.....	58
2. MRI Based Technique for Analysis of Murine Cardiac Function, Structure and Infarct Volume after Ischemia-Reperfusion.....	80
2.1 Introduction.....	80
2.2 Materials and Methods.....	86
2.3 Results and Discussion.....	111

2.4 Conclusions.....	117
2.5 Figures.....	120
3. Implications of Progressive Myocyte Death after Ischemia-Reperfusion Injury on LV Remodeling in Mouse Heart.....	140
3.1 Introduction.....	140
3.2 Materials and Methods.....	143
3.3 Results and Discussion.....	155
3.4 Conclusions.....	175
3.5 Figures.....	178
4. Functional Significance of Oxygen as a Modulator of Perceived Hyperoxia during Ischemia-Reperfusion.....	194
4.1 Introduction.....	194
4.2 Materials and Methods.....	197
4.3 Results and Discussion.....	205
4.4 Conclusions.....	208
4.5 Figures.....	210
5. Summary and General discussion	216
Bibliography	223

LIST OF FIGURES

Figure		Page
1.1	Mouse cerebrovascular anatomy.....	58
1.2	T2 and diffusion weighted MRI is consistent with TTC staining in rat brain after MCAO surgery.....	59
1.3	Comparison of lesion volume calculated with MRI and TTC staining.....	60
1.4	Maximum Intensity Projections of a 3D angiogram of the mouse brain after permanent ligation of External Carotid artery.....	61
1.5	Mouse brain angiogram acquired during surgery shows successful occlusion of the MCA and associated infarct damage.	62
1.6	Mouse brain angiogram acquired after reperfusion showing a hemorrhage, with associated infarct damage.....	63
1.7	T2 weighted MRI on 11.7 T has higher signal to noise ratio than 4.7 T.....	64
1.8	Time course of lesion volume in brain after 90 min Middle Cerebral Artery Occlusion in rat.	65
1.9	Line broadening of nitroxide with increase in concentration.....	66
1.10	Topical EPR spectroscopy of wounds.....	67
1.11	Presence of superoxide at wound site.....	69
1.12	Superoxide production peaks 2d post wounding as measured from DMPO spin adduct taken from wound rinsate.....	70
1.13	Slow wound healing response of Rac2 ^{-/-} animals.....	72

1.14	Decreased superoxide production at wound site in Rac2 ^{-/-} mouse corresponds to slow healing response of animals.....	73
1.15	Neutrophil recruitment to wound-site is increased in Rac2 ^{-/-} mice.	75
1.16	Macrophage recruitment to wound-site is increased in Rac2 ^{-/-} mice.....	76
1.17	Lower lipid peroxidation at wound site in Rac2 ^{-/-} mice.....	77
1.18	Impaired angiogenesis Rac2 ^{-/-} mice.....	79
2.1	Coronary arteries of human heart.....	120
2.1	Anatomy of postnatal mouse and human heart.....	121
2.3	k-space filling for multiple frames of an ECG-triggered cine gradient echo sequence.....	122
2.4	T1-weighted fast spin echo and inversion-recovery fast spin echo pulse sequences.....	123
2.5	Structure of contrast agent Gd-DTPA.....	124
2.6	Contrast agent distribution in normal and reperfused myocardium.....	125
2.7	Timing diagram of segmented inversion-recovery fast gradient echo pulse sequence.....	126
2.8	Inversion Recovery Fast Gradient Echo sequence.....	127
2.9	Process workflow for evaluation of cardiac function using MRI....	128
2.10	Regional Analysis of LV Wall motion.....	129
2.11	Bright-blood image of a mouse heart in end-diastole as part of a cine loop.....	130

2.12	Serially acquired bright-blood images of mouse heart in end-diastole as part of individual cine loops.....	131
2.13	Short axis cine gradient echo cine images.....	132
2.14	Black blood images of mouse heart.....	133
2.15	Subdermal echocardiogram recording during IR.....	134
2.16	Time course of signal enhancement in heart after contrast agent administration.....	135
2.17	Time course of hyper intense region area and signal intensity after Gadolinium contrast agent administration.....	136
2.18	Comparison of FLASH with IR-FLASH for DHE MRI.....	137
2.19	Contrast-enhanced mouse heart MR images compared with corresponding tissue slices photographed post-mortem.....	138
2.20	Statistical comparison between infarct volume measured with TTC and MRI.....	139
3.1	Serial Electrocardiogram recordings from mice show myocardial injury early after IR.....	178
3.2	Time course of MRI infarct progression.....	179
3.3	Infarct volume progression measured with MRI.....	180
3.4	Time course of TTC infarct progression.....	181
3.5	Infarct volume progression measured with TTC staining.....	182
3.6	Time course of infarct progression observed with Masson's trichrome staining.....	183
3.7	Infarct volume progression measured with Hematoxylin-Eosin staining.....	185

3.8	Quantification of Infarct volume progression measured with MRI, TTC and H/E staining techniques.....	186
3.9	Progressive loss of cardiac function after IR injury.....	187
3.10	Segmental LV wall thickening analysis before and after IR.....	190
4.1	Magnitude of reduced cardiac function after IR injury is dependent on hyperoxic shock at reperfusion.....	210
4.2	Quantitative analysis of p21/Cip1/Waf1/Sdi1 gene expression using laser captured tissue.....	214
4.3	Change in quantitative expression of p21/Cip1/Waf1/Sdi1 gene using laser captured tissue in 10% and 100% oxygen group.....	215

LIST OF TABLES

Table		Page
2.1	Extracellular Fluid Space Contrast agents that are available for cardiac MRI.....	95
3.1	Time course of procedures done on various animal groups at specified time points before and after IR surgery.....	145
3.2	Statistical analysis of wall motion abnormalities.....	193
4.1	Summary of experimental plan.....	198

INTRODUCTION TO THE DEGREE OF DOCTORATE OF PHILOSOPHY

“I fully agree with you about the significance and educational value of methodology as well as history and philosophy of science. So many people today - and even professional scientists - seem to me like somebody who has seen thousands of trees but has never seen a forest. A knowledge of the historic and philosophical background gives that kind of independence from prejudices of his generation from which most scientists are suffering. This independence created by philosophical insight is - in my opinion - the mark of distinction between a mere artisan or specialist and a real seeker after truth.”

- Albert Einstein in a letter to Robert Thornton, 7 December 1944 (1)

Doctor of Philosophy, abbreviated PhD for the Latin Philosophiæ Doctor, meaning "teacher of philosophy", is the most advanced academic degree for graduates in a wide array of disciplines in the sciences and humanities. The PhD has become a requirement for a career as a university professor or researcher in many fields. The US Department of Education defines a PhD as "the highest earned academic degree in U.S. postsecondary education". It is always awarded for independent research at a professional level in either academic disciplines or professional fields. Research doctorates earned at accredited institutions are not awarded merely for completing coursework, professional preparation, or for passing examinations.

In an attempt to standardize PhD theses for US schools, Minkel suggested that although graduate degree documents differ according to academic discipline, most "deal with a topic related to the major field of study; embody the results of individual research; possess a unity of theme, as opposed to [being] a collage of separate, distinct topics; show mastery of the literature on the subject; demonstrate mastery of appropriate research tools and techniques... provide evidence of originality and critical judgment; illustrate the development of broad capabilities, as well as an intensive focus on the subject of research; meet any special criteria of the major professor, thesis committee, and academic department; [are] written in a creditable literary style; constitute a significant contribution to knowledge; and [are] worthy of publication (2)."

Lately, the thesis has become a report with an emphasis on training rather than the detailed description of a scientific project (3). This modern-day definition of a PhD helps to maintain strict standards for the degree, but unfortunately fails to grasp the underlying philosophical insight that forms the core of the PhD.

History of the PhD

European universities in the Middle Ages generally placed all academic disciplines outside the fields of theology, medicine and law under the broad heading of “philosophy” (or “natural philosophy” when referring to science). The degree of Doctor of Philosophy was the most junior of the doctorates, generally granted as honorary degrees to select and well-established scholars (4). In 1861, Yale University adopted the German practice (first introduced in the 19th century at the Friedrich Wilhelm University in Berlin) of granting the degree to younger students who had completed a prescribed course of study and successfully defended a thesis containing original research in science or in the humanities (5). From the United States the degree spread to Canada in 1900, and then to the United Kingdom in 1917 (6). This displaced the existing Doctor of Philosophy degree in some Universities; for instance, the D.Phil. (higher doctorate in the faculty of philosophy) at the University of St Andrews was discontinued and replaced with the Ph.D. (research doctorate). Some UK universities such as Oxford retain the D.Phil. abbreviation for their research degrees, as do some universities in New Zealand.

Academic costumes of today have a history of nearly eight hundred years. In Medieval Europe men and women typically wore gowns or robes. There was a great deal of variety in color and material, depending upon the position and wealth of the wearer. Gradually there developed distinctive gowns for various professions, trades and religious orders. Students and teachers in many medieval universities such as Paris, Bologna, Oxford and Cambridge organized themselves into guilds. Gradually the academic costume became distinctive for Bachelors of Arts (the apprentices), Masters of Arts (the teachers), and Doctors (teachers who had completed postgraduate studies). Most of the distinctive characteristics appeared in the hood, which was originally a practical element of dress, but which evolved into a separate and purely ornamental article, draped over the shoulder and down the back. The academic cap was a later development. It was first conferred as a symbol of the M.A. degree. Some of these Master's caps were stiff, some soft, some square, and some round with a tuft in the center. Today's tassel is an elaboration of the tuft. Although round caps are still used at some universities, Oxford University's "mortar board" style is more common.

The Purpose of a PhD

Most scientists seem to know exactly what a PhD is and for what it stands. But on closer inspection, a PhD has as many meanings as there are educational systems. It is not - and has never been - a single, well-defined qualification. As

research practices and funding change, the situation becomes even more confused, with consequences for the quality of both scientific training and research (3).

There is debate about the broader “purpose of PhD training” and a plethora of definitions. For example, a recent British Academy Review of The Graduate Studies Committee viewed the purpose of PhD training “as a preparation for a research or academic career, and as a preparation for a wide range of advanced research support in industry, civil service, culture, media and the heritage sector. Research training makes a crucial contribution to the high level skills required to sustain a high value added knowledge-based economy (7).”

In the recent review of PhD supervisors, when asked to select the best description of the purpose of PhD training, a minority (6 per cent) of supervisors described a “purist” view of PhD training, where the primary purpose was “training for a career in academic research” with a commitment to academia.” Taking a wider view, a fifth of respondents (20 per cent) described the purpose in its broadest sense as “training for a range of careers”. They contend that it is no longer tenable to train people solely for research in an academic setting. Also industrial research has moved much closer in style and content to academic research in the last ten years. The majority of supervisors, however, took a middle position, with nearly three-quarters (72 per cent) believing the purpose of PhD training to be “training for a career in scientific research in general.” There

was general consensus that it was neither realistic nor necessarily appropriate to train students solely for a career in academic research. Skills learned during PhD can be applied to a wide range of careers. In addition, and more importantly, not all PhD students are suited to remain in research.

Research with students found that the primary reason for doing a PhD was an inherent curiosity and a love of science, indeed many students described the profound influence of a school science teacher on their decision to pursue science at a higher level (8). While an interest in science was a common motivation among students, there were also interesting differences between students pursuing different types (and duration) of PhD.

Research has found that the quality of the PhD training experience is a strong influence on the decision to pursue a long-term career in scientific research (9). Research suggests that for the PhD student the potential working environment and the nature of training provided is as important, if not more so, than the research project itself.

The Process of Obtaining a PhD

Ph.D. is the highest academic degree anyone can earn. Because earning a Ph.D. requires extended study and intense intellectual effort, less than one percent of the population attains the degree (10). The ability to conduct research in an area requires deep knowledge in that area, knowledge about related areas,

and the experience of working on research problems, i.e. problems whose outcomes are not known. To develop these critical abilities, most PhD programs have three components in them – some course work to provide the breadth of knowledge, some methods to develop the depth of knowledge in the chosen area of study, and a thesis that provides the experience of working on research problems.

Pankaj Jalote from Indian Institute of Technology notes that PhD training should form the basis of a career in research, with emphasis on development of a list of abilities and not the actual research results (11). However, in the overall research career, it is possessing these abilities that is more important, particularly if one wants to work in industry where the needs may change and problems that a researcher works on may be quite different from the ones chosen in PhD. For a career in academics, however, the actual results are equally important as the evaluative processes often focus on the quality and quantity of research work that has been done during the PhD.

Independent research and writing the dissertation can take anywhere from one to several years depending upon the topic selected and the research work necessary to prepare the dissertation. When the academic adviser is convinced that the dissertation is of an acceptable standard to put before the dissertation committee, the student delivers it to all committee members and is scheduled for the dissertation defense. The defense consists of an oral examination in depth before the committee and invited guests during which the student must establish

mastery of the subject matter, explain and justify his or her research findings, and answer all questions put by the committee. A successful defense results in the award of the degree.

The Concerns of the Purists

May believe that the PhD today is used an 'access card' to the laboratory. It must be standardized to conform to international standards. More information should be made available: how the candidate was examined, who sat on the examination committee and what comprised training in the applicant's university. Most importantly, it must be understood that a PhD is not merely a vague title but actually means what it implies: it is an award to an expert who has proven their scientific worth and not to someone who stayed in a tolerant group for long enough.

In 1926, the distribution of scientific productivity was analyzed by Alfred J. Lotka (12). The result of his investigation, which remains largely valid, was an inverse square law of productivity, by which the number of people producing n papers is inversely proportional to n^2 . This means that for every 100 authors who produce, say, one paper in a given period of time, there are approximately $100/2^2$, or 25 authors, who produce two papers and one author, who will produce 10 papers. Thirty years later, the same law was found to be applicable to patents. A generalization of this law is that 50% of the papers are produced by 6% of the scientific community. Another calculation based on this law states that an

average scientist publishes only 3 papers in his/her lifetime. These statistics speak volumes regarding the questionable quality of PhD training, at least in some fields of study.

To complicate matters, in most graduate programs there is only a limited amount of money available to support a PhD student. Once that is spent, the student must survive by the most precarious means: relying on parents or partners to cover the gap, finding a grant to stay afloat, or taking a part-time job, even if this eats into the precious time and energy needed to complete the thesis. If we accept these realities, it makes sense that a PhD is awarded on the basis of time and effort spent, rather than on scientific work alone. But in that case, a PhD is merely an apprenticeship and no longer represents a stamp of achievement.

The purists are alarmed (3). It is suggested that all PhD programs should follow the same rules and regulations for enhancing the quality of PhD work. But then there would be many theses documenting failure rather than achievement. If we collectively become unconcerned about what a PhD is, then we have little basis for expecting students to go through the diligent work that ultimately enables experiments to work and provides robust results. The 'three years and out' mentality of obtaining a PhD concentrates on time and investment rather than quality, and runs the risk of producing substandard scientists.

The Philosophy behind the PhD

A philosophical habit of mind provides the scientist with an 'independence of judgment'. Einstein explains the importance of questioning long-followed concepts in science, "It has often been said, and certainly not without justification, that the man of science is a poor philosopher... Concepts that have proven useful in ordering things easily achieve such an authority over us that we forget their earthly origins and accept them as unalterable givens. Thus they come to be stamped as 'necessities of thought,' 'a priori givens,' etc. The path of scientific advance is often made impassable for a long time through such errors. For that reason, it is by no means an idle game if we become practiced in analyzing the long commonplace concepts and exhibiting those circumstances upon which their justification and usefulness depend, how they have grown up, individually, out of the givens of experience. By this means, their all-too-great authority will be broken. They will be removed if they cannot be properly legitimated, corrected if their correlation with given things be far too superfluous, replaced by others if a new system can be established that we prefer for whatever reason."

Graduate study is fundamental to the development of higher level skills and the preparation of people who will engage with the problems of the next generation. The process of achieving a doctorate develops an enquiring mind, problem solving abilities and the ability to assimilate and defend new ideas. This intensive training equips the students to rise to challenges and be flexible and

adaptable; all valuable attributes for today's knowledge-based environment. The Italian scientist Riardo Giacconi, a Nobel Laureate in Physics, said: "A scientist is like a painter. Michelangelo became a great artist, because he had been given a wall to paint. My wall was given to me by the United States."

The philosophical view of science, termed "historical-critical" method of philosophical analysis, attempts for a critical contemplation of the theoretical assumptions, foundations, and implications of science. Philosophers of science are interested in the history of concepts and terms and how they are currently used in science; the relation between propositions with arguments (Formal logic); the reasoning connecting hypotheses and conclusions (Scientific method); the manner in which science explains natural phenomena and predicts natural occurrences (observation); the types of reasoning that are used to arrive at scientific conclusions (deduction, induction, abduction); the formulation, scope, and limits of scientific understanding; the means that should be used for determining when scientific information has adequate support (objectivity); and the implications of scientific methods and models, along with the technology that arises from scientific knowledge for the larger society (applied science).

While it might not be practical in today's day and age for graduate students to be critical of *all* scientific concepts used to build upon their research, critical thinking must be involved not just in interpretation of experimental outcomes, but in the interpretation of underlying reasons as to how and why the experiment itself means something at all. In a reference to the benefit he

received from the body of work done by others before him, Newton said, “If I have seen farther than others, it is because I stand on the shoulders of giants”. It’s advisable to give the giants some rest – critical evaluation of these giants is warranted, and will definitely help a PhD to learn and re-learn science.

Statistical Analysis Techniques

In this dissertation, statistical analysis of data was done as part of each experiment, wherever appropriate. A standard hypothesis testing paradigm was used. For comparison between means of two groups, Student’s t-test was used. Analysis of Variance (ANOVA) was used for comparisons between multiple groups. Tukey’s post-hoc test was used for evaluating differences between the various groups. The statistical packages SPSS and KyPlot were used for statistical analysis. Results were considered significantly different at $p < 0.05$. All figures are represented as group mean \pm standard deviation, unless otherwise noted.

All these statistical tests were used based on the underlying assumption that the acquired data was part of a normal distribution. All experimental studies reported in this dissertation were done on in-bred animal strains which resulted smaller variation in experimental results caused by difference in the genetic makeup of the animals. This further led to more accurate results following a normal distribution with smaller variance.

Content of this Thesis

This thesis is divided into five chapters. This introduction presented a philosophical viewpoint of the basis of the PhD degree, in addition to describing the statistics used throughout the thesis. Chapter 1 describes the research work done by the candidate while getting introduced to magnetic-based imaging techniques. Chapter 2, 3 and 4 are based on the results of conventional hypothesis testing applied to one major study. Chapter 5 is used to summarize the content of the thesis, have a general discussion of the area of interest and to field open questions. To increase readability of the thesis and provide continuity of text, figures are provided at the end of each chapter.

CHAPTER 1

EXPOSURE TO BIOMEDICAL IMAGING TECHNIQUES

1.1 Introduction

The biomedical imaging field actively engages several areas of translational research and is a perfect example of successful collaboration between traditionally diametrically-opposite fields of biology and engineering. Biomedical imaging brings together conventional biology fields of molecular biology and genetics, with hardware, instrumentation, and computer engineering groups. The results of this successful tie-up have led to the development of groundbreaking imaging modalities that have changed the face of clinical care with countless applications in various disease models. In the past 10 years, development of imaging modalities and techniques specifically for experimental animal models has also taken place at a fast pace. This has led to a dramatic shift in the ability to study in-vivo disease with greater accuracy and versatility.

This work describes the application of two magnetic field-based modalities, Magnetic Resonance Imaging (MRI) and Electron Paramagnetic

Resonance (EPR) spectroscopy, used for small animal models of stroke and wound healing, respectively. The two techniques are based on similar principles and have gone through identical development phases since their discovery more than 50 years ago. MRI has particular advantages in that it is non-invasive, uses non-ionizing radiation, and has a high soft-tissue resolution and discrimination in any imaging plane. EPR is an experimental technique that has been successfully applied to study the role of paramagnetic species (reactive oxygen and nitrogen species) cancer biology, atherosclerosis, ischemia-reperfusion injury, stroke, diabetic vascular disease and a variety of inflammatory diseases (13). EPR data provide a wealth of information (hyperfine structures; g-factor; line-shape; saturation) which serves as fingerprints of the paramagnetic species for unequivocal identification.

The following sections describe the candidate's exposure to MRI and EPR spectroscopy. A brief history of the techniques is presented with introduction to the specifics involved with small animal models. Description of the methods used is followed by results and their discussion. Conclusions from the application of each imaging modality to the respective disease models are drawn at the end.

1.1.1 History of Magnetic Resonance Imaging

Magnetic Resonance Imaging (MRI) or its spectroscopic version, Nuclear Magnetic Resonance (NMR), was discovered in the 1940s. Felix Bloch, working at Stanford University, and Edward Purcell, from Harvard University,

independently discovered the magnetic resonance phenomenon. Irish physicist Sir Joseph Larmor had earlier demonstrated that atomic nuclei in a strong magnetic field rotate with a frequency that is dependent on the strength of the magnetic field. Bloch and Purcell observed that the energy of these nuclei can be increased if they absorb radio waves with the same resonant frequency. When the atomic nuclei return to their previous energy level, radio waves are emitted, which can be used to describe certain properties of the nuclei. This phenomenon was termed NMR given the requirement of a 'nucleus' to 'resonate' and absorb RF energy in a 'magnetic field'. For this discovery Bloch and Purcell were awarded the Nobel Prize for Physics in 1952.

The 1970s marked a big shift in the development of MRI. In 1971 Raymond Damadian, an American doctor at the State University of New York in Brooklyn, after finding that cancerous and normal tissues have remarkably different relaxation times, proposed that NMR could be used for the development of a diagnostic technique for cancer detection (14). This discovery provided a clinical application for NMR and marked a shift from its major utility as a chemical analysis tool.

In his 1973 paper in *Nature* Paul Lauterbur proposed a method for NMR imaging (15). In this seminal paper Lauterbur described a new imaging technique which he termed zeugmatography (from the Greek zeugmo meaning yoke or joining together). This referred to the joining together of a weak gradient magnetic field with the stronger main magnetic field allowing the spatial

localization of two test tubes of water. Under magnetic field gradients, the analysis of the emitted radio waves could determine their origin inside the subject. This made it possible to build up two-dimensional pictures of structures that could not be visualized with other methods. The technique was called magnetic resonance imaging rather than nuclear magnetic resonance imaging (NMRI) because of the negative connotations associated with the word nuclear in the late 1970's. In 1975 Richard Ernst proposed magnetic resonance imaging using phase and frequency encoding, and the Fourier Transform (16). This technique is the basis of current MRI techniques. Peter Mansfield further developed the utilization of gradients in the magnetic field. He showed how the signals could be mathematically analyzed, which made it possible to develop a useful imaging technique called echo planar imaging. In 2003, Lauterbur and Mansfield were awarded the Nobel Prize in Physiology or Medicine for their discoveries concerning MRI.

The development of MRI as a clinical tool was, however, not a straightforward translation of an idea into a machine. The first MRI for clinical use was developed in the first half of the 1980s. MRI became one of the first medical technologies to require the US Federal Drug Agency's approval, which it received in 1984 (17). Since the 1970s, new imaging techniques, coils, and magnets have led to a continued and open-ended development of MRI, which in turn has led to a variety of new diagnostic and research possibilities.

1.2 Magnetic Resonance Imaging of brain stroke in rodents

Stroke is the third leading cause of death in the United States. With 700,000 cases per year, a person dies from stroke every 3-4 min (18). These statistics have propelled the search for neuroprotective therapies to reduce cell death and infarct volume after stroke. Stroke is also the leading cause of adult disability, because 76% of people survive their stroke, but live with serious disability. Thus, stroke is a lethal disease, but it disables more than it kills imposing a serious cost to society. This fact has led a recent effort to develop strategies for cerebral repair after stroke.

MRI is the clinical gold standard for assessment of cerebral ischemic damage and has also been successfully applied to various animal models for stroke lesion monitoring. Several animal models have been designed specifically to determine reparative events in the brain after stroke (19). Rodent models are best suited to testing neuroprotective therapies, given the serious ethical issues and high cost involved in executing primate and higher mammal models of stroke. Different methods are available for measuring the infarct size in animals, i.e. histological (20; 21) and immunohistological (22) staining, TTC staining (23) and MRI (24; 25). The advantage of MRI is the possibility to perform repetitive in vivo measurements that spares the tissue for further molecular biology and histological methods. The accuracy of assessment of ischemic lesion size with MRI has already been validated by comparison with histological scores (26). These factors lead credence to the use of MRI for evaluation and monitoring of

ischemic damage in stroke models of rodents. Thus, MRI is also now the gold standard for lesion monitoring in small animal models of focal cerebral damage.

1.2.1 Introduction to brain stroke

A stroke refers to an umbrella of conditions caused by the occlusion (ischemic stroke) or hemorrhage of blood vessels (hemorrhagic stroke) supplying the brain (27). Most often, blood flow is compromised within the territory of an occluded blood vessel. Stroke ultimately involves death and dysfunction of brain cells, and neurological deficits that reflect the location and size of the compromised brain area. Nearly 700,000 Americans are afflicted by a new or recurring stroke each year. Although stroke represents the third leading cause of death in the United States (18), only 1% of NIH funding supports stroke research (28). Such a high mortality rate and under-funding point to the difficulty in carrying out stroke research. The specific cellular mechanisms that trigger neurodegeneration following a transient ischemic attack are not well understood. There is a significant gap in the scientific literature in elucidating the mechanism for neuronal cell death following stroke and possible therapeutic treatment to impede such stroke-induced brain damage.

One of the reasons for this has been the difficulty in standardizing experimental stroke models in small animals that are relevant to human stroke (29). The small size of rodent brain, coupled with non-availability of reliable techniques for monitoring of infarct progression make experimental stroke

surgery in rodents a challenging procedure. Also, as residual cerebral blood flow may be required for potential treatments for stroke, and because cerebral ischemia subsequent to cerebrovascular disease is hardly ever complete, models of controlled focal ischemia are favored for testing potential cerebroprotective treatments. We standardized the Middle Cerebral Artery Occlusion (MCAO) model for induction of transient focal cerebral ischemia.

MRI is an effective tool for monitoring lesion caused by experimental stroke and can greatly aid the standardization of a robust stroke model. We hypothesized that high-resolution MRI has requisite technical prowess to establish and validate surgical procedures in experimental stroke in rodents to monitor infarct development. Thus, our objectives with this study were two-fold: 1) to establish a robust stroke model in rat and mice, and 2) to investigate the temporal evolution of stroke-associated damage during 1 week with a model of reversible focal cerebral ischemia.

Significance of proposed research: A robust animal model (especially mice, offering opportunities to work with a large number of genetically modified varieties) is an absolute necessity for stroke research. A comparison of different animals for a treatment paradigm, or study of disease progression is possible only if all surgeries are identical. The current MCAO model has room for improvement and surgery failures might manifest themselves as similar looking infarcts on T2 and diffusion-weighted MRI. This could potentially generate false positives on a treatment paradigm, and increase variability in data. We propose

to use MRI for improving the MCAO method and develop an MRI-based technique to monitor stroke infarct progression that involves interplay of anatomical (T2-weighted) MR imaging and angiography. This would increase repeatability in MCAO model and vitalize stroke research eventually leading to an understanding of underlying mechanisms causing stroke injury.

Considerations for the use of animals in biomedical research: The work described in this dissertation required the use of rat and mouse models of tissue injury. All animal protocols were approved by the Ohio State University Institutional Laboratory Animal Care and Use Committee (ILACUC). Care was taken to minimize animal discomfort, distress, pain and injury at all steps as much as possible. The rat is an established model that we have worked with in the laboratory over the years and is an accepted model for MCAO surgery within the scientific community. Being larger than the mouse, the surgery is much easier to handle and can be performed by researchers with limited experience. The laboratory mouse is a commonly used experimental animal with a wealth of data on their physiology and genetics already available. Mouse models of cardiac occlusion are commonly used in the scientific community. Additionally, genetically altered (gene knockout) mice were used to perform proposed experiments.

1.2.2 Methods

1.2.2.1 Middle Cerebral Artery Occlusion model for induction of stroke

Human cerebral infarcts are mostly found in the MCA region (30), given the deficient collateral blood supply in this area (31). Thus, focal ischemia models involve unilateral, transient or permanent MCA occlusion (32). We employed the well-known transient middle cerebral artery occlusion (MCAO) surgery technique for inducing stroke in mice (32-35). The technique of endovascular filament (intraluminal suture) MCAO as an animal model of ischemic stroke was described first by Koizumi et al (35). It can be applied to both rats and mice. A piece of surgical filament is introduced into the internal carotid artery and forwarded until the tip occludes the origin of the MCA, resulting in a cessation of blood flow and subsequent brain infarction in its area of supply. If the suture is removed after a certain time interval, reperfusion is achieved (transient MCAO); if the filament is left in place the procedure is suitable as model of permanent MCAO. The most common modification is based on Longa who described filament introduction via the external carotid artery, allowing closure of the access point with preserved blood supply via the common and internal carotid artery to the brain after the removal of the filament (34).

The mouse cerebrovascular system is shown in Fig 1.1. Suture insertion depth to block blood flow to MCA is the most critical parameter involved in this surgery. The marker for gauging correct distance of insertion is a mild resistance felt while pushing the occluder, at distance of 16-18 mm from the carotid bifurcation in rat and 8 mm in mice (34; 36). It is believed that this is a fickle marker of MCA occlusion and varies from mouse to mouse (37). A change of

less than 1 mm in suture insertion depth can potentially cause a failed surgery with either no ischemia at all or vessel perforation and brain hemorrhage.

We initially standardized the MCAO surgical model using 8-10 week old mice. Anesthesia was induced with 3% halothane mixed in air and maintained with 1.5% halothane delivered through a facemask. Throughout the surgery, body temperature was maintained at $37\pm 0.5^{\circ}\text{C}$ through the use of a heated surgery table and monitored with a rectal thermometer probe. A 5 mm incision was made between the right ear and eye to expose the skull for laser Doppler blood flow measurement. The animal was then turned over ventrally and a 10 mm incision was made along the neck to expose the right common carotid artery, the right internal carotid artery and the right external carotid artery. The small occipital artery branching off the internal carotid was ligated. The external carotid artery was then tied off with 6-0 nylon suture. The common carotid and internal carotid were clamped and a small incision was made in the external carotid to permit the passage of a 6-0 nylon suture occluder with a blunted tip (0.25 mm wide x 1.0 mm long). Upon successful insertion of the occluder, the external carotid was ligated and the occluder was advanced a distance of 8-9 mm past the common carotid bifurcation into the internal carotid artery to occlude the middle cerebral artery (MCA). A 70- 80% drop in blood flow as determined by laser Doppler flow meter confirmed successful MCA occlusion. The occluder was then fixed in place by tightly tying the stump of the external carotid around the end of the nylon suture. The incisions were sutured and the mouse was brought out of anesthesia for a clinically relevant 90 minutes of MCA occlusion (25).

Following 90 minutes of MCA occlusion, the mouse was reanesthetized, and the occluder was removed. All incisions were again sutured shut and the mouse was brought out of anesthesia. The animal was then returned to its cage and monitored closely for an hour prior to further experimental procedure.

A similar MCAO procedure was used for inducing focal cerebral ischemia in rats. We chose to occlude the MCA for a time period of 90 min, a clinically relevant ischemia duration (25). The major difference in the surgical procedure was the use of a 4-0 suture which was advanced 16-18 mm beyond the carotid bifurcation to occlude the MCA. Presence or absence of ischemic damage was evaluated with MRI or TTC staining as described below.

1.2.2.2 MRI procedure after stroke and histological verification

To non-invasively visualize the extent of brain damage caused by stroke, we initially used rat as our animal model because the larger size of rat brain makes it easier to induce focal cerebral ischemia and standardize MRI scan parameters. One of the manifestations of CNS damage after cerebral ischemia is the formation of brain edema (accumulation of fluid) caused by the breakdown of the blood-brain barrier (38). Since fluid has a much longer T2 compared to surrounding brain tissue, we employed T2 weighted MRI for stroke imaging as it would show distinct contrast between edema (bright) and viable tissue (darker).

We performed T2-weighted MRI on rats on a 4.7 T MRI system with a surface coil placed on the head 2 days after MCAO surgery. A fast spin echo imaging protocol was used to obtain T2-weighted images. An echo train factor of 16 was used to shorten acquisition time. We used the following image parameters which provided an acceptable compromise between image resolution, contrast and time of acquisition: Field of view 35 X 35 mm, acquisition matrix 256 X 256, TR 6000 ms, TE 10.53 ms, slice gap 1.8 mm, rare factor 16, and number of averages 4.

We also standardized a diffusion-weighted imaging (DWI) protocol to evaluate infarct damage. DWI is clinically used for stroke imaging in the acute phase (few hours post) after cerebral occlusion, where T2 weighted imaging might fail to delineate stroke infarct (39; 40). DWI produces images of biological tissues weighted with the local microstructural characteristics of water diffusion, called Brownian motion (41). At acute time points after stroke, intravoxel incoherent motion of water molecules in the MR field gradients produces incoherent phase shifts that result in signal attenuation on DWI images (42). This can be used for infarct delineation with DWI even before T2 weighted imaging can locate the infarct. At time points beyond 24 h after cerebral ischemia-reperfusion, DW images were expected to closely match T2 weighted images to delineate extent of infarct lesion.

After optimization of imaging protocols in rat, similar experiments were performed in mice. Because of the small size of mice, the 4.7 T MRI system

failed to provide good SNR and image resolution. Thus, the mice study was done on 11.7 T vertical bore MRI system with a 30 mm birdcage resonator. Higher field strength and small bore of the magnet especially suited for mice provided good Signal to Noise Ratio (SNR) and resulted in very high resolution T2-weighted images (< 50 micron). Such unparalleled image resolution proved to be an effective tool as it was easy to visualize stroke infarct in mice 24-48 hours after MCAO surgery, confirming surgery success. We used a fast spin echo pulse sequence with the following parameters: Field of view 30 X 30 mm, acquisition matrix 256 X 256, TR 3000 ms, TE 30 ms, echo train factor 8, and number of averages 4.

Histological verification of stroke lesion volume was done using Triphenyltetrazolium Chloride (TTC) staining. TTC is routinely used to quantify infarcted brain tissue and has great specificity, reproducibility, and efficacy (43). TTC produces a red product upon reaction with the respiratory enzymes (dehydrogenases) present in non-infarcted tissues. Irreversibly damaged tissues, lacking dehydrogenases, do not form red reaction products (43). Animals were killed immediately after MR imaging for TTC staining of brain. Animal brains were removed from the skull and rinsed with phosphate-buffered saline. The cerebellum was cut away and 2 mm thick sections (1 mm thick for mouse) of rest of the brain were made using a brain matrix. The sections were incubated with freshly prepared 2% TTC solution at 37°C for 20 min with rotation every 2 min for uniform staining. Each section was photographed with a digital camera mounted

on a dissecting microscope. Extent of infarct observed with TTC and MRI was expected to be tightly associated.

1.2.2.3 Vascular imaging with 3D Magnetic Resonance Angiography

Transient MCAO procedure requires occlusion of MCA and then successful restoration of blood flow. To visualize blood flow through major arteries of the brain and ascertain if and where blood flow was occluded, we performed 3D Time-of-Flight Magnetic Resonance Angiography (TOF MRA) in mice and imaged the vasculature before, during and after MCAO surgery. We conducted MRA experiments on mice on 11.7T MRI system given the higher SNR available on that system. MRA does not require the application of exogenous contrast agents, since the phase or intensity of the MRI signal depends on the macroscopic motion of water protons, yielding an intrinsic contrast between the stationary tissue and flowing blood. High-resolution angiograms were obtained from normal mice, as well as in models of permanent and temporal occlusion. A 3D gradient-echo sequence with the following imaging parameters was employed: TR 30 ms; TE 0.9 ms; flip angle 45° , matrix 128 X 128 X 32; FOV 2 X 2 X 0.8 cm³. The radiofrequency (RF) pulse was frequency-selective, thereby exciting a coronal slice 0.8 cm thick. A birdcage resonator of 30 mm diameter was used for excitation and detection. Raw data was zero-filled to increase the matrix size to 256 X 256 X 256 in an attempt to increase image

resolution. Angiograms were obtained by generating maximum intensity projections (MIPs) using standard software from the MR system.

1.2.2.4 Image Processing

The image processing software ImageJ (from NIH) was used for infarct volume calculation from T2-weighted MRI and TTC images. Raw MR images were converted to standard DICOM (Digital Imaging and Communications in Medicine) format and transferred to an image processing workstation. Infarct area appeared bright both in MRI and TTC images. After appropriate software contrast enhancement of the images, manual planimetry was performed to delineate infarct region, left (ipsilateral) hemisphere and right (contralateral) hemisphere. Only slices from front of brain not including the olfactory lobe to back of brain but not including the cerebellum will be used. Hemispheric volumes were determined on T2-weighted imaging by use of following neuroanatomic landmarks: falx cerebri, corpus pineale, fissura longitudinalis, infundibulum, aqueductus cerebri, and third ventricle (29). Lesion areas were then summed and multiplied by the slice gap to obtain infarct volume. We employed this technique to quantitate stroke injury as a fraction of contralateral hemisphere and total brain volume.

Potential problems, solutions and alternative approaches:

The method described above fails to correct for the space-quantifying effect of edema (29; 44). Edema causes a midline shift in brain, changing relative hemispherical size, and leading to a miscalculation in lesion volumes. Since there is a strong presence of edema in brain after MCAO surgery, we used the following method for edema corrected lesion volume calculation. This calculation is based on 3 assumptions: 1) compression of the contralateral hemisphere is comparable to compression of the entire healthy brain tissue, whereas the lesion is not compressed; 2) The contralateral hemisphere is compressed to the same extent as the affected hemisphere is extended. Total brain volume does not change; and 3) volume extension occurs only within the lesion, not in the unaffected tissue. With these assumptions, a compression factor F may be defined as follows (44):

$$F = \frac{(HV_c + HV_i) / 2}{HV_c} = \frac{HV_c + HV_i - LV^c}{HV_c + HV_i - LV^u},$$

where LV_c and LV_u indicate corrected and uncorrected lesion volume, respectively, and HV_c and HV_i indicate volume of the contralateral and ipsilateral hemisphere, respectively.

Solving this equation for LV_c results in the following:

$$LV_c = HV_c + HV_i - (HV_c + HV_i - LV_u) \cdot \frac{HV_c + HV_i}{2 \cdot HV_c}$$

The uncompressed volume of the contralateral hemisphere is calculated as:

$$HV^u_c = \frac{HV_c + HV_i}{2}$$

Thus, the hemispherical lesion volumes, uncorrected (%HLV_u) and corrected for edema (%HLV_c), were calculated as follows:

$$\%HLV_u = \frac{2 \cdot LV_u}{HV_c + HV_i} \cdot 100$$

$$\%HLV_e = \frac{2 \cdot LV_e}{HV_c + HV_i} \cdot 100 = \frac{HV_c - HV_i + LV_u}{HV_c} \cdot 100$$

1.2.3 Results and Discussion

1.2.3.1 Middle Cerebral Artery Occlusion surgery

MCAO surgery was validated real-time with the use of a laser Doppler flow meter. We consistently observed an expected 70-80% drop in blood flow after occlusion. An animal with blood flow drop outside this range was not included in the study to achieve consistency within results. T2 weighted imaging was done on animals 24-48 h after surgery. MCAO induced infarct was clearly seen as a bright area in the stroke-affected hemisphere. Figure 1.2 shows a T2-weighted image from a rat brain 2d after stroke surgery, depicting the feasibility of T2-weighted imaging for validation of stroke outcome. As expected, a bright region indicative of infarct damage was also observed on DW image in the contralateral hemisphere. Since the earliest time point at which we performed MRI after stroke surgery was 24h, consistent sized infarcts were observed with both T2-weighted

and DW imaging. TTC staining done on animal brain sections after MRI also yielded infarcts that were tightly associated with MRI, thereby confirming our surgical MCAO and MRI techniques (Fig 1.3).

1.2.3.2 Magnetic Resonance Angiography validation of stroke surgery

High-resolution MRA proved to be a very useful tool for verifying the success of MCAO technique. Although MRA application to focal cerebral ischemia models in rats is well documented, descriptions of murine models of MCA occlusion and the experimental difficulties associated with them are scant. In addition to strain-related differences, infarct volume, neurological outcome, and cerebral blood flow appear to be importantly affected by temperature during the ischemic and post ischemic periods, mouse size, and size of the suture that obstructs the vascular lumen. Hata *et al* showed that, by matching the diameter of the thread to the weight of the mouse, the reproducibility of cerebral infarction could be improved (37). These reports point to the difficulties in achieving a consistent MCA occlusion in mice, and that reproducible ischemia requires precise standardization of the experimental conditions.

We observed that high-resolution MRA can be applied to verify the success of MCA occlusion; therefore, it was used to standardize the surgical procedures for MCAO murine brain ischemia model. Figure 1.4 shows maximum intensity projections along the coronal, oblique axial directions of an angiogram of the brain of a mouse acquired in under 5 min. No external contrast agent was

used in these scans and all contrast was generated with inherent time-of-flight effects of moving blood. The high-resolution angiogram revealed mainly the arterial cerebrovascular anatomy. Venous structures were almost completely suppressed because of the low flow velocity. This allowed us to visualize the path taken by the occluder for MCAO technique, and check for hemorrhage in the major arteries caused by this surgical approach. When using TOF techniques with short TR values, signals from both stationary tissues and slowly flowing venous blood are saturated or suppressed. TOF MRA without the use of contrast agents is sensitive to fast flowing blood, as only unsaturated blood entering the imaging volume between subsequent RF pulses produces high signal. By varying TR, some qualitative information on flow velocities can be obtained, especially in the case of ischemic animals (4, 13). The disadvantage is that slowly flowing blood is more difficult to detect by just applying TOF techniques. When blood in the region of interest is not completely exchanged during TR, low flip angle RF pulses have to be used in order to provide optimal signal intensity.

Next, we tested whether the 3D MRA technique had enough sensitivity to show the loss of blood flow during an occlusion episode. MRA was performed on mice where the right ECA was tied off with a suture around it at the bifurcation of carotid artery. This blocked all distal blood flow to the right side of the brain. Figure 1.4 shows 3D MRA on a mouse with such a permanent occlusion. A missing right ICA was observed (arrow) caused by lack of blood flow in that artery. This proved that loss of blood flow to an artery could be observed via this

MRA technique. We applied this observation to visualize blood flow loss to MCA during focal cerebral occlusion.

An angiogram of the cerebrovascular system of the mouse brain acquired 30 min after occlusion of the MCA by a suture is shown in Fig. 1.5. The absence of flow on the occluded MCA and in the ICA; i.e., flow on the ipsilateral part of the circle of Willis was interrupted by the suture, and was clearly visualized. Due to the surgical procedure, the ipsilateral extracranial vessels remained permanently occluded. After pulling the thread following an ischemic period of 90 min, flow on the MCA was reestablished. However, signal intensity was lower than on the contralateral MCA, indicating a slight reduction on blood flow after reperfusion. The infarcted region was verified by T2-weighted fast spin echo imaging 24 h after occlusion (Fig. 1.5B). Infarcts encompassed typically the territory supplied by the MCA, i.e., striatum and cerebral cortex.

Figure 1.6 shows an angiogram acquired 30 min after reperfusion of the MCA. In this case, the MCAO surgery was not successful, since a hemorrhage of the ACA was observed. The transient focal cerebral insult caused by an MCAO surgery cannot be compared to this surgical outcome as a hemorrhage is a permanent insult. In this animal, an infarct was detected 24 h after surgery (Fig. 1.6B), but was not consistent with the expected region of brain to be infarcted. In all mice that presented a remaining flow in the MCA because of misplacement of the thread during occlusion, no infarcted region was detected 24 h later. All such animals were excluded from the study.

1.2.3.3 Dynamics of Stroke-induced infarct

Armed with a robust surgical technique, we performed MCAO surgery on rat and mouse models and tracked infarct damage with MRI. Mice study was done on 11.7 T vertical bore MRI system with a 30 mm birdcage resonator. Higher field strength and small bore of the magnet especially suited for mice provided good SNR and resulted in very high resolution T2-weighted images (< 50 micron). An in-plane resolution of 40 micron was routinely obtained for high resolution scans. Such unparalleled image resolution proved to be an effective tool as it was easy to visualize stroke infarct in mice 24-48 hours after MCAO surgery, confirming surgery success. Figure 1.7 shows comparative T2-weighted images in mice on a 4.7 T and 11.7 T MRI, demonstrating much better image resolution and detail obtained with 11.7T.

Time course of infarct lesion in rat brain was monitored using T2 weighted imaging. We used Wistar rat strain for stroke surgery as these animals have a complete Circle of Willis and focal cerebral ischemia can be induced with MCAO technique (45-47). The time course provided us control data that could be used to test the efficacy of potential treatment options against neurodegeneration associated with cerebral ischemia. Fig 1.8 shows the time course of infarct volume as measured with MRI after 90 min MCAO surgery. Between 2 and 7 days after reperfusion, apparent lesion size as measured with T2WI decreased considerably. Similar decreases in apparent lesion volumes have been reported in a serial MRI study that investigated lesion evolution in human stroke (48). The

decrease in apparent lesion volume and lesion conspicuity on T2-weighted images between 2 and 7 days may be explained in part by the resolution of vasogenic edema. Other factors that could contribute to a reduced lesion conspicuity on T2-weighted images include the invasion of inflammatory cells into the infarct, an increase in the number of glial cells (gliosis), or petechial hemorrhages.

Limitations of our study:

There are a number limitations of our study which are of importance when trying to extrapolate from our results obtained with the MCAO model to human stroke. One important difference between MCAO model and human stroke is that there is a sudden onset of reperfusion after removal of the intraluminal suture, whereas recanalization with either spontaneous or recombinant tissue plasminogen activator (rtPA)-induced thrombolysis in humans is a comparatively slow process (25). In addition, with thrombolysis, partial clot fragmentation may occur and lead to the lodging of clot fragments in smaller downstream arteries and to microembolism of the peripheral vasculature (49). There may be other additional adverse pharmacological processes specific to rtPA treatment that are not encountered in mechanical occlusion-reperfusion models (50). On the other hand, the abrupt restoration of blood flow in the suture model and the resulting early postischemic hyperperfusion may exacerbate the effects of postischemic BBB disturbances, particularly with ischemia times sufficiently long to cause damage to the microvasculature.

1.2.4 Conclusions

The overall objectives of this study were two-fold: to establish a robust MCAO model of focal cerebral ischemia in rodents; and to follow a time-course of the dynamics of ischemic lesion. We chose to perform occlusion for 90 min, a time period that is clinically relevant for length of an ischemic attack. We employed high-resolution MRI and MRA as tools for surgical technique perfection and validation to enhance reproducibility of MCAO induced brain lesion. MRI was also used as a diagnostic tool for the measurement of ischemic lesion volume with time.

We observed that suture insertion depth was the most important parameter that induced variability in MCAO surgery. Shallow suture placement in the mouse vasculature either led to little or no ischemia of MCA, or hemorrhage of the ACA if suture was inserted too deep. Employment of a laser Doppler flow meter provided us with a real-time report of cerebral blood flow, but even then it could not be specified which artery was occluded, and whether a hemorrhage had taken place. 3D MRA was used to generate a model of the rodent cerebrovascular system. All major arteries of the brain were clearly visualized with this technique and confirmation of MCA occlusion was easily done. MRA was done during occlusion and after reperfusion to confirm that only transient occlusion and no hemorrhage took place. This technique enabled us to confirm that all MCAO surgeries were similar and accurately represented brain damage caused by a transient focal MCA occlusion.

To monitor stroke-induced lesion progression in the brain, we employed T2-weighted MRI. T2 weighted imaging is the clinical gold-standard for infarct delineation after stroke. We generated a time course of infarct volume in the brain, with the striking observation that cerebral edema shrinks between 2 and 7 days after reperfusion with an associated decrease in infarct intensity. This has been reported before in some animal studies, but the underlying mechanisms have not been studied systematically and warrant further examination. The time course of infarct points to the presence of dynamic mechanisms in place that can potentially modulate cerebral damage post stroke and reperfusion.

Other groups that have studied the acute effects of stroke injury in rats have tried to define the therapeutic window of opportunity where ischemic damage can be prevented and essentially reversed with therapeutic techniques (51-55). MRI studies suggest that brief ischemic periods (30 to 60 min) may indicate a relatively long therapeutic window, but further work is needed to establish whether secondary ischemic tissue damage can be prevented. Longer ischemic episodes (2.5 h) cause blood brain barrier damage which leads to pronounced subacute vasogenic edema, both of which can be readily assessed with MRI (33; 56). Based on these results, the prevention of both delayed ischemic damage after brief ischemic episodes and subacute vasogenic edema after more prolonged ischemia appears to be a valuable therapeutic target, and treatment efficacy may be evaluated with serial MRI.

In conclusion, we established a robust MCAO model of focal cerebral ischemia in rats and mice. Serial evaluation of ischemic damage showed that in the MCAO model, MRI characteristics of ischemic regions change dynamically during the reperfusion period. We conclude that the prevention of subacute vasogenic edema after ischemia appears to be a valuable therapeutic target, and treatment efficacy may be evaluated with serial MRI.

1.3 Redox Measurement using Electron Paramagnetic Resonance

Electron Paramagnetic Resonance, EPR, is a spectroscopic technique which detects species that have unpaired electrons. These include free radicals, many transition metal ions, and defects in materials. Free electrons, often short-lived, play crucial roles in many processes such as photosynthesis, oxidation, catalysis, and polymerization reactions. As a result EPR crosses several disciplines including: chemistry, physics, biology, materials science, medical science and many more.

EPR detects unpaired electrons unambiguously. Other techniques such as fluorescence may provide indirect evidence of free radicals, but EPR alone yields incontrovertible evidence of their presence. In addition, EPR has the unique power to identify the paramagnetic species. EPR samples are very sensitive to local environments. Therefore, the technique sheds light on the molecular structure near the unpaired electron. Sometimes, the EPR spectra exhibit dramatic lineshape changes, giving insight into dynamic processes such as

partial pressure of oxygen. The EPR spin-trapping technique detects and identifies short-lived free radicals. This technique has been vital in the biomedical field for elucidating the role of free radicals in many pathologies. Another important application for quantitative EPR is radiation dosimetry. Among its uses are dose measurements for sterilization of medical goods and foods, detection of irradiated foods, and the dating of early human artifacts.

In this study, we standardized a novel and effective electron paramagnetic resonance (EPR) spectroscopy based approach to assess the redox environment of dermal wound site in vivo.

1.3.1 Introduction to redox control of wound healing

The traditional view regarding the primary role of oxidants in biology is that they incite oxidative damage. Classically, reactive oxygen species (ROS) have been extensively studied as damaging by-products accidentally leaked from the mitochondrial respiratory chain (57). It is estimated that 3–5% of total oxygen consumed by the mitochondria generates ROS under basal conditions (58). It is now argued that cells deliberately produce ROS which act as cellular messengers that drive numerous aspects of molecular and cell biology (59). Specifically, we have previously reported that H₂O₂ is actively generated by cells at the wound-site and that H₂O₂-driven redox signaling support wound angiogenesis and healing (60; 61).

Disrupted vasculature limits the supply of oxygen to the wound site. Compromised tissue oxygenation or wound hypoxia is viewed as a major factor that limits the healing process as well as wound disinfection (62). The general consensus has been that, at the wound site, oxygen fuels tissue regeneration (63) and that oxygen-dependent respiratory burst is a primary mechanism to resist infection (64). Recent works from our laboratory have developed a new paradigm supporting that oxygen-derived reactive species at the wound site not only disinfect the wound but directly contribute to facilitate the healing process (58; 60; 61; 65).

Wound healing commences with blood coagulation followed by infiltration of neutrophils and macrophages at the wound site to release reactive oxygen species (ROS) by oxygen consuming respiratory burst. In 1999, the cloning of *mox1* (later named as *Nox1*) marked a major progress in categorically establishing the presence of distinct nicotinamide adenine dinucleotide phosphate (NADPH) oxidases in non-phagocytic cells (66). Taken together, the wound-site has two clear sources of ROS: (i) transient delivery of larger amounts by respiratory burst of phagocytic cells; and (ii) sustained delivery of lower amounts by enzymes of the *Nox/Duox* family present in cells such as the fibroblasts, keratinocytes and endothelial cells (58). Recent studies show that, at low concentrations, ROS may serve as signaling messengers in the cell and regulate numerous signal transduction and gene expression processes (67). Inducible ROS generated in some non-phagocytic cells are implicated in mitogenic signaling (68). A direct role of NADPH oxidases and ROS in facilitating

angiogenesis has been proven (61). In line with these observations we have previously reported that at the wound site, ROS may promote wound angiogenesis by inducing VEGF expression in wound-related cells such as keratinocytes and macrophages (60).

The overall objective of this study was to develop an EPR spectroscopy and spin trapping based technique to assess wound-site redox environment (69) and to develop an understanding of the role of Rac2-dependent oxidant production (70) in wound healing.

1.3.2 Materials and Methods

1.3.2.1 EPR probe

¹⁵N-PDT (4-oxo-2,2,6,6-tetramethylpiperidine-d16-1-oxyl, CDN Isotopes, Canada) was used as the nitroxide spin probe. At low concentration (<2 mM), ¹⁵N-PDT produces a well separated doublet EPR spectrum with a hyperfine-coupling constant of 2.2 mT. At higher concentrations, there is spin-spin broadening which causes the two peaks to merge into one broad middle peak of lower amplitude (Fig. 1.9). ¹⁵N-PDT provides for enhanced sensitivity and a narrower line-width than non-isotope enriched tempone. The nitroxide solution was prepared at 50 mM concentration in phosphate-buffered saline, sub-aliquoted, and kept frozen until use.

Spin trap 5,5-dimethyl-1-pyrroline-N-oxide (DMPO) was obtained from Dojindo Laboratories (Kumamoto, Japan) and was used to quantitate oxidant

radical production. Spin trapping is a technique in which transient radicals, e.g., hydroxyl (OH \cdot), superoxide (O $_2^{\cdot-}$), or relatively stable radicals such as NO that are undetectable under normal conditions react with spin traps to form a radical adduct that is detectable by EPR (71). We used DMPO for spin trapping of superoxide radical at the wound site.

1.3.2.2 Excisional dermal wound model

C57BL/6 mice between the ages of 8-10 weeks were used. Punch biopsy (3 mm) wounds were developed on the back of mice in pairs (Fig. 1.10A) for L-band EPR experiments. The back of the mouse was shaved with standard animal hair clippers (#40 blade) and disinfected with betadine (Fisher, USA). Using micro-dissecting forceps, skin of the animal was lifted along the line as shown and a 3 mm dermal biopsy punch was driven through the two folds of skin. Axially, the wounds were made just above the bridge of the back to avoid motion artifacts during EPR measurements. This resulted in two symmetrical full thickness 3 mm diameter wounds in mouse without any underlying tissue damage. The separation between the two wounds was kept between 10-15 mm. A similar technique was used to create 8 mm punch wounds for X-band EPR spin trapping experiments.

For wound closure experiment, two 8 mm X 16 mm full-thickness excisional wounds (60) were placed on the dorsal skin, equidistant from the midline and adjacent to the four limbs. Digital photographs of wounds in full view and in one plane were taken with a digital camera on specified days after

wounding. Images were transferred to a computer and wound areas were calculated using WoundMatrix software (61).

1.3.2.3 EPR spectroscopy instrumentation for measurements in wound

EPR spectroscopy experiments were performed on an L-band spectrometer (Magnettech GmbH, Germany) which was set up for topical measurements on the skin of mice. A surface coil resonator of 10 mm diameter with automatic tuning and matching control was used. Mice were anesthetized with an intra-peritoneal injection of ketamine (90 mg/kg) and xylazine (20 mg/kg) and placed in prone position between the poles of the magnet. Position of the animal was adjusted to place the surface resonator around the wound and in contact with the skin. After tuning and matching the system, 6 μ l of 50 mM PDT was topically applied to the wound site and EPR spectroscopy measurements were started. Measurements were taken for a minimum of 45 minutes or till the nitroxide EPR signal decayed completely, whichever was later. EPR spectroscopy parameters were chosen as follows: Center field 44.4 mT, modulation amplitude 0.0135 mT, scan width 0.81 mT, scan time 20 s, microwave power 25 mW, time constant 0.1 s.

EPR spectra for spin trapping were recorded using quartz flat cells at room temperature with a Bruker ESP 300E spectrometer operating at X-band with 100 kHz modulation frequency and a TM110 cavity. DMPO (50 μ l of 1 M) was topically applied to two day-old 8 mm punch biopsy wounds. After 10 min,

the wound rinsate was collected from the wound cavity, diluted 20X in PBS containing DTPA, and its EPR spectra was recorded.

1.3.2.4 Direct H₂O₂ measurements

H₂O₂ levels in wound fluid were measured using a real-time electrochemical H₂O₂ measurement as described (72). The Apollo 4000 system (WPI, Sarasota, FL) was used for analysis. H₂O₂ was measured using the ISO-HPO-2 2.0 mm stainless steel sensor, with replaceable membrane sleeves and an internal refillable electrolyte. This electrode technology includes a H₂O₂ sensing element and separate reference electrode encased within a single Faraday-shielded probe design (WPI, FL). Wound fluid was harvested from mice and was immediately used for direct H₂O₂ measurement as reported (61).

1.3.2.5 EPR data acquisition and analysis

EPR spectra were acquired and stored using the *Analysis* software (Magnettech GmbH). The data was then converted into a special format that was read using custom-built software in our laboratory for visualization, analysis and export of spectral parameters (e.g. intensity and linewidth) into Microsoft Excel, where the final decay curves of the nitroxide were generated. Table Curve 2D software was used for mathematical modeling of nitroxide kinetics. Quantitation of X-band EPR spectra was performed using custom-built software developed in our laboratory. Quantitation of the observed free radical signals was performed by computer simulation of the spectra and comparison of the double integral of

the observed signal with that of a TEMPO standard (1 μM) measured under identical conditions (73).

1.3.2.6 Histology

Immunohistochemistry: Wounds developed with a 3 mm biopsy punch were collected on day 1 and day 2 using a 6 mm biopsy punch and embedded in OCT. Cryosections (10 μm) were cut and fixed in ice-cold acetone for 5 minutes. Peroxidase blocking was done by incubating the section with 0.3% H_2O_2 for 5 min prior to serum-blocking with 10% goat serum. Primary antibody incubations were done as follows: anti-mouse neutrophil (Serotec), 1:100 for 1 h at room temperature; rabbit anti-HNE (Alexis), 1:500 for 1 h at room temperature; rat anti-mouse F4/80, 1:50 for 1 h at room temperature. Color was developed after incubating the section with the appropriate biotinylated secondary antibody (1:200) utilizing the ABC/DAB method (Vector) according to the manufacturer's instructions. Sections were counterstained with hematoxylin, dehydrated sequentially in alcohol with two changes of xylene and mounted with permanent mount.

Immunofluorescence: Two-day old 3 mm punch biopsy wounds, including the wound edge, were harvested with a 6 mm punch biopsy. Skin tissue was embedded in Optimal Cutting Temperature (OCT) compound and frozen. Sections (10 μm) were cut with a cryostat and fixed in acetone. Subsequently sections were blocked with 10% goat serum before incubating with rabbit anti-Hydroxynonenal (1:500; Alexis) and rat anti-mouse neutrophil (1:100; Serotec)

together for one hour at room temperature. After washing, the sections were incubated in anti-mouse IgG conjugated to Alexa 488 and anti rat IgG conjugated to Alexa 568 for 30 min at room temperature (both 1:100). Sections were counterstained with DAPI (1:10,000) and visualized under a Zeiss Axiovert 200M microscope.

For CD31 staining, cryosections were fixed in acetone and blocked with 10% BSA Fraction V (Acros) for 30 minutes. Sections were then incubated with PE conjugated anti-mouse CD31 (1:100; eBiosciences) overnight at 4°C, counterstained with DAPI, and visualized as above.

1.3.2.6 Computer Assisted Image Analysis

A color subtractive-computer assisted image analysis system was used to quantitatively label and calculate immunostained area after staining and subsequent digital imaging (74). We employed Adobe Photoshop 6.0 with Image Processing Toolkit 5.0 (www.reindeergraphics.com) software for image analysis. This method, instead of positive color selection, serially removes all non-specific color from the images using a sequential method of color background removal leaving behind only the positive stain on a white background. To remove sampling error caused by imaging only a part of the stained tissue, each tissue slide was imaged in three different areas at 20X magnification on a Zeiss microscope. Images were converted from the Zeiss ZVI format to standard JPEG format and loaded into Adobe Photoshop for analysis.

All steps involved in image analysis were stored in a macro in Adobe Photoshop. The macro was developed on an image selected at random from the images of the tissue sections. First, a copy of the layer containing the tissue section image was initially made. The color subtraction routine as described before (74) was modified as required for our images and executed on this new layer. Purple-pink stain of hematoxylin and other background color was colorimetrically removed and replaced with white, leaving behind a dark brown DAB color which was the positive stain. The color subtraction process was continued till all non-specific color was removed from the image. The color subtraction layer was then duplicated and binary thresholding was performed on it. A threshold level of 252 was used. The thresholding routine converts all darker pixels above selected threshold level to black, and all pixels lighter than that to white. This results in a black and white image with positively stained areas in black on a white background. Feature measurement was then performed on this thresholded image to objectively calculate the area of stained tissue as a percentage of the complete image. The macro recording was then stopped, and the macro was saved. This macro was instrumental to generate immunostained areas from all sections automatically and efficiently without user bias.

1.3.3 Results and Discussion

1.3.3.1 Nitroxide kinetics in wound and its modeling

Using a non-invasive EPR-based technique we sought to quantify the oxidant concentration at the wound site in mice during the inflammatory phase,

which lasts for about 2-3 days after wounding (75). A nitroxide probe was topically applied to the open wound. Signal decay of the probe applied to the wound was monitored to generate a mathematical model to derive oxidant levels at the wound site. The nitroxide solution was topically applied to the dermal wounds (Fig. 1.10A) of mice and the resonator placed directly above and around the wound site (Fig. 1.10B). EPR spectroscopy measurements performed immediately after wounding were collected as a function of time, and are shown in Fig. 1.10C. At the beginning, one broad peak was observed (0 min). This broad signal is attributed to electron spin exchange interaction of the nitroxide radicals in the concentrated solution at the surface of the skin (76). With time, the broad central peak became narrower and weaker. In addition, another component with two sharp peaks (doublet) appeared, increased over the first 10 min and then gradually declined because of reduction of nitroxide. Only the left peak is shown here in Fig. 1.10C, as the two side peaks were symmetrical. This component is a result of the diluted ^{15}N -PDT within the tissue which gives rise to a doublet with hyperfine-coupling constant $a_{\text{N}} = 2.2 \text{ mT}$ (77).

Next, we sought to mathematically model the observed pattern of nitroxide kinetics at the wound site with the objective to quantitatively describe the level of oxidants at wound site that attribute to signal decay. A two-step exponential procedure was employed to describe nitroxide kinetics in wounds as standardized previously (77). In our model we assume that there are two processes in the system – penetration and reduction of nitroxide. There is an initial penetration of nitroxide into the wound site, which is a physical process

defined exponentially by a first order equation with rate constant k_p . The nitroxide (initial concentration M_0) gets diluted (given by M_1) as it penetrates the wound tissue. This causes a loss in intensity of middle peak and increase in intensity of side peaks. Wound tissue reductants reduce the nitroxide and cause decay in signal intensity of the side peaks. This reduction process, which goes on in conjunction with the first process, is described by a first order rate equation with decay constant k_r . Fig. 1.10C shows EPR spectra of the left peak taken at different time points in a wound at day 0. We observed that signal intensity increases at first and then decreases. If $M_2(t)$ describes concentration of nitroxide during the reduction process (at any given time t), the nitroxide signal intensity in the wound is given by the following equation:

$$M_2(t) = c + \frac{k_p M_0}{k_r - k_p} (e^{-k_p t} - e^{-k_r t})$$

The constant c denotes the background level of EPR signal from nitroxide, for example, on the wound surface that is not subjected to the bioreduction. Using EPR spectroscopy we measured M_2 with time and using equation 1 we calculated the reduction rate constant k_r , which is a measure of the level of oxidants at the wound site (77). Table Curve 2D software was used for data fitting. Fig. 1.10D shows that the 2-step exponential model closely fits the acquired EPR data. In all experiments, correlation coefficient $r^2 = 0.94$ between observed data and the mathematical model. To confirm that at least part of signal-loss observed was because of nitroxide reduction, 4 μ l of freshly prepared potassium ferricyanide (10 mM) was topically administered to the wound 25 min

after initial application of PDT. Ferricyanide is well-established to oxidize the hydroxylamine form of spin labels to their parent nitroxide (78-80). After a brief delay, an increase in signal intensity was observed (shown by arrow in Fig. 1.10E) which was attributed to oxidation of the reduced nitroxide back to its original form. This experiment was performed at time points day 0, day 1 and day 2 after wounding with nitroxide regeneration observed at each time point.

1.3.3.2 Oxidant levels at wound site peak 2 days after wounding

To estimate the level of oxidants at wound site in the inflammatory phase of wound healing, the above-described EPR measurements were performed on day 0, day 1 and day 2 after wounding because the inflammatory phase in wounds lasts from day 0 to day 3 in mice (75). Nitroxide half-life was calculated as $0.693/k_r$. Figure 1.10F shows the change in half-life of nitroxide at the wound site with healing. It is known that lower stability of the probe corresponds to a more reductive state, and a higher stability corresponds to a more oxidative state of the wound tissue (77). We observed that subsequent to wounding, the stability of nitroxide probe at the wound site is higher (Fig. 1.10F). Thus, a higher concentration of oxidants was evident at the wound site on day 2 after wounding, which is the peak time for respiratory burst by the inflammatory cells (75). We concluded that a healing wound is significantly rich in oxidants two days after wounding, which corresponds to the inflammatory phase.

1.3.3.3 Spin trapping of superoxide radical with DMPO

After observing an oxidizing environment at the wound site with the nitroxide clearance approach, we employed DMPO as spin trap to quantitate superoxide radical production *in vivo*. In the presence of DMPO, EPR analysis of wound rinsate in phosphate-buffered saline containing the metal ion chelator DTPA indicated formation of the spin trap radical adduct DMPO-OH. The spectrum in Fig. 1.11A, a 1:2:2:1 quartet that is not evident in the absence of wound rinsate (Fig. 1.11C), exhibited isotropic hyperfine splitting of $a_N = a_H = 1.49$ mT, characteristic of the hydroxyl radical adduct of DMPO, DMPO-OH. DMPO-OH can be formed by direct trapping of hydroxyl radical by DMPO, or as a product of decomposition of the superoxide radical adduct DMPO-OOH (22; 23). DMPO-OOH, with a half time of 45 s in aqueous media, decomposes into a number of products, including DMPO-OH (81). The abolishment of the DMPO-OH spectrum by the addition of superoxide dismutase (SOD1) (Fig. 1.11B), further suggests that the DMPO-OH adduct is derived from superoxide. Thus, we concluded that the DMPO-OH spectrum noted at the wound site in our studies was caused by superoxide, the direct product of NADPH oxidases (58).

Next, we investigated the time course of superoxide generation at the wound site following wounding. Fig. 1.12 shows EPR spectra of wound rinsate collected at specific time-points after wounding. We noted that superoxide production was at its maximum on day 2 when the inflammatory cells are actively engaged in respiratory burst activity. Quantitation of superoxide at the wound site is shown in Fig. 1.12F, where the data is normalized to show relative

concentrations. This corroborates our data on nitroxide decay (Fig. 1.10F) showing higher oxidant levels at wound site two days after wounding.

This work presents first evidence demonstrating the production of superoxide radicals at the wound site using a DMPO spin trapping technique. Basal superoxide production in the intact skin was below detection limits. Superoxide levels, however, sharply increased as a function of time. Superoxide levels were the highest at day two of healing which corresponds with the peak time of respiratory burst of invading phagocytes (61).

1.3.3.4 Impaired healing and compromised superoxide production in Rac2 knockout mice

Rac2 is a Rho GTPase that is expressed in cells of hematopoietic origin, including neutrophils and macrophages. Rac2 regulates reduced NADPH oxidase activation and other functional responses in neutrophils. Although not required for translocation of p47phox and p67phox, Rac2 is necessary for optimal activity of the assembled oxidase complex (82). Mice deficient in hematopoietic-specific Rac2 exhibit agonist-specific defects in neutrophil functions including superoxide production elicited by phorbol ester, fMLP, or IgG-coated particles, despite expression of the highly homologous Rac1 isoform. Although Rac2 is a relatively minor isoform in murine macrophages, it plays a non-overlapping role with Rac1 to regulate host defense functions in this phagocyte lineage (82).

NADPH oxidase deficiency impairs wound healing as is noted in chronic granulomatous disease (58). Defect in the expression of any of the essential subunits of NADPH oxidase *e.g.*, Rac2 is expected to compromise respiratory burst dependent oxidant production (82). Rac2^{-/-} mice suffer from significantly delayed wound closure (Fig. 1.13) indicating that Rac2- dependent NADPH oxidase activity is important in supporting wound healing. Rac2 deficiency has been reported in humans and is associated with poor wound healing (83). In humans, Rac2 plays a critical and unique role to maintain normal neutrophil function (66).

Consistent with these observations we also noted that Rac2^{-/-} mice suffer from impaired oxidant production at the wound site. EPR spectra of wound rinsate collected from wild type and Rac2^{-/-} mice 2 days after wounding is shown in Fig. 1.14A and B, respectively. We chose this time point because the amount of superoxide production at the wound site in wild type animals was found to be highest at day 2 (Fig. 1.10F, Fig. 1.12F). We observed a three-fold decrease in superoxide production at the wound site in Rac2^{-/-} mice compared to wild type (Fig. 1.14C). Quantitation of H₂O₂ in wound fluid using the electrochemical detection system showed significantly decreased peroxide concentration in wound fluid in rac2^{-/-} mice compared to matched wild-type (Fig. 1.14D). These data point to a decreased respiratory burst dependent oxidant production in Rac2^{-/-} animals.

1.3.3.5 Rac2^{-/-} mice: recruitment of phagocytic cells to wound site is not affected, but their function is impaired

When skin is wounded, the local tissue rapidly recruits inflammatory cells. Neutrophils reach the wound site in hours followed by macrophages which peak in day 2 after wounding (84). We examined the wound-edge tissue from Rac2^{-/-} mice and their corresponding wild-type mice. The number of neutrophils recruited to the wound-edge tissue on day 2 was imaged and scored using a color subtractive-computer assisted image analysis method. Two days after wounding, Rac2^{-/-} mice tended to recruit more neutrophils to the wound-site but the difference was not statistically significant ($p = 0.07$, Fig. 1.15). Consistent with the pattern noted for neutrophils, macrophage recruitment in Rac2^{-/-} mice tended to be higher but the difference was not statistically significant ($p = 0.11$, Fig. 1.16). Taken together, it can be concluded that Rac2^{-/-} did not compromise the ability of the mice to recruit inflammatory cells to the wound site.

At the wound site, inflammatory cells exhibit potent respiratory burst activity. 4-Hydroxy-2-nonenal (HNE) is a major product of endogenous lipid peroxidation, which is found as a footprint in the aftermath of respiratory burst (85). 4-HNE levels were clearly lower in the wound-edge tissue of Rac2^{-/-} mice compared to that of wild-type controls (Fig. 1.17 A-C). This observation is consistent with other results in this study demonstrating lower levels of reactive oxygen species in the wound of Rac2^{-/-} mice. Employing a double immunostaining approach it was evident that in wound-edge tissue of wild-type mice neutrophils co-localize with 4-HNE stain indicating active respiratory burst of the

inflammatory cells (Fig. 1.17D). In the wound-edge tissue of *Rac2*^{-/-} mice, however, neutrophils did not associate with strong 4-HNE stain supporting other data in this study that indicate compromised respiratory burst activity in *Rac2*^{-/-} mice (Fig. 1.17E).

Rac GTPases are believed to contribute to migration in leukocytes by transducing signals from cell surface receptors to the actin and microtubule cytoskeletons. Mammals have three closely related Rac isoforms, Rac1, Rac2 and Rac3, and it is widely assumed that cell migration requires the activity of these Rac GTPases. Rac1 and Rac2 have distinct roles in regulating cell morphology, migration and invasion, but are not essential for macrophage migration or chemotaxis (86). Consistent with this observation we noted that a lower level of oxidants at the wound site in *Rac2*^{-/-} mice was not caused because of impaired level of recruitment of phagocytic cells. The recruitment of both macrophages and neutrophils to the wound site was not impaired in *Rac2*^{-/-} mice.

1.3.3.6 Impaired angiogenesis in Rac2^{-/-} mice

Rac2^{-/-} mice suffer from significantly delayed wound closure (Fig. 1.13) indicating that *rac2* is an essential component for wound closure. CD31 is characteristic of endothelial cells. To study role of *rac2* in angiogenesis we performed immunohistochemical staining for CD31 (red) and DAPI (blue, nuclei) on cryosectioned wound-edge tissue from wild-type and *rac2*^{-/-} mice sampled 8 days after wounding (Fig. 1.18). Compared to wild-type mice, the lower

abundance of CD31 stain in the sections obtained from *rac2*^{-/-} mice (right) suggests impaired endothelial cell proliferation in mice deficient in *rac2*.

1.3.4 Conclusions

The overall objective of this work was to develop an EPR-based analytical technique for evaluation of wound-site redox environment. We specifically applied this technique to study the effects of deletion of *rac2*, a Rho GTPase expressed in neutrophils and macrophages which regulates NADPH oxidase activation and other functional responses, on wound healing.

In this work, using nitroxyl spin probe ¹⁵N-PDT we observed that a healing wound is significantly rich in oxidants two days after wounding, which corresponds to the inflammatory phase. This work presents first evidence demonstrating the production of superoxide radicals at the wound site using a DMPO spin trapping technique. We have previously developed instrumentation and methodology for non-invasive measurement and imaging of nitroxide spin labels in the skin of normal human volunteers (77). This work represents a maiden effort to employ L-band and X-band EPR for quantitative measurement of redox environment and spin trapping of superoxide radicals in full thickness dermal wounds in mice.

NADPH oxidase-dependent superoxide generation is highly active at the wound site. The highest level of peroxide in bodily fluids is found in the wound (61). At the wound sites, hydrogen peroxide drives wound angiogenesis by inducing redox signaling (67). Such redox-dependent mechanisms are

compromised under conditions of NADPH oxidase deficiency. Thus, individuals with defective NADPH oxidase suffer from impaired healing such as in chronic granulomatous disease (58). Consistent with these observations we noted that *Rac2*^{-/-} mice suffer from impaired oxidant production at the wound site. EPR results showed that in *Rac2* deficient mice oxidant production during the inflammatory phase was 3-fold lower than that in corresponding wild-type control mice. Lower level of oxidants, under conditions of *Rac2* deficiency, was associated with impaired wound closure.

Rac1 and *Rac2* have distinct roles in regulating cell morphology, migration and invasion, but are not essential for macrophage migration or chemotaxis (86). Consistent with this observation we noted that a lower level of oxidants at the wound site in *Rac2*^{-/-} mice was not caused because of impaired level of recruitment of phagocytic cells. The recruitment of both macrophages and neutrophils to the wound site was not impaired in *Rac2*^{-/-} mice.

Taken together, the findings of this study support that the wound site is rich in oxidants. *Rac2* significantly contributes to oxidant production at the wound site and supports the healing process.

1.4 Figures

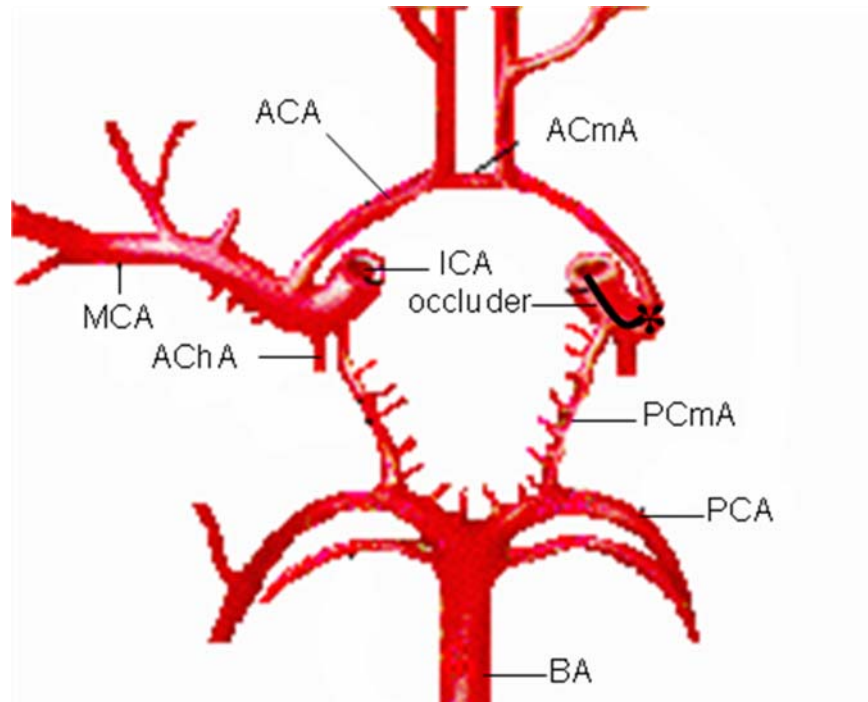


Figure 1.1: Mouse cerebrovascular anatomy. The basilar artery (BA) enters the Circle of Willis from the posterior side and the internal carotid arteries (ICA) enter from the ventral side. Communicating arteries (PCmA, ACmA) complete the circle and the anastomosis which then leads to anterior (ACA), middle (MCA), and posterior cerebral arteries (PCA) which carry blood into the brain. Anterior Choroidal Artery (AChA) branches off the ICA just before MCA. An occluder (shown in black) is pushed through the ICA till the branch off point of MCA to cause focal ischemia.

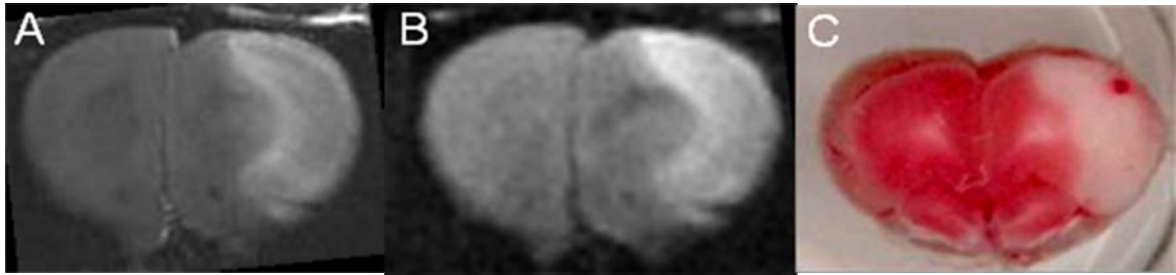


Figure 1.2 | T2 and diffusion weighted MRI is consistent with TTC staining in rat brain after MCAO surgery.

(A) T2-weighted MRI from rat brain acquired on 4.7 T MRI system 2 days after stroke surgery using a RARE sequence with the following parameters: FOV 35X35 mm, acquisition matrix 256 X 256, TR 6 s, TE 10.53 ms, slice gap 1.8 mm, rare factor 16, number of averages 4. Image processing was done using ImageJ software. For infarct volume calculation from 2D images, raw MRI images were first converted to DICOM format and read into ImageJ. After suitable contrast enhancement of the images, manual delineation of the infarct region was done. Infarct areas were summed from all brain slices and multiplied by slice thickness to get infarct volume. This process was repeated with images acquired in coronal and sagittal planes to verify infarct volume calculation method. (B) Diffusion-weighted image from same rat 2 days after surgery with following parameters: FOV 35X35 mm, acquisition matrix 128X128, TR 3093.5 ms, TE 40 ms, slice gap 1.8 mm, rare factor 4, b- value 1067.9. (C) After MRI, the animal was decapitated under deep anesthesia and brain was excised. 2 mm-thick slices of the brain were made in a brain matrix. All slices were stained in 2% TTC for 20 minutes and were then scanned. The brain atlas by Paxinos and Watson was used to co-register MRI images with TTC stained slices. Images shown above are +3.2 mm from the bregma. We observed that MRI images were tightly associated with TTC staining.

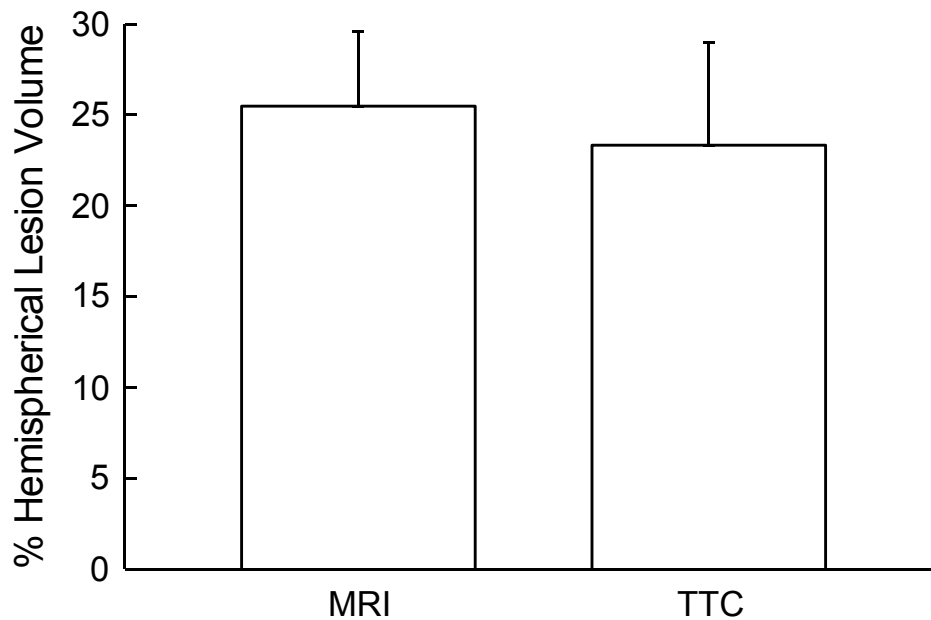


Figure 1.3 | Comparison of lesion volume calculated with MRI and TTC staining. T2 weighted MRI was performed on rat 2 d after MCAO surgery. Immediately after MRI, animals were killed and brain was excised. Brain tissue was sectioned into 2 mm thick slices and stained with 2% TTC for 20 min. Infarct volume was calculated both with MRI and TTC with manual planimetry using ImageJ software. No statistical difference was observed between the two groups ($p = 0.40$). Data are shown as mean \pm SD, $n = 5$.

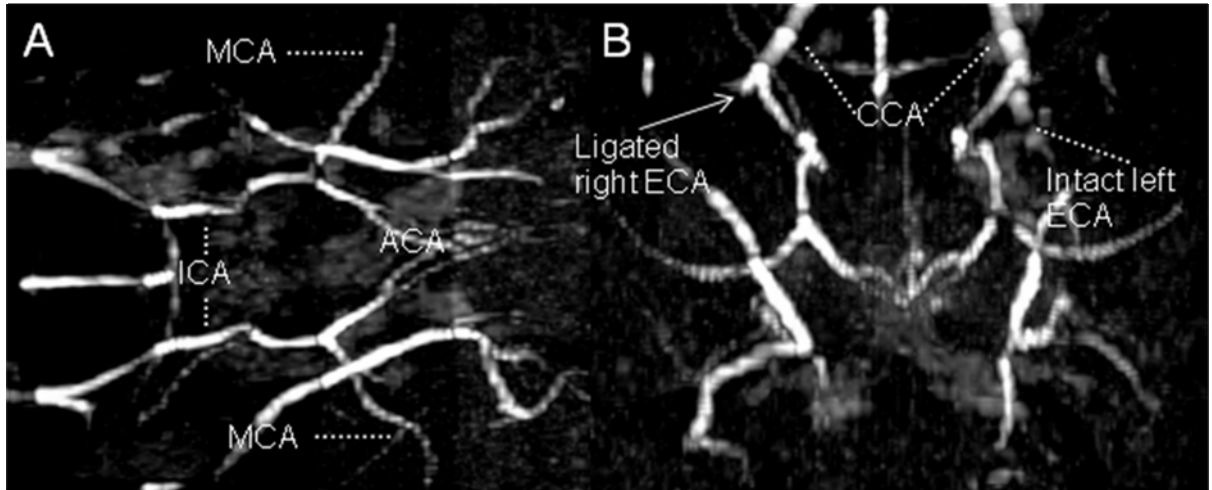


Figure 1.4 | Maximum Intensity Projections of a 3D angiogram of the mouse brain after permanent ligation of External Carotid artery. Coronal (A) and axial (B) angiograms of the mouse cerebrovascular system are shown here. Major arteries can be easily visualized. Imaging was done 30 min after permanent occlusion of the right ECA (arrow) whereas left ECA remained intact. Imaging parameters used were: TR = 30 ms, TE = 0.94 ms, flip angle 45°, one average, 2.5 min acquisition time. ICA – Internal Carotid Artery, MCA – Middle Cerebral Artery, ACA – Anterior Cerebral Artery, CCA – Common Carotid Artery, ECA – External Carotid Artery.

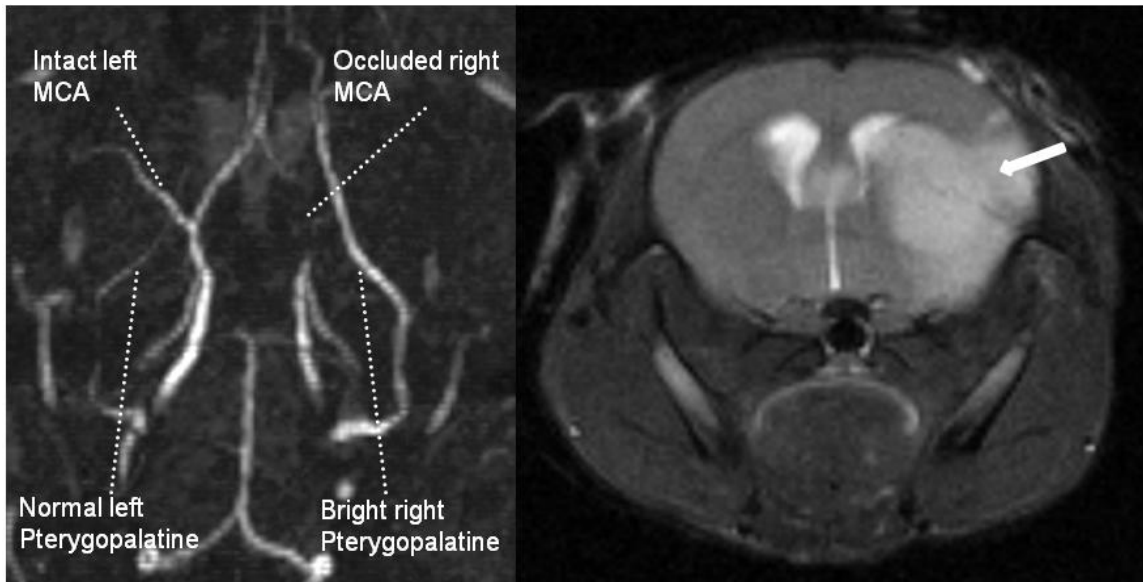


Figure 1.5| Mouse brain angiogram acquired during surgery shows successful occlusion of the MCA and associated infarct damage. MRA done 30 min after introduction of suture during MCAO surgery showed loss of blood supply to the anterior Circle of Willis, especially the MCA (left). The Pterygopalatine artery was much brighter on the ipsilateral side compared to the contralateral side, indicating increased blood flow in the right arterial system because of occlusion of the MCA. T2 weighted imaging (right) done 24h post reperfusion showed an infarct region (solid arrow) encompassing the striatum and cortical regions, consistent with a successful MCAO surgery outcome.

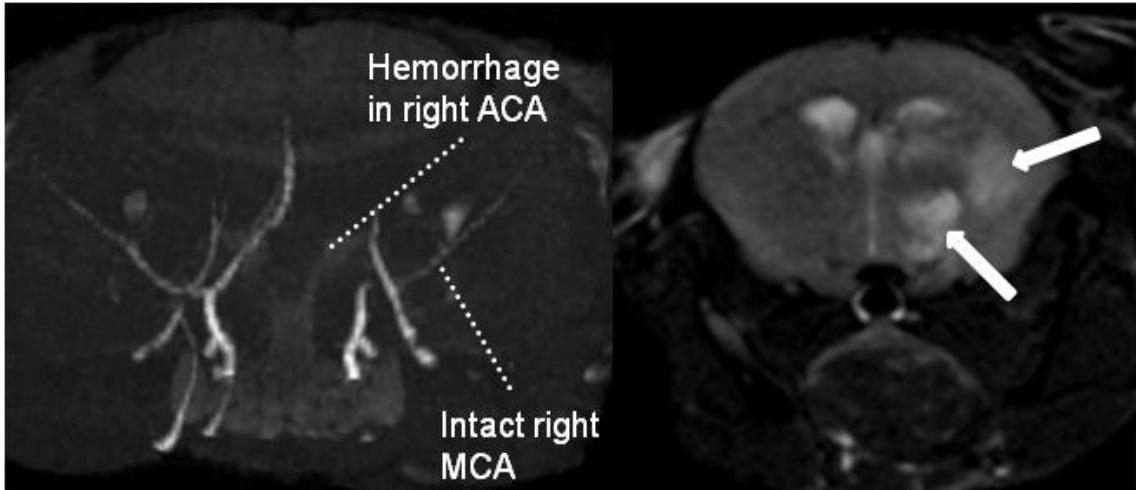


Figure 1.6| Mouse brain angiogram acquired after reperfusion showing a hemorrhage, with associated infarct damage. Coronal MIP of a 3D TOF angiogram (left) of the mouse brain was acquired 30 min after introduction of a suture into the ICA to block the MCA. A hemorrhage of the right ACA was observed. T2 weighted imaging (right) done 24h post reperfusion showed an abnormal infarct in the brain (solid arrows) which was not consistent with successful MCAO surgery outcomes observed in other animals.

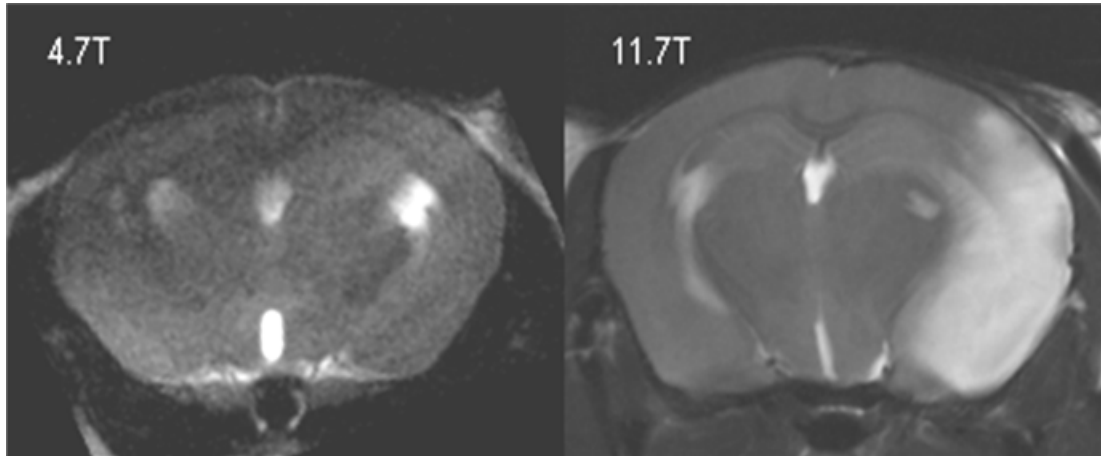


Figure 1.7| T2 weighted MRI on 11.7 T has higher signal to noise ratio than 4.7 T. MR images of a mouse before surgery taken at 4.7T MRI system (left) using a RARE sequence with the following parameters: FOV 25X25 mm, acquisition matrix 256X256, voxel volume 0.0095 cm³, TR 6 s, TE 10.53 ms, RARE factor 16, number of averages 6, and flip angle 90°. T2-weighted MRI of mouse brain 2d after stroke taken on 11.7 T vertical bore MRI system (right) with a RARE sequence shows much better signal to noise ratio. Imaging parameters were: Field of view (FOV) 30X30 mm, acquisition matrix 512X512, voxel volume 0.0035 cm³, TR 3 s, TE 50 ms, RARE factor 8, number of averages 16. Clearly, the 11.7 T MRI has much better resolution which is required for mouse brain imaging.

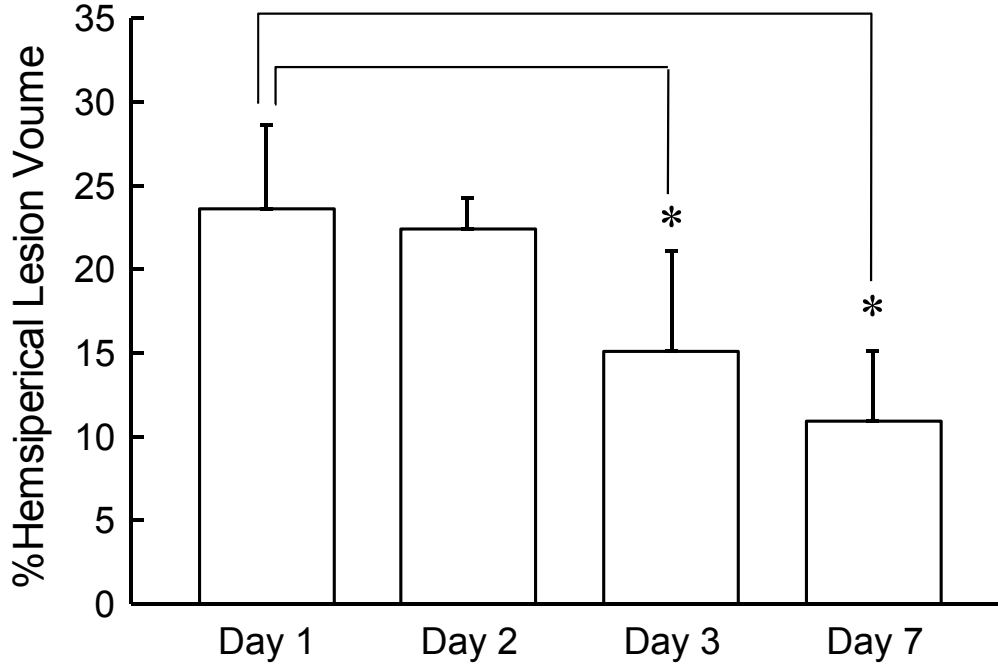


Figure 1.8 | Time course of lesion volume in brain after 90 min Middle Cerebral Artery Occlusion in rat. T2 weighted MRI was performed on the rat and coronal slices of the brain were acquired. Image processing was done using ImageJ software. After suitable software contrast enhancement of the images, manual tracing of the infarcted region was done. Lesion volume was corrected to remove error caused by space quantifying effect of edema. The position of the midline was done using standard neuroanatomic landmarks. The brain atlas by Paxinos and Watson was used to ascertain which coronal slices to be used for brain volume measurement. Only part of the brain from olfactory lobe to the cerebellum was used. Data are shown as mean \pm SD, n = 5, * indicates p < 0.05.

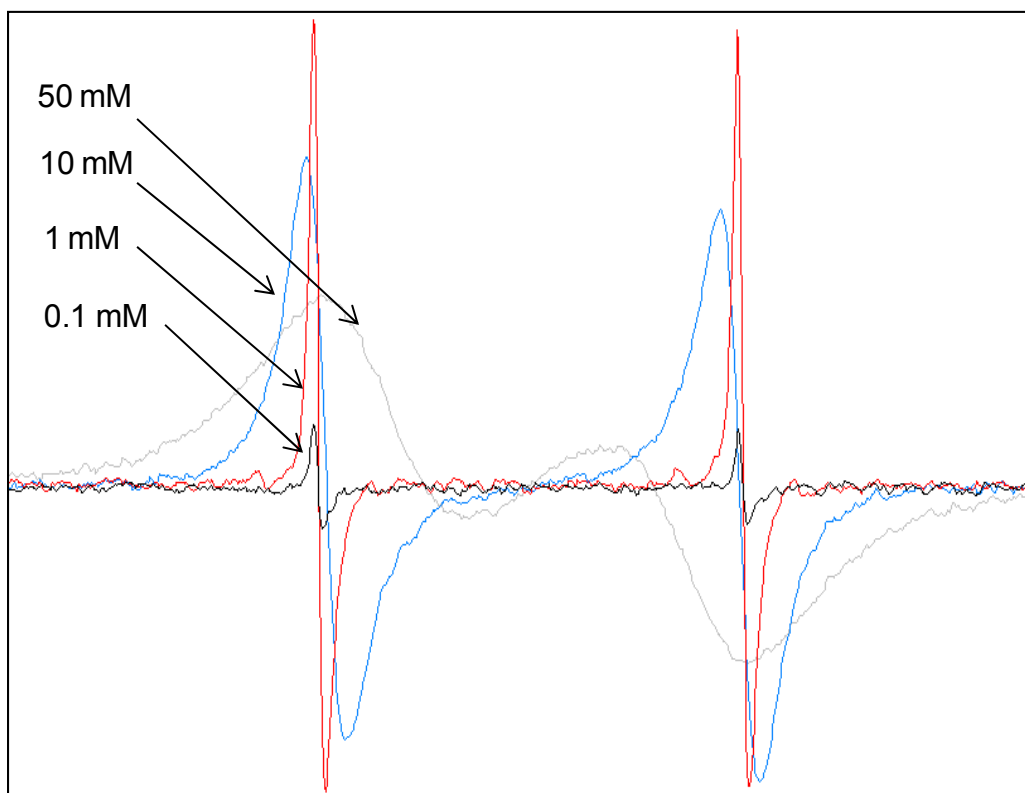


Figure 1.9| Line broadening of nitroxide with increase in concentration. At low concentration of ^{15}N -PDT (1 mM, red), two distinct peaks are observed with hyperfine splitting of 22.47 G and linewidth 0.22 G. At higher concentrations (50 mM, grey), there is spin-spin broadening which causes the two peaks to merge into one broad middle peak of lower amplitude.

Figure 1.10 | Topical EPR spectroscopy of wounds. (A) Mouse sketch with a pair of 3 mm full thickness dermal punch wounds (not drawn to scale). The distance between the wounds was 10-15 mm. These wounds were made above the bridge of the back so as to avoid motion artifacts caused by breathing while EPR spectroscopy measurements were being done. (B) The mouse was anesthetized and placed on a height adjustable table which allows exact positioning of resonator above and around wound site. (C) Time course of EPR spectra of ^{15}N -PDT after topical application to wound. The spectra were taken at L-band using a surface resonator. A 6 μl solution of 50 mM PDT was applied to wound site and spectral acquisitions were immediately started. Data acquisition parameters were as stated in the text. At the beginning of experiment the left and right peaks (only left peak shown here) were non-existent. With time, these peaks appear and increase in intensity, and then gradually decline. (D) Mathematical fitting of nitroxide in wound tissue in vivo. The solid line is a mathematical fit as described in text, fitting the data points shown in open circles. $r^2 = 0.97$. (E) Nitroxide regeneration at wound site. To confirm that at least part of signal loss observed is because of nitroxide reduction at wound site, 4 μl of 10 mM potassium ferricyanide was topically administered to the wound (shown by arrow) 25 min after initial application of 6 μl of 50-mM PDT. After a brief delay, an increase in signal intensity was observed which was attributed to oxidation of the reduced nitroxide back to its original form. (F) Oxidant level at wound site increases 2 days after wounding. 3 mm punch biopsy wounds were made on back of C57BL/6 mice. 6 μl of 50 mM ^{15}N PDT was topically applied on the wound and EPR spectra were immediately started. EPR spectra maxima of left peak was used to generate decay curves which were mathematically fitted as described in text and half life was calculated. Measurements were taken from the same wound on day 0, day 1 and day 2 after wounding. Data is shown as mean \pm SD, n = 6, * indicates p < 0.05.

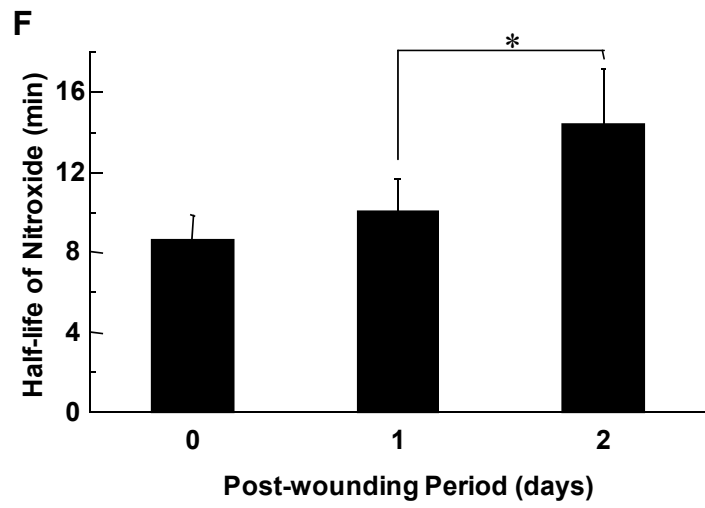
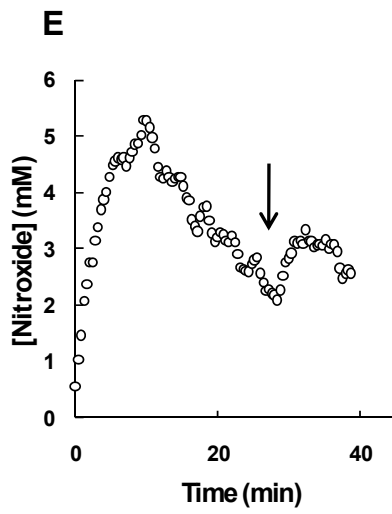
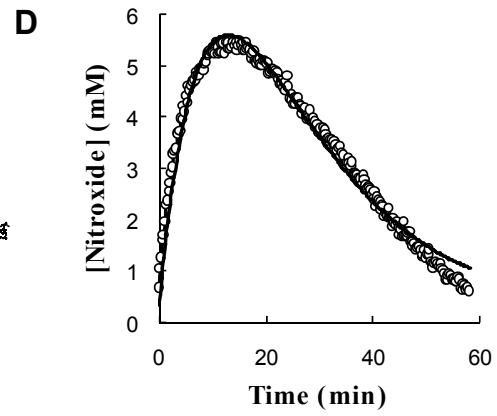
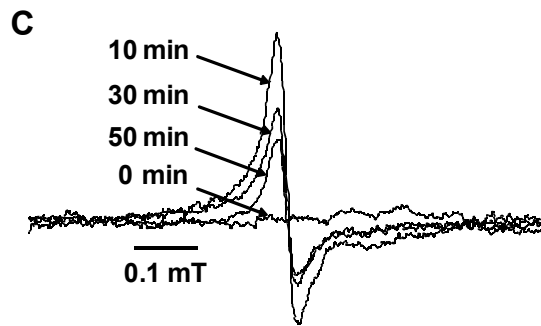
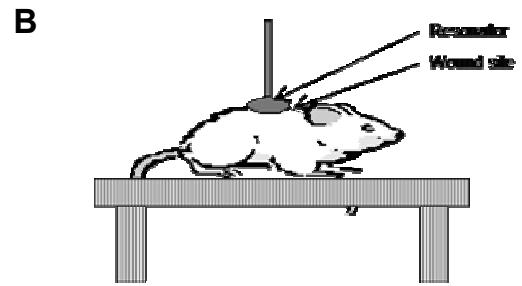
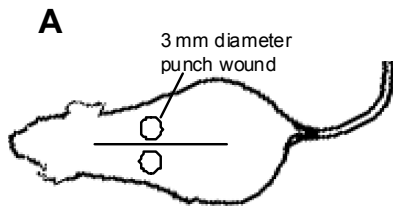


Figure 1.12 | Superoxide production peaks 2d post wounding as measured from DMPO spin adduct taken from wound rinsate. EPR measurements were carried out as described before. X-band EPR spectra was recorded from wound rinsate collected at various time points as shown: (A) 0 hour, (B) 12 hour, (C) 24 hour, (D) 48 hour, and (E) 6 day. Clearly the maximum signal is obtained 48 hours after wounding. (F) Quantitation of DMPO-OH spin adduct formation in wound rinsate normalized to maximum intensity observed on day 2 after wounding. Quantitation was performed by computer simulation of the spectra and comparison of double integral of observed signal with that of a TEMPO standard (1 μ M) measured under identical conditions. The increased production of superoxide correlates with the respiratory burst of inflammatory cells, which peaks at day 2 post wounding. n = 3, * indicates p < 0.05.

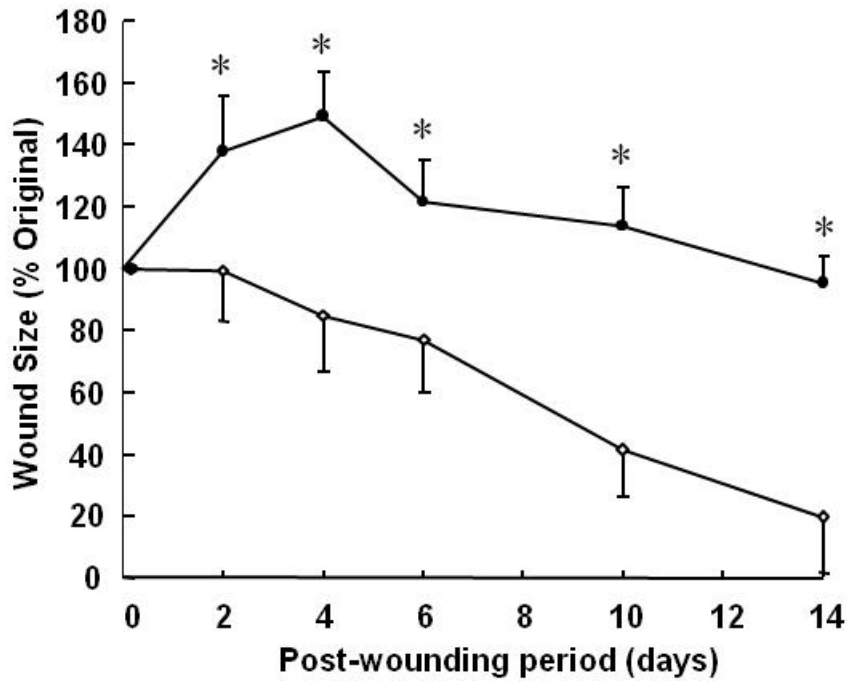
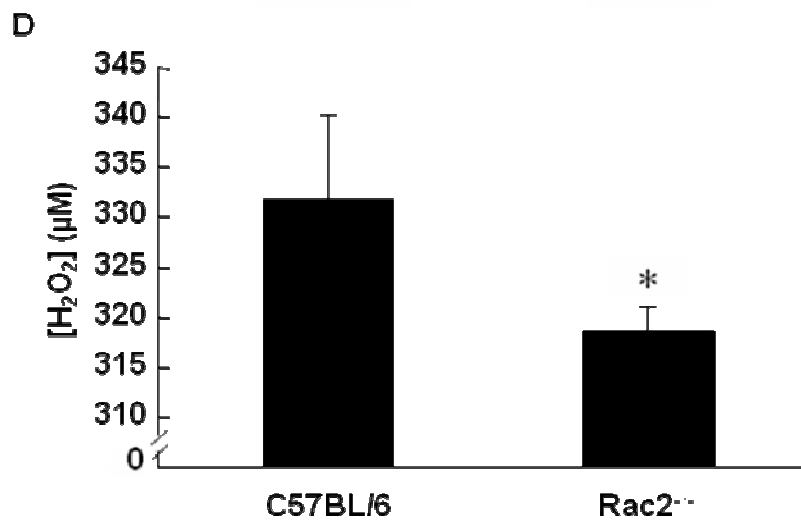
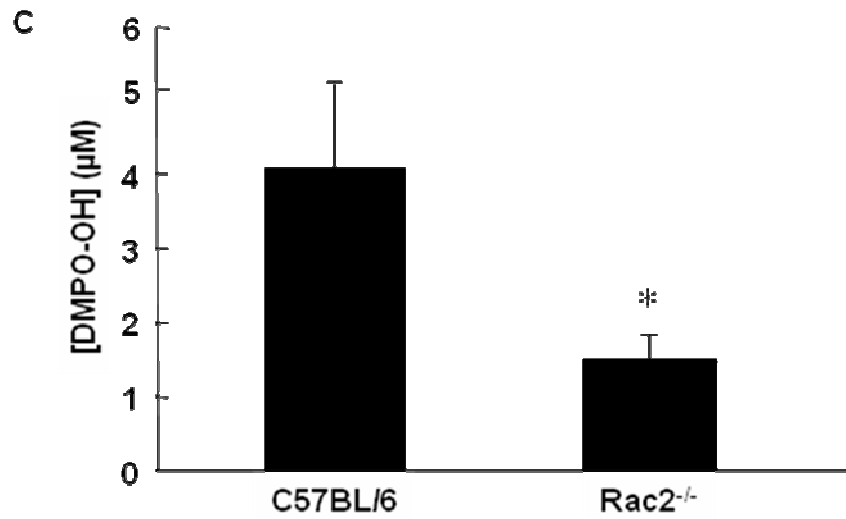
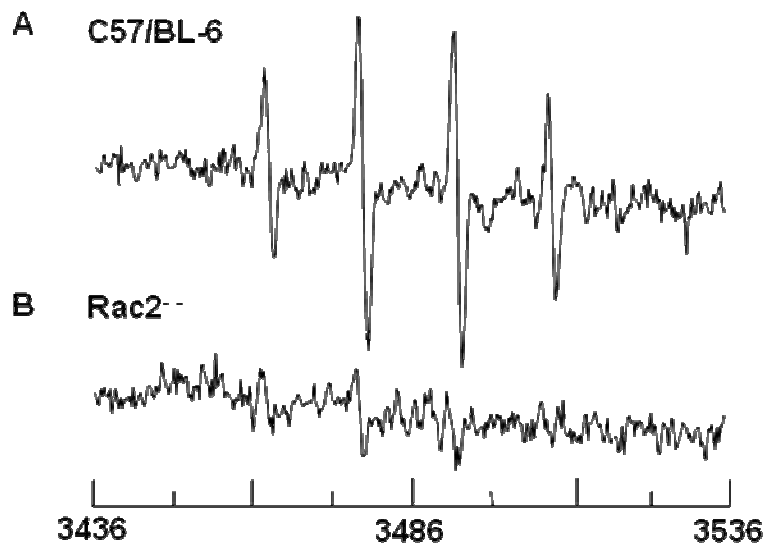


Figure 1.13 | Slow wound healing response of Rac2^{-/-} animals. Two 8 mm X 16 mm full thickness dermal wounds were created on backs of Rac2^{-/-} (filled circles) and wild type (open circles) mice. Digital Photographs of wounds in full view and in one plane were taken with a digital camera (Sony Mavica) on specified days after wounding. Wound areas were calculated using WoundMatrix software. * indicates $p < 0.05$, $n = 4$ in each group.

Figure 1.14 | Decreased superoxide production at wound site in Rac2^{-/-} mouse corresponds to slow healing response of animals. (A) EPR measurements were done as described in the text at day 2 after wounding in wild type and Rac2^{-/-} mice. (A) and (B) show X-band EPR spectra of wound rinsate in PBS from wild type and Rac2^{-/-} mice, respectively. (C) Quantitation of DMPO-OH production in wild type and Rac2^{-/-} mice, indicating that a much lower amount of superoxide is produced in Rac2^{-/-} mice given the compromised NADPH oxidase system in phagocytic cells. For this experiment, n = 3 in each group. (D) H₂O₂ concentration in wound fluid. Hunt–Schilling cylinders were implanted in each of five 8 to 10-week old C57BL/6 and Rac2^{-/-} mice. On day 2, fluid was collected. 200 mM NaN₃ was added to inhibit peroxidase activity. To discern the H₂O₂- sensitive component of the signal detected in wound fluid 0.03 ml of the azide-free fluid was treated with 350 units of catalase. The catalase-sensitive component was interpreted as H₂O₂. Standard curve was generated using authentic H₂O₂ tested for UV absorbance. Data is shown as mean ± SD, n = 5 in each group, * indicates p < 0.05.



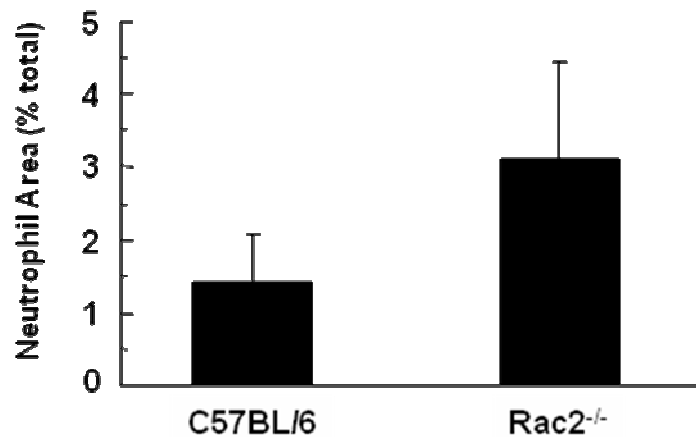
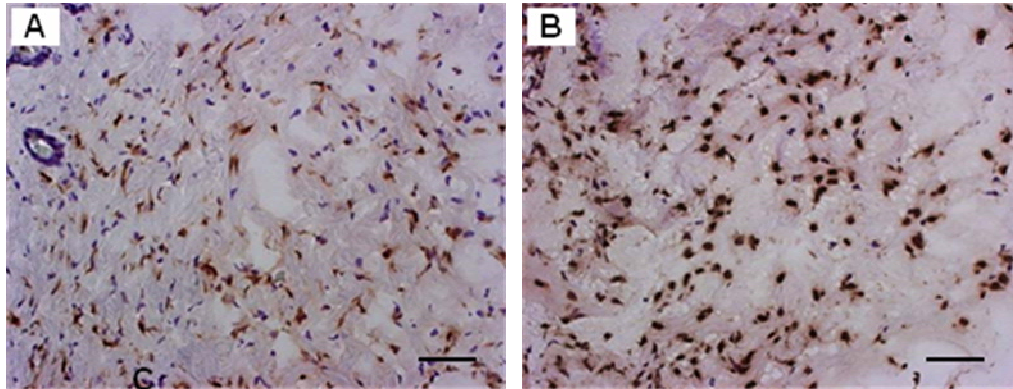


Figure 1.15 | Neutrophil recruitment to wound-site is increased in Rac2^{-/-} mice. Neutrophil staining of C57BL/6 mice (A) and Rac2^{-/-} mice (B) was performed on frozen sections of regenerated skin at the wound-site sampled 2 days after wounding. (C) Bar graph representing image analysis outcome. Three different regions from each wound were imaged on a microscope and analyzed with Adobe Photoshop using a color subtractive-computer assisted image analysis system. Rac2^{-/-} mice show a trend towards higher recruitment of neutrophils to the wound-site compared to wild type, possibly to compensate for the lower NADPH oxidase activity in the neutrophils. All images at 20X magnification, Scale bar = 50 microns, n = 4 in each group.

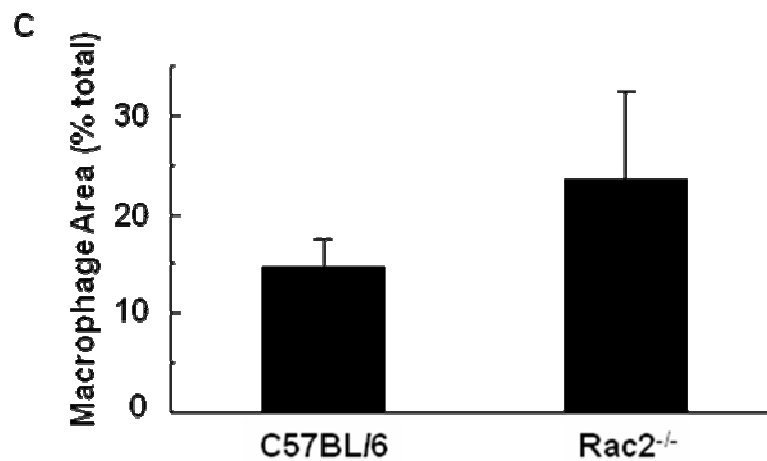
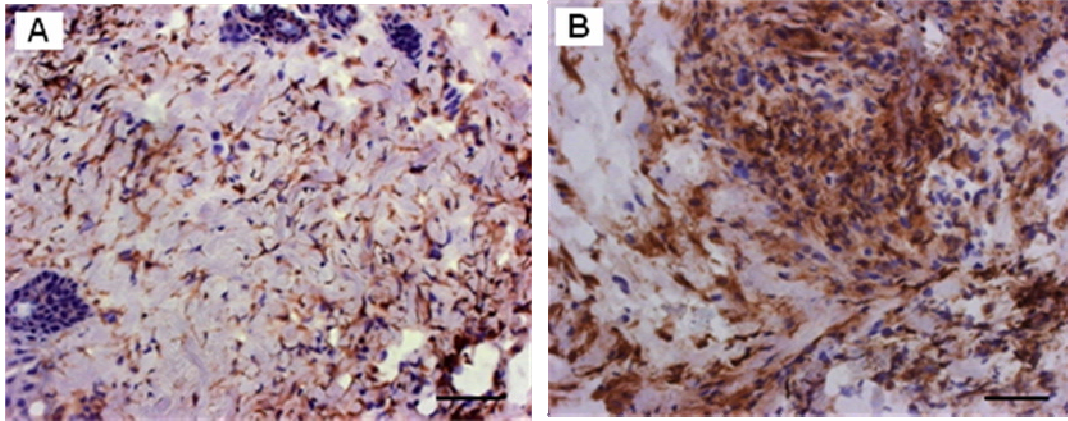
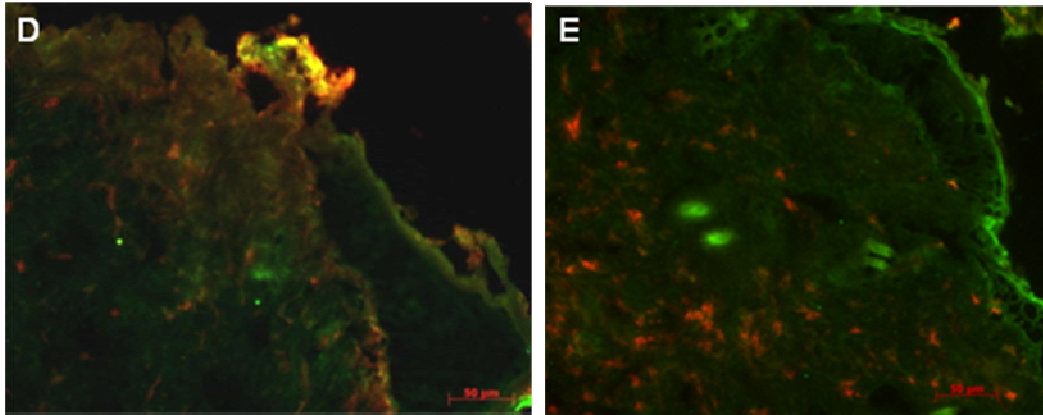
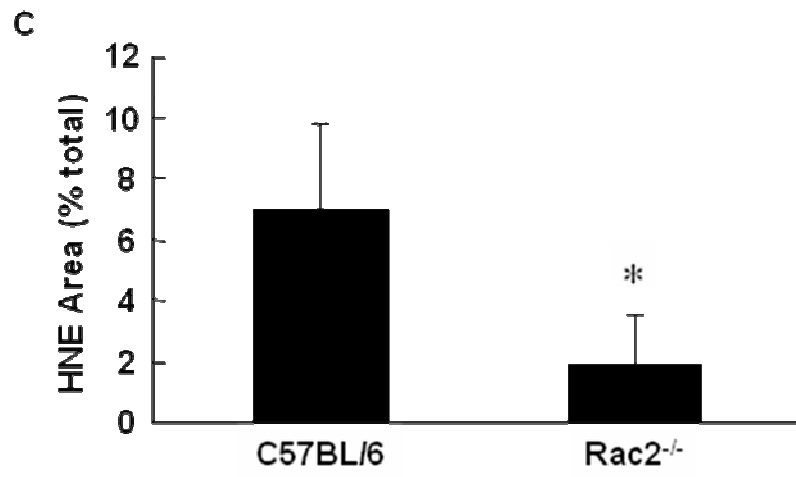
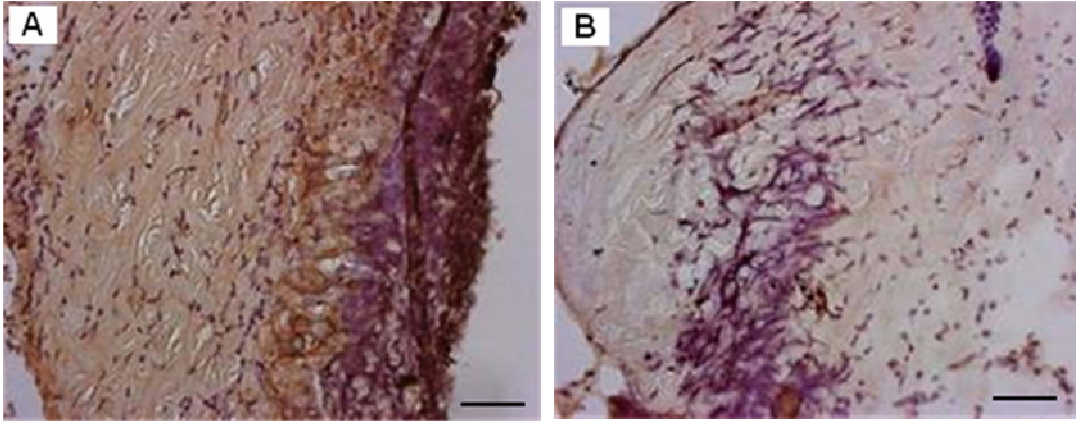


Figure 1.16 | Macrophage recruitment to wound-site is increased in Rac2^{-/-} mice. F4/80 macrophage staining of C57BL/6 mice (A) and Rac2^{-/-} mice (B) was performed on frozen sections of regenerated skin at wound-site sampled 2 days after wounding. (C) Bar graph representing image analysis outcome. Rac2^{-/-} shows a trend towards higher recruitment of macrophages to the wound-site compared to wild type. All images at 20X magnification, Scale bar = 50 microns, n = 4 in each group.

Figure 1.17 | Lower lipid peroxidation at wound site in $Rac2^{-/-}$ mice. HNE staining was performed on OCT fixed frozen sections of regenerated skin at the wound-site sampled 1 day after wounding. $Rac2^{-/-}$ (B) shows lesser lipid peroxidation indicative of lower (vs. wild type in A) activity of inflammatory cells. (C) Bar graph represents Image Analysis outcome. (D) and (E) Double immunostaining was performed on OCT-fixed frozen sections of regenerated skin at the wound-site sampled 2 days after wounding. Wild type (D) shows higher level (vs. $Rac2^{-/-}$ on right) of co-localization of lipid peroxidation (green) and neutrophils (red) producing an orange/yellow hue all over the section indicating that in $Rac2^{-/-}$ mice neutrophils infiltrate into the wound site but do not cause lipid peroxidation as they lack sufficient NADPH oxidase activity. All images at 20X magnification, Scale bar = 50 microns. Data is shown as mean \pm SD, n = 4 in each group, * indicates $p < 0.05$.



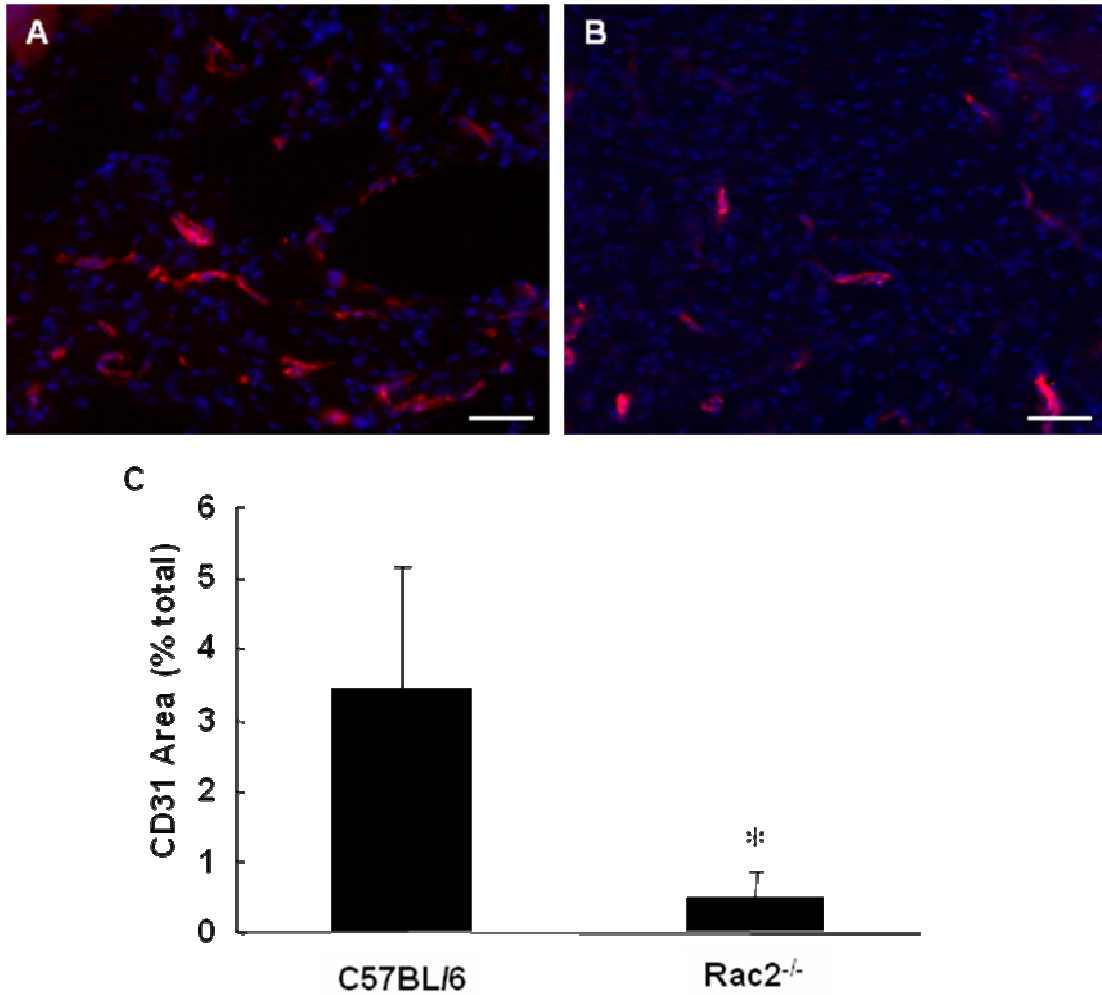


Figure 1.18 | Impaired angiogenesis *Rac2*^{-/-} mice. For estimation of vascularization, we performed immunohistochemical staining for CD31 (red) and DAPI (blue, nuclei) on cryosectioned wound tissue from wild-type (A) and *Rac2*^{-/-} mice (B) sampled 8 days after wounding. (C) Bar graph representing image analysis outcome. The higher abundance of CD31 red stain in the section obtained from wild-type mice (left) demonstrates better vascularization and angiogenesis versus *Rac2*^{-/-} (right). All images at 20X magnification, Scale bar = 50 microns, n = 4 in each group.

CHAPTER 2

MRI BASED TECHNIQUE FOR ANALYSIS OF MURINE CARDIAC FUNCTION, STRUCTURE AND INFARCT VOLUME AFTER ISCHEMIA-REPERFUSION

2.1 Introduction

The primary function of heart is to pump blood throughout the body. The regular and continuous contracting of heart muscle, myocardium, generates and sustains a positive arterial blood pressure necessary to provide adequate perfusion of organs. Adequate blood circulation is a necessary condition for adequate supply of oxygen to all tissues, which, in return, is synonymous with cardiovascular health, survival, longevity and quality of life. Regular functioning of myocardium and cardiac function is maintained by heart valves, the electrical conduction system, neural influences and metabolic conditions.

Figure 2.1 shows the exterior anatomy of a human heart. The four chambers of the heart are illustrated along with major coronary arteries. On note is the Anterior descending branch of the Left Coronary Artery, which are prone to coronary artery disease (CAD). CAD occurs when the coronary arteries become

hardened and narrowed because of build up of plaque on their inner walls (solid arrow in Fig 2.1). This condition is called atherosclerosis. As the plaque increases in size, the insides of the coronary arteries get narrower and less blood can flow through them. Eventually, reduced or cutoff blood flow and oxygen supply to the heart muscle can result in myocardial infarction (MI) - permanent damage to the myocardium. The region of heart supplied by the atherosclerotic artery is at risk of getting an MI (shaded region of heart in Fig 2.1). MI triggers tissue remodeling in the heart and eventually reduces the ability of heart to adequately pump blood to all tissues. This can lead to heart failure and death.

To understand the mechanisms of cardiac remodeling after MI, this clinical condition is experimentally modeled in the laboratory in mouse heart. Fig 2.2 shows the cardiac anatomy of human and mouse heart. The cardiac anatomy in mouse and human is, with the exception of some small variations, remarkably similar (87). Thus in both species the heart has four chambers; two atria, separated by an interatrial septum (IAS), and two ventricles, separated by an interventricular septum (IVS). One of the major differences, other than size, is that resting mouse heart rate is 600 beats per minute compared to 70 bpm in human. This difference is well-characterized and is defined by the Allometric equation (88; 89). Otherwise, even the developmental events that lead to the formation of the four-chambered heart are also very comparable. Consequently, the mouse can serve as a good model with which to study the human heart.

In this chapter, an MRI-based technique for the functional and structural evaluation of mouse heart is described. In addition, a method for surgically inducing cardiac ischemia-reperfusion injury in mice, and non-invasive infarct volume measurement with MRI is illustrated.

To fully realize the mechanistic insights into cardiovascular function, it is essential to have accurate measures of murine cardiac physiology. The important murine cardiac function parameters include heart rate, left ventricular end systolic volume (LV ESV), left ventricular end diastolic volume (LV EDV), stroke volume (SV), cardiac output (CO), ejection fraction (EF) and LV mass. Current techniques for study of murine cardiac function and structure include Magnetic Resonance Imaging (MRI), electrocardiography (ECG), post-mortem histology, hemodynamic catheters and echocardiography. Techniques other than MRI have several major disadvantages, which collectively leads to MRI as the preferred modality for overall cardiac assessment.

ECG is a semi-quantitative technique which only provides limited information as to the presence of major cardiac abnormalities like ischemia. Furthermore, resting ECG might be normal in many patients as certain cardiac abnormalities occur only during stress, limiting its application to a subset of the population (90). Murine ECG can be effectively used to report presence or absence of ischemia in models of cardiac occlusion. The early ECG manifestations of transmural MI include diminished R wave amplitude, marked ST segment elevation and the development of a significant Q wave (91).

Although there are some reports of 6-lead ECG used for characterization of myocardial infarction in mice, the limited information it provides coupled with significant expertise and training required to analyze ECGs limit this technique's widespread use (91; 92).

A variety of histological techniques can be employed in study of murine cardiac structure. It is possible to quantitatively assess infarct volume and regenerative cardiac growth, provided that rigorous morphological criteria are used (93). Gross histological staining techniques include 2,3,5-triphenyltetrazolium chloride, which provide a quick estimation of infarct size (94-98). Since all histological techniques are performed ex-vivo, they fail to provide any information from a live animal. In addition, data is obtained at only one time point per animal yielding large inter-animal differences and necessitating large experimental animal numbers.

Hemodynamics is an important part of cardiovascular physiology dealing with the forces the heart has to develop to circulate blood through the cardiovascular system. These hemodynamic forces demonstrate themselves as blood pressure and blood flow paired values at different nodes of the cardiovascular system. Systemic hemodynamics is the study of blood pressure and blood flow at output of the left side of heart. A significant majority of all cardiovascular diseases and disorders is related to systemic hemodynamic dysfunction (99; 100). Hypertension and congestive heart failure are two best known systemic hemodynamic disorders (100). Cardiac hemodynamic

parameters like LV Diastolic Pressure, LV dP/dt and arterial pressure can be measured in mice with in-vivo catheters (101). This is an invasive technique causing trauma to the animal, and still does not provide important structural parameters needed to completely evaluate cardiac function.

The echocardiogram is an ultrasound of the heart. Using standard ultrasound techniques, two-dimensional slices of the heart can be imaged. Ultrasonographic imaging of the heart is a noninvasive technique that depends on the differing ability of the structures within the heart to reflect ultrasound waves. Clinical echocardiography is one of the most widely used diagnostic tests for heart disease. It provides a wealth of information, including cardiac structural parameters, pumping strength and wall motion velocity, location and extent of any damage the cardiac tissue (102). It is especially useful for assessing diseases of the heart valves and can detect abnormalities in the pattern of blood flow, such as the backward flow of blood through partly closed heart valves, known as regurgitation. Echocardiography can also help detect hypertrophic cardiomyopathy, in which the walls of the heart thicken in an attempt to compensate for heart muscle weakness (103). Echocardiography is a versatile non-invasive technique and has no known risks or side effects (104). Murine echocardiography has been hampered by sub-optimal temporal and spatial resolutions of most 2D echocardiography systems available today limiting their practical utility in assessing cardiac structure and function of the intact heart (105). Furthermore, the geometrical assumptions necessary to derive chamber volumes from short- and long-axis 2D acquisitions may not hold true in mouse

hearts that have been rendered asymmetric by large MI (106). Transthoracic echocardiography (TE) has been reportedly used to examine cardiac function in rodents (107). TE has been used to measure LV function in rats and mice with heart failure induced with coronary artery ligation (108), cryoinjury of the myocardium (109), and with hypoxia (110), demonstrating the sensitivity of this technique in the rodent under a variety of conditions. Measurements made with TE yield similar results compared with invasive hemodynamic measurements thus making TE an exciting technique for non invasive cardiac function evaluation (109).

MRI has emerged as the most accurate imaging modality currently available for making detailed assessments of cardiac structure and function in mice (111-120). MRI methods for determining cardiac function utilize tomographic acquisition techniques and are free from complications of numerical assumptions for calculation of chamber volumes (121). MRI has been shown to yield accurate and reliable quantification of murine global myocardium function, left ventricular (LV) mass, and right ventricular size (98; 104; 112; 113; 117; 119; 121-124). MRI is non-invasive, reproducible, accurate, has high signal to noise ratio (SNR) and is very sensitive to changes in cardiac structure and function. Thus, we chose to standardize protocols for cardiac imaging in mice using MRI.

Our overall objective was to standardize a technique to obtain a quantitative measure of cardiac function, structure and myocardial infarct volume in a mouse model of cardiac ischemia-reperfusion. Cardiac MRI in mice is not

routinely done in mice because of poor SNR given the small size of mouse (voxel size 250 times smaller than human MRI), fast heart rate (500-600 bpm) and non-availability of standard human cardiac pulse sequences on small-animal MR scanners. We innovated several hardware and software techniques to generate high-resolution and reproducible mouse heart MR images in quick scan times for routine quantitative analysis of cardiac function.

2.2 Materials and Methods

2.2.1 Animal preparation and setup for MRI

We used wild-type mouse strain C57BL/6 (C57 black 6) in this study. This strain is widely used in MRI literature and cardiac parameters on these mice have been previously standardized by other MRI groups (98; 122-124). All animal protocols were approved by the Ohio State Institutional Laboratory Animal Care and Use Committee (ILACUC). Animals were anesthetized with 3% isoflurane mixed with 1.5 liter per minute carbogen (95% O₂, 5%CO₂) and maintained with 1.5% isoflurane. A small animal monitoring system (Model 1025, Small Animals Instruments, Inc., Stony Brook, NY) was used to provide ECG triggering and monitor respiration and temperature of the animal. To obtain ECG signal for cardiac triggering, subdermal ECG leads on the right forepaw and leg were secured. Respiratory motion was monitored using a pneumatic sensor attached to the animal's abdomen. Core temperature of the animal was monitored using a rectal probe and maintained at 37±0.5°C using a warm air blower.

After confirmation of a good ECG and respiratory signal trace, the animal was placed in a 30 mm birdcage RF resonator and positioned in the scanner with the heart at MRI isocenter. Manual tuning of the RF coil to resonant frequency was then done. Imaging was performed on a Bruker 11.7 T vertical MR scanner with maximum gradient strength of 1000 mT/m. Shim currents were initialized to previously saved values from earlier imaging experiments, and then automatic volume shimming was done. Proton linewidth of less than 600 Hz (1.2 ppm) was routinely obtained in less than 30 s, and yielded good SNR on the MR images. Slice-selective automatic shimming or manual shimming was performed in cases where an acceptable shim profile and linewidth was not obtained with automatic shimming.

2.2.2 Bright-blood cine cardiac MRI data acquisition

Bright-blood imaging is a cardiac MRI technique that yields both morphologic and functional data. Blood generates bright signal intensity (SI), and multiple consecutive images (frames) are acquired that can be viewed dynamically as a movie to depict cardiac motion. Several frames can be acquired for each cardiac cycle with high temporal resolution. Sequences for bright blood imaging include gradient-recalled echo (GRE), fast GRE (fGRE), segmented k-space fGRE, and steady state free precession (SSFP) (fast imaging employing steady-state acquisition (FIESTA), fast imaging with steady precession (FISP), and true FISP) techniques.

We used GRE method for cardiac imaging because of high inherent SNR with short scan time. Blood appears bright in these images compared to adjacent myocardium due to time-of-flight effects as well as the relatively long T2. The timing diagram of such a sequence is shown in Fig 2.3.

A segmented k-space approach can also be used as it provides high-resolution dynamic images of the heart that can be acquired much more rapidly than prior techniques (82; 125). Using short TEs (1.5 ms) and TRs (8-10 ms), multiple lines (segments) of k-space can be acquired during each cardiac cycle. This is unlike other GRE techniques in which only a single line of k-space was acquired per cycle. However, the segmented approach is limited in mice given the extremely fast heart rate (400-500 beats per min) yielding small R-R intervals (120-150 ms). This fast cardiac motion necessitates high temporal resolution (approx. 8 ms for 16 frames) which makes k-space segmentation unviable. Segmentation of k-space for mouse heart imaging would yield faster scan times, but poorer temporal resolution. This could lead to a situation where the end systolic phase of cardiac cycle is not imaged, which would lead to incorrect cardiac function analysis. Thus, we performed cine cardiac imaging with GRE-based ECG-triggered 2D FLASH pulse sequence with one k-space line acquired for each cardiac frame in one cardiac cycle.

FLASH uses a variable spoiler gradient after each echo to spoil the steady state and destroy any remaining transverse magnetization by causing a spatially dependent phase shift. The transverse steady state is spoiled but not the

longitudinal steady state, which depends on tissue T1 and flip angle. Extremely short TR times are thus possible with this sequence while retaining good SNR. TE must be kept as short as possible to suppress magnetic susceptibility artifacts, especially at high fields like 11.7 T. With large flip angles and short TR, T1-weighted images can be obtained.

Low resolution ECG-triggered localizer FLASH scans were initially performed to obtain long-axis images of the heart. The oblique and double-oblique long axis cardiac localizer images were used to generate geometrically accurate slices of short-axis cine loops. The axial slices were located so as to be perpendicular to an imaginary line drawn between the apex and the aortic valve. For baseline cine images, a flip angle of 20° was used as it generated good contrast between blood and myocardium at heart rates from 400-500 beats per minute (R-R interval from 150 ms to 120 ms). 16 frames were obtained in each cardiac cycle that led to a TR between 7.5 and 10 ms. TE was kept as small as possible at 1.43 ms to reduce B₀ inhomogeneity effects. Spatial resolution of 117 micron in-plane (FOV 3 cm X 3 cm, matrix size 256 X 192) with 1 mm slice thickness was obtained. This provided a good balance between spatial and temporal resolution of the acquired cine images.

We observed that respiratory gating did not improve image quality in most cardiac slices, and was thus not employed. Prospective ECG-triggering was used in the study as much as possible for the cine scans, given the poor reliability of retrospective gating software available on the Bruker MRI system. Retrospective

gating was used only in cases where ECG signal was very weak and the gating software was unable to reliably detect R waves from the ECG trace.

2.2.3 Black-blood cardiac MRI data acquisition

Spin-echo (SE) was the first sequence used for evaluating cardiac morphology and provide good contrast between myocardium and blood (126). Such images are called black-blood images because of the signal void created by flowing blood. Presaturation with radiofrequency (RF) and reduction of the echo time (TE) minimizes blood signal and increases contrast on gated SE images (127). Although it is widely available, SE imaging has limited temporal resolution and is degraded by respiratory and other motion artifacts. Shorter acquisition times are achieved with fast SE (FSE) pulse sequences, also known as rapid acquisition relaxation enhancement (RARE). Although it is faster, soft-tissue contrast is less optimal than with SE techniques because of the wide range of acquired TEs inherent in FSE methods (128).

Clinically, double inversion spin echo T2-weighted sequences are currently used for black-blood imaging and depiction of cardiac morphology (129). We employed the same sequence to null blood signal for black-blood imaging in mice. This technique consists of two 180° RF pulses: a nonselective 180° pulse, which inverts all of the protons in the field, immediately followed by a slice-selective 180° pulse, which reverts the photons in the imaging slice back to their original alignment, leaving all protons outside of the imaging slice inverted.

The timing diagram for the sequence is shown in figure 2.4. For stationary tissue in the imaging slice, the net effect of the two pulses is negligible because the net 360° RF excitation returns magnetization to its original state. By the time the imaging sequence begins, blood in the imaging slice will have been completely replaced by blood containing protons that originate outside the slice which have experienced only the nonselective 180° pulse. When the magnetization vector for blood crosses the null-point, the pulse sequence is started. The sequence completely nulls blood signal and provides excellent delineation of myocardial-blood interfaces.

2.2.4 Ischemia-Reperfusion surgery in mouse heart

Current treatment of myocardial infarction is directed to restore blood flow to the ischemic region by thrombolysis, coronary artery bypass surgery, or percutaneous transluminal coronary angioplasty (130). Depending on the degree of success of the therapeutic intervention, the area at risk remains either hypoxic or is fully salvaged. When the area at risk remains hypoxic, the myocardial tissue loses its contractile function and becomes necrotic. In contrast, when blood flow through the myocardium is reestablished in time, hibernating myocardial tissue may regain some of its function but may also experience additional damage due to the reperfusion process itself. Our overall goal was to experimentally model this situation by a reversible left coronary artery (LCA) occlusion technique, and image the myocardial infarct with MRI.

We standardized a 60 minute reversible LCA occlusion surgical method to induce IR in mice. This technique was chosen because it is a well-documented method to study IR in mice (131-135). Our laboratory experience points to a post reperfusion mortality rate of less than 10% for animals operated upon with this model. Mice were be anesthetized, held on a warm tray (37°C), and intubated endotracheally. The mice were ventilated on air-isoflurane at an appropriate rate and tidal volume. Cardiac electrophysiology was monitored throughout the surgery using a standard three-lead ECG setup, and changes in electrical conduction were measured using PC Powerlab software (AD Instruments). The heart was accessed via a left thoracotomy. The left lung was retracted to allow entrance to the pericardium. The left auricle was elevated to expose the coronary (left anterior descending) artery, which was isolated using 7-0 silk suture on a taper needle. The suture was tightened over a piece of PE-10 tubing to provide for reversible ischemia via occlusion of the coronary artery. Ischemia was continued for 60 min after occlusion. After 60 min, the suture was released to allow for reperfusion of the injured myocardium. Successful determination of ischemia and reperfusion was be done by laser Doppler flow measurement. On successful reperfusion, the thorax was closed with interrupted sutures, and the skin incision was closed with surgical clips. A catheter was used to aspirate the left thorax to reestablish the negative thoracic pressure and facilitate lung reexpansion (130).

A change in ECG pattern was used to document successful induction of ischemia and presence of myocardial infarction. ECG is well-known to document

acute and chronic ischemic damage to myocardium (91; 92; 136; 137). Animal ECG was monitored during the surgical procedure for an elevation of ST segment of the ECG trace, a reliable indicator of myocardial ischemia (92; 137). In a subset of animals, ECG was also monitored 24 h after reperfusion when chronic development of large Q waves and abnormal negative ventricular potentials can be observed (91). Thus, we employed ECG as a diagnostic tool that allowed us to document animals that do not have ischemic injury after IR surgery.

2.2.5 Delayed Hyper Enhancement imaging for Myocardial Infarct Delineation

Myocardial infarction can be imaged with MRI after administration of a contrast agent. These contrast agents can be classified as extracellular fluid space contrast agents, as opposed to blood pool contrast agents that stay in the blood and have limited but specific applications in angiography and perfusion imaging. The technique involving the use of Gadolinium-based contrast agents for myocardial infarct delineation is called Delayed Hyper Enhancement (DHE) imaging. Infarcted myocardium appears bright on images acquired after contrast injection, as compared to normal and viable myocardium (138).

The immediate availability of gadolinium contrast agents, safety for experimental animal studies, extensive literature on their successful application and ease of use make them the best available technique for infarct delineation studies. It is understood though, that they are incapable of making explicit

distinctions between reversibly and irreversibly injured myocardium, between acute and chronic infarction, and between ischemic and inflammatory lesions (139). Therefore there has been a continuing strategy for searching more specific contrast agents that can offer unambiguous and indisputable imaging diagnosis. Necrosis-avid contrast agents have shown promise, but lack of widespread clinical data has hampered their use for experimental animal studies (140; 141).

2.2.5.1 Gadolinium Based Contrast Agents

Gadolinium is a lanthanide element that is paramagnetic in its trivalent state (Figure 2.3). Although toxic by itself, gadolinium can be given safely in a chelated form, such as Gadolinium-Diethylenetriamine Pentaacetic Acid (Gd-DTPA). When injected before MRI (0.6 mM/kg body weight), gadolinium tends to change signal intensities on the MR image by shortening T1 time in surrounding tissues through interactions between electron spins of its paramagnetic center and proton nuclei in the tissue (129). This results in a signal hyper intensity on T1 weighted images. There are several Gadolinium based contrast agents that are commercially available for DHE MRI as shown in table 2.1.

Short name	Generic name	Trade name
Gd-DTPA	Gadopentetate dimeglumine	Magnevist
Gd-DTPA-BMA	Gadodiamide injection	Omniscan
Gd-HP-DO3A	Gadoteridol injection	ProHance
Gd-DOTA	Gadoterate meglumine	Dotarem
Gd-DTPA-BMEA	Gadoversetamide	Optimark
Gd-DO3A-butriol	Gadobutrol	Gadovist
Gd-BOPTA	Gadobenate dimeglumine	Multi-Hance
Porphyrin and Nonporphyrin NACAs		

Table 2.1 | Extracellular Fluid Space Contrast agents that are available for cardiac MRI. Magnevist and Omniscan are the most commonly used contrast agents.

Toxicology:

Gadolinium-based contrast agents are injected IV in humans and IV or IP in animals for DHE imaging. It is important that the contrast agent be safe for use and be excreted out of the system soon after injection. The prominent feature of Gadolinium(III) is the high number of unpaired electrons - seven. The Gd^{3+} ion retains a number of unpaired spins when bound to the organic ligand. The free Gd^{3+} ion is extremely toxic but most of its complexes are very stable and thus exhibit much less toxicity. Previous studies have shown that Gd-DTPA does not bind to plasma proteins nor interact with other biological structures and is

eliminated unmetabolized by the kidneys where excretion is determined by glomerular filtration rate (142; 143). However, the results of a recent study indicates that Gd^{3+} ions in the Gd-DTPA complex can exchange with Cu^{2+} and Zn^{2+} ions under physiological conditions, and that the released Gd^{3+} may exist in the form of Gd^{3+} -citrate (144).

The relationship between the thermodynamic stability of the Gd-complex and the acute toxicity in vivo is more complicated, as demonstrated by Cacheris et al (145). Authors investigated the stability of a series of complexes of several ligands with Gd^{3+} versus acute toxicity on mice. They also measured the rate of transmetallation of Gd^{3+} by Cu^{2+} and selectivities of different ligands towards Gd^{3+} as compared to Zn^{3+} , Cu^{3+} and Ca^{3+} . Iron (III) was not considered because it is tightly bound in vivo by the storage proteins ferritin and hemosiderin and is essentially unavailable for interaction with Gd^{3+} complexes. The main competitor to Gd^{3+} was found to be Zn^{2+} and the most important thermodynamic criterion of toxicity is the selectivity of the ligand for Gd^{3+} over other endogenous metal ions. Zinc transmetallation was found to be the most likely mode of both acute and subchronic toxicity in experiments on rats. Slower clearance from the body is likely to significantly increase the toxicity of any Gd^{3+} complex.

Gd-DTPA-BMA (gadodiamide), contrast agent used in our study, was introduced in 1993 as a paramagnetic contrast agent for use in MRI (146). Free Gd ions can form precipitates with anions, such as phosphate, because of its poor solubility, and it is considered highly toxic in its ionic form (147). Marckmann et al suggested that nephrogenic systemic fibrosis may result from liberated Gd

ions deposited in the tissues (148). These molecules are known to be extremely toxic and to produce deposits of Gd with calcium phosphates in the tissues of rodents (149). The US Food and Drug Administration recently issued a public health advisory regarding these agents, citing “the risk of nephrogenic systemic fibrosis following exposure to gadolinium based contrast agents” (150).

Mechanism of Hyper Enhancement:

Tissue contrast enhancement patterns on MRI after Gadolinium injection depend on contrast agent concentration, blood perfusion, diffusion of the contrast agent from the intravascular space into the extracellular space (permeability) and size of the extracellular space. Delayed enhancement of non-viable tissue after injection of Gd-DTPA for imaging of myocardial infarction is caused by multiple factors such as loss of cell membrane integrity in acute infarction, differences in wash-in and wash-out time constants of contrast agent, and expanded extracellular space due to interstitial edema in acute infarction or collagenous scar in chronic infarction. Figure 2.4 shows a schematic drawing of contrast agent distribution in infarcted and normal myocardium. Experimental studies have shown a close estimation of areas of irreversibly injured myocardium by the area of late enhancement for both acute and chronic MI (151).

Initial clinical studies on the detection of myocardial viability with use of Gd-DTPA focused on the presence or absence of delayed enhancement because of lower spatial resolution available on MR scanners at that time. A transmural differentiation of the extent of enhancement was not possible – something current imaging hardware allows for, even in small animals. DHE MRI

is an important diagnostic tool as it has been shown that lower the extent of delayed enhancement, higher the probability of functional recovery of the myocardium (152).

The extent of myocardial infarction after IR is an indicator of cardiac fate towards heart failure or tissue remodeling for damaged but sustained cardiac function. Infarct areas delineated by Delayed Hyper Enhancement (DHE) MRI are similar to TTC staining, one of the most common histological technique to measure infarct volume after IR, making MRI far more superior and effective tool to study infarct progression after IR over time (95; 98; 153; 154). The overall goal of the proposed experiments was to standardize a method for DHE imaging of mice after IR.

2.2.5.2 Delayed Hyper Enhancement imaging techniques

DHE MRI can be performed with spin echo, gradient echo, inversion recovery spin and gradient echo, and balanced steady state gradient echo pulse sequences. Application of spin echo and gradient echo sequences has been effectively demonstrated in several murine cardiac MRI studies (98; 106; 111; 114; 117-119; 121-124). Balanced steady state sequences have more severe artifacts at ultra-high fields and have not been effectively used in murine cardiac MRI (155). We tested several sequences to standardize an imaging technique with a balance of spatial resolution, temporal resolution, time of acquisition and image quality. Some of these techniques are described in the following sections.

Spin Echo

A spin-echo (SE) is the most common pulse sequence used in MR imaging. SE sequences and its variants acquire images where blood appears dark as compared to myocardium. These were the first sequences to be used for DHE imaging and have been now replaced by better methods, as SE sequences suffer from problems like long acquisition time or poor signal to noise ratio (SNR) or both.

Fast Spin Echo

Practically, a spin echo sequence is not used with cardiac MRI because of slow acquisition time which causes motion artifacts. Fast (turbo) spin echo readout is generally used, where several k-space lines are acquired after each 90° - 180° RF pulse pairs. This technique is also called Rapid Acquisition Relaxation Enhancement (RARE). This method reduces the time of acquisition several fold as determined by Echo Train Length (ETL) – the number of k-space lines acquired after each 180° pulse. For DHE imaging, this sequence is modified to add ECG triggering, dark blood magnetization preparation and inversion recovery (IR) pulses. The pulse sequence is described in next section.

Inversion Recovery Fast Spin Echo

Inversion recovery fast spin echo sequences have been demonstrated to be very effective for use in DHE MRI to image myocardial infarction (156). Dark blood magnetization preparation is performed in this pulse sequence to null all

signal from blood and obtain good contrast between normal and infarcted myocardium. A spatially nonselective 180° pulse is followed immediately by a section-selective 180° pulse. The net effect is to invert all spins outside the imaging section, while spins within the section experience both 180° prepulses and therefore undergo zero net rotation. Blood flowing into the section plane during the long inversion time (TI_1) is affected only by the nonselective inversion. TI_1 is chosen close to the null point of blood which suppresses signal from blood. Another inversion pulse is applied at a time TI_2 before each 90° - 180° RF pulse pair. TI_2 is set to null normal myocardial signal intensity after Gd-DTPA administration. Fast Spin Echo readout is used to acquire MRI signal. This pulse sequence generates better contrast between hyperenhanced myocardium and all other tissues in the imaging slice compared to conventional spin echo and fast spin echo.

Inversion Recovery Fast Gradient Echo (IR-FGE)

Gradient Echo sequences are fast sequences and are used to generate a T1 contrast image. Blood appears bright in these images because of inflow effects. Because of the fast acquisition times associated with these sequences, cine images of the heart can also be obtained where several images of the heart are taken at various times in a cardiac cycle. IR-FGE sequences have been demonstrated for differentiating injured from normal myocardium in DHE in both clinical and animal studies (157). Other acronyms for FGE are FLASH (Fast low angle shot), SPGR (spoiled GRASS) and FFE (Fast Field Echo). This technique

for delayed enhancement imaging has been shown to be effective, in both animals and humans, in identifying the presence, location, and extent of acute and chronic myocardial infarction.

Segmented IR-FGE

This is a variant of the Inversion Recovery Fast Gradient Echo sequence where several lines of k-space are acquired after each heart beat. The pulse sequence is drawn in Figure 2.7. After the onset of the R wave trigger, there is a wait time called trigger delay (TD) after which a nonselective 180° hyperbolic secant adiabatic inversion pulse is applied. TD is selected to allow data acquisition in mid-diastole when the heart is relatively motionless. After a wait of TI, which is set to null normal myocardium after Gadolinium infusion, a series of gradient echoes are generated in quick succession during a portion of longitudinal recovery. The inversion pulse accentuates differences between tissues with different T1 times. The flip angle used for RF excitation for each k-space line is small (20° - 30°) to retain regional differences in magnetization that result from the inversion pulse and TI delay. TR and TE are kept minimum, because image contrast does not depend on recovery of longitudinal signal between RF pulses. In order to allow for adequate longitudinal relaxation between successive 180° inversion pulses, these pulses are applied every other heartbeat.

The data acquisition window is generally 140–200 ms long, depending on the patient heart rate, and is placed during mid-diastole. A group of k-space lines

are acquired during this acquisition window. The number of k-space lines in the group is limited by the repetition time between each k-space line (~8 ms for most scanners) and the duration of mid-diastole. In the implementation shown in figure 6, 23 lines of k-space are acquired during each data acquisition window. This amounts to 184 ms for each acquisition, which is fast enough to be insensitive to cardiac motion in mid-diastole. With this implementation, typically a manageable breath-hold duration of 12 cardiac cycles is required to obtain all the k-space lines for the image matrix.

A segmented FGE sequence without the use of an IR pulse can also be used for DHE imaging. It has shown to be very effective for achieving contrast-enhanced images in small animals (98). A higher flip angle (60°) is used for each RF excitation to accentuate differences in T1 decay of different tissues, or between infarcted myocardium filled with gadolinium and normal myocardium. This technique can also be used in conjunction with a cine imaging protocol to simultaneously obtain results for cardiac motion and myocardial infarction (98).

2.2.5.3 Delayed Hyper Enhancement imaging and TTC staining in mice after IR

We tested the pulse sequences described in the previous section for murine DHE MRI. We observed that segmented k-space acquisition pulse sequences could not be used effectively in mice because of their fast heart rate of 400-500 bpm. As opposed to humans, the mouse heart beats much faster and is never relatively stationary in the end-diastolic phase to acquire several lines of

k-space. Thus, we standardized an ECG-triggered inversion recovery gradient echo sequence with one k-space line acquired after each heart beat for DHE imaging.

We performed DHE experiments 3 days after IR. We chose this time point because our preliminary results showed a discernible infarct at this time point with TTC staining. We used 0.6 mM/kg body weight (BW) contrast agent Gadodiamide (Gd-DTPA-BMA) injected IP in the mouse for DHE MRI. An inversion recovery gradient echo sequence was used to obtain contrast enhanced images of infarcted myocardium 40 minutes after contrast administration (Fig 2.8). Appropriate inversion time (TI) was selected from a series of TI between 100-250 ms, to completely null viable myocardium and obtain best possible contrast between infarct region (hyper intense) and viable myocardium (dark) (154). An Inversion Time of 150-175 ms, based on heart rate of the animal, provided best contrast between infarcted and normal myocardium. Double inversion preparation pulses were used as required to null blood signal and improve image contrast. In addition, contrast-enhanced images were obtained by using a 60° flip angle in FLASH based cine imaging. Contrast enhanced images from cine loops were later correlated with inversion recovery images to provide additional frames of reference for measurement of extent and area of infarct. The complete imaging protocol was finished inside 1 hour after anesthetizing the animal.

We expected to see a hyper intensity in the infarct region and a dark viable myocardium on DHE MR images. Previous studies have shown that DHE MRI overestimates infarct size if imaging is done earlier than 20 minutes after contrast agent administration (158). To find the correct time for DHE imaging after contrast administration and delineate the true infarct size, we obtained a time course of DHE images from 20 to 120 minutes after contrast administration. A time window for DHE imaging was established by following the time course of area of hyper intensity region and mean intensity of that area. TTC staining of heart was performed on the same animals after MR imaging to correlate infarct size with the two techniques and obtain the 'true' infarct size on DHE imaging. Based on our preliminary data and previous studies, we expected to obtain true infarct volume with DHE images obtained 40-60 minutes after contrast injection (154).

Animals were killed immediately after MR imaging for cardiac TTC staining. TTC staining is a technique for gross determination of infarct volume in tissues post-mortem (159). Animal hearts were excised and encased in 2% agarose solution. After settling the agarose for 2 minutes, the heart was laterally cut just below the left auricle and 1 mm thick sections were made using a heart matrix. The agarose was removed and sections were incubated with 2% 2,3,5-triphenyltetrazolium chloride (TTC) at 37°C for 20 min, with rotation every 2 min to allow uniform tissue staining. Each slice was photographed with a digital camera mounted on a dissecting microscope.

2.2.6 Image Processing

The overall objective of our experiments was to standardize a technique for quantitative evaluation of cardiac function, structure and infarct volume in mice after IR. The final step in the process after image acquisition was to extract quantitative data from the MR images. Figure 2.9 shows the workflow involved in the full MRI procedure. Raw data was first converted to DICOM (Digital Imaging and Communications in Medicine) format using Bruker Paravision 4.0 software. DICOM images were used for further image processing either with ImageJ image processing software or with custom-written software in our lab.

We modified the image analysis procedure used for clinical evaluation of cardiac MRI to extract functional information from our data. Higher SNR of clinical MRI allows for routine use of automated LV contouring algorithms which can generate functional data from cine images with minimal operator supervision. We also developed such a software package for automated cardiac function and structural analysis of mouse MRI images. The comparative lower SNR of mouse cine images led to poor LV contouring in several scans, requiring tremendous operator input at several steps. Thus, we chose to perform functional analysis with manual contouring of LV borders using ImageJ software. Regional analysis of wall motion was done by software developed in-house exclusively for that purpose.

2.2.6.1 Infarct Volume Calculation

For determination of infarct volume, Gadolinium enhanced MR images in DICOM format were processed in ImageJ software. Appropriate software contrast enhancement of the images was done to maximize signal from hyperintense region and null signal from non-enhanced region. Manual planimetry was performed on images obtained from inversion recovery imaging sequence. The hyperintense region area, hyperintense area intensity and LV myocardial area was traced by an investigator blinded to the study. The DICOM format MR image tag contains information about image resolution and field of view. This yielded an area of the infarct region and total LV area. Planimetry was done on all cardiac slices and slice hyperintense areas were then summated to generate infarct volume as a percentage of LV myocardial volume. To help exclude artifacts during planimetry, contrast-enhanced images obtained with FLASH cine sequence were also examined as required to provide an additional frame of reference.

ImageJ was also used for infarct volume calculation using cardiac slices stained with TTC. Manual planimetry of entire heart border, infarct region and non-infarct region on TTC images was performed. Infarct volume was calculated as a percentage of total left ventricular volume (including septum). Exact correlation between TTC and MRI heart slices was not always possible because of slice thickness mismatch and partial voluming effects.

2.2.6.2 Analysis of Cardiac Function

Cardiac function analysis was done by processing cine loops in ImageJ image processing software. End-diastolic (ED) and end-systolic (ES) phases were identified on the cine loops by visual inspection of LV lumen area. A trigger delay of 1 ms after detection of R-wave was used in cine imaging, automatically making the first frame in the image sequence as the end-diastolic frame. The frame with smallest LV lumen area was identified as end-systolic frame. After the end-diastolic and end-systolic phases of the heart were identified, endocardial and epicardial borders of the heart were traced and their areas were measured. LV end-systolic volume (LVESV) and LV end-diastolic volume (LVEDV) were calculated from the following formula:

$$\text{LVESV} = \sum_{\text{base}}^{\text{apex}} (\text{epicardial area at end systole}) \times \text{slice thickness}$$

$$\text{LVEDV} = \sum_{\text{base}}^{\text{apex}} (\text{epicardial area at end diastole}) \times \text{slice thickness}$$

From these two volumes, ejection fraction, stroke volume and cardiac output were further calculated as:

$$\text{Ejection Fraction} = \frac{\text{LVEDV} - \text{LVESV}}{\text{LVEDV}} \times 100 \%$$

$$\text{Stroke Volume} = \text{LVEDV} - \text{LVESV}$$

$$\text{Cardiac Output} = \text{Stroke Volume} \times \text{Heart Rate}$$

The average of the initial and final heart rate during a scan was used to obtain the average heart rate for the scan, and was used to measure cardiac output.

2.2.6.3 Analysis of LV Mass

Endocardial and epicardial contours were traced on images acquired at the ED and ES phases. LV mass was determined using ImageJ according to the following equation:

$$\text{LV mass} = \gamma_{\text{myocardium}} \sum_{\text{base}}^{\text{apex}} (\text{epicardial volume} - \text{endocardial volume}) \times \text{slice thickness}$$

where the specific gravity (γ) of the myocardium is 1.055 g/cm³ (106). This measure of LV mass has been shown to be very close to actual LV mass measured with a weigh balance (94; 98; 106). The MRI technique actually measures LV myocardial tissue volume, and was extrapolated to calculate LV mass based on specific density of the myocardium. We assumed that the specific density of myocardium stays constant after IR, and thus can make a comparison to LV mass before and after IR.

2.2.6.4 Analysis of Regional Wall Motion

Regional wall motion analysis is a technique for quantitative estimation of regional LV contractility. Assessment of LV wall motion is considered one of the

most important procedures in evaluating LV function (160). It is important to diagnose and quantitatively evaluate regional wall motion as it is a manifestation of number of myocardial pathophysiological conditions (161). Doppler tissue imaging (DTI) is an echocardiographic technique used for wall motion analysis. It is a non-invasive imaging modality that directly interrogates myocardial velocity and is routinely used for making clinical evaluations (162). But the high spatial and temporal resolution required for small animal imaging is not available in commercial systems which makes data generated from the Doppler technique difficult to interpret and evaluate (163; 164). MRI, given its high spatial and temporal, has been successfully used in mice for regional wall motion analysis (94; 98; 106). LV contractility is qualitatively assessed by viewing images in cine loops by quantitative measures of wall motion and thickening can also be made from these images. LV wall thickness at ED and ES provides a measure of contractile motion of the heart to track LV remodeling after IR.

The first step toward computer analysis of the image data was segmenting the images' interesting features. We developed a semi-automatic method of extracting the inner and outer contours of the LV myocardium. For these tasks, we used a custom-designed variant of active contours (often referred to as *snakes*) (165). An active contour's shape changes in an iterative manner to minimize one or more energy terms. Energy terms in this algorithm promoted contour smoothness and pulled the contours toward certain image features (for example, edges indicated by image intensity gradients). The user was given the option to interactively modify the contour shape by dragging the mouse along the

contour. Epicardial and endocardial contours thus made were further processed with a centerline method for calculation of wall thickness all around the LV.

Regional contractile function post IR was assessed as percent transmural wall thickening (Fraction Shortening, FS). One slice was selected from mid-ventricular section of heart 4.2 mm from apex for segmental wall thickness analysis. Typically, this slice has both infarcted and non-infarcted regions. Wall thickness analysis was done with custom written software in our lab using Matlab (166). After automatic contouring of epicardial and endocardial borders in end systole and end diastole, LV wall thickness was calculated at each 2° angular distance from center of LV using an automated segmentation algorithm. Contiguous wall thickness measurements were averaged to segment the LV into 8 equiangular sectors of 45° each (Fig. 2.10). Averaged wall thickness was indexed to right ventricular insertion point in the anterior wall and was plotted against angle at each time point after IR injury. Fractional Shortening was calculated as:

$$FS = \frac{\text{Wall thickness at ES} - \text{Wall thickness at ED}}{\text{Wall thickness at ED}}$$

Potential Problems and Troubleshooting

As with any analysis of segmental wall thickening, results obtained from the infarcted and adjacent sectors are limited by imperfect registration between the boundaries of the contrast-enhanced regions and the corresponding sectors.

Also, wall thickening in these sectors may also be affected by tethering effects. It was observed that the heart was sometimes attached to the anterior chest wall after surgery. This was possibly caused by inflammation in the chest wall at the site of incision made to gain access to the heart. This caused a tortioning motion of the heart which could affect appearance of wall motion. However, results from the areas further removed from the infarct region should be largely free of these two potential sources of error.

2.3 Results and Discussion

2.3.1 Bright-blood cine cardiac MRI

Cine imaging relies on ECG-gating for an accurate representation of cardiac motion. Heart rate of anesthetized mice was routinely in the range of 400-500 beats per minute, six times that of humans. ECG amplitude was less than 2 mV even after amplification. Also, a change in ECG was observed with time as the depth of anesthetic changed the respiration patterns of the animal. Faithful R-wave detection was not always possible with default parameters of the R-wave detection algorithm. Thus, the ECG detection algorithm parameters were modified for each animal until a robust parameter set was found to regularly detect all or most R-waves. We obtained good quality images with 16 frames in a cine loop at a resolution of 117 μm in-plane. This temporal resolution was better than that reported by other groups at 12 frames, or a lower spatial resolution

(98). Quantitatively, SNR was calculated to monitor image quality of acquisition as follows:

$$\text{SNR} = \frac{\text{Mean Intensity of Signal}}{\text{Standard Deviation of Noise}}$$

SNR of 25 was routinely obtained in acquisition times less than 3 minutes per 1 mm thick cardiac slice.

Spatial resolution has been the limiting factor in mouse cardiac imaging given the small size of mouse heart, limiting LV lumen segmentation and quantification of functional parameters. We observed that optimized MR imaging at high fields of 11.7 T is not limited by poor spatial resolution, and can be effectively applied for serial studies in cardiac morphology and function. Figure 2.11 shows one frame taken from a bright-blood cine loop. The left ventricle, right ventricle, septum, papillary muscles, chest wall and lungs can be clearly identified and are annotated. SNR of this image was 26.4. B_0 field inhomogeneity artifacts from the chest wall and lung can affect images obtained at high-field at interface of air and tissue, but are not observed in this image. Such good image quality allows precise LV contouring for accurate analysis of cardiac function.

Figure 2.12 shows nine end-diastolic frames from serial 1 mm thick sections. Distance of the imaging slice from apex is mentioned on each image. Each heart consisted of six-eight 1 mm thick slices that were used for cardiac function analysis. Cardiac slices above at the level of aortic valve were not considered to be as part of LV and were not included in functional analysis.

Figure 2.13 shows 16 frames of an axial cine loop from a wild-type mouse imaged at baseline. Blood appeared bright in these images with a dark myocardium. Lumen size of the left ventricle showed that frame 1 corresponded to end-diastole and frame 10 to end-systole. Frame 1 was obtained immediately after an R-wave was detected (Trigger Delay <1 ms) by the gating software and a trigger was sent to the MRI console. Each subsequent image was obtained after a gap of 8 ms. The full image set was acquired in 2 min. Six-eight heart slices were acquired in one imaging session, leading to a total imaging time for cine acquisitions to about 20 min. This approach allowed us to calculate LV volumes accurately and consistently for all mice at ED and ES. Since one of our objectives was to obtain a quantitative measure of LV EDV and ESV, this bright blood imaging technique proved suitable for this purpose.

We obtained exceptional spatial and temporal resolution with bright-blood cine imaging which allowed for precise LV border contouring and measurement of cardiac functional parameters. There is turbulent blood flow in the LV immediately at the end of systolic phase of cardiac cycle (frames 11, 12, 13). This is caused by the sudden inflow of fresh blood from the atrium which mixes with the already saturated blood in the LV in the relatively stationary phase of end systole (frames 6-10). This causes blood in the imaging slice to partially contain some saturated blood that was imaged before the influx of fresh blood. When that cardiac slice is imaged in the next frame (frame 12), a portion of the 'bright' blood signal is lost because of this effect. A high temporal resolution

clearly splits the cardiac phases so that no such artifact can hamper contouring of the end-systolic frame.

2.3.2 Black-blood cardiac MRI

We used a double inversion spin echo T2-weighted sequence for black-blood cardiac MRI. Adiabatic 180° sech pre-pulses were used before each spin echo pulse pairs. A TI of 100-125 ms was used to null blood signal, depending on heart rate. Complete nulling of blood signal was obtained and good myocardium-blood contrast was obtained. These images were used for delineation of cardiac morphology and not for cardiac motion, thus no cine loops were obtained with black-blood contrast. Black-blood images were obtained at end-diastolic phase of cardiac cycle by changing the trigger delay as required. Figure 2.14 shows baseline black-blood images obtained from a wild-type mouse. Good demarcation between dark blood and myocardium was observed.

2.3.3 Documentation of successful ischemia reperfusion surgery

Electrocardiogram recordings were used to confirm successful induction of ischemia in the animals. Figure 2.15 shows subdermal echocardiogram recording from lead II in a wild-type C57BL/6 mouse. A distinct elevation in the ST segment of the ECG waveform compared to pre-occlusion level was observed within 5 s of occlusion of LCA. The elevation persisted for the entire duration of ischemia. ST

elevation is a classical hallmark of acute transmural myocardial ischemia, and thus indicated successful cardiac ischemia in the mouse (137). Post-reperfusion, the ST-segment elevation reduced considerably but still stayed above baseline level. In addition, Q wave became stronger and more pronounced. These two factors are indicative of ischemic damage to the tissue (92). In a subset of animals, TTC staining done 24 h post reperfusion on animals with ST segment elevation during ischemia. All the animals with ECG indicators of ischemic damage were found to have a transmural myocardial infarct.

We were successfully able to confirm the presence or absence of ischemia in animals using ECG as a diagnostic tool. This technique improved surgical success by providing real-time information on status of ischemia in the myocardial tissue. Using these qualitative ECG indicators as feedback, changes in the surgical technique were made as appropriate to improve success ratio.

2.3.4 Delayed Hyper Enhancement MRI

The MRI protocol for DHE MRI involved IP administration of gadodiamide outside the scanner. After contrast injection, animal was secured inside the scanner and localizer scans were completed. Earliest contrast-enhanced images were obtained 20 min post contrast administration. A thin layer of viable tissue was observed between blood and a region of hyper intense myocardium, which allowed for easy delineation of infarct region (open arrows in Fig 2.16). DHE imaging scans were repeated serially for 2 hours to get a time course of delayed

hyper enhancement in the heart. Infarct size measured with MRI was almost constant from 40-60 min post contrast injection (Fig 2.17A), thus providing a wide window of time for acquiring DHE MR images.

Signal intensity of hyper intense region increased with time and peaked at 40 min (Fig 2.17B). Hyper intensity in some regions was observed even up to 2 hours after contrast injection, indicating a slow wash off in those infarcted regions. Even though hyperintense region intensity dropped appreciably with time, there was enough contrast difference between infarcted hyperintense region and normal region to contour the infarcted region and measure its area. Thus, the decrease in infarct size observed with time was not as steep as the decrease in hyper intense region intensity.

Contrast enhanced MRI images of myocardial infarction were also obtained with T1-weighted FLASH cine sequence. This allowed for simultaneous evaluation of cardiac function and infarct volume calculation from the same scan. Figure 2.18 shows images acquired with this sequence. IR based sequences generated better contrast between infarct and non-infarct regions as compared to T1-weighted FLASH. Thus, IR sequence was used for infarct volume calculation and FLASH images were used to provide additional frames of reference for manual contouring of infarct region. This proved to be a robust technique for generating quantitative cardiac function and infarct volume data.

TTC staining was done on heart sections 20 min after MRI data acquisition was complete. Figure 2.19 shows contrast-enhanced MRI heart

images and corresponding tissue slices photographed post-mortem after staining with TTC. Visual comparison yielded close correspondence of infarct areas measured with MRI and TTC. To test the relationship between between infarct volumes obtained with DHE MRI and TTC staining, we plotted the two sets of data against each other and performed simple linear regression (Fig 2.20). Good positive correlation was found between measured MRI and TTC infarct volumes with $r^2 = 0.86$, slope = 1.07 and intercept = -0.87. The correlation was especially strong in infarcts smaller than 20% of LV. This confirmed that infarct volume measured with DHE MRI closely matched that measured by TTC staining.

Thus, we established an MRI technique that enabled us to non-invasively monitor infarct volume in mice after IR, eliminating the need to sacrifice animals at each time point to study infarct progression.

2.4 Conclusions

Our overall objective was to establish an MRI technique to evaluate murine cardiac function, study regional wall motion and measure infarct volume in an ischemia-reperfusion injury model. We established a 60 min transient LCA occlusion model to induce IR in mice and determined the functional electrophysiological consequences of ischemia and myocardial infarction. Cardiac MRI protocols were standardized on an 11.7 T vertical-bore MRI (Bruker AVANCE).

To delineate the true infarct size with DHE imaging we obtained a time course of DHE images from 20 to 120 minutes after contrast administration. A time window for DHE imaging was established by matching infarct volume on MRI with infarct volume obtained with TTC staining post mortem. We concluded that DHE imaging done 30-60 minutes after IP contrast administration closely correlated with infarct volume measured with TTC staining.

Cardiac function was evaluated by cine imaging of cardiac motion. We used an ECG-triggered FLASH pulse sequence for obtaining bright-blood cine loops of cardiac motion with a temporal resolution of 6-8 ms and a spatial resolution of 117 μm with 1 mm slice thickness. Black-blood imaging sequences were also standardized for accurate measurement of LV wall thickness and other wall structures.

Manual planimetry was used for calculation of LVEDV and LVESV using open source software ImageJ. Other functional parameters were also calculated using previously described analysis techniques. Custom-written software in MATLAB® was used for regional wall motion analysis. A high resolution (2°) radial sector approach was used for measurement of LV wall thickness at ED and ES. This provided the requisite resolution needed to perform regional wall motion analysis, given the small size of a mouse heart.

This technique does have some limitations. Cine imaging quality to evaluate cardiac function is heavily dependent on ECG gating. After IR injury, it is sometimes not possible to get a reproducible ECG trace which leads to irregular

and unfaithful R-wave detection and causes a drop in SNR. A poor shim can lead to susceptibility artifacts which can cause a loss of signal from lung-tissue interfaces, especially the posterior wall of heart. Furthermore, Gadolinium based contrast agents have been questioned for their ability to detect infarct region. It is suggested that hyper intense region observed on DHE images consists of both reversibly and irreversibly injured myocardium, and cannot be classified as a myocardial infarct without confirmation with other techniques. Even with all these limitations, MRI represents the best available technique for mouse cardiac imaging in terms of the copious amounts of information generated from one experiment, high image resolution, low operator bias and ease of data interpretation.

In conclusion, we established a non-invasive MRI-based technique to evaluate murine cardiac function, study regional wall motion and measure infarct volume in an ischemia-reperfusion injury model.

2.5 Figures

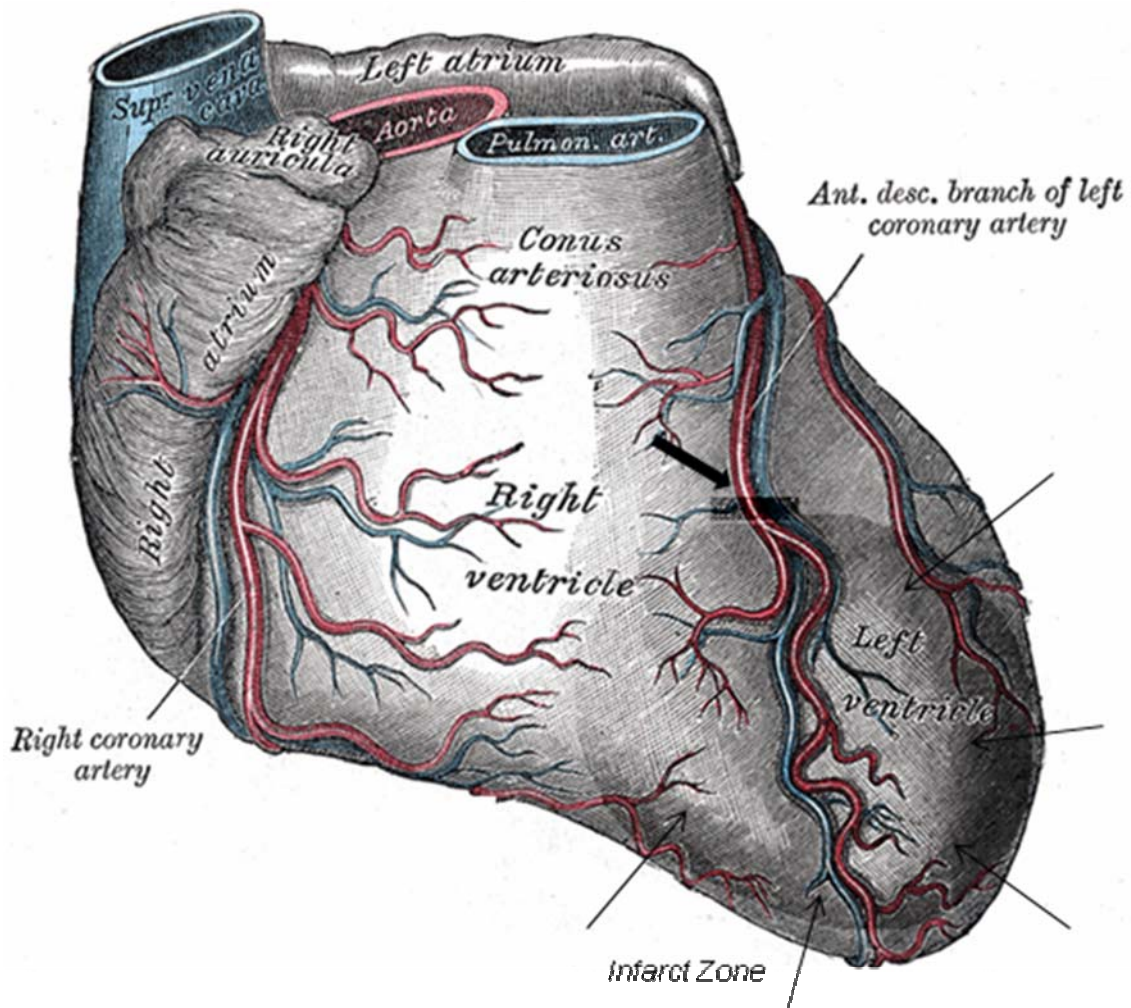


Figure 2.1 | Coronary arteries of human heart. An anterior view of human heart showing the right coronary artery and the anterior descending branch of the left coronary artery (LAD). Occlusion of LAD artery (at the site pointed by solid arrow) puts the downstream region of left ventricle (shaded region bounded by thin arrows) at risk for a myocardial infarction. Experimental modeling of this pathophysiological condition is surgically done in laboratory mouse. (Image obtained from the 20th U.S. edition of *Gray's Anatomy of the Human Body*)

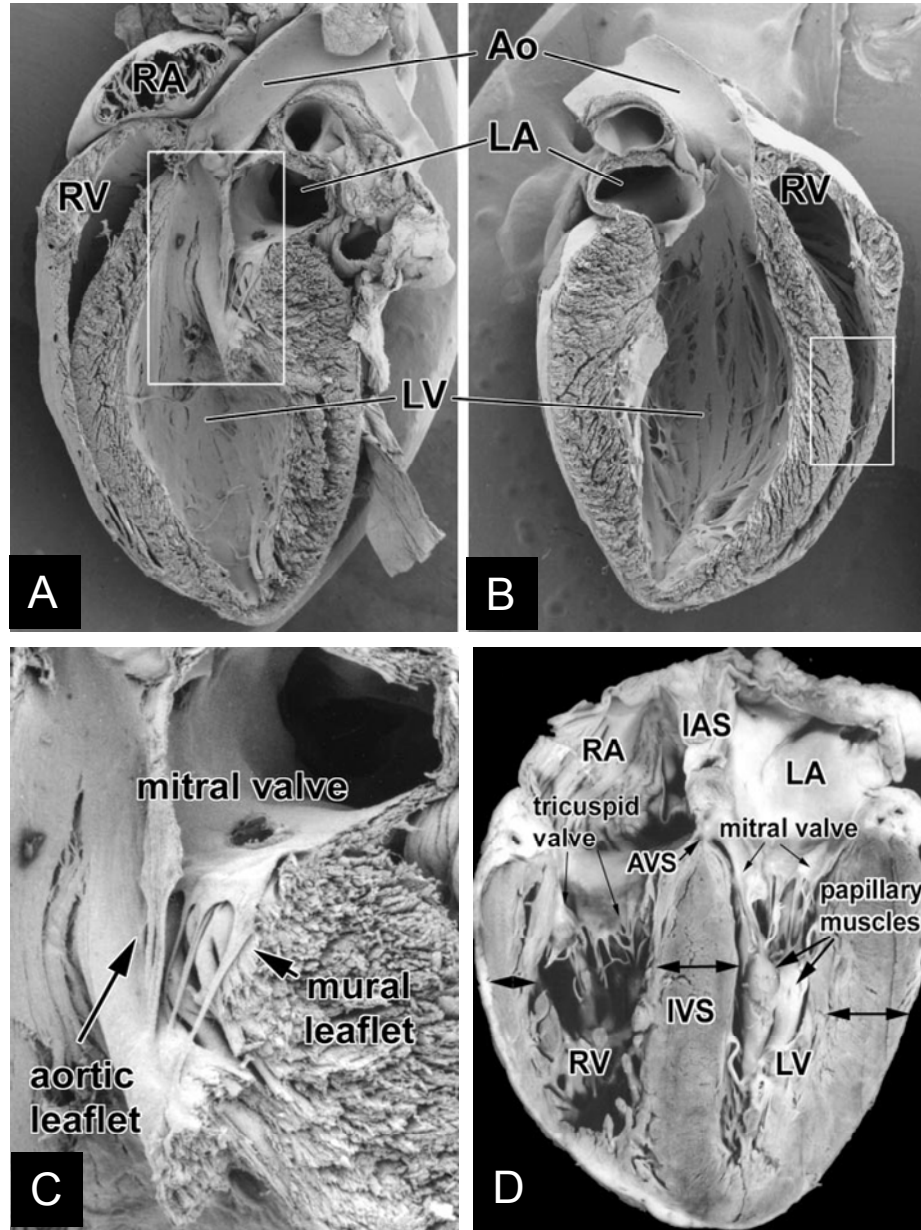


Figure 2.2 | Anatomy of postnatal mouse and human heart. *A* and *B*: SEM images of the posterior (*A*) and anterior (*B*) half of an adult mouse heart. *C*: an enlargement of the boxed area in *A*, showing the relatively small leaflets of the murine mitral valve. *D*: a postnatal human heart in 4-chamber view. Note the orientation and comparable thickness of the human but not mouse interventricular septum (IVS) in relation to the left and right ventricular free wall. Ao, aorta; AVS, atrioventricular septum; IAS, interatrial septum; LA, left atrium; LV, left ventricle; RA, right atrium; RV, right ventricle (from Wessels et al (87)).

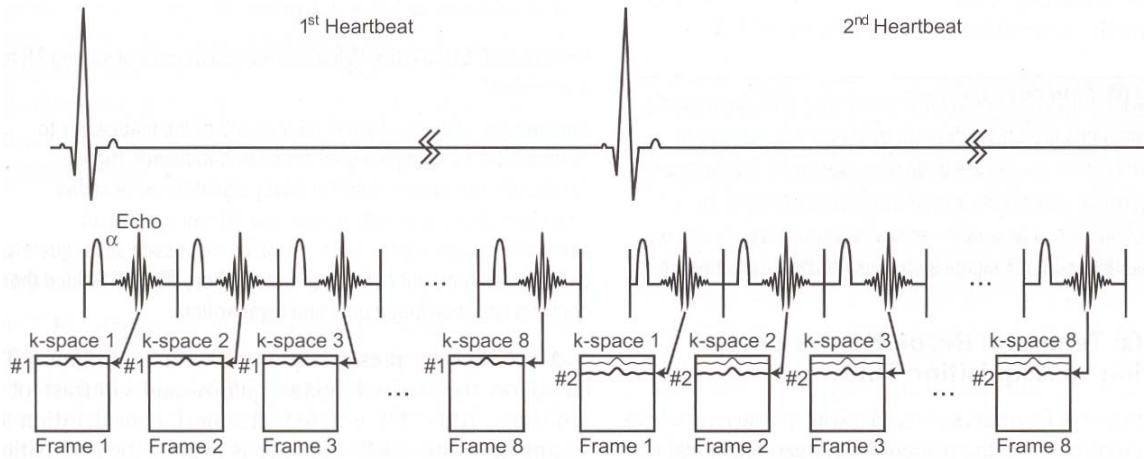


Figure 2.3 | k-space filling for multiple frames of an ECG-triggered cine gradient echo sequence. In this example, with each heartbeat, one line of k-space is acquired for each of the 8 frames in the cine loop. The total number of heartbeats needed to complete each image set depends on the number of phase-encoding steps. For example, if there are 192 phase encoding steps, total acquisition time for the 8 frames is 192 heart beats.

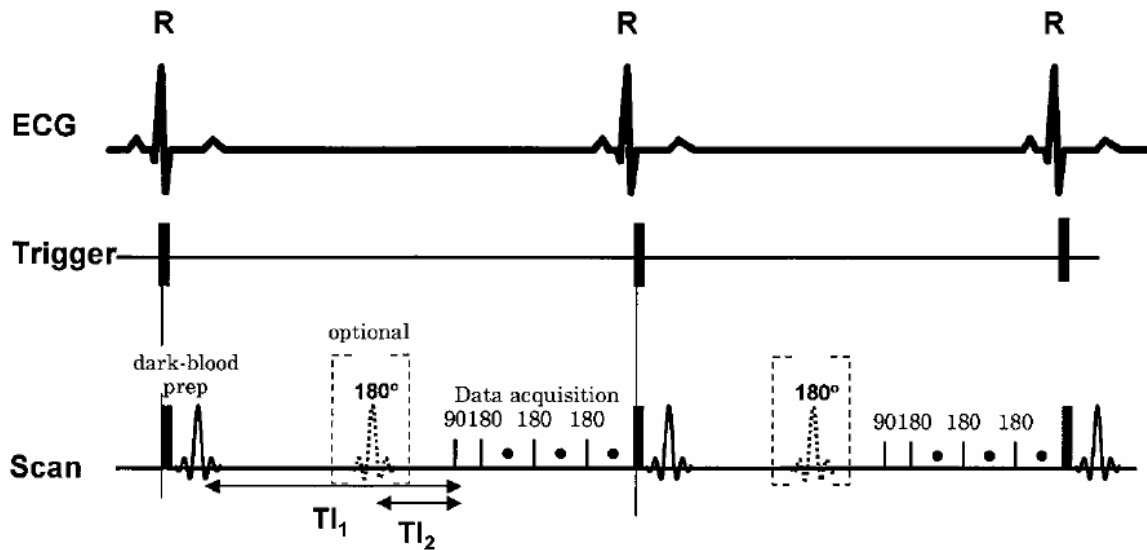


Figure 2.4 | T1-weighted fast spin echo and inversion-recovery fast spin echo pulse sequences. Dark-blood preparation pulses (denoted by dark-blood prep) are used to null blood signal by using two 180° pulses in quick succession without and with slice selective excitation. An optional third pulse can be used to null either fat signal intensity, or null normal myocardial signal intensity. T_1 is set to null blood signal intensity, and T_2 is set to null normal myocardial signal intensity after Gd-DTPA administration (from (156)).

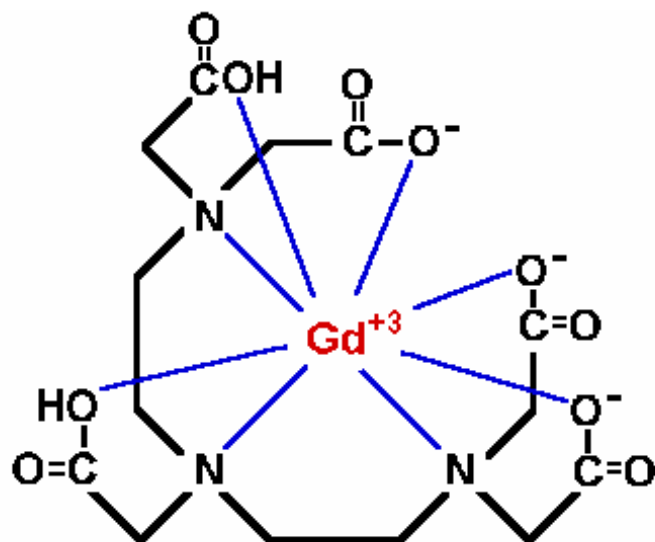


Figure 2.5 | Structure of contrast agent Gd-DTPA. Gd^{3+} ion has nine sites where water can bind but is chelated to DTPA in eight of those sites. The ninth site is open for water to approach the paramagnetic center of the molecule.

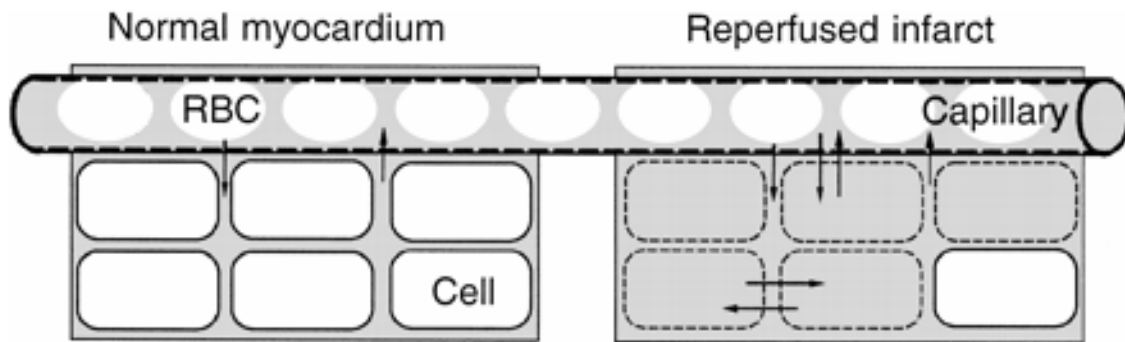


Figure 2.6 | Contrast agent distribution in normal and reperfused myocardium. Contrast agents (shown in gray), distribute rapidly in the extracellular space in normal myocardium, which constitutes about 20% of the myocardial tissue volume - that is, its fractional distribution volume is about 0.2. In reperfused infarcted myocardium, where myocardial cells have lost membrane integrity, the extracellular tracer passively distributes also into the intracellular space of irreversibly injured cells, and the fractional distribution volume approaches 1, or plasma levels (from Arheden et al(167)).

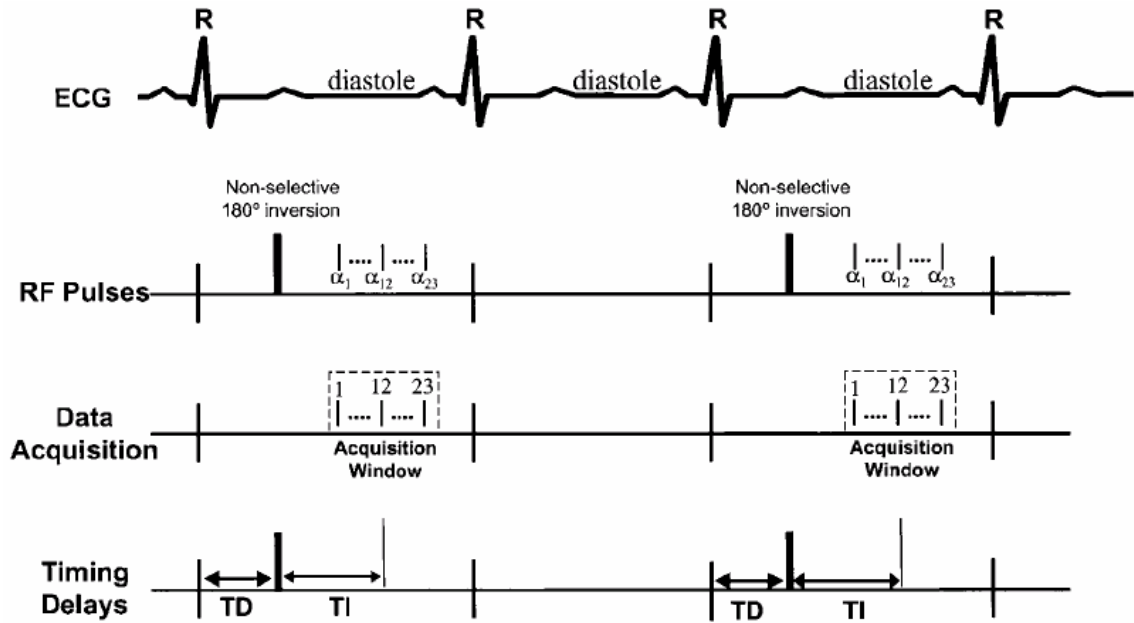


Figure 2.7 | Timing diagram of segmented inversion-recovery fast gradient echo pulse sequence used for clinical imaging. This sequence generates fast T1 weighted images. Here, 23 lines of k-space are acquired every other heartbeat (R-R interval 1 s). In order to allow for adequate longitudinal relaxation between successive 180° inversion pulses, these pulses are applied every other heartbeat (from Kim et al (157)).

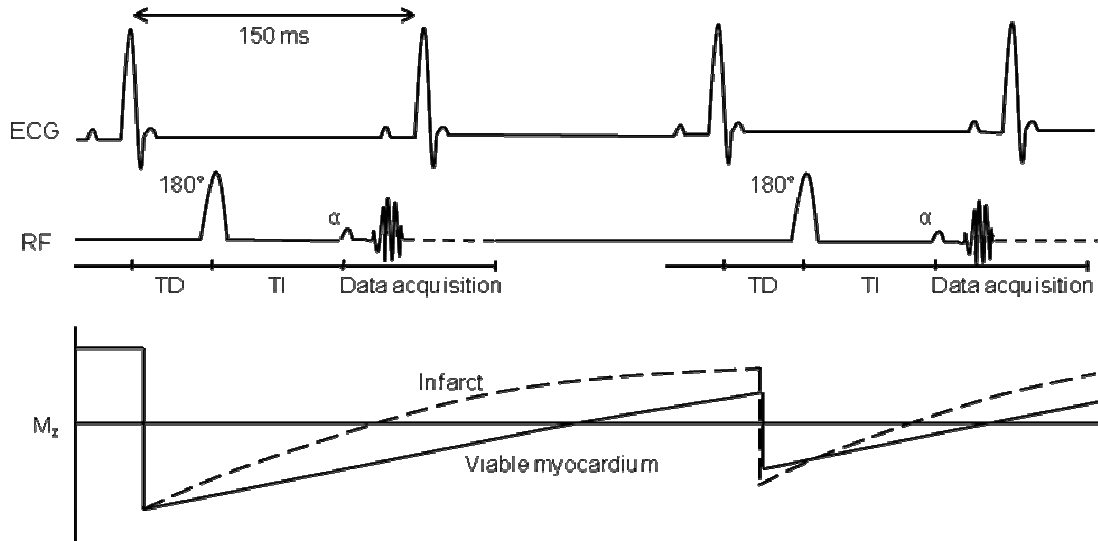


Figure 2.8 | Inversion Recovery Fast Gradient Echo sequence used in mouse imaging. This sequence achieves nulling of viable myocardium by a careful selection of an inversion time such that longitudinal magnetization associated with viable myocardium is 0 during filling of central lines of k-space (from (129)).

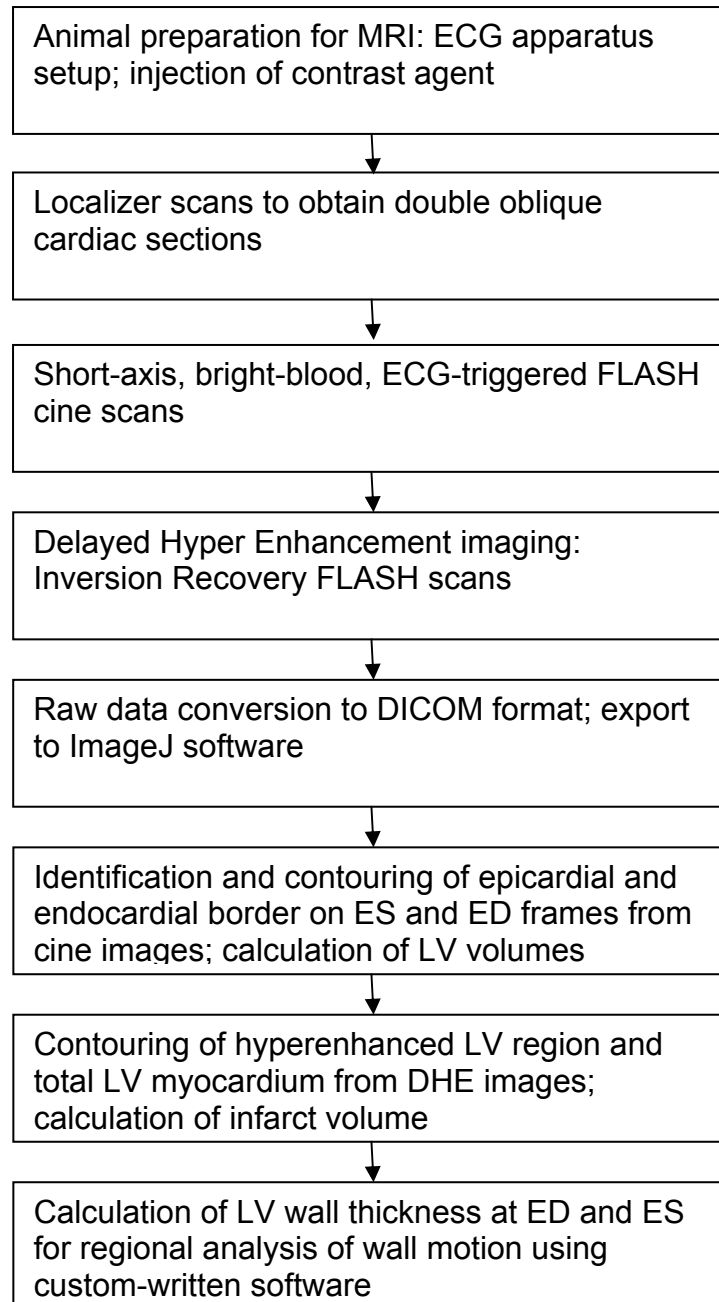


Figure 2.9 | Process workflow for evaluation of cardiac function using MRI. MRI images were acquired as described in the text. Raw MRI data was converted to DICOM format using Paravision 4.0 software. DICOM images were used for further image processing with ImageJ image processing software.

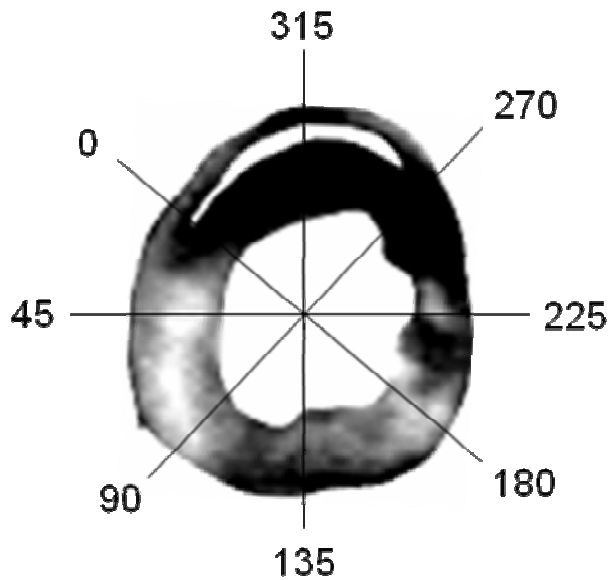


Figure 2.10 | Regional Analysis of LV Wall motion. LV wall was segmented into 8 equiangular 45° sectors using custom written software in Matlab. Wall thickness was calculated radially at 2° increments and was averaged for each sector at ED and ES. Wall thickness and fractional shortening data was indexed to right ventricular insertion point in the anterior wall and plotted against angle for representation of regional wall motion.

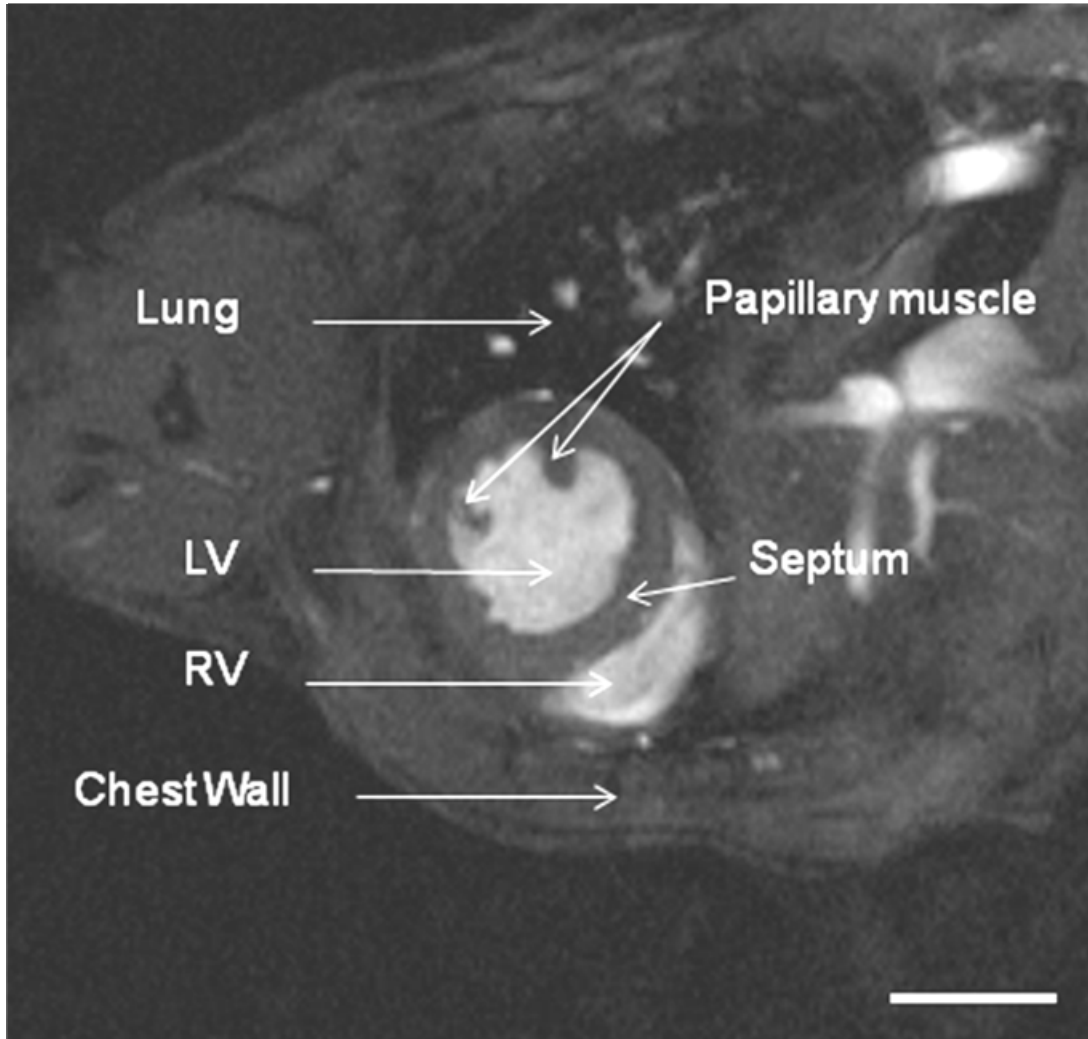


Figure 2.11 | Bright-blood image of a mouse heart in end-diastole as part of a cine loop. MR images were acquired with an ECG-triggered cine gradient echo pulse sequence. Image shown here is end-diastolic phase of the cardiac cycle. Good contrast is obtained between the blood (white) and myocardium (dark). The left ventricle, right ventricle, septum and papillary muscles can be clearly seen. Field inhomogeneity artifacts from the chest wall and lung can affect images obtained at high-field at interface of air and tissue, but are non-existent in this image. Such high image quality (SNR = 26.4) allows precise LV contouring for accurate analysis of cardiac function. Image parameters: FOV: 3 cm X 3 cm, matrix size: 256 X 256, no. of frames: 16, TR: 10 ms, TE: 1.4 ms and no. of averages: 4.

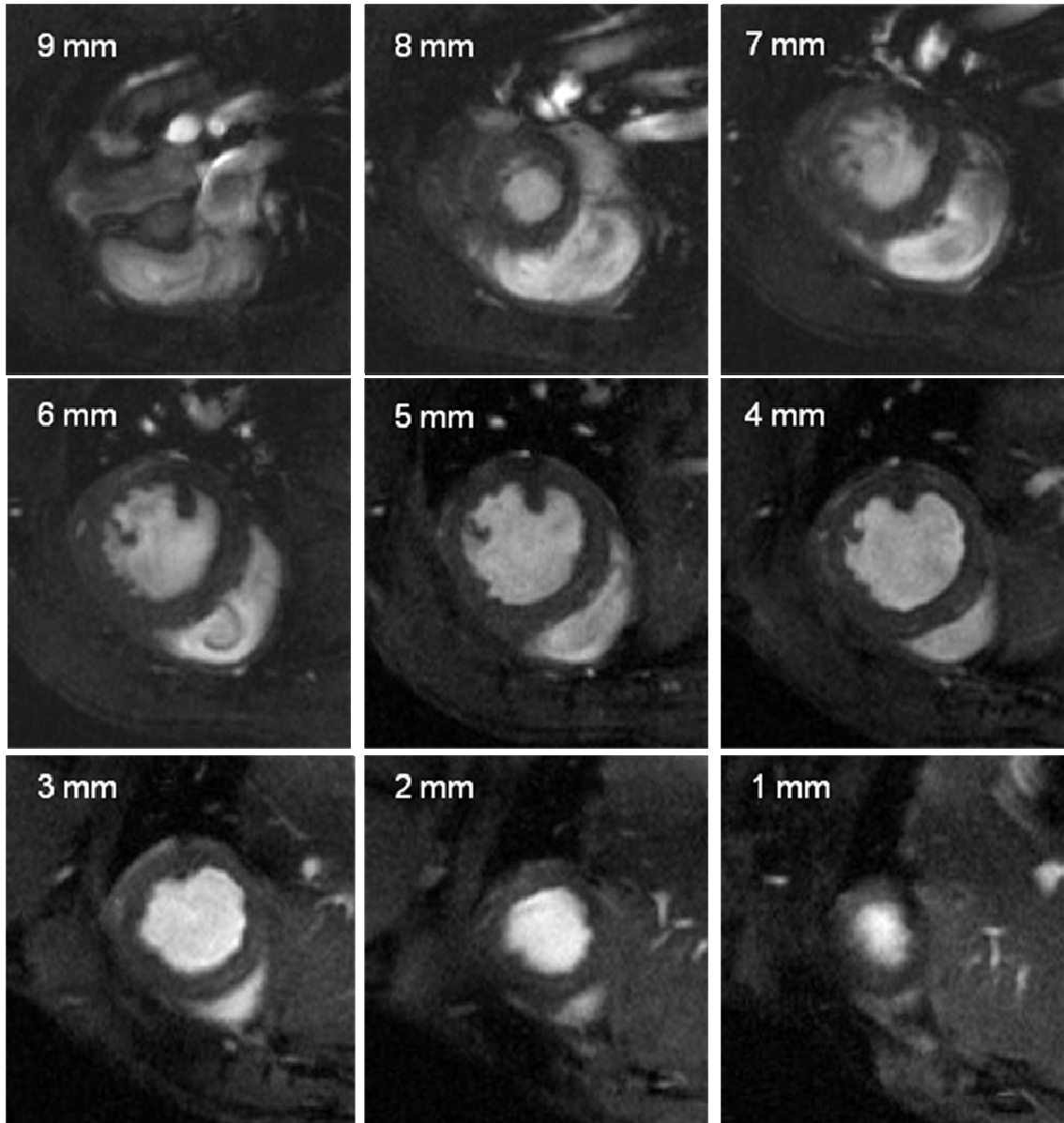


Figure 2.12 | Serially acquired bright-blood images of mouse heart in end-diastole as part of individual cine loops. MR images were acquired with an ECG-triggered cine gradient echo pulse sequence. Each image depicts the heart in end-diastolic phase of the cardiac cycle. Distance of middle of cardiac slice from apex is mentioned on each image. Cardiac slices at and above the level of aortic valve were not used for cardiac function analysis. Image parameters: FOV: 3 cm X 3 cm, Matrix size: 256 X 256, no. of frames: 16, TR: 10 ms, TE: 1.4 ms and no. of averages: 4.

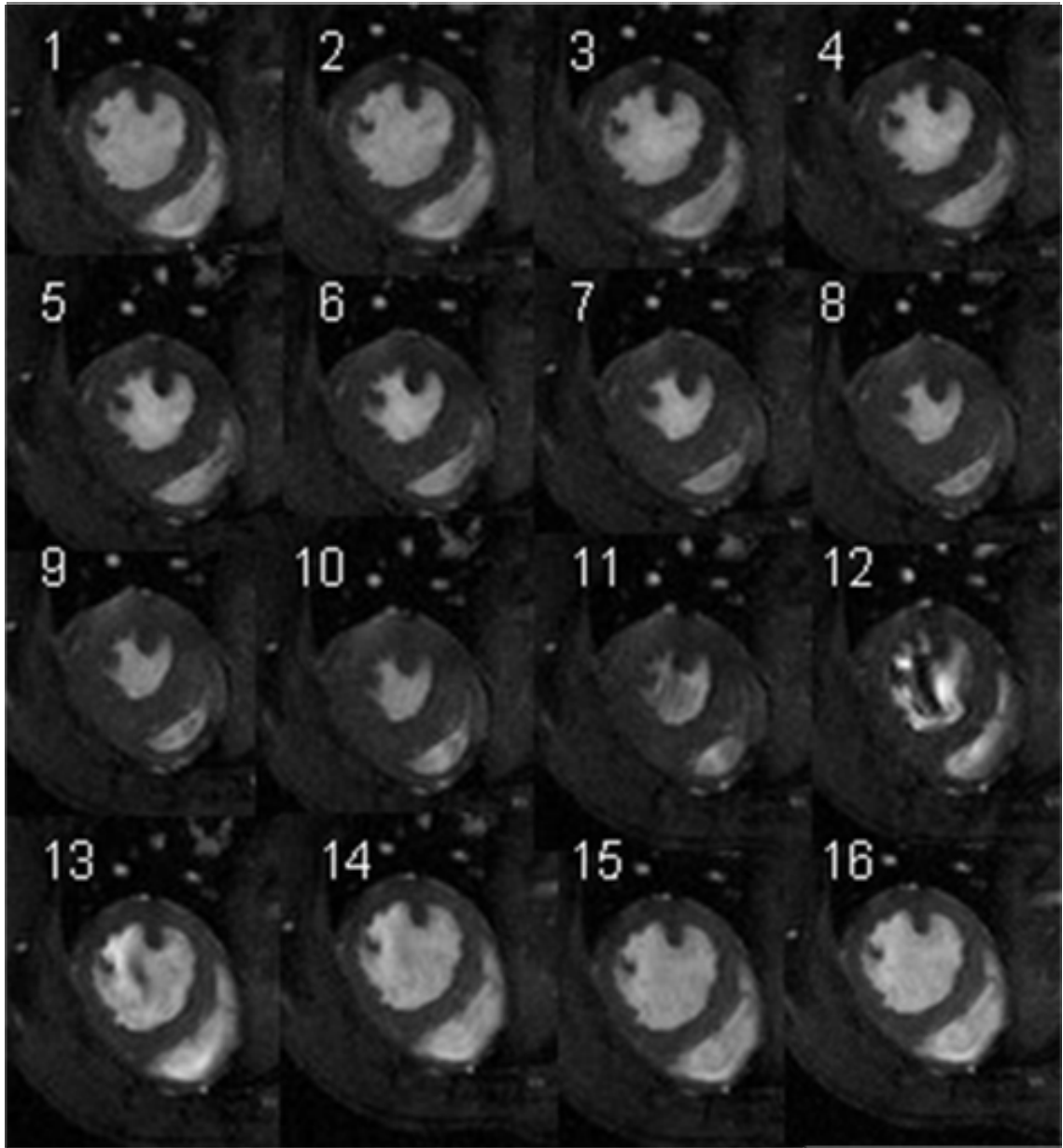


Figure 2.13 | Short axis cine gradient echo cine images. 16 frames were acquired from a cardiac slice 5 mm above the apex. Frame 1 was imaged immediately after the R-wave was detected, and shows end-diastolic phase of heart, whereas frame 10 shows end-systolic phase. Temporal resolution between frames was 8 ms which allowed for precise determination of end systolic phase and account for turbulent blood flow artifacts after end-systole. Image parameters: FOV: 3 cm X 3 cm, Matrix size: 256 X 256, no. of frames: 16, TR: 10 ms, TE: 1.4 ms and no. of averages: 4.

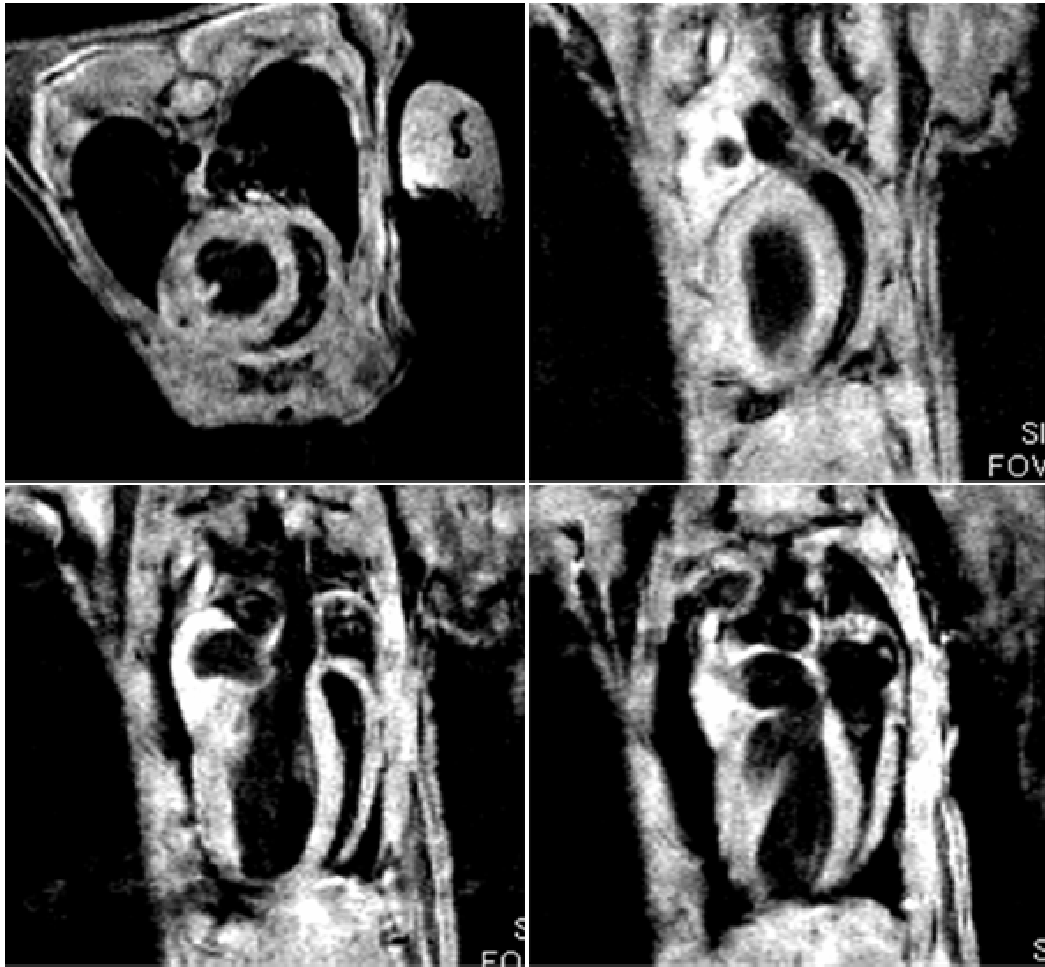


Figure 2.14 | Black blood images of mouse heart. Double inversion pre-pulses were used with a TI of 100 ms before a spin echo sequence to null blood signal. A) Short axis slice at 5 m above apex. B-D) Long axis images of mouse heart with complete blood nulling in all areas of heart.

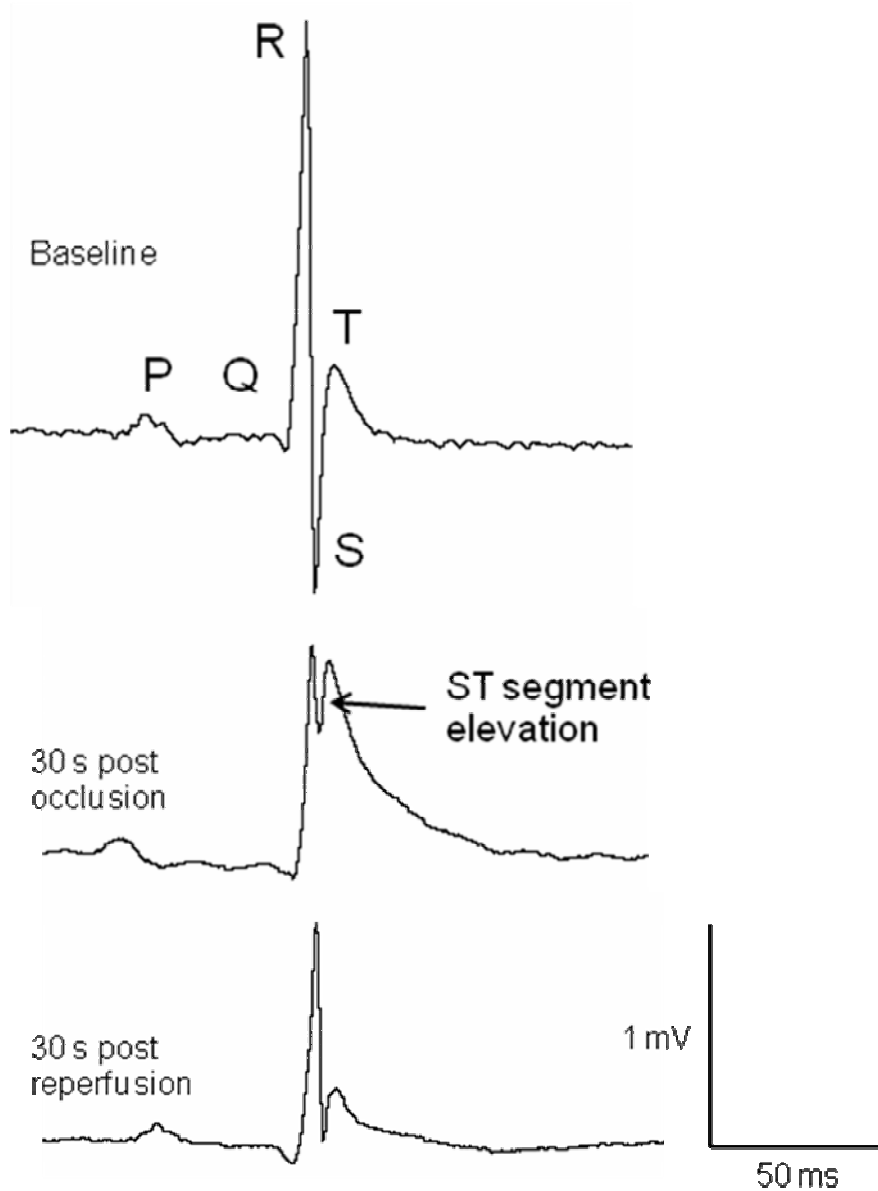


Figure 2.15 | Subdermal echocardiogram recording during IR. Subdermal ECG recording from lead 1 in a wild-type C57BL/6 mouse at baseline (A), 30 s post LCA occlusion (B) and 30 s post reperfusion (C). A distinct and immediate elevation in the ST segment of the ECG waveform was observed compared to pre-occlusion level. The ST segment elevation dropped after reperfusion, but stayed above baseline levels.

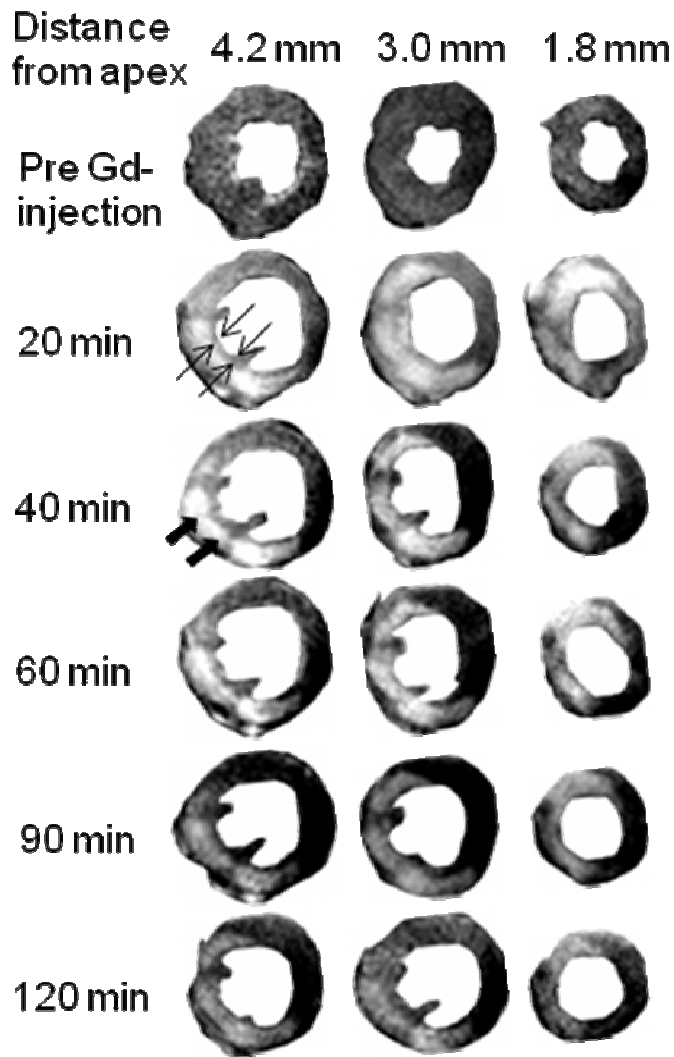


Figure 2.16 | Time course of signal enhancement in heart after contrast agent administration. Contrast agent Gd-DTPA-BMA was injected IP (0.6 mM/kg body weight) in mouse 3 days after 60 minute transient LCA occlusion surgery. The mouse was then immediately placed into the MRI and data acquisition was started. Contrast enhanced images were acquired with an inversion recovery pulse sequence with TI 150-200 ms. Time course of signal enhancement in three heart slices is shown with hyper enhanced regions (white) indicating myocardial tissue damage. MR images were segmented with Photoshop for better display of left ventricle. Solid arrows indicate region of hyperintensity which was interpreted as infarct. Open arrows indicate a thin layer of viable tissue between the infarct region and LV lumen, which aided in infarct segmentation and planimetry.

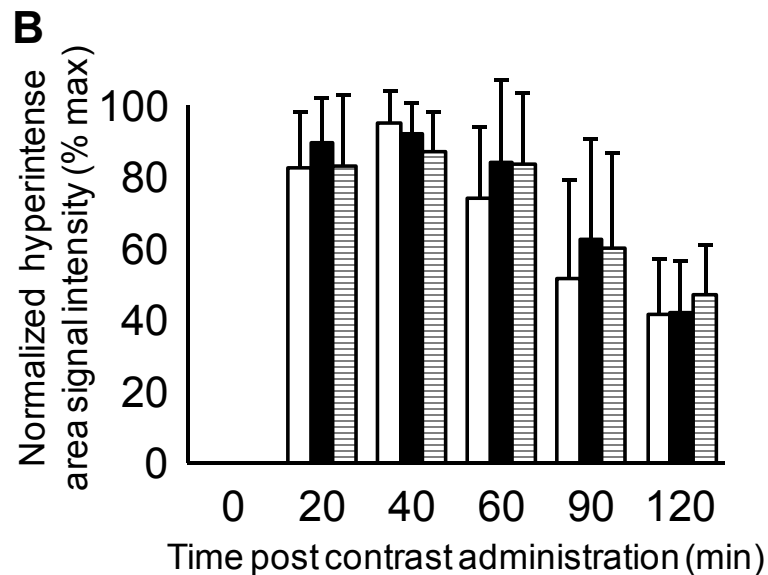
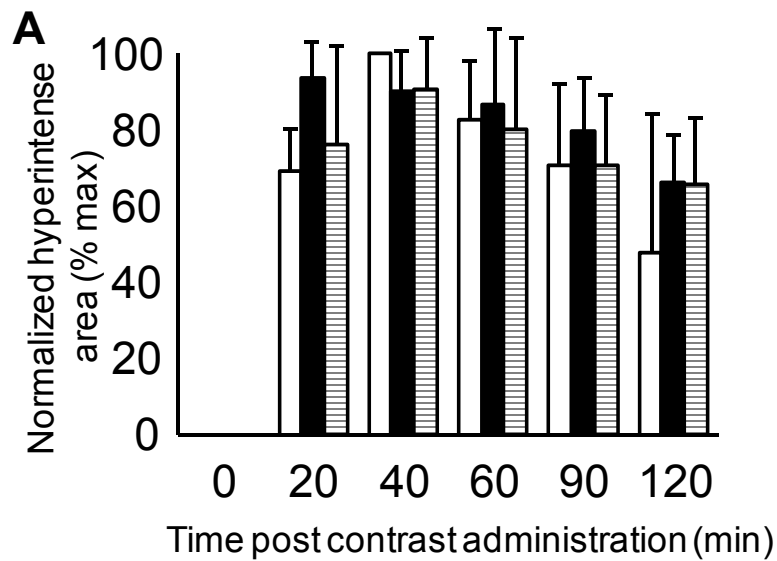


Figure 2.17 | Time course of hyper intense region area and signal intensity after Gadolinium contrast agent administration. (A) Hyper intense area on each image remains constant from 40-60 minutes post contrast administration. MR slices in left column of Fig 2.15 are represented by open bars, middle column by solid bars, and right column by striped bars. (B) Signal Intensity of hyper intense region was normalized to maximum level of each slice. Peak signal intensity was observed 40 minutes after contrast agent administration. All contrast enhanced images in this study were acquired 40-60 minutes after contrast agent administration, providing a wide window of time for data acquisition.

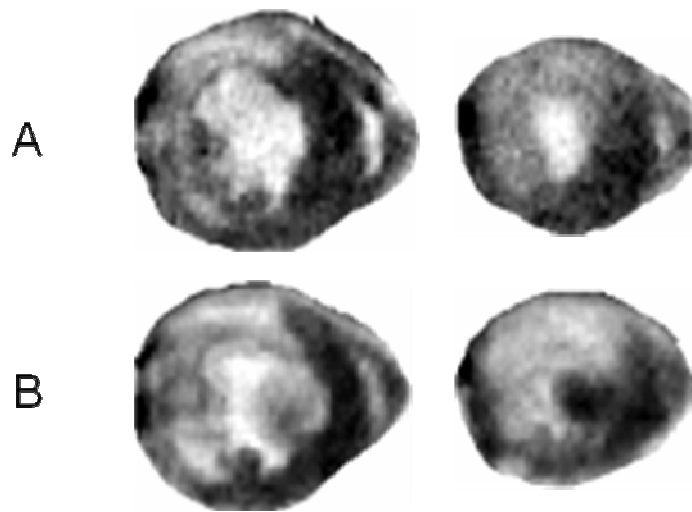


Figure 2.18 | Comparison of FLASH with IR-FLASH for DHE MRI. Serial sections of heart 3d after 60 min IR surgery represented by contrast enhanced MRI images obtained with T1-weighted FLASH cine sequence (row A) compared to IR-FLASH (row B). Both sequences show similar hyper intense areas indicative of infarct damage, although SNR of FLASH cine sequence is expectedly lower.

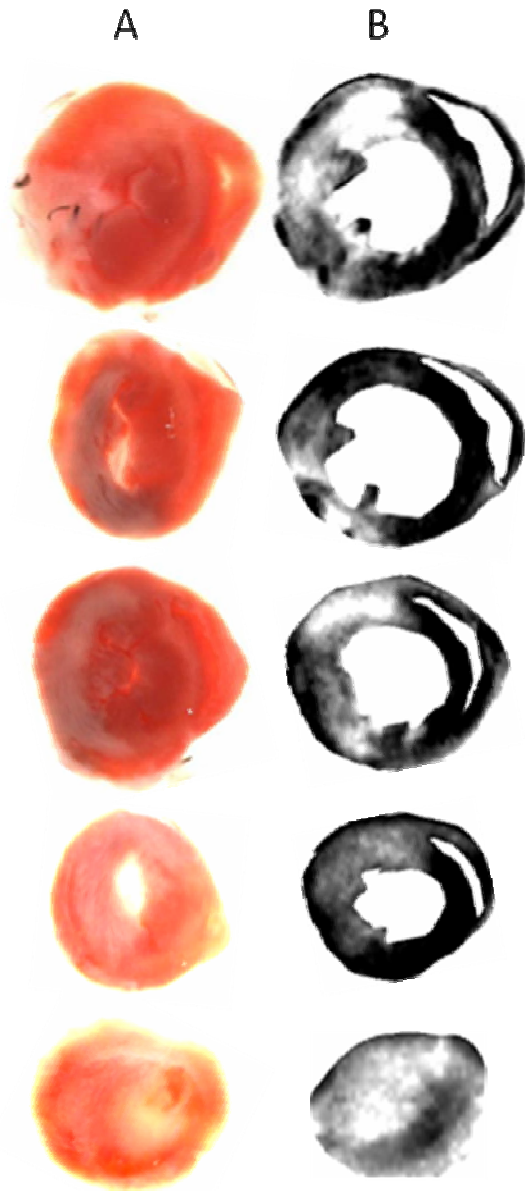


Figure 2.19 | Contrast-enhanced mouse heart MR images compared with corresponding tissue slices photographed post-mortem. (A) MR images were obtained 3 days after 60 minute occlusion of LCA coronary artery and 40 minutes after injection of Gd-DTPA-BMA contrast agent. (B) Color images obtained by digital photography of corresponding tissue sections stained with TTC.

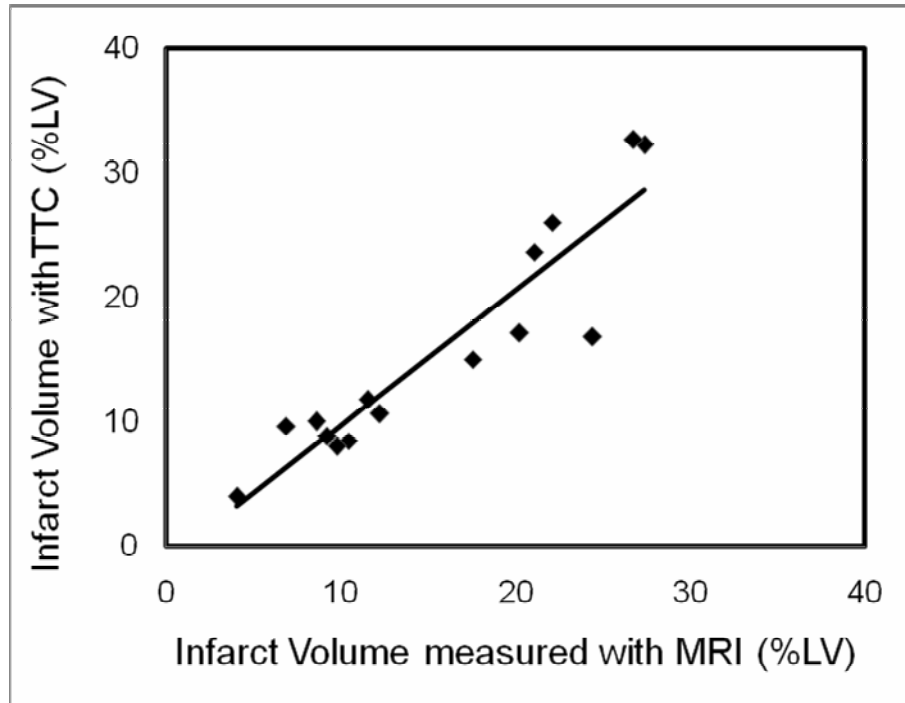


Figure 2.20 | Statistical comparison between infarct volume measured with TTC and MRI. Good correlation ($r^2 = 0.86$) was found between spatial location and extent of myocardial damage delineated by enhanced regions (white) in MR images and necrotic regions (white) not stained red by TTC. Best-fit linear trendline is drawn through the individual data points ($n = 15$).

CHAPTER 3

IMPLICATIONS OF PROGRESSIVE MYOCYTE DEATH AFTER ISCHEMIA- REPERFUSION INJURY ON LV REMODELING IN MOUSE HEART

3.1 Introduction

In spite of its eminent clinical importance, the understanding of the causal mechanisms of myocardial ischemia-reperfusion injury is still incomplete. The introduction of therapeutic interventions that allow early reperfusion of the ischemic myocardium gave rise to the question of whether modification of reperfusion conditions could influence infarct size development. It is argued that if it is possible to limit infarct size with an intervention at the time of reperfusion, a part of the injury developing without such an intervention in ischemia–reperfused hearts must be due to causes originating within the reperfusion period (168). Injury produced by such causes has been termed “reperfusion injury” or, more specifically, “lethal reperfusion injury” if one refers to causes leading to cell death and therefore infarct size enlargement. Lethal reperfusion injury is defined as injury caused by restoration of blood flow after an ischemic episode leading to death of cells that were only reversibly injured during that preceding ischemic

episode (169). It classically includes myocardial stunning, reperfusion arrhythmias and lethal reperfusion injury.

In a large number of studies on reperfusion injury, the effects of antioxidants have been investigated. These studies were based on the hypothesis that oxygen-derived free radicals produced upon reperfusion of ischemic myocardium represent the predominant cause of lethal reperfusion injury. This hypothesis was based on two well-documented facts: free radicals are indeed produced during reperfusion (170-176), and exogenously applied free radicals have negative effects on many cellular and subcellular systems (177; 178). It is understood that the principal mediators of reperfusion injury are free radicals and invasion by activated neutrophils (179). Upon reflow, oxygen radicals are generated in large amounts, overwhelming cellular defenses and inducing oxidative tissue damage; biochemical markers of oxygen radical formation and attack can be found in postischemic myocardium. Oxidants can also modulate various events, ultimately leading to tissue injury, such as nitric oxide formation, platelet-activating factor metabolism, tissue factor synthesis, and exposure of adhesion molecules. Reintroduction of neutrophils in postischemic tissues is accompanied by their activation, with release of lytic enzymes that directly induce tissue damage and proinflammatory mediators that amplify the local inflammatory reaction. Neutrophils may also plug capillaries, mechanically blocking flow.

However, the existence of lethal reperfusion injury has been debated for years by scientists and is still controversial (169; 180; 181). One of the problems is that the development of cell death cannot be accurately followed in time, both in experimental animals and in humans. It is another question whether reperfused myocardium may also become subject to apoptosis, i.e. programmed cell death, even if effectively protected against immediate necrotic injury. Apoptosis is a transcriptionally controlled cellular response to moderate cell injury or to the influence of various cytokines. In contrast, necrotic cell death is the consequence of severe structural cell damage and is not transcriptionally regulated. Recently, evidence for apoptotic cell injury in ischemic-reperfused myocardium and in border zones of ischemic myocardium has been demonstrated (182-189). This gives rise to the question if reperfusion of severely ischemic myocardium followed by delayed apoptotic cell death could abolish all short-lived protective effects against the acute onset of necrosis during reperfusion. The real contribution of apoptosis to cardiomyocyte death has not yet been established. More importantly, the functional significance of such a secondary death process has also not been examined.

It is well established that oxygen free radicals increase in concentration upon reperfusion of ischemic cardiac tissue and can damage various cellular components (170-176). Although restoration of blood flow is essential for salvaging ischemic tissue, oxidative damage may occur during reoxygenation and contribute to IR injury. This reperfusion-induced injury of the myocardium is a well-accepted paradigm of cardiac damage. In addition to this, it has been

suggested that myocytes in the ischemic heart region are prone to death via secondary apoptotic mechanisms (168; 182-189). It is understood that cardiac damage observed after IR is attributed solely to reperfusion injury and the functional significance of the secondary death process has not been examined.

We hypothesized that IR also causes secondary progressive myocyte loss leading to a worsening of LV function and regional wall motion over time. We used histology and high resolution cardiac MRI to study LV function, structure and infarct volume progression in mice after IR injury in an attempt to address the functional significance of secondary damage suffered by myocardium after reperfusion induced injury.

3.2 Materials and Methods

3.2.1 Experimental Plan

Our overall objective was to evaluate the functional implication of progressive myocyte death to LV remodeling in mouse heart. We evaluated cardiac function and myocardial infarct volume in mice over a period of 14 days after 60 minute transient LAD occlusion surgery using MRI and histology.

A total of thirty four young adult (10–12 wk of age) male C57BL/6 mice (Harlan Technologies, IN) were used in this study. Mice were randomly divided into 5 groups. After IR surgery, MRI was done at specific time points on each group of animals. Immediately after MRI, animals were harvested for histology of

cardiac tissue. Group 1 was harvested 1 hour after reperfusion; group 2 at day 1 after reperfusion, group 3 at day 3 after reperfusion, group 4 at day 7 after reperfusion, and group 5 at day 14 after reperfusion. Table 3.1 shows the time table for the study. Baseline MR scanning was initially done to obtain control parameters of cardiac function and LV wall thickness. LAD occlusion surgery was done 3-5 days after baseline MRI for normalization of physiologic parameters to baseline levels. Serial MRI was done on mice at day 1, day 3, day 7 and day 14. MRI was done immediately after reperfusion only on the group that was harvested for tissue at 1 h post reperfusion. This was done to avoid anesthetic stress on the animals immediately after surgery. Animal mortality was an issue only in this group, given the prolonged time the animals need to be anesthetized for surgery and then for MRI. Animals from no other group died inside the MRI scanner.

Within 20 min of completion of MRI scanning, animals were killed and their hearts were excised for TTC staining. TTC staining protocol is described in section 2.2.5.3. After staining and photography, the heart sections were stored in 10% formalin for 7 days for fixation. The sections were processed and embedded in paraffin as per standard tissue embedding protocols. Sections of 5 μ m thickness were cut and stained with Hematoxylin-Eosin and Masson's Trichrome. Infarct volume was calculated from these sections using planimetry and was compared to MRI outcome.

These experiments allowed us to study the functional implication of secondary death processes after IR to LV remodeling in mouse heart.

Time Point	Procedure done
-5 d	Baseline MRI
0 h	60 min IR
1 h	1h group: MRI + histology
1 d	1d group: MRI + histology 3d group: MRI 7d group: MRI
3 d	3d group: MRI + histology 7d group: MRI 14d group: MRI
7 d	7d group: MRI + histology 14d group: MRI
14 d	14d group: MRI + histology

Table 3.1 | Time course of procedures done on various animal groups at specified time points before and after IR surgery. MRI was not done on all animal groups at 1h post IR to avoid mortality caused by extreme stress involved with excessive anesthetic use during surgery and MRI.

3.2.2 MRI protocol for analysis of cardiac function, LV wall motion and infarct volume

Serial evaluation of murine cardiac parameters after IR was done using MRI at specific time points. We performed bright-blood gradient echo imaging to obtain cine loops of cardiac motion from which cardiac function data was extracted. The imaging method is described in section 2.2.2. We used an ECG-triggered FLASH pulse sequence for generation of cine loops. After IR surgery, most animals showed a pathological ECG trace with a large chronic Q wave and an abnormal negative R wave indicative of myocardial infarction. Also, ECG patterns changed over the course of the study as the depth of anesthetic and core body temperature of animals fluctuated. It was not possible to obtain a reliable ECG trace with any lead position in some of these animals. Since most of the data was acquired with prospectively-triggered scans, a robust ECG detection system was absolutely required for cine imaging.

To detect a consistent R wave pattern, we modified the R wave detect algorithm parameters continuously for consistent gating pattern. The ECG detection unit (Model 1025, Small Animal Instruments, Stony Brook, NY) was based on optical transmission of ECG signal to the gating hardware control unit. Subdermal ECG leads were fixed on the right forepaw and right leg (lead I) of the animal. Electrical ECG signal was then transduced to an optical signal produced from a Light Emitting Diode (LED) and passed through a fiber optic cable that ran the distance from MR system to the MR workstation. Optical transmission of the

ECG signal makes it impervious to other electrical noise from the hardware of the MRI unit. The optical signal was converted back to electrical signal at the gating hardware control unit. Since the initial ECG detection was done via electrical leads, it was sensitive to gradient noise which is present at all times during cine imaging. After amplification, the ECG signal was around 1.5 mV in amplitude with a SNR of less than 5. Although animal heart rates were consistently above 400 bpm, ECG hardware bandwidth was sufficient to sample all frequency components of the ECG signal.

The poor ECG trace and presence of gradient noise made it challenging to detect the R-wave reliably in animals after IR. We set certain conditions for R wave detection on the gating software. When the following two conditions were met, an R wave was detected and a trigger was sent to the MRI console:

1. An increase in ECG signal amplitude by 50 mV in 10 ms.
2. A decrease in ECG signal amplitude by 30 mV in 8 ms.

Also, the blanking period (period of time after detection of R-wave when no other triggers are detected) was kept just 20 ms less than the R-R interval to remove effect of gradient noise in the ECG signal from affecting R wave detection. This led to missed R-wave triggers in mice with cardiac arrhythmias, but the frequency of those incidences was low and was not a major problem in cine imaging.

The ECG-triggered FLASH pulse sequence used for generation of cine loops to evaluate cardiac function and wall motion did not involve segmentation

of k-space because of the fast heart rates of mice. Thus, only 1 line of k-space was acquired after each heart beat. The total time of acquisition of each cine loop was: 192 (no. of phase encoding steps) X 150 ms (R-R interval at heart rate of 400 bpm) X 4 (no. of averages) \approx 2 min. A total of six-eight cardiac slices were acquired for each animal with the following imaging parameters- FOV: 3 cm X 3 cm, Matrix size: 256 X 192, no. of frames: 16, TR: 10 ms (variable, dependent on heart rate) and TE: 1.4 ms. Each scan was averaged 4 times to improve image quality and increase SNR. All cine loops were acquired within 20-25 min for each animal.

Delayed hyper enhancement (DHE) imaging was done to image the myocardial infarct in mice after IR. We used contrast agent gadodiamide (Gd-DTPA-BMA, diethylenetriamine pentaacetatobis(methylamide)gadolinium(III)) which was injected IP (intra peritoneal) at a concentration of 0.9 mM/kg body weight in the mouse. Most clinical and large animal DHE imaging techniques involve intra venous (IV) administration of contrast agent (138; 190-193). In mice, both IV and IP routes of contrast administration have been used for DHE imaging (98; 122). Since it is much more technically challenging to catheterize the tail vein of a C57BL/6 mouse compared to an IP infusion, we chose to administer contrast agent as an IP bolus. We modified our imaging protocols to accommodate the change in method of contrast administration. We used an inversion recovery FLASH pulse sequence for DHE imaging. This sequence is well-documented for myocardial infarct delineation in animals and humans (96; 97; 158; 193). Using software image processing techniques we were able to extract

quantitative information about cardiac function, regional wall motion and infarct volume for each mouse at each time point after IR.

The complete MR imaging protocol used for cardiac functional imaging and DHE imaging is listed below:

1. IP injection of contrast agent (time $t = 0$)
2. Resonator frequency matching and shimming ($t = 10$ min)
3. Localizer scans ($t = 20$ min)
4. Cine gradient echo scans ($t = 40$ min)
5. DHE imaging scans ($t = 60$ min)

The MRI technique described above was used for serial evaluation of cardiac function and structure after IR to evaluate the impact of progressive myocyte death on LV remodeling.

3.2.3 Histology of Cardiac Tissue

Histology is defined as the study of tissue sectioned as a thin slice. The concept of histology as a subject includes understanding of the structure and function of cells, tissues, organs and organ systems. It can be described as a technique for visualization of microscopic anatomy. Clinically, it is the gold standard for detection of several pathologies (194-196). Histological staining is a

post-mortem technique for study of myocardial infarction. We used histology of cardiac tissue to visualize time course of myocardial infarction after IR at a microscopic level and compare it to the non-invasive technique of MRI. We performed cardiac staining on tissue with three kinds of stains: TTC, Hematoxylin-Eosin and Masson's Trichrome for delineation of infarct region. Our objective was to compare MRI with histology to evaluate the differences in infarct volume as measured with the two techniques at each time point after IR.

TTC Staining:

TTC staining is a technique for gross determination of infarct volume in tissues post-mortem. TTC staining can be done very quickly and is used routinely after IR for delineation of myocardial infarction (94; 98; 106). Necrotic infarct region appears white and viable non-infarct region appears red after the tissue has been stained with TTC. For staining, animals were killed and their hearts were excised 20 minutes after MRI scanning was completed. Cardiac tissue was harvested quickly after MRI to limit any changes to the cardiac tissue that might occur with time.

Animal hearts were excised, washed and rinsed in phosphate-buffered saline at room temperature. Hearts were encased in warm 2% agarose solution. The agarose quickly cooled and formed a hard layer around the heart that aided in tissue sectioning. After waiting for 2 minutes to let the agarose set, the heart was laterally cut just below the left auricle and 1 mm thick sections were made using a heart matrix. Using forceps, the agarose was then removed from around

the heart. Sections were incubated with 2% 2,3,5-triphenyltetrazolium chloride (TTC) at 37°C for 20 min, with rotation every 2 min to allow uniform tissue staining. After visual confirmation that a portion of the tissue had stained red and a white infarct region could be observed, the slices were placed on a glass slide. Each slice was photographed with a digital camera mounted on a dissecting microscope at 5X magnification.

Hematoxylin-Eosin and Masson's Trichrome staining:

Hematoxylin and eosin (H&E) are the most commonly used stains in histology. Hematoxylin colors nuclei blue, and eosin colors the cytoplasm pink. This stain provides a good morphological delineation of myocytes in cardiac sections. Infarct region on H&E stained sections was defined as region with loss of myocytes.

Masson's trichrome is a three-color staining protocol and is suited for distinguishing myocytes from surrounding connective tissue. The stain produces red keratin and muscle fibers, blue or green collagen, light red or pink cytoplasm, and dark brown to black cell nuclei. Infarct region on Masson's trichrome stained sections was defined as region with loss of myocytes.

After photography for TTC staining was completed, sections were fixed in 10% buffered formalin solution for 2 weeks. Formalin used was buffered with phosphate salts to achieve a pH of 7.0 which prevented the formation of formic acid. Formalin fixation is required as it stabilizes the proteins throughout the tissue slice and prevents changes typically caused by postmortem activities such

as mold or bacterial attack (putrefaction) and the continuation of enzyme metabolic processes (autolysis). Importantly, formalin fixation protects the cardiac tissue from the denaturing effects of the dehydrating agents and the ravages of subsequent processing steps. Formalin fixes a tissue in two steps (197). The first step, which occurs as the fixative penetrates the cells and stops the metabolic processes, involves one end of the formaldehyde molecule reacting with and loosely attaching to a select tissue protein. The second step is much slower and can continue for a period of years. It consists of the formation of a more stable bond, or crosslinking, between the remaining reactive end of the formaldehyde molecule onto the same macromolecule with the loose bond or with one that is nearby. This causes firming of the macromolecules and masking of biologically active sites.

Fixed tissue slices were “processed” to remove the fixative and move the sample into a non-aqueous paraffin support medium. Tissue samples were dehydrated by passing through graded alcohol solutions and embedded in paraffin blocks. Tissue blocks were stored at -4 °C overnight for tissue hardening. Sections of 5 µm thickness were obtained using a microtome and mounted on glass slides.

Masson’s trichrome staining and Hematoxylin & Eosin staining was done on the heart sections using standard staining techniques. The stained sections were photographed using a camera (model D30, Hitachi) mounted on a microscope (Axiovert 200M, Zeiss). Manual planimetry on H & E stained sections

was performed on the microscope using PALM RoboSoftware v 2.2 to calculate infarct volume.

3.2.4 Image Processing

MR images were quantitatively analyzed by ImageJ (NIH) image analysis software to measure infarct volume, cardiac function and regional wall motion parameters as described in section 2.2.6. Endocardial contours were manually traced by a blinded image analyst at end diastole (ED) and end systole (ES) for each slice. The LV end-diastolic volume (EDV), ESV, stroke volume (SV), cardiac output (CO) and ejection fraction (EF) were computed for mice at each time point after IR. We were able to track changes in cardiac function in mice over a period of 14 d after IR. For analysis of LV mass (section 2.2.6.3), the epicardial and endocardial borders were manually traced at end-diastole. The endocardial area was subtracted and multiplied by myocardial density (1.05 g/cm^3) to calculate LV mass.

The hyper intense infarct region from DHE images was traced on each cardiac slice and was summed over the entire cardiac volume to calculate infarct volume. Image quality was consistently below par in animals imaged 1 h after reperfusion because of arrhythmias of the heart. It is well-documented that cardiac arrhythmias arise at time of reperfusion in a surgical IR model (198-201). Arrhythmias lead to imaging of heart in different cardiac phases at each heart beat. Combining such data that reflects the heart in different states of contraction

severely degrades image quality. Infarct volume calculations were challenging in such cases where SNR of cardiac slices was too low for accurate contouring. Cine MRI frames of same cardiac slice, and DHE images of serial slices were interrogated as required to get an accurate estimation of infarct area from each slice.

Analysis of regional wall motion was done using custom written software in our lab. The technique is described in section 2.2.6.4. Using cine images from mid-ventricular section, automatic contouring of epicardial and endocardial borders was done at ED and ES and wall thickness was calculated radially. LV wall thickening was then calculated and plotted versus angle as a means to assess regional wall motion.

ImageJ software (NIH) was also used for infarct volume calculation using cardiac slices stained with TTC and Hematoxylin-Eosin. Manual planimetry of entire heart, infarct region (white) and non-infarct region (red) on TTC images was done by a blinded image analyst. Infarct region on H&E stained tissue slides was defined as area with loss of myocytes. Histological infarct volume was calculated as a percentage of total left ventricular volume (including septum) using Simpson's rule by summation of planimetered areas and multiplication by slice thickness.

3.3 Results and Discussion

3.3.1 Electrocardiographical characterization of murine myocardial ischemia and infarction

Electrocardiography is a well-known clinical tool for analysis of cardiac health which yields important diagnostic information by plotting electrical activity of the heart with time. It involves analysis of the various waves and normal vectors of depolarization and repolarization. Clinically, it is the gold standard for the diagnosis of cardiac arrhythmias, and guides therapy and risk stratification for patients with suspected acute myocardial infarction (202). It is routinely used as a screening tool for ischemic heart disease in cardiac stress tests. Our objectives to employ ECG as a diagnostic tool were two-fold: one, documentation of successful ischemia and reperfusion in mice, and two, serial assessment of ECG changes observed after IR and their correlation with functional changes of heart measured with MRI.

Documentation of successful ischemia reperfusion surgery in mice was done by real-time monitoring of ECG. Baseline ECG in mice is similar to humans with the exception of an early T wave. One characteristic for the mouse ECG is that no clear ST-segment can be distinguished, and the T wave merges with the final part of the QRS-complex (92; 203). Thus, ST segment had to be evaluated for its elevation with respect to baseline ECG levels (136). The details of this real-time monitoring technique and expected ECG patterns with successful ischemia are described in section 2.3.1. Lead I ECG was recorded from all mice

used in this study during the surgical procedure. The subdermal ECG recordings proved to be a very useful tool in determining the operative procedure of ligating the coronary artery to induce ischemia. A representative lead I ECG from a mouse 30 s after occlusion of a 60 min ischemia-reperfusion surgery is shown in Fig 2.15B. ECG patterns that reflect acute cardiac ischemia include ST segment elevation and an inverted T wave (136). All animals that developed myocardial infarction, as proven later by MRI and histological examination, exhibited such a pathologic, infarct typical ECG pattern during and after the operative procedure. The pathologic ECG pattern persisted over the entire study period of 14 days post reperfusion.

Serial electrocardiogram recordings from mice at 5 time points after IR are shown in Figure 3.1. Within 1 h of 60 min ischemia and reperfusion, a dramatic change in ECG pattern was observed (Fig 3.1B). Marked ST segment elevation compared to baseline (Fig 3.1A), a classic indicator of myocardial ischemia (136; 137; 204), and an inverted T wave were observed indicative of IR damage. Even though blood flow had been restored via removal of ligation around LAD, the ST segment was still elevated although not as high as pre-reperfusion level. This indicated a delay in restoration of blood flow to heart, or additional damage to LV that manifested itself as a pathological ECG pattern. Other early ECG changes indicative of transmural MI included diminished R wave amplitude and the development of a significant Q wave.

ECG recorded 1d after reperfusion pointed towards a transmural myocardial infarct (Fig 3.1C). An inverted T wave was consistently observed at this time point suggesting the presence of ischemic injury in the LV (91). The T wave represents the repolarization (or recovery) of the ventricles. The interval from the beginning of the QRS complex to the apex of the T wave is referred to as the absolute refractory period. The last half of the T wave is referred to as the relative refractory period (or vulnerable period). A wide inverted T wave in an indicator of a myocardial infarct caused by ischemia (205). No change was observed in the shape of P wave and length of PR segment indicating that IR surgery had no effect on the atria or atrio-ventricular electrical conduction system. The QRS complex was replaced by an abnormal negative Q wave that indicated a myocardial infarct in the LV (91). The R wave was not clearly discernible in the QRS complex, which had lost its distinct appearance as recorded at baseline.

ECG recorded in mice 3d, 7d and 14d after reperfusion also indicates the presence of a myocardial infarct (Fig 3.1D-F). Striking pathological patterns were observed on the ECG at these time points. The QRS complex was abnormally negative and wide (solid arrows in Fig 3.1). Resolution of Q, R and S waves was lost as the QRS complex was comprised mainly of a large a negative Q wave. Such an ECG pattern indicates sub endocardial LV damage (92). We could not further localize the infarct damage within the LV with ECG because only I measurements were made in this study. A persistent wide and negative T wave was also recorded indicating a region of ischemic damage within the LV. No

changes were observed in the P wave or the PR segment length indicating no damage to the atria. Lead I ECG recorded at d3, d7 and d14 after reperfusion was consistent in its pathological appearance at all those time points.

Our results of electrocardiographical characterization of myocardial ischemia and reperfusion were consistent with previous studies in mice. Gehrmann et al used a six lead ECG setup to examine the effects of ischemia and myocardial infarction on murine cardiac electrophysiology (91). They reported that murine ECG shows acute ST elevation during ischemia and negative chronic Q waves at 4d and 14 d after reperfusion in a 60 min IR model. They also report that animals operated with sham surgery do not show these pathologic ECG patterns at any time point. Wehrens et al also reported that murine IR surgery induced specific ECG patterns – a broadening of the QRS complex, ST segment elevation and negative Q waves (203). Other groups employing similar ECG techniques also report that ECG is a reliable technique for characterization of IR surgery (199; 205).

Human ECG is recorded via a standard 12 lead ECG system (206). In mice, a six lead and a 3 lead system has been used for electrophysiological characterization of cardiac ischemia (92; 203; 207; 208). We used lead I of a 3 lead system for serial ECG monitoring in mice. Analysis of all the different ECG leads for complete characterization of a specific pathology requires tremendous expertise in mouse cardiac pathophysiology. We employed this technique to test the hypothesis that ECG can be used as a diagnostic tool to indicate a successful IR surgery. As reported by other groups, we characterized presence

of ischemia and ischemic injury in the LV using specific pathological ECG patterns during and after IR. Also, we performed serial assessment of ECG changes in mouse heart after IR. We observed that ECG changes that reflect presence of a myocardial infarct are present 1d after IR. These ECG patterns persisted till 14d after IR, after which our study was terminated. It was not possible using the 3 lead ECG monitoring method used in our study to evaluate if there was an increase in myocardial infarction size with time after IR.

The functional significance of these pathological ECG patterns was evaluated using MRI, as described in the following sections. A correlation between myocardial infarction as observed with ECG and actual loss of myocytes from the ischemic regions was also made using histology.

3.3.2 Serial MRI analysis of infarct volume after IR

IR induced infarct progression was studied in mice with DHE MRI over 14 days after reperfusion. Mice were imaged at 5 time points: 1 h, 1 d, 3 d, 7 d and 14 d post reperfusion. Infarct volumes at each time point were calculated as described in section 3.2.4. Fig 3.2 shows serial sections obtained with DHE MRI from one animal after 60 minute IR surgery. Infarct volume from these images was calculated as a percentage of LV myocardial volume and is plotted in Fig 3.3. This study was used to test the hypothesis that there are secondary cell-death mechanisms responsible for myocyte death in the LV after IR, and that these processes have a functional impact on the heart.

We observed a small transmural infarct in animals imaged 1h after IR. A distinct region of hyper intensity was observed that was not visible in images acquired at baseline. This region was demarcated as the infarct region. Most of the infarct damage was observed in anterior and high lateral region of heart in apical short axis slices. We expected this region to be infarcted because the LAD passes through this region as observed in apical short axis sections (209). Occlusion of the LAD was done proximal to the first column of cardiac slices in Fig 3.2. Thus, all distal slices that were perfused with LAD and its offshoots were expected to be partially infarcted. Infarct volume measurement with MRI at the acute time point of 1h after IR has not been reported before in mice. This is possibly because of non-availability of high field MRI scanners that can provide the quality of resolution required for mouse cardiac MR imaging. In addition, cardiac arrhythmias are present at acute time points after reperfusion that makes DHE imaging in mice a challenging technique for routine operation.

Infarct volume measured 1d after IR was higher than that observed 1h post IR (Fig 3.2). Infarct areas measured were consistent with that reported previously (98). We observed an increase in infarct size in the LV towards the anterolateral region of the heart, in addition to the anterior and high lateral region of heart in apical slices. In addition to an infarct zone in the apical slices as observed 1h after IR, a region of hyper intensity was also observed in the mid apical slices of the heart. This observation of such an increase in infarct size after IR is unique. Since we performed serial MRI in the same animals over time, we inferred that this observation was not an artifact caused by surgical variation

which could lead to different infarct sizes in different animal groups. We deduced that there was an actual increase in infarct volume after IR in mice.

The results of MRI from mice 3d after IR were striking. Infarct volume was significantly higher than the level measured 1h after IR (Fig 3.3). The infarct zone grew to include the anterior, high lateral, inferolateral and inferior region of LV in mid-ventricular cardiac slices (5.4 mm - 3 mm from apex, Fig 3.2). Some apical slices were completely infarcted, even in the inferoseptal and anteroseptal region (1.8 mm from apex). The infarct size was calculated to be 22.6% of the LV, an increase of over 300% from 1h post reperfusion level. Infarct volume remained constant in size till d7 post reperfusion. Infarct areas were localized in similar regions as observed on d3, with the apical sections completely infarcted. A minor decrease in signal intensity of infarct zone was observed in mid-ventricular slices. As observed between time point 1h and 1d, and between 1d and 3d post IR, the increase in myocardial infarct volume was consistent. This led us to believe that there is a secondary cell death mechanism active in the border zone which caused further cell death leading to an increase in infarct volume at d3 post IR. This line of reasoning is supported by a number of studies in humans (186-188; 210; 211) and experimental animals (184; 212; 213) that suggest apoptotic mechanisms of myocyte death are active in the border zone in addition to lethal reperfusion injury.

A significant decrease in infarct volume was observed in mice 14d after reperfusion compared to the maximum observed at d3. This was an expected

result, as it has been shown in dog model of IR that the infarct size shrinks to a much smaller size 8 weeks after reperfusion, as the myocardial infarct turns into a scar (95; 153). Although we could not qualify the infarct zone as a scar at this time point in this study, the myocardial infarct kinetics followed expected timelines (96). Also, there was a decrease in the signal intensity of hyper intense region, suggesting a change in the composition of tissue that made up the infarct region. Infarct zone appears bright on DHE MRI because of a delayed washout of the contrast agent from dead and dying cells with a compromised plasma membrane (167). A decrease in the intensity of the hyper intense infarct area led us to believe that the individual cell population in that region consisted of other viable cells which did not take up the contrast agent. A majority of those cells could be neutrophils, which are known to be present in large numbers in an injured cardiac tissue after 7-14d of the initial insult (214; 215). Berr et al used DHE MRI in conjunction with Positron Emission Tomography to conclude that a large number of neutrophils were present in the infarct zone at 7d and not at 28d after IR (216). Formation of a myocardial scar typically takes place after 14d after IR (217). We explained the reduction in infarct size at 14d after IR on the basis of a fibroproliferative response, which over the ensuing weeks would lead to scar tissue formation.

In conclusion, we evaluated the role of secondary myocyte death processes after IR. We presented the first MRI based evidence that there is an increase in infarct size in mice over time after IR. We observed that infarct size increased with time from 7.9% of LV at 1h after IR to a maximum of 22.6% of LV

at 3d after IR. This increase in infarct volume over time suggested a presence of a secondary cell death mechanism besides the well-studied lethal reperfusion injury. A minor reduction in infarct size and intensity of infarct region was observed 14d after IR as compared to 3d and was attributed to a fibroproliferative response which leads to scar formation.

3.3.3 Serial analysis of infarct volume with Triphenyltetrazoliumchloride (TTC) staining after IR

In addition to MRI, IR induced infarct progression was studied in mice by staining cardiac tissue with TTC, Hematoxylin-Eosin and Masson's Trichrome. Animals were killed and cardiac tissue was harvested for histology 20 minutes after MRI scanning was completed. Cardiac tissue was collected at 5 groups of animals at specific time points: 1 h, 1 d, 3 d, 7 d and 14 d post reperfusion. Infarct volumes at each time point were calculated from stained cardiac tissue as described in section 3.2.4.

Fig 3.4 shows 1 mm thick serial sections obtained with TTC staining after 60 minute IR surgery at specific time points. Each time point represents serial sections from one animal. Infarct volume comparison at each time point is shown in Fig 3.5. In the presence of intact dehydrogenase enzyme systems, TTC forms a red-colored formazan precipitate while the infarcted area lacks dehydrogenase activity and therefore stays white/gray (218; 219). This leads to clear demarcation of infarcted and viable tissue. TTC staining has been extensively

used in literature for assessment of infarct size after IR in experimental animals, and is considered the 'gold standard' in most cases (220-224). Visual inspection yielded a similar infarct pattern with TTC staining and MRI at all time points (Fig 2.19). Statistical correlation was done between infarct volume calculated using MRI and TTC, and the following parameters were obtained: $r^2 = 0.86$, slope = 1.07 and intercept = -0.87 (Fig 2.20). Thus, we observed that TTC infarct volume was well-correlated with MRI. This confirmed our MRI technique of infarct volume measurement by comparing it to the gold standard TTC. We concluded that TTC reflects the infarct size measured with MRI, and either of the two methods could be used for infarct volume measurement.

Time course of infarct volume observed with TTC staining after IR pointed to an increase in infarct size after reperfusion, similar to the infarct volume kinetics measured with DHE MRI. Very little infarct damage (6.8% LV) was observed in the myocardium 1h post reperfusion after 60 min IR surgery (Fig 3.4). This is consistent with earlier reports that a small infarct region in mice is observed with TTC at such an acute time point (225). The infarct was consistently observed in the mid-apical sections and was confined to anterior LV. Staining done on animal hearts 1d after IR showed a greater infarct area (18.4% LV) compared to 1h group. Infarcted tissue was present in the high lateral and inferolateral region of LV, in addition to the anterior region observed at 1h. Infarct volume measured in animal hearts 3d and 7d after IR increased to approximately 23% of LV. The infarct size matched with the measurements made with DHE MRI, and indicated that the infarct zone had swelled to include other parts of LV

that were not infarcted 1h post IR. This agreed with our hypothesis that a secondary cell death mechanism was present in the border zone which caused further cell death and an increase in infarct volume with time post IR.

As also observed with MRI, a smaller infarct volume (9.6% LV) was measured with TTC staining of cardiac tissue 14d post IR. This was possibly caused by the red staining of TTC by inflammatory cells that infiltrate the infarct zone 7-14d post IR. TTC stains viable tissue red in color by reacting with their intact dehydrogenase enzyme systems (159). We deduced that the infiltration of neutrophils, which were functionally intact cells, into the infarct zone caused a portion of it to stain positive for TTC. This gave the appearance of a relative reduction in infarct region.

In conclusion, we used TTC staining to confirm the MRI-based infarct volume measurement technique, and to follow the time course of infarction in mice after IR. We observed that infarct size measured with TTC correlated very well with MRI ($r^2 = 0.86$), and increased from 6.8% LV at 1h post reperfusion to a maximum of 23% LV at d3 and d7 post reperfusion. This increase in infarct size pointed towards a secondary mechanism of cell death active in and around the infarct zone affected with lethal reperfusion injury.

3.3.4 Serial analysis of infarct volume with histological staining after IR

After staining with TTC, the cardiac sections were individually placed in plastic cassettes and fixed in formalin for 1 week. Hematoxylin-Eosin and Masson's Trichrome staining was then done on processed tissue sections. 5 μ m thick sections were cut from each 1 mm thick cardiac slice that was used for TTC staining from each animal. Infarct volume was calculated as described in section 3.2.4.

Fig 3.6 shows a mid-ventricular tissue section stained with Masson's Trichrome obtained from mice harvested at specific time points after 60 minute IR surgery. This stain produces red keratin and muscle fibers, blue or green collagen, light red or pink cytoplasm, and dark brown to black cell nuclei. Infarct region on Masson's trichrome stained sections was defined as region with loss of myocytes (white/blue) as opposed to non-infarcted tissue (red). Serial sections were also stained with Hematoxylin and Eosin to delineation of myocardial infarct. H and E is a quick stain for infarct demarcation and was done on all tissue slices for infarct volume calculation.

Infarct volume comparison from mice harvested at specific time points after IR is shown in Fig 3.7. Time course of infarct volume observed with TTC staining after IR pointed to an increase in infarct size after reperfusion, similar to the infarct volume kinetics measured with MRI and TTC. There was a distinct increase in infarct region in animal hearts stained at 7d after IR compared to 1h,

1d and 3d groups. This led us to believe that our hypothesis regarding the presence of secondary cell-death mechanisms in the infarct border was correct.

A significant difference was observed in the level of infarct volume measured with H/E staining compared to MRI and TTC techniques at acute time points 1h, 1d and 3d after IR. A comparison between all three techniques is plotted in Fig 3.8. We observed that MRI and TTC data were closely associated with each other at all time points, but not with histologically defined infarct volume. Histology is unquestionably the gold standard in evaluation of necrotic tissue (194-196). Thus, this remarkable observation questioned the evaluation and implication of infarcts measured with MRI and TTC. It is well-known that MRI is an indirect infarct measurement technique, and it delineates a region of impaired myocardium. There is considerable debate whether myocardial infarct measured with MRI reflects permanently damaged tissue or reversibly injured myocardium (96). It is possible that infarcts measured at acute time points with MRI were overestimated in size by hyper enhancement of border zone tissue.

It is not clear in literature whether hyper enhancement occurs in injured myocardium surrounding regions of myocyte necrosis that might be salvaged by revascularization therapy, particularly in the acute phase after infarction (226). Jennings et al suggested that one way to address this question is to examine myocardium subjected to severe but reversible ischemic injury by occluding a coronary artery for 15 minutes (227). Schaefer et al reported that in the first few hours after infarction, regions of hyper enhancement overestimated infarct size

when the contrast agent was injected 5 minutes after reperfusion (228).

McNamara et al evaluated myocardial contrast enhancement in dogs that underwent 15 minutes of LAD occlusion followed by 24 hours of reperfusion (229). They reported that ex vivo MRI did not show hyper enhancement of the LAD territory, indicating that reversible myocardial injury does not hyper enhance with MRI. On the same lines, Kim et al reported that hyper enhancement does not occur in purely reversibly injured regions and that the spatial extent of hyper enhancement is identical to that of acute myocyte necrosis and scar (96; 230).

Based on TTC staining, our results mimic those of the groups claiming that hyper enhancement only occurs in permanently damaged tissue. A closer look at these studies reveals that permanent myocardial injury was evaluated only with TTC staining, and no other histology was performed. We also calculated infarct volume with H/E staining and observed that the 'true' infarct region is much smaller compared to what was calculated with MRI and TTC. We observed that the myocytes in infarct region and border zone were structurally present but were functionally inactive with compromised cell structure, which yielded large infarcts on MRI and TTC. ECG recording from mouse heart at d1 post IR also points to functional inactivation of myocytes.

In conclusion, histological staining of cardiac tissue suggested that, as observed with MRI and TTC, infarct size in mice increased over the first 7 days after IR pointing to secondary cell death mechanisms active in the border zone. Our observation that until day 3 post-IR the infarct size as measured by TTC and

MRI were much larger than the myocyte-silent regions in trichrome or H&E stained sections lead to the conclusion that at such early phase the infarct site contains structurally intact myocytes that are functionally compromised.

3.3.5 Serial analysis of cardiac function after Ischemia-Reperfusion

Mortality after ischemia-reperfusion is strongly associated with extent of LV dysfunction, which is clinically evaluated by quantitative parameters of LV volume and Ejection Fraction (EF) (231). EF is an important parameter of healthy cardiac function, and a powerful indicator of clinical outcome (232-234). Based on these clinical norms, LV remodeling after IR in experimental animals has been routinely studied by evaluation of cardiac function (235-237). We evaluated the functional significance of secondary myocyte death mechanisms by serial evaluation of cardiac function in mice with MRI at baseline and at five time points after IR: 1h, 1d, 3d, 7d and 14d. Data was pooled from several animals, several of which were serially evaluated at all time points and is shown in figure 3.9.

We observed that IR injury caused a progressive worsening of all global LV functional parameters (Fig 3.9). There was a significant increase in left ventricular End Diastolic Volume (EDV) and End Systolic Volume (ESV), and a significant decrease in Stroke Volume (SV), Cardiac Output (CO) and EF post IR. Worst cardiac function was measured at day 7 where IR caused a 46% increase in EDV, 340% increase in ESV, 25% decrease in SV, 32% decrease in CO, 47% decrease in EF and 38% increase in LV mass.

EDV and ESV are clinically important parameters for evaluating cardiac function and are the first signs in diagnosis of congestive heart failure (238; 239). After IR surgery in mice, we observed a trend towards increased LV EDV and ESV (Fig 3.9 A, B). The results were more striking in ESV measurement, where a significant increase in ESV was evident 1d post IR. Together, these two parameters led to a compromised SV and EF. Clinically, it is accepted that EF below 35% is considered high risk (240). LVEF is a major predictor of mortality in patients with severe acute heart failure symptoms requiring admission to intensive care units (241). Thus, EF measurement in animals was considered an important functional parameter that reflected upon cardiac health after IR. A statistically significant drop in EF was observed at all times after IR. Baseline EF in mice was close to 80% (Fig 3.9 D), consistent with published results (94; 98; 106). There was a drop in EF 1h post IR, and a progressive worsening of EF was observed consistently in all mice. The progressive worsening in EF, in addition to the increase in LV EDV and ESV, was consistent with the increase in infarct volume measured with time after IR. EF at 7d post IR was the lowest out of all studied time points, and matched well with the maximum infarct volume measured at the same time point.

SV and CO were calculated from LV volumes, with a constant heart rate for normalization of results. Worsening of SV and CO was also observed with the worst function measured 7d post IR. LV mass was measured by multiplying myocardial volume with density, which was assumed constant before and after IR. We observed an increase in LV mass with a maximum at 7d post IR. This

was consistent with results of other studies where an increase in LV mass was observed after IR (94).

One of the objectives of this study was to test the functional significance of secondary cell death mechanisms after IR. With serial MR imaging of mice, we show that there is a progressive loss of myocardial function up to 7d post IR. This data is supported by infarct measurements performed by MRI and histology where an increase in infarct size is observed till 7d after IR. Taken together, the data suggests the presence of secondary myocyte death mechanisms present in the infarct border zone that not only lead to progressive myocyte death, but also have a significant effect on cardiac function.

3.3.6 Serial analysis of left ventricular wall motion after Ischemia-Reperfusion

Regional wall motion analysis is a technique for quantitative estimation of LV contractility. Assessment of LV wall motion is considered one of the most important procedures in evaluating LV function (160). The traditional concept of the results of LAD occlusion, with or without reperfusion (medical or surgical), is the production of a myocardial scar that does not contract (i.e., akinesia), or that paradoxes or bulges in the opposite direction during systole (i.e., dyskinesia) (242). Clinically, these regions are defined as nonparadoxing (akinetic) or paradoxing (dyskinetic) segments. Impairment of systolic wall thickening is known to be a sensitive marker of myocardial ischemia and has been shown to be a reliable indicator of segmental contractile dysfunction after myocardial infarction (98).

In some studies it was reported that LVEF showed a poor correlation to the infarct size measured by MRI (243). One possible reason is that LVEF describes global LV function whereas the infarcted area and reduced function is regional. A decrease in LVEF supposes that several LV segments are involved, but that might not be the case. Methods that measure LV regional function could therefore prove to be more sensitive measures than EF to identify systolic dysfunction. Thus, we evaluated temporal changes in regional wall motion to test the significance of secondary myocyte death mechanisms present after IR to affect regional LV wall motion.

Regional myocardial contractile function in mice with MRI post IR was assessed as percent transmural wall thickening (Fraction Shortening, FS). The technique is described in section 2.2.6.4. Mid-ventricular slices were chosen for all thickness analyses as these typically have both infarcted and non-infarcted regions. Regional impact of myocardial infarction on a portion of the LV wall can then be observed. LV wall thickness was measured at ES and ED, which was used to calculate FS at baseline and four time points after IR: 1d, 3d, 7d and 14d.

Fig 3.10A shows the approach used to segment the heart into 8 sections for regional assessment of wall motion. Wall motion parameters were calculated for each section and plotted against angle indexed to the right ventricular insertion point in the anterior wall. We observed a progressive decrease in LV ES and ED wall thickness post IR in the anterior and high lateral regions (Fig 3.10B,C). The change in LVES was very dramatic and was statistically significant

compared to baseline at all time points. A more subtle change was observed in ED wall thickness at 3d post IR and beyond in high anterior region of LV. These results are consistent with other studies that report wall thickness abnormalities in mice after IR (98; 106).

The changes in ES and ED wall thickness led to much larger and striking changes in FS. A progressive drop in FS of infarct region was observed post IR at all time points (Fig 3.10D). Akinesis of the LV wall was observed in anterior (0° - 90°), high lateral (90° - 180°) and parts of anteriolateral region (180° - 225°) of the LV. Hyper enhancement of the LV on DHE images was typically observed in sectors encompassing 45° - 180° . It follows that wall motion abnormalities were present not just in infarct region, but also in adjacent regions. This trend has been reported in clinical and in experimental animal studies (98; 244). At d7 post IR, dyskinesia of infarct region was observed. The region of dyskinesia was also observed to have reduced wall thickness at ES, suggesting compromised wall structure and contractility in the infarct zone. The wall motion abnormalities associated well with the progressive decrease in EF measured post IR, as poor contractile function directly leads to poor EF (244).

Interestingly, an improvement in wall motion parameters was observed in the remote regions of LV. FS increased in remote regions at 7d and 14d post IR compared to baseline. This trend has been previously observed in long-term experimental studies with mice after IR (245). It was also reported that this response is not observed with a permanent occlusion model of myocardial

infarction. The recovery of cardiac contractility in remote regions at 7d and 14d after IR occurred simultaneously with morphological adaptations and was paralleled by a significant increase in ventricular weight. Part of this hypertrophic response is due to normal physiological growth. However, the enlargement of the end-diastolic volume and relative thickening of remote regions of LV suggest an eccentric hypertrophic response to IR injury. De Celle et al studied LV remodeling in mice till 8 weeks post IR and also reported a positive correlation between infarct size and ventricular weight. This remodeling response can be explained as a compensation mechanism for reduced cardiac contractility caused by progressive functional and structural damage caused by IR surgery.

Statistical analysis of the progressive worsening of wall motion abnormalities is shown in Table 3.2. For each myocardial sector, wall motion parameters were serially compared to the previous time point using ANOVA. We observed a statistically significant worsening in wall motion at each time point in several myocardial segments. This data corresponded positively with the progressive loss of cardiac function observed after IR.

We conclude that progressive worsening of LV wall motion and structure were observed following IR. Contractility of the heart was depressed at all time points, and was worst at 7d after IR. A significant negative correlation between infarct size and cardiac contractility was also observed. After reoxygenation of the ischemic heart, akinesis of infarct and adjacent region, dyskinesis and wall thinning of infarct region and minor hypertrophy of remote region characterized

the LV remodeling process. Thus, we observed significant functional and structural changes in LV that could be construed as a manifestation of secondary myocyte death mechanisms post IR.

3.4 Conclusions

Our overall objective with this study was to evaluate the functional significance of secondary myocyte death processes post IR. We performed 60 min IR surgery in mice and monitored LV remodeling for 2 weeks. In addition to electrocardiographical characterization of IR, high resolution MRI was done at 6 time points (baseline, 1h, 1d, 3d, 7d, 14d post IR) to evaluate global cardiac function, LV wall structure and regional wall motion in an attempt to study the effects of progressive myocyte death after IR.

ECG recorded in mice at all time points after reperfusion indicated the presence of a myocardial infarct (Fig 3.1). ECG changes indicative of cardiac ischemia were observed immediately after occlusion. After reperfusion, ECG never went back to normal and showed the presence of a transmural infarct at d1 even before myocytes were found to be dead at occlusion site. This suggests that the myocytes lost their functional ability without losing their structure at d1 post IR.

Myocardial infarction volume was measured by three techniques: DHE MRI, TTC staining and H/E staining. Time course of infarct volume indicated an

increase in infarct volume with time, with a maximum observed at 3d/7d post IR. Infarct size measured with MRI and TTC matched closely with each other but not with H/E staining at acute time points (1h, 3d, 7d). One possible explanation is that myocytes that hyper enhance with MRI and stain TTC are functionally dead but structurally viable, and thus do not stain with H/E. In either case, the data points to the presence of secondary cell death mechanisms active in the post infarcted myocardium that cause an increase in infarct size with time.

Global measurement of cardiac function clearly pointed to progressive worsening of LV function post IR. EF, a clinically important indicator of mortality after myocardial infarction, decreased continuously till d7. A steady increase in LV EDV and ESV was observed which indicated loss of myocardial contractility. In general, a progressive worsening of cardiac function was observed post IR, with worst function at d7 post IR.

Analysis of LV wall thickness and FS yielded similar results. Regional wall motion abnormalities were observed in infarct and adjacent regions after IR. Significant LV wall thinning took place in infarct region. Calculation of FS clearly indicated a region of poor contractility in the infarct zone which eventually became dyskinetic with time. An increase in contractility of remote regions of LV was observed coupled with an increase in LV mass at 7d-14d post. This indicated an eccentric compensatory mechanism involving hypertrophy of the remote region of LV.

In conclusion, we established that post IR cell death processes have a significant negative effect on global cardiac function, LV structure and myocardial contractility in a mouse model of ischemia-reperfusion.

3.5 Figures

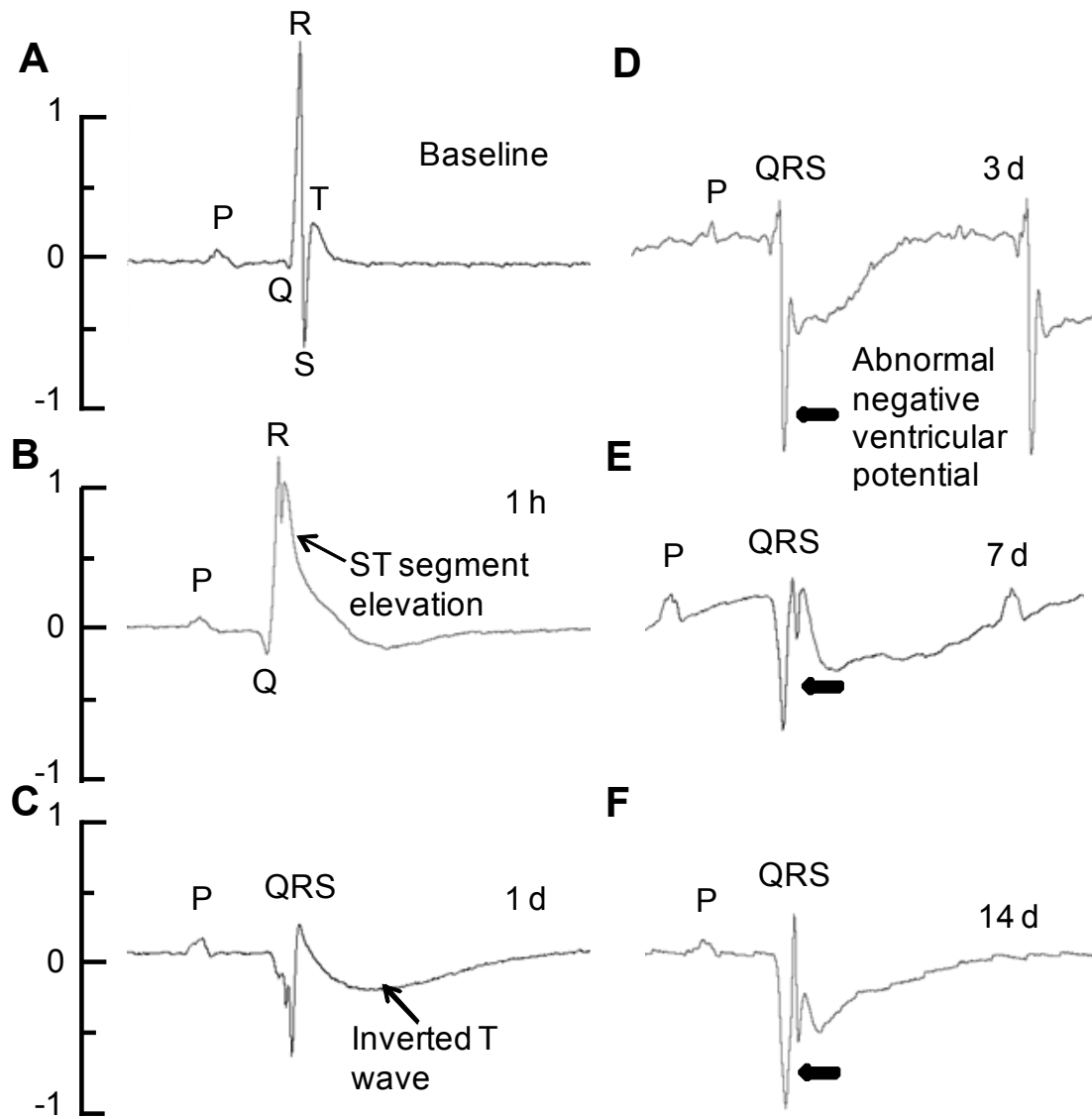


Figure 3.1 | Serial Electrocardiogram recordings from mice show myocardial injury early after IR. Animals were lightly anesthetized and lead I ECG was recorded using subdermal leads before and after IR at specific time points as shown. The P waves, QRS and T waves were visible and are annotated. Following infarct, there is acute ST segment elevation, followed by development of chronic negative Q waves and an inverted T wave which is an indicator of ischemia. Abnormal negative ventricular potentials that develop 1-3 d after IR (solid arrow) reflect LV damage.

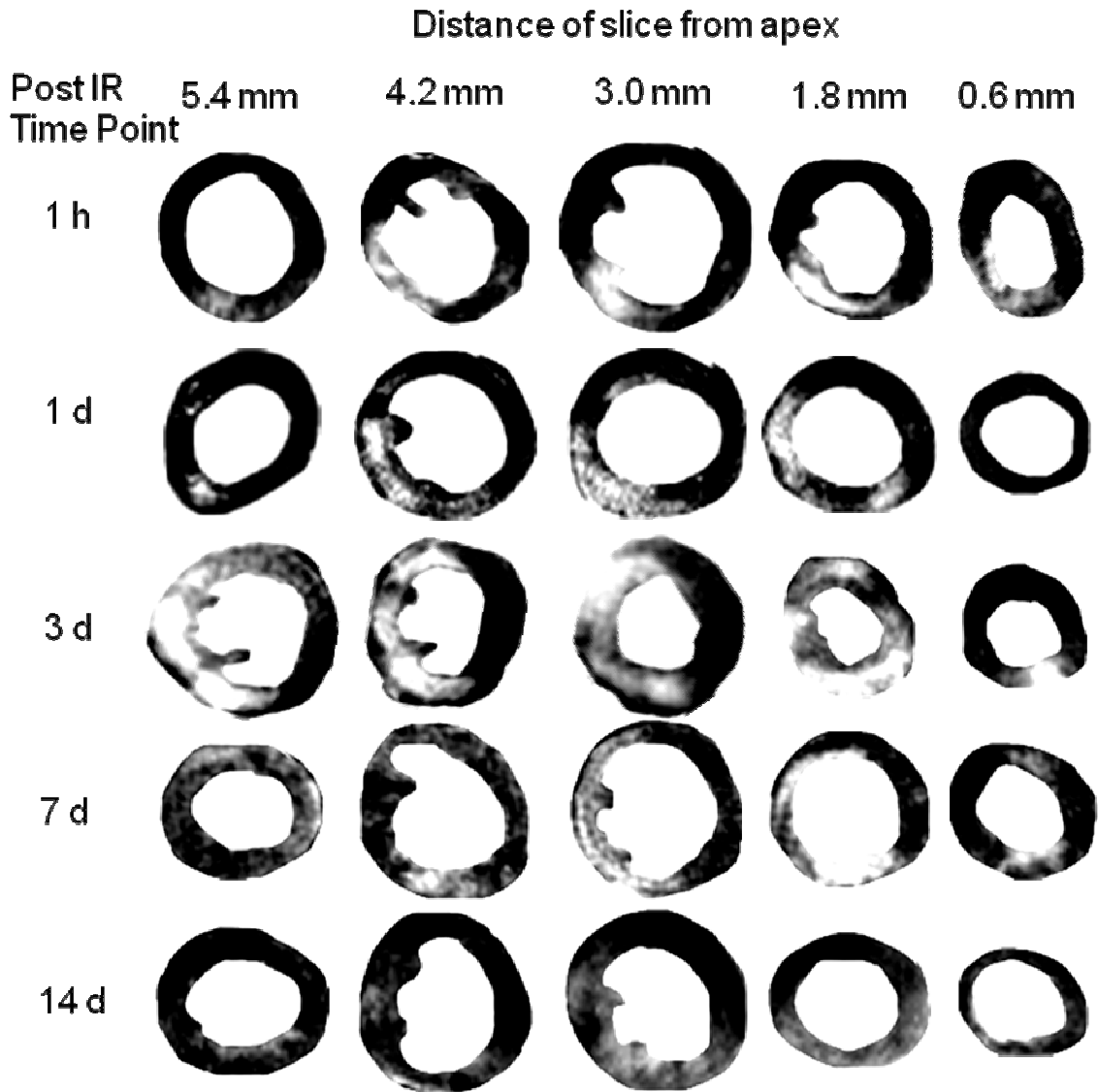


Figure 3.2 | Time course of MRI infarct progression. Mouse hearts were imaged at 5 time points with DHE MRI after 60 minute transient LAD occlusion and reperfusion. Five sequential tissue slices from one animal are shown, where slice thickness is 1 mm and distance of center of slice from apex is given. Hyper enhanced region in the LV represents infarcted region. MR images were segmented in Adobe Photoshop for depiction of LV. Infarct volume was calculated with planimetry at each time point. Maximal infarct damage was observed 3 days after surgery (n=4 in 1h group, n=6 in 1d group, n=9 in 3d group, n=7 in 7d group and n=4 in 14d group).

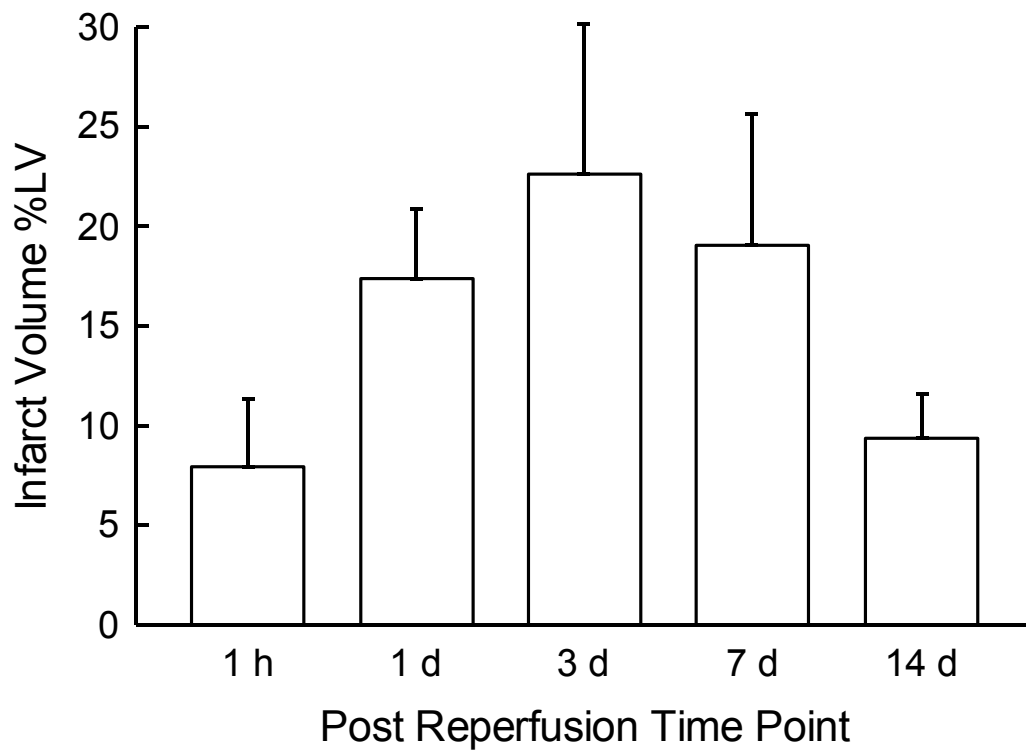


Figure 3.3 | Infarct volume progression measured with MRI. Infarct volume was calculated by planimetry of DHE MRI images obtained at 1 h, 1 d, 3 d, 7 d and 14 d after IR surgery. * indicates $p < 0.05$, $n = 4$ in 1h group, $n = 6$ in 1d group, $n = 9$ in 3d group, $n = 7$ in 7d group and $n = 4$ in 14d group.

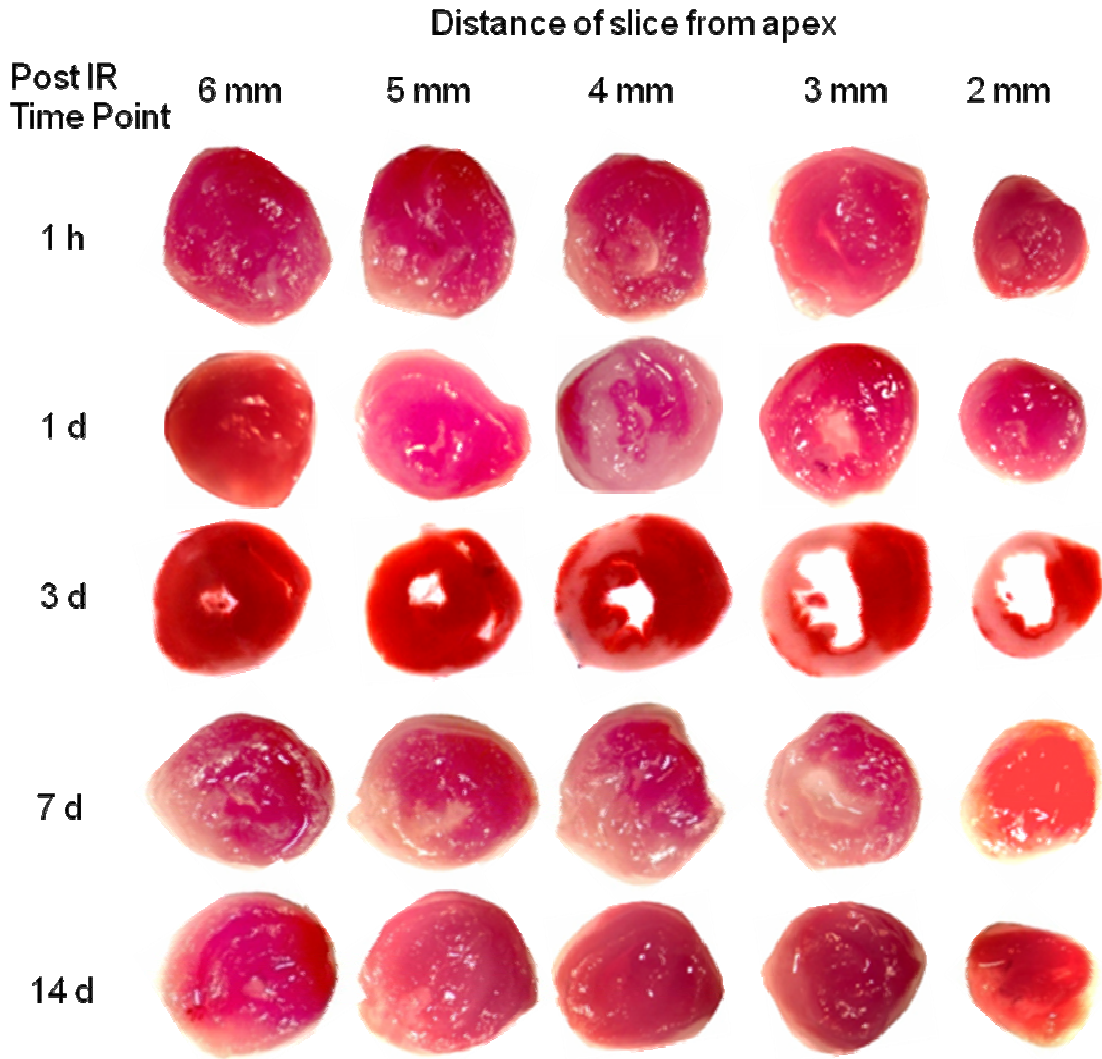


Figure 3.4 | Time course of TTC infarct progression. Mouse hearts were stained with TTC at 5 time points after 60 minute transient LAD occlusion and reperfusion. Five sequential tissue slices from one animal are shown, where slice thickness is 1 mm and distance of center of slice from apex is given. Viable myocardium was stained in red and infarct region in white. Digital photographs of the cardiac slices were segmented in Adobe Photoshop for depiction of LV. Infarct volume was calculated with planimetry at each time point. Maximal infarct damage was observed 3 days after surgery (n=4 in 1h group, n=6 in 1d group, n=9 in 3d group, n=7 in 7d group and n=4 in 14d group).

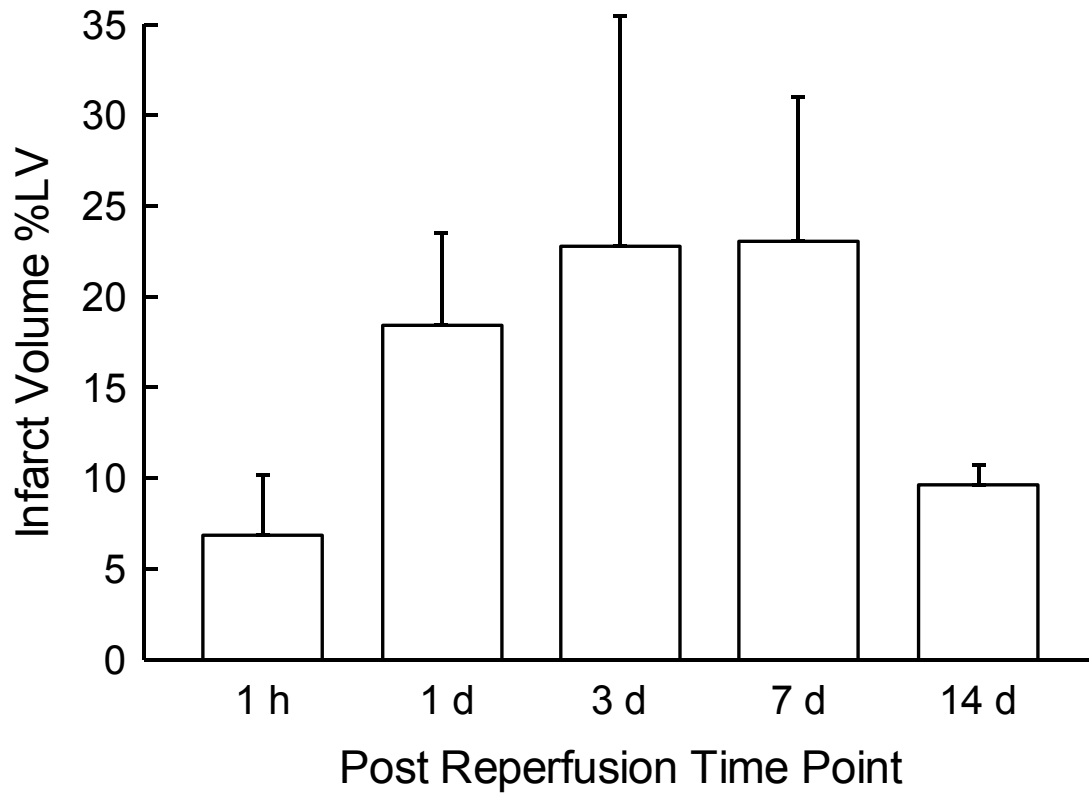
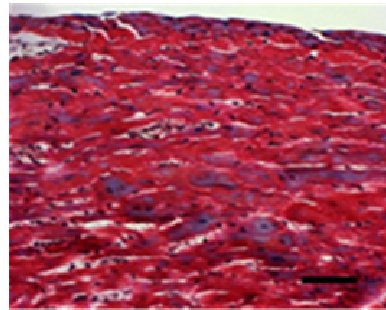
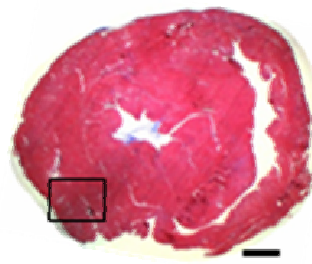


Figure 3.5 | Infarct volume progression measured with TTC staining. Infarct volume was calculated by manual planimetry of digitally photographed TTC stained cardiac sections obtained at 1 h, 1 d, 3 d, 7 d and 14 d after IR surgery. * indicates $p < 0.05$, $n = 5$ in 1h group, $n = 6$ in 1d group, $n = 9$ in 3d group, $n = 7$ in 7d group and $n = 4$ in 14d group.

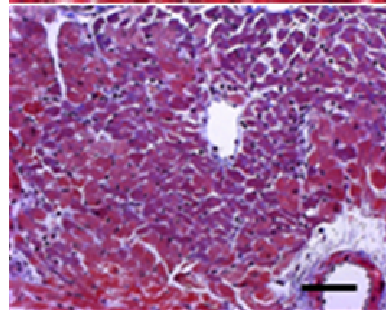
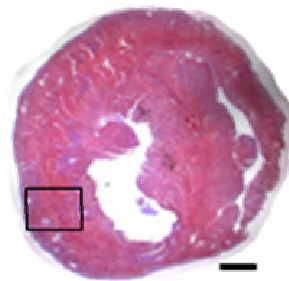
Figure 3.6 | Time course of infarct progression observed with Masson's trichrome staining. Tissue sections were obtained from formalin fixed heart slices that had been used for TTC staining. Masson's trichrome staining was done on 5 μm thick sections obtained from each 1 mm thick tissue slice. Infarct was defined as region with loss of myocytes (white/blue) as opposed to non-infarct region (red). Infarct volume was calculated by manual delineation of infarct region using a digital camera mounted on a microscope. Images shown here represent heart sections from 4 mm above the apex. Images shown in left column were taken at 1.25X magnification (scale bar = 1 mm). Right column shows magnified view at 20X magnification of boxed region (scale bar = 50 μm). Maximum loss of myocytes was observed at 7 days after IR injury.

Post IR
Time Point

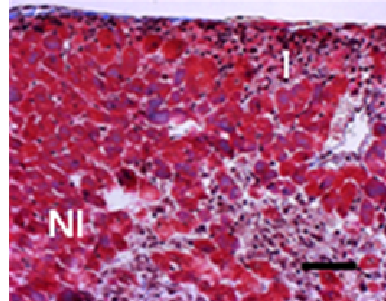
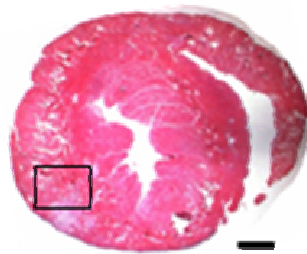
1 h



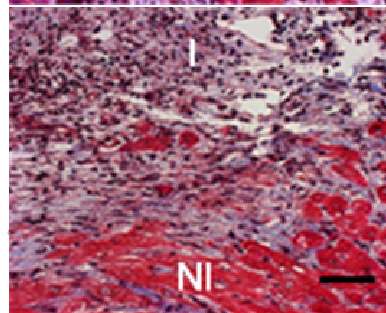
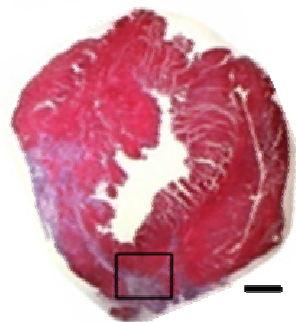
1 d



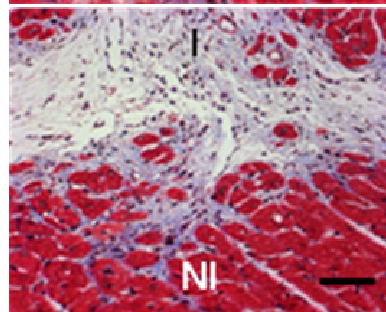
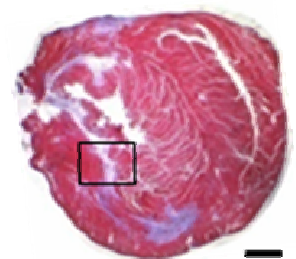
3 d



7 d



14 d



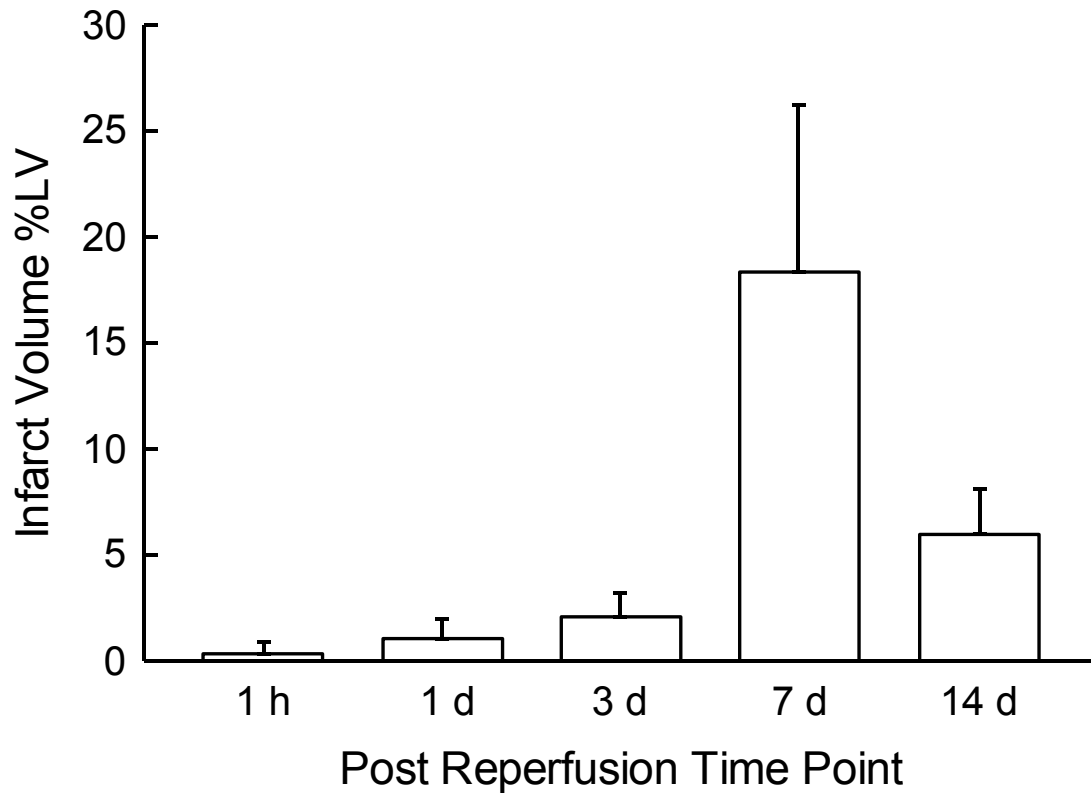


Figure 3.7 | Infarct volume progression measured with Hematoxylin-Eosin staining. Infarct volume was calculated by manual planimetry of digitally photographed stained sections obtained at 1 h, 1 d, 3 d, 7 d and 14 d after IR surgery. * indicates $p < 0.05$, $n = 4$ in each group.

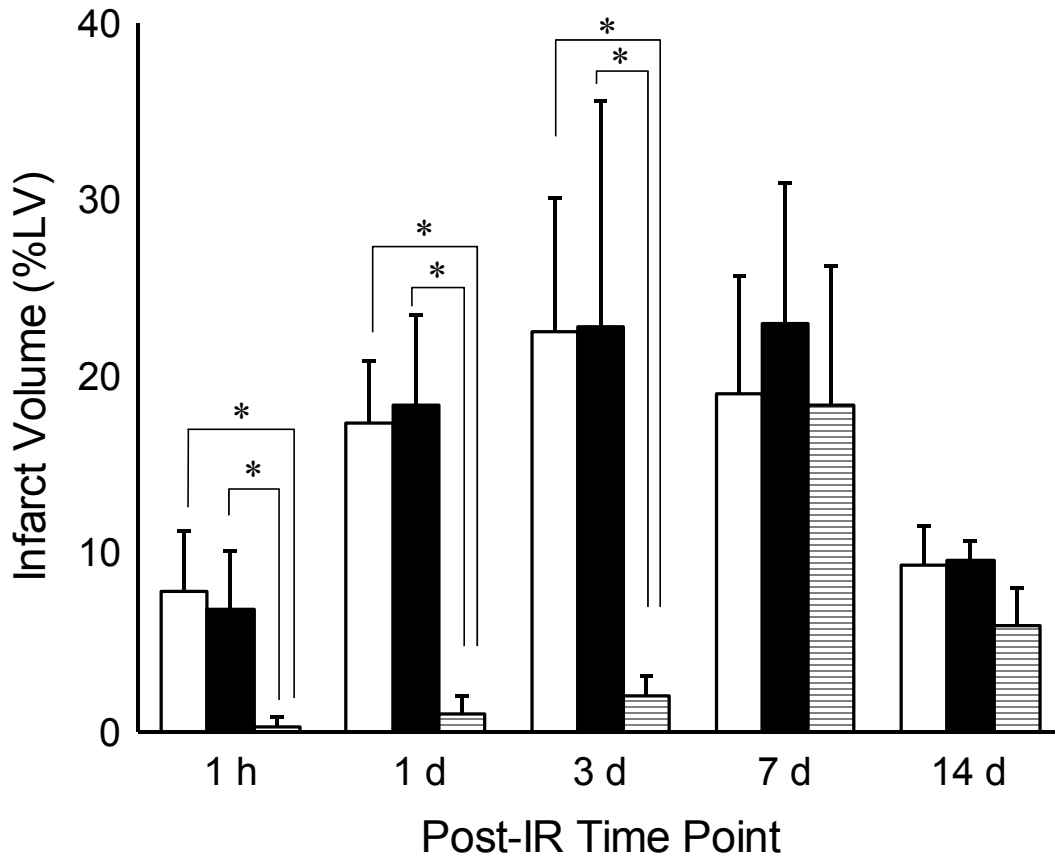
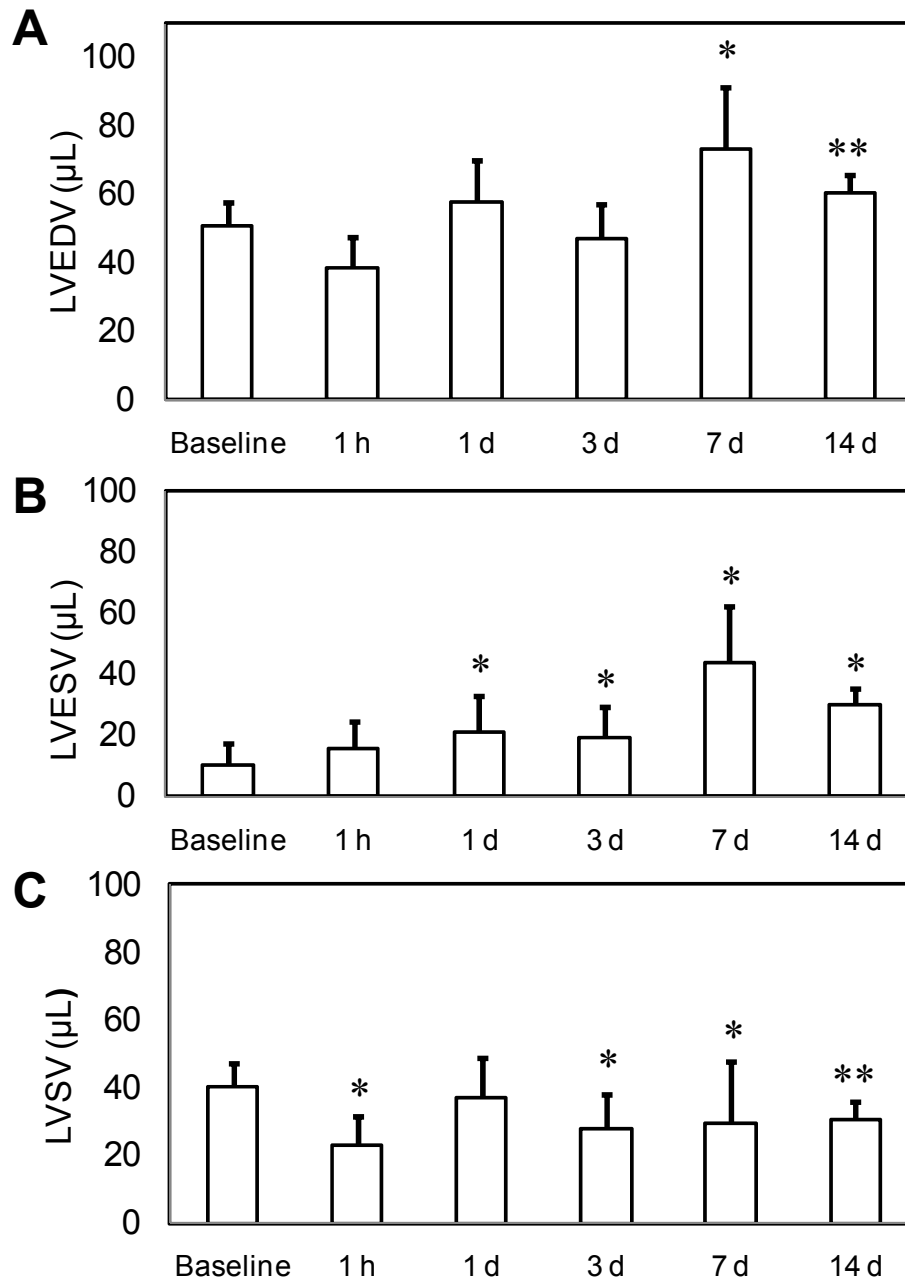


Figure 3.8 | Quantification of Infarct volume progression measured with MRI, TTC and H/E staining techniques. Infarct volume was calculated using MRI (open bars), TTC (solid bars) and histology (striped bars) using digital planimetry at 1h, 1d, 3d, 7d and 14d after IR surgery. Infarct volume was calculated as a percentage of left ventricular myocardial volume. MRI and TTC data were closely associated with each other at all time points, but not with histologically defined infarct volume. * indicates $p < 0.01$, $n=4$ in each group at each time point.

Figure 3.9 | Progressive loss of cardiac function after IR injury. Global parameters of LV volume and function were measured with MRI at six time points. IR caused a significant increase in LV End Diastolic Volume (A) and LV End Systolic Volume (B), while causing a significant decrease in LV Stroke Volume (C). * indicates $p < 0.01$ and ** indicates $p < 0.05$ compared to baseline values (n = 9 in baseline group, n=5 in 1h group, n=6 in 1d group, n=9 in 3d group, n=7 in 7d group and n=4 in 14d group).



continued

Figure 3.9

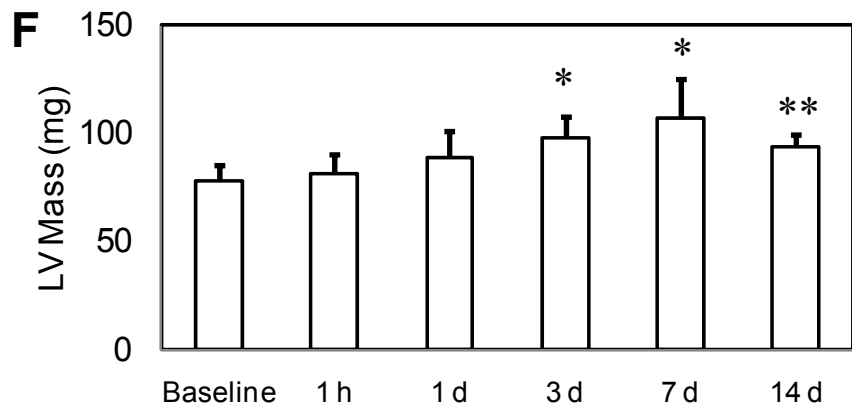
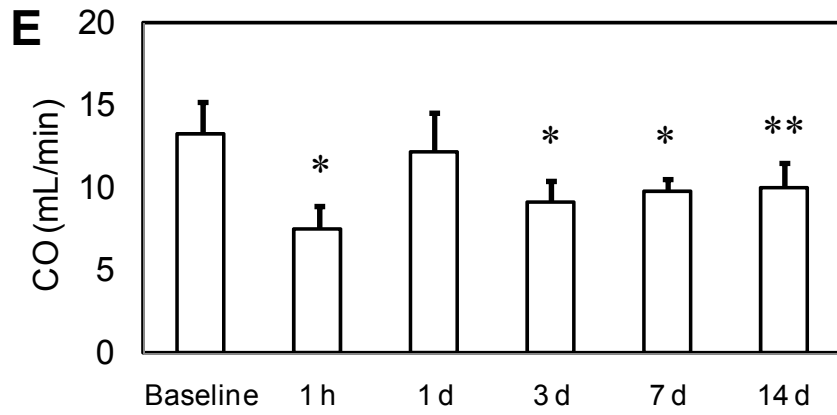
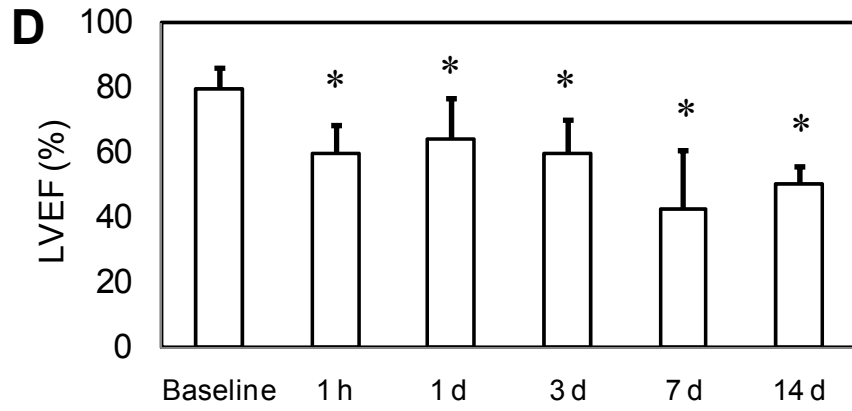
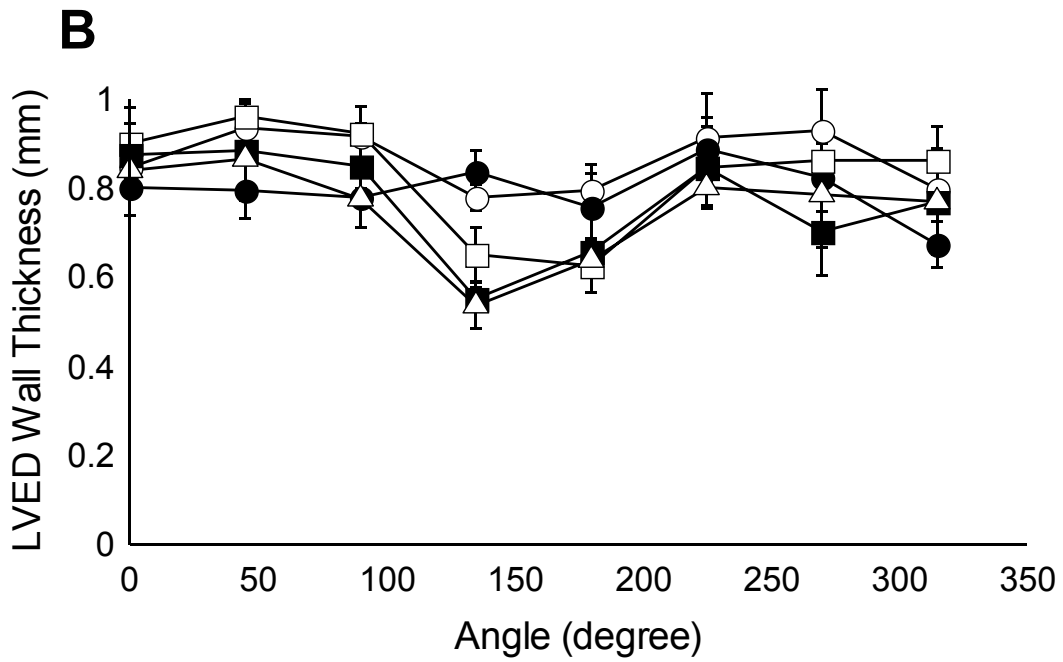
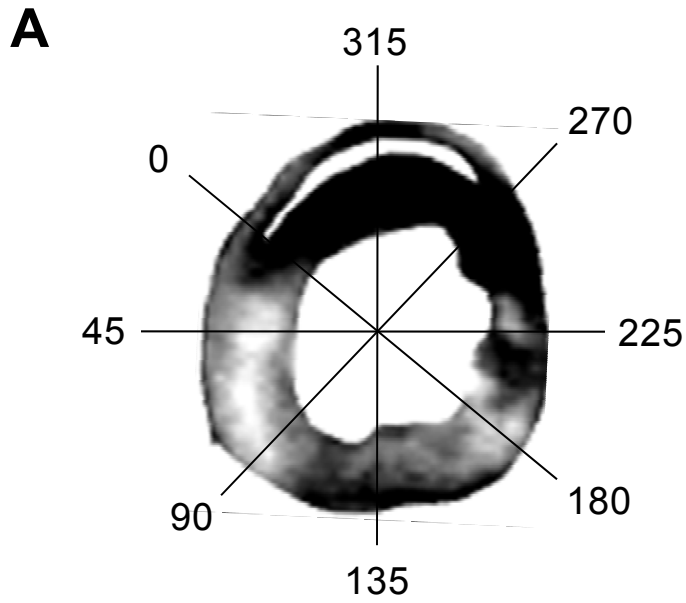
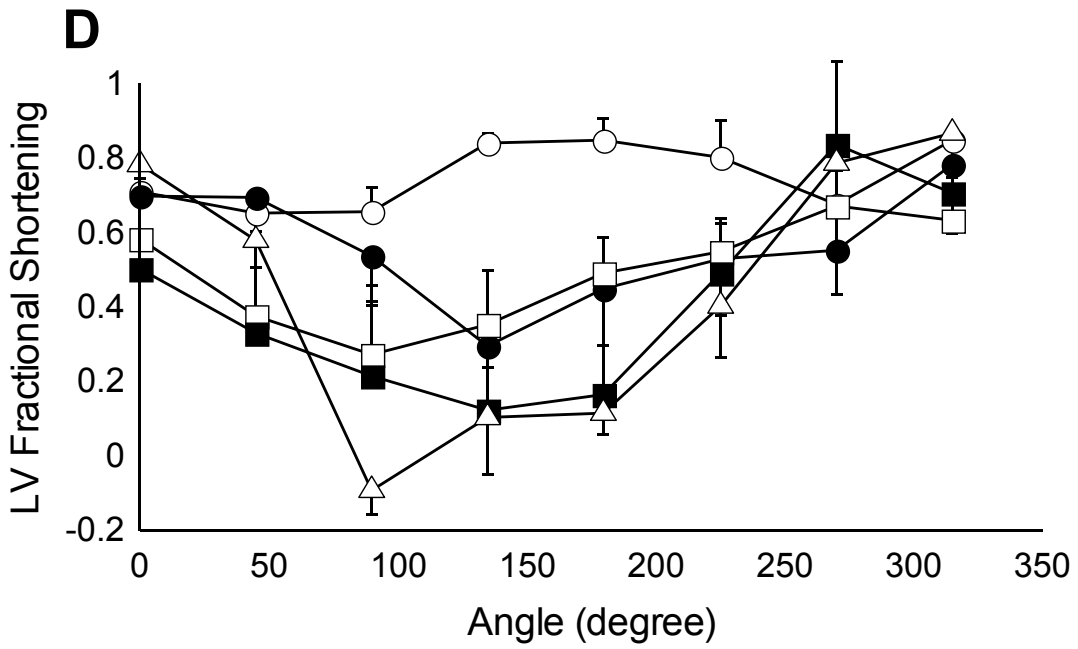
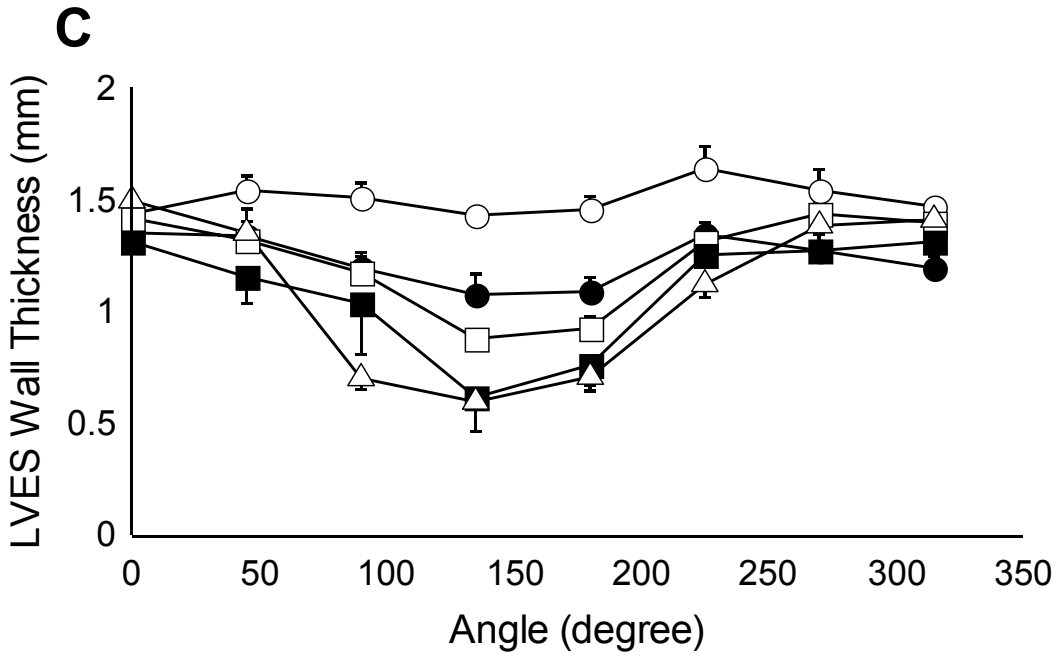


Figure 3.10 | Segmental LV wall thickening analysis before and after IR. (A) LV wall was segmented into 8 equiangular 45° sectors using custom written software in Matlab (A). Wall thickness was calculated radially at 2° increments and was averaged for each sector. Thickness data was indexed to right ventricular insertion point in the anterior wall. (B) and (C), Segmental LV wall thickness at ES and ED, respectively. (D) FS of LV wall in one cardiac cycle. A significant decrease in FS of LV wall was observed after IR injury in infarct and adjacent regions. An improvement in FS is observed in remote regions of LV, possibly to compensate for poor wall motion elsewhere in infarct region. Baseline data is represented by open circles, 1d by filled circles, 3d by open squares, 7d by filled squares and 14d by open triangles (n=4 in each group).



continued

Figure 3.10



continued

Figure 3.10

	Angle (degree)							
	0	45	90	135	180	225	270	315
ES								
1 d vs baseline		*		*	*	*		
3 d vs 1 d		*	*	*				
7 d vs 3 d				*	*			
14 d vs 7 d	*		*					
ED								
1 d vs baseline		*		*	*	*		
3 d vs 1 d		*	*					
7 d vs 3 d					*			
14 d vs 7 d	*		*					
FS								
1 d vs baseline				*	*	*	*	
3 d vs 1 d		*	*					
7 d vs 3 d					*			
14 d vs 7 d	*		*					

Table 3.2 | Statistical analysis of wall motion abnormalities. LV ES thickness, ED thickness and FS were compared at five time points – baseline, 1d, 3d, 7d and 14d after IR. These wall motion parameters were compared serially to the previous time point using ANOVA for each myocardial sector. A progressive worsening of LV wall motion is observed after IR. n = 6 in each group, * indicates $p < 0.01$.

CHAPTER 4

FUNCTIONAL SIGNIFICANCE OF OXYGEN AS A MODULATOR OF PERCEIVED HYPEROXIA DURING ISCHEMIA-REPERFUSION

4.1 Introduction

Cellular oxygen (O_2) concentrations are maintained within a narrow “normoxic” range to avoid the risk of oxidative damage resulting from excess O_2 (hyperoxia) and of metabolic demise from insufficient O_2 (hypoxia) (246). Physiologic oxygen tensions of adult mammalian tissues range from 150 mm Hg at the lung apices to ≈ 40 mm Hg in mixed venous blood and most organs, to ≈ 20 mm Hg in parts of the bone marrow (247). Thus, “normoxia” for cells is an adjustable variable that is dependent on the specific localization of the cell in organs and functional status of the specific tissue.

Oxygen sensing is required to adjust to physiological or pathophysiological variations in pO_2 . Current work in this field is almost exclusively focused on the study of hypoxia. Reoxygenation, on the other hand, has been mostly investigated in the context of oxidative injury. Over 25 years ago, it was published

in *Nature* that pO_2 beyond the comfort of the “perceived normoxic range” is a significant stressor, leading to growth arrest (248). The molecular bases of these observations and the signal transduction pathways are not yet clearly understood (247).

Microarray analyses of different cell types, including stem cells, cancer cells, and cardiac myocytes, reveal 100–200 genes that respond positively to exposure to hypoxia (249; 250). More than 100 of these appear to be regulated directly by a transcription complex, Hypoxia Inducible Factor -1 (HIF-1) (251). Hypoxia and HIF-1 also induce growth factors, such as the insulin-like growth factor-2 and transforming growth factor- α (252). Not quite so obvious in the context of adaptation is the simultaneous activation of pro-apoptosis genes. Hypoxia has been shown to stimulate Fas and its ligand, depress anti-apoptotic Bcl-2, and activate caspases (253). Therefore, by activating HIF-1, hypoxia simultaneously induces pro-survival and pro-death genes. The outcome of the mixed signals generated by hypoxia is cell specific and determined by the severity of hypoxia as well as by the presence of ancillary conditions associated with hypoxic metabolism (247).

Ischemia in the heart results in a hypoxic area containing a central focus of near-zero O_2 pressure bordered by tissue with diminished but non-zero O_2 pressures (254). These border zones extend for several millimeters from the hypoxic core, with the O_2 pressures progressively increasing from the focus to the normoxic region (255). Moderate hypoxia is associated with a 30-60%

decrease (1-3% O₂) in pO₂ (256). During chronic hypoxia in the heart, cells adjust their normoxic set point such that the return to normoxic pO₂ after chronic hypoxia is perceived as relative hyperoxia (254; 257; 258). We recently demonstrated that reoxygenation of a focal ischemic site of the heart, in addition to being a trigger for reperfusion injury, induces tissue remodeling. We reported that marginal relative elevation in pO₂, compared with pO₂ to which cells are adjusted during chronic moderate hypoxia, serve as a signal to trigger cardiac fibroblast (CF) differentiation and tissue remodeling. p21^{Waf1/Cip1/Sdi1} was identified as a key mediator of signaling triggered by perceived hyperoxia (254; 259). We showed that in reoxygenated tissue, a sudden elevation of pO₂ profoundly influenced the cellular phenotype even at those sites where oxidative injury was not predominantly evident.

Thus, acute insult caused during reperfusion may be lethal to cells localized at the focus of insult, elevation of O₂ tension in the surrounding ischemic tissue triggers phenotypic changes in the surviving cells that may be associated with tissue remodeling. We hypothesized that tissue remodeling induced by 'perceived hyperoxia' in the heart post-reperfusion has a detrimental effect on cardiac function, and this diminished function can be circumvented by a lower oxygen shock suffered by the reperfused tissue. We used MRI to evaluate the effect of a graded hyperoxic insult to cardiac function by modulating the hyperoxic shock suffered by cardiac tissue at reperfusion.

4.2 Material and Methods

4.2.1 Experimental Plan

Our overall objective was to test the functional significance of the tissue remodeling process induced by 'perceived hyperoxia' in the heart in a mouse IR model. A transient 60 min LAD occlusion technique was used to induce cardiac ischemia. Cardiac tissue was given a specific hyperoxic shock at reperfusion, based on the level of oxygen inspired by the animal during surgery. Animals were randomly divided into three groups and each group inspired either 21% O₂ (room air, control), 100% O₂ or 10% O₂ during the 60 min occlusion period, and room air before and after reperfusion. Animals were switched to breathing room air just before reperfusion. Fractional Inspiration of oxygen (FIO₂) of 100% during occlusion and room air reperfusion corresponded to the group that suffered lowest hyperoxic shock. On the other hand, the group with FIO₂ of 10% during occlusion represented the group with maximum hyperoxic shock.

LV myocardial pO₂ in mice breathing room air is ≈30 mm Hg (254; 260), which drops to about 5 mm Hg during LAD occlusion (261). Inhalation of 10% O₂ during occlusion further drops the pO₂ to near 0 levels. In animals breathing 100% O₂, there is only a minor increase in cardiac pO₂, which stays less than 10mm Hg because of the presence of LAD occlusion. Reperfusion of the LAD artery in addition to inhalation of room air brings a different degree of hyperoxic shock to cardiac tissue in the three groups. Angelos et al reported significant depression in myocardial pO₂ first few min of reperfusion with 2% O₂ compared

with 95% O₂ in a mouse model of IR (260). The three groups of animals were expected to have a different degree of hyperoxic response. We tested the functional significance of the different degree of hyperoxic insults using cardiac MRI 3d and 7d post reperfusion.

Cardiac tissue was harvested at 3d and 7d post reperfusion immediately after MRI. Hearts were fixed in Tissue-Tek OCT (Optical Cutting Temperature) compound and stored at -80°C. Tissue blocks were cryo-sectioned to get 10 µm thick slices. Hematoxylin and Eosin staining was done to delineate infarct area.

Animal Group	FIO₂ During LAD Occlusion	MRI time point
Group 1	21 % O ₂ (room air)	3d, 7d
Group 2	10 % O ₂	3d, 7d
Group 3	100 % O ₂	3d, 7d

Table 4.1 | Summary of experimental plan. Animals were randomly divided into three groups. FIO₂ during occlusion was different for each group, with reperfusion done with room air breathing. Analysis of cardiac function was done using MRI at 3d and 7d post reperfusion.

4.2.2 Modified Ischemia-Reperfusion Technique

Our objective for standardizing the cardiac IR technique was to experimentally model the clinical situation of a medical intervention used to

restore blood flow in cases of acute myocardial infarction. We have previously reported that during occlusion cardiac myocytes reset their normoxic set point to a lower level. At reperfusion, in addition to lethal reperfusion injury at the core of infarct, cells in ischemic border zone experience a 'perceived hyperoxia' which causes CF differentiation and LV remodeling via a p21 dependent pathway. We sought to characterize the functional effects of a perceived hyperoxia based insult by modulating hyperoxic shock intensity in different groups of mice.

A 60 min LAD occlusion surgery was used to induce IR in mice as described in section 2.2.4. Mice were anesthetized, intubated and ventilated on a specific concentration of oxygen at an appropriate rate and tidal volume. A custom-made ventilation system was developed that delivered 21%, 100% or 10% O₂ to mice while occlusion. Mice were switched to breathing room air just before reperfusion. All other surgical procedures remained similar to described before.

4.2.3 MRI protocol for analysis of cardiac function

LV remodeling after IR in experimental animals is routinely studied by evaluation of cardiac function (235-237). Cardiac function analysis with MRI was done in all mouse groups at 3d and 7d post reperfusion. These time points were selected because serial MRI analysis had revealed a significant change in cardiac function at these time points (Fig 3.9). We decided to terminate the study and harvest cardiac tissue at 7d post reperfusion because cardiac function and

structural abnormalities were the worst as observed with MRI and histological staining (Fig 3.8, Fig 3.10). Also, a substantial remodeling response involving macrophage infiltration, myocyte loss from infarct site and myofibroblast formation takes place at from 7d-14d post reperfusion (130; 259; 262). Since we sought to evaluate the functional effects of perceived hyperoxia as it pertains to tissue remodeling at acute time points after IR, we performed MRI at 3d and 7d post reperfusion

An ECG-triggered cine FLASH sequence was used to obtain bright-blood images of the heart as described in section 2.2.2. These images were analyzed with appropriate image processing techniques to extract parameters of cardiac function as described in section 2.2.6. Each imaging slice was 1mm thick, which resulted in a total of 6-8 cardiac slices for each experiment. In a sub-group of the animals, delayed hyper enhancement imaging was also done to track infarct volume progression as described in section 2.2.5.3. Statistical analysis to evaluate differences in cardiac function between groups was done using one way ANOVA.

4.2.4 Cardiac tissue procurement and processing

After MRI, animals were killed and their hearts were excised. The heart was cut laterally just above or below the infarcted area, and the tissue containing the infarcted area was frozen in optimum cutting temperature compound (OCT) using liquid N₂. OCT is a substance similar to wax and is used for embedding

tissue after fixation and before cryo-sectioning. The frozen mouse hearts were cut into 10- μ m-thick sections using a Leica 3500S cryostat (Leica, Germany). The sections were placed on RNAPrep-treated thermoplastic (polyethylene naphthalate, PEN)-covered glass slides from PALM Technologies (Bernried, Germany) and used immediately or stored at -80°C. One section was typically cut at a time and placed on the slide immediately before use to minimize RNA degradation.

To histologically distinguish between infarcted and noninfarcted areas, the frozen sections were stained directly with hematoxylin QS only (Vector Laboratories, Burlingame, CA). For this procedure, frozen sections were thawed for 1-2 min at room temperature, two to three drops of hematoxylin QS were added to each section, and the slides were incubated at room temperature for 1-4 min. The slides were rapidly rinsed with distilled water to remove excess stain and then allowed to air dry for 5-10 min at room temperature. The stained sections were photographed using a camera (model D30, Hitachi) mounted on a microscope (Axiovert 200M, Zeiss). In some cases, tissue sections were stained with Masson's trichrome or hematoxylin-eosin using standard protocols.

4.2.5 Laser Microdissection and Pressure Catapulting Technique for site-specific analysis of gene expression

In contrast to traditional whole tissue homogenization techniques for gene and protein analysis, laser micro-dissection pressure catapulting (LMPC) is a

novel tool that allows for the analysis of proteins and genes at a micro-environment resolution (263-265). LMPC technology was developed and commercialized by the National Institutes of Health through a collaboration between bioengineering, cancer pathology groups and Arcturus Engineering (Mountain View, CA) (266; 267). Under direct microscopic visualization, LCM permits rapid procurement of histologically defined tissue samples. The approach can be employed to collect pathologically defined (e.g., infarct core) tissue elements down to the resolution of a single cell (93). LMPC can be applied to the procurement of DNA, RNA or protein from selected pure cells. The capture process does not damage these macromolecules because the laser energy is absorbed by the film. The starting tissue can be fixed (e.g., formalin or ethanol) and embedded in paraffin or frozen. The tissue section can be stained with a variety of standard stains in order to highlight the cell population of interest.

We employed LMPC technique to perform site specific gene expression measurement in mouse heart after IR surgery. Frozen cardiac sections were stained with Hematoxylin were mounted on a PEN membrane slide and placed on the robotic stage of the PALM LMPC system. The membrane acts as a support, or scaffolding, to allow for catapulting relatively large amounts of intact material at one time. Under a 10x-laser objective lens, the portion of the section to be captured was outlined on the monitor display with the software running the LMPC system. A focused laser beam was used to cut out an area of the membrane and corresponding biological material. Typical settings used for laser cutting were a beam diameter of 30 μm and laser strength of 30 mV for 10 μm

thick sections. An optimized cutting speed of 40 (arbitrary units) was used for capturing elements from the sections. Following cutting, the beam was then defocused and the energy used to catapult the membrane and material from the slide several mm into the air into 8-well micro-centrifuge caps containing 25 μ l of membrane lysis buffer. 4-6 laser catapult points were selected around the cut element for ejection from the slide. After elements were catapulted and captured, micro-centrifuge caps were removed from the collection tray and affixed to micro-tubes for proteomic or genomic isolation.

4.2.6 RNA isolation and real-time PCR to measure gene expression

RNA from LMPC samples was isolated using the RNAqueous Micro (Ambion) kit. The 25 μ l of lysis solution used to capture the catapulted tissue in LMPC was spun into a tube, and another 75 μ l of lysis solution, along with 3 μ l of the supplied LCM additive and either 129 μ l (to collect large and small RNA) or 52 μ l (to collect >200-bp RNA) of ACS grade 100% ethanol, were added. This solution was spun through a silica-based spin column to bind the RNA. The columns were washed with the supplied buffers, and the RNA was eluted in two 9- μ l washes using the supplied elution solution or nuclease-free distilled water. The RNA solution was then treated with DNase for 20 min at 37°C to remove DNA. The quality and approximate quantity of the resulting RNA were determined using the microfluidics system (Agilent 2100 Bioanalyzer, Agilent Technologies).

In some cases, RNA quantity was verified using the RiboGreen fluorescence dye assay (Molecular Probes, Eugene, OR).

RNA isolated as described above was reverse transcribed into cDNA using the Superscript III RT kit (Invitrogen, Carlsbad, CA). For each reaction, 8 μ l of the 20 μ l of RNA solution were used. In some cases, the entire RNA solution was used after it was concentrated to 8 μ l using a Speed Vac concentrator system. Reactions were typically carried out using the supplied random hexamers. In some cases, however, the supplied oligo(dt)₂₀ primer was used. One microliter each of random hexamers (50 ng/ μ l) and dNTPs (10 mM) were added to 8 μ l of RNA solution, and the resulting solution was incubated for 5 min at 65°C and then placed on ice for \geq 1 min. Ten microliters of a 2x reaction mixture containing Tris·HCl (pH 7.4), 25 mM MgCl₂, 0.1 M dithiothreitol, 40 U of RNase Out, and 200 U of Superscript III RT were added, and the solution was incubated at 25°C for 10 min, 50°C for 50 min, and, finally, 85°C for 5 min. RNA was degraded by further incubation for 20 min at 37°C with 2 U of RNase H. The cDNA generated in reverse transcriptase reactions was separated on 3% agarose gels. Ethidium bromide was added directly to the sample, and electrophoresis was conducted at 125 V constant voltage.

The cDNA generated in RT reactions was used directly in real-time PCR with gene-specific primers using the MX3000P system (Stratagene, La Jolla, CA). The PCR included 5 μ l of cDNA solution, 7.3 μ l of nuclease-free distilled water, 0.1 μ l of each primer solution (50 μ M), and 12.5 μ l of SYBR Green real-

time PCR mixture (Applied Biosystems, Warrington, UK). The solution was initially incubated at 50°C for 2 min and then at 95°C for 10 min to activate the polymerase. Typically, 40 cycles with 45-s steps each were performed at 95°C, 58°C, and 72°C. The dissociation (i.e., melting) temperature (T_m) of each sample was compared with that of an included known cDNA standard to partially ensure fabrication of the correct cDNA product. The cDNA standard was also used to obtain relative quantities. GAPDH gene expression was measured to correct for differences in extraction efficiency between infarcted and noninfarcted samples. Collagen Ia and collagen IIIa gene expressions were measured to monitor our protocol, because it is well established that each is significantly increased in infarcted tissue.

4.3 Results and Discussion

4.3.1 Effect of Hyperoxic Shock on Cardiac Function

We evaluated the functional significance of three different levels of hyperoxic shock (10% oxygen – largest shock, 100% oxygen – smallest shock, 21% oxygen – control group) caused by reperfusion of LAD artery in mouse model of IR. Serial evaluation of cardiac function in mice with MRI was done at baseline and at two time points after IR: 3d and 7d.

Worst overall cardiac function was observed in 10% oxygen group. There was a significant increase in LV End Diastolic Volume (EDV) and End Systolic

Volume (ESV), and a significant decrease in Stroke Volume (SV), Cardiac Output (CO) and EF in the 10% oxygen group as opposed to control group post IR (Fig 4.1). Post IR, worst cardiac function was observed at day 7 with a 41% increase in EDV, 340% increase in ESV, 32.5% decrease in SV, 32% decrease in CO, 23% decrease in EF and 30% increase in LV mass was observed.

On the other hand, the 100% oxygen group showed an ameliorated response to IR surgery as opposed to control group. We observed significant changes in cardiac function from baseline levels, but those changes were not significantly worse as compared to control group breathing 21% oxygen. On the contrary, a trend towards improvement of cardiac function was noted in most functional parameters. At day 7, EDV of 100% group improved by 15%, ESV by 36% and EF by 20% over control group.

These results support our hypothesis that change in pO_2 of the border region during IR modulates the level of perceived hyperoxia and affects cardiac function. We have recently proposed that reoxygenation of an ischemic site, in addition to being a trigger for injury, may induce tissue remodeling. Previously, we established that exposure of isolated cardiac fibroblasts (CF) to a higher pO_2 , relative to which cells are adjusted, induces the differentiation of CF to myofibroblasts. This is of significant relevance to cardiac tissue remodeling in the context of reoxygenation. We reported that solely by maintaining the O_2 ambience of the culture condition to a level closely matching *in vivo* LV pO_2 , such culture dependent switch of phenotype may be prevented. In this *in vivo* study,

we report that upon impact of perceived hyperoxia the phenotype switching observed in isolated CF has a significant functional correlation in mouse model of IR. We provide first direct *in vivo* evidence of a linear response of perceived hyperoxia to functional damage.

4.3.2 Quantification of p21 in peri-infarct region

Previously, we have reported that perceived hyperoxia induces the expression p21, which in turn leads to differentiation of the fibroblasts at that site to myofibroblasts (130; 208; 254; 262). Here, we sought to apply our LMPC technique to investigate whether p21 is induced in mouse heart in tissue located at the site of infarct. The noninfarct region was used as a control. Consistent with previously published data from mixed heart tissue and cultured fibroblasts, tissue captured from the infarct region of the ischemia-reperfused heart in mice breathing 21% oxygen during surgery had significant upregulation of p21 expression (Fig. 4.2). This spatially resolved molecular analysis of infarcted myocardial tissue using a specialized microdissection technique confirmed that the infarct region had upregulation of p21, implicating it as a player in oxygen-induced LV remodeling.

Further, p21 gene expression was calculated from tissue obtained from 10% and 100% oxygen groups. A ratio of p21 expression in infarct region to normal region was generated to estimate the upregulation of p21 post IR. We observed a significant increase in p21 expression in 10% oxygen group as

opposed to 100% group (Fig 4.3). The 100% group received lesser hyperoxic shock at IR compared to 10% group. Previously, we had demonstrated that, in cardiac fibroblasts, inducible p21 expression is oxygen sensitive (254). That observation led to the paradigm of perceived hyperoxia which postulates that sublethal hyperoxic shock in the peri-infarct region of the ischemic heart results in differentiation of cardiac fibroblasts to myofibroblasts. In this study we obtained first evidence demonstrating that, in response to ischemia-reperfusion, the induction of p21 is directly proportional to the amount of hyperoxic shock suffered by the tissue. The study proves that relative hyperoxic shock, as noted during ischemia-reoxygenation of the heart, serves as a trigger for the phenotypic switch of CF to myofibroblasts, and has a significant functional effect on LV remodeling. In addition, cardiac functional damage is proportional to the level of hyperoxic shock, which in turn can be defined by the proportional upregulation of p21.

4.4 Conclusions

There were two major objectives of this study: 1) to quantitatively assess, based on the paradigm of perceived hyperoxia, effects of tissue remodeling induced by graded levels of hyperoxic shock in the mouse heart post IR, and 2) to evaluate if the p21 pathway is involved resulting in adverse effects on cardiac function. We further tested whether this diminished function could be avoided by a lower oxygen shock to the reperfused tissue. Using MRI, we evaluated the

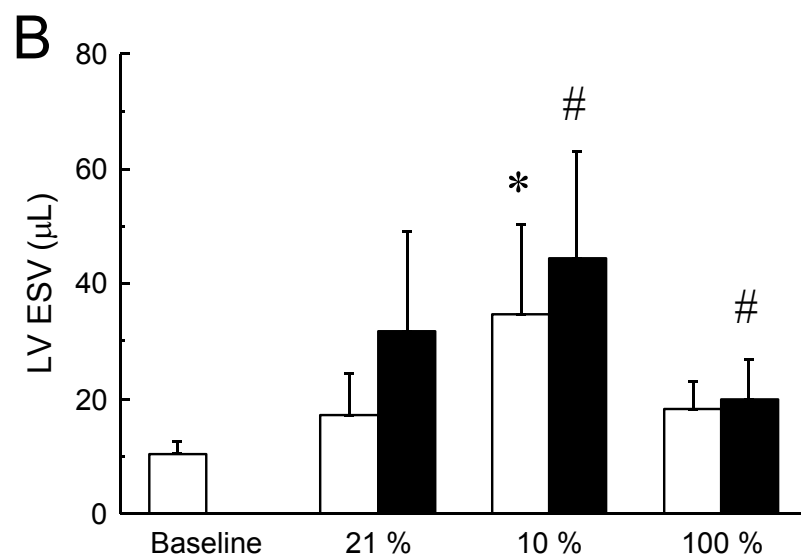
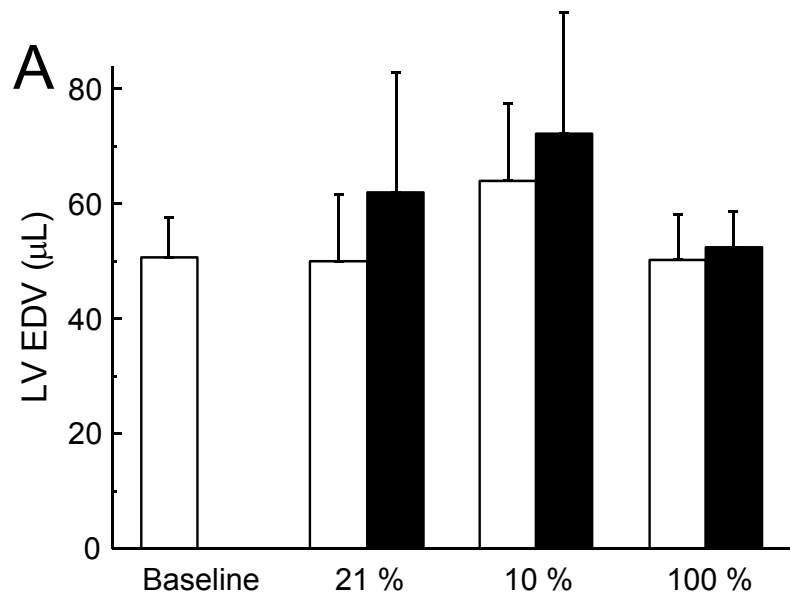
effect of a graded hyperoxic insult to cardiac function by modulating the hyperoxic shock suffered by cardiac tissue at reperfusion.

Evaluation of cardiac function post IR of the various animal groups indicated worst function in the 10% oxygen group (highest oxygen shock), and best function in the 100% group (least oxygen shock). Room air group (control) cardiac function was in-between the other two groups. The results indicated a proportional negative effect of hyperoxic shock on cardiac function post IR. We further observed that ratio of p21 expression in peri-infarct region to normal region was significantly higher in 10% oxygen group compared to 100% oxygen group. Thus, it was clear that a higher level of perceived hyperoxia resulted in an increase in the expression of p21. This observation, in association with our previous findings that implicate p21 as the causal mechanism for phenotypic switching of CF to myofibroblast, led us to believe that the p21 pathway plays a major role in deciding the final fate of cardiac tissue as it relates to its structure and functional capacity.

In conclusion, the results of this study indicate that p21 is a major player in executing tissue remodeling outcomes in the post IR heart. Increasing oxygen shock to the cardiac tissue, via the p21 pathway, results in worsening of cardiac function.

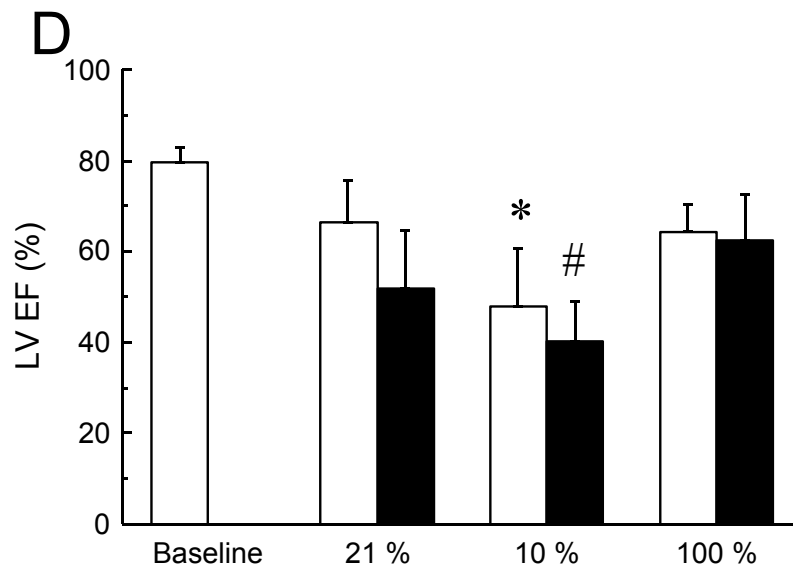
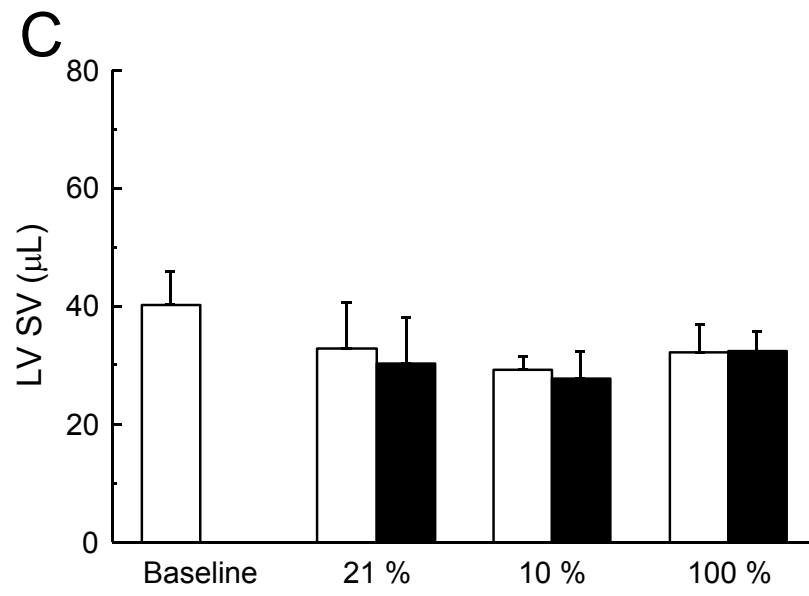
4.5 Figures

Figure 4.1 | Magnitude of reduced cardiac function after IR injury is dependent on hyperoxic shock at reperfusion. Global parameters of LV volume and function were measured with MRI at two time points: 3d (open bars) and 7d (solid bars) post IR in addition to baseline. Animal group breathing 21% oxygen during surgery acted as control. Increased LVESV (B) and reduced EF (D) compared to control group were observed in 10% oxygen group. Improvement in SV and a trend towards reduction in worsening of cardiac parameters was observed in the 100% oxygen group. * indicates $p < 0.05$ between 3d MRI measurements; # indicates $p < 0.05$ between 7d MRI measurements (n = 9 in baseline group, n=9 in 21% group, n=4 in 10% group and n=5 in 100% group).



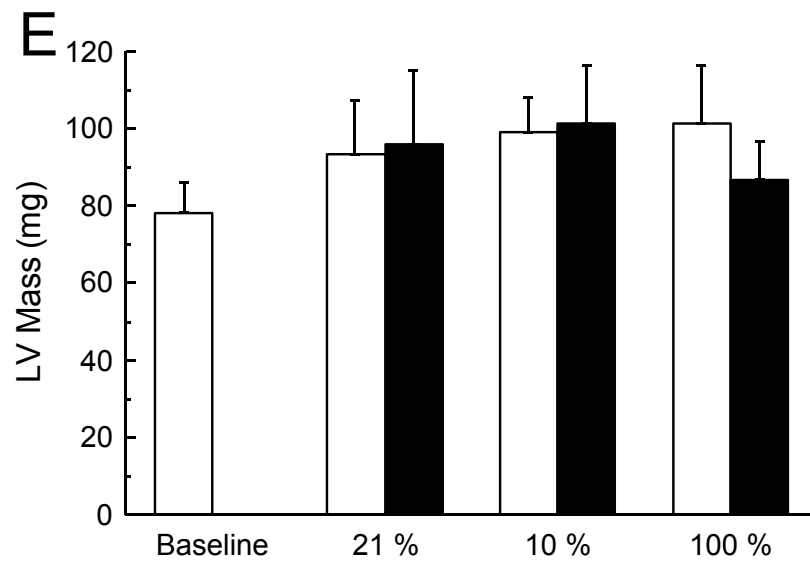
continued

Figure 4.1



continued

Figure 4.1



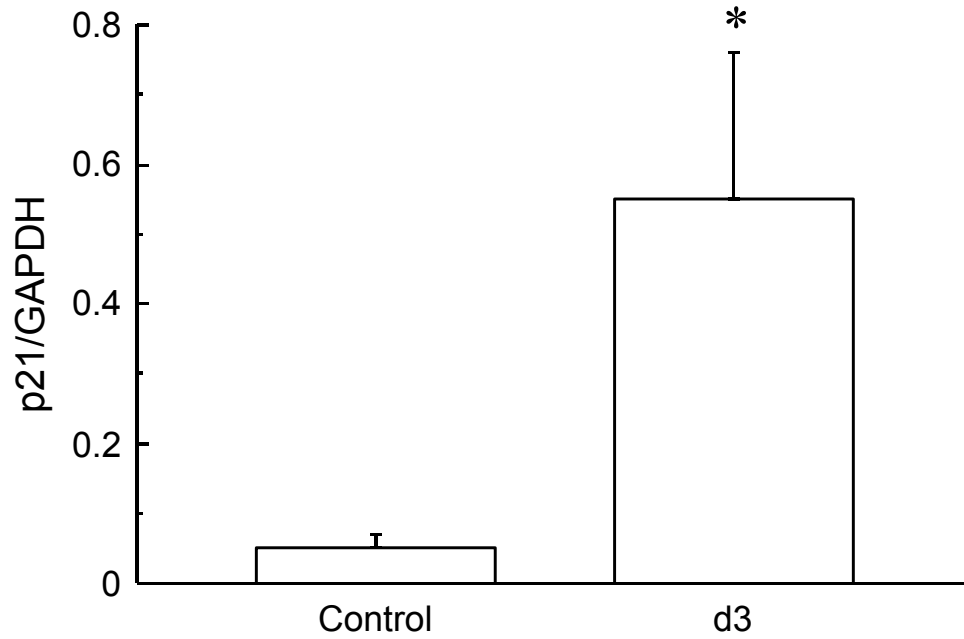


Figure 4.2 | Quantitative analysis of p21/Cip1/Waf1/Sdi1 gene expression using laser captured tissue. Expression of p21 was calculated from tissue captured from within the infarct region, as delineated with H/E staining. Cycle threshold values from real-time PCR were normalized to GAPDH expression. * indicates $p < 0.01$

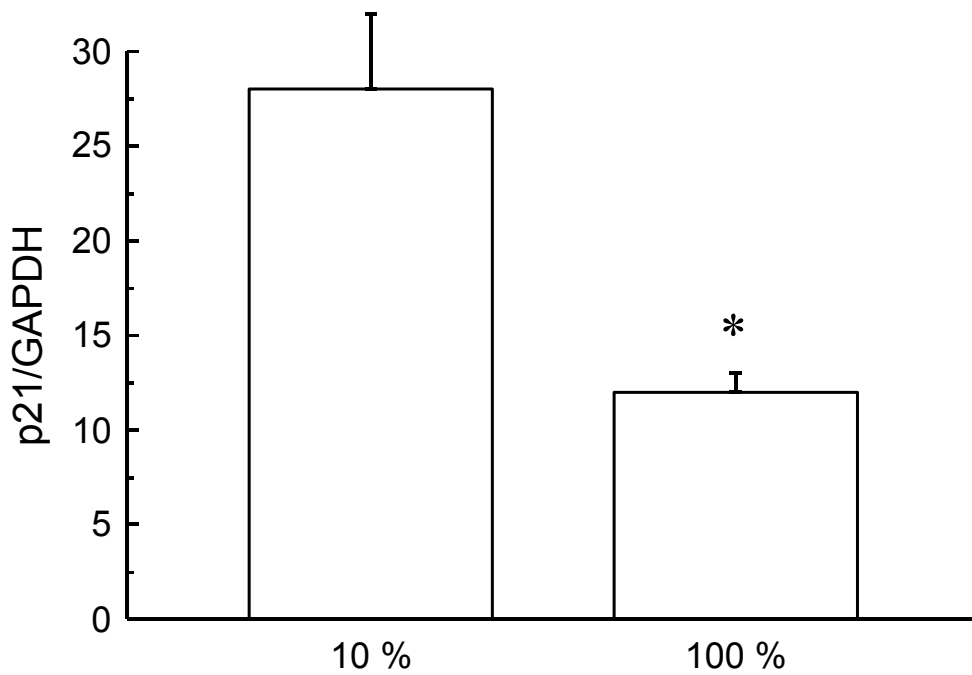


Figure 4.3 | Change in quantitative expression of p21/Cip1/Waf1/Sdi1 gene using laser captured tissue in 10% and 100% oxygen groups. Ratio of p21 expression in infarct region to normal region in IR heart was calculated. A significantly subdued p21 expression response is observed in the 100% group, which has lesser hyperoxic shock at reperfusion. Cycle threshold values from real-time PCR were normalized to GAPDH expression. * indicates $p < 0.01$.

CHAPTER 5

SUMMARY AND GENERAL DISCUSSION

5.1 Summary

This thesis began with three major objectives:

1. To characterize oxygen and oxidant damage in tissue using MRI and EPR spectroscopy techniques.
2. To develop an MRI based cardiac imaging technique for analysis of murine cardiac function, structure and infarct volume after Ischemia-Reperfusion in an attempt to characterize the effects of secondary myocyte death processes on LV remodeling.
3. To establish the functional significance of oxygen as a modulator of perceived hyperoxia during ischemia-reperfusion.

In chapter 1, MRI was introduced and its application to animal models of stroke was discussed. It was shown that high resolution MRI had the technical prowess to play an active role not just as a diagnostic modality for end-point confirmation

of stroke-induced brain damage, but also for modification and perfection of the surgical technique used for induction of focal cerebral ischemia. Mouse and rat models of MCA occlusion were employed in the study. A time course of infarct volume in the brain was generated, with the striking observation that cerebral edema shrunk between 2 and 7 days after reperfusion with an associated decrease in infarct intensity. This time course points to the presence of dynamic mechanisms in place that can potentially modulate cerebral damage post stroke and reperfusion.

In chapter 1 another magnetic-based technique, EPR, was described for its application to study redox control of dermal wound healing in an in vivo mouse model. This technique was used to study the effects of rac2, a Rho GTPase expressed in neutrophils and macrophages which regulates NADPH oxidase activation, on wound healing. It was concluded that the wound site is rich in oxidants in the inflammatory phase. Rac2 significantly contributes to oxidant production thereby supporting the healing process.

In chapter 2, a cardiac MRI technique for the analysis of murine cardiac function, structure and infarct volume after Ischemia-Reperfusion was discussed. We innovated on several hardware and software techniques to generate high-resolution and reproducible mouse heart MR images in quick scan times for routine quantitative cardiac analysis.

Chapter 3 described the application of MRI techniques standardized in chapter 2 to a mouse model of cardiac ischemia-reperfusion. We hypothesized that, in addition to lethal reperfusion injury, IR also causes secondary progressive

myocyte loss leading to worsening of LV function and regional wall motion over time. We used histology and high resolution cardiac MRI to study LV function, structure and infarct volume progression in mice after IR injury in an attempt to address the functional significance of secondary damage suffered by myocardium after reperfusion induced injury. We established that post IR cell death processes have a significant negative effect on global cardiac function, LV structure and myocardial contractility in a mouse model of IR.

Chapter 4 described the results of *in vivo* functional evaluation of our previously published *in vitro* work where we showed that exposure of isolated cardiac fibroblasts to a higher pO_2 , relative to which cells were adjusted, induced the differentiation of CF to myofibroblasts. We studied the effect of a graded hyperoxic insult to cardiac function by modulating the hyperoxic shock suffered by cardiac tissue at reperfusion. We hypothesized that tissue remodeling induced by 'perceived hyperoxia' in the heart post-reperfusion has a detrimental effect on cardiac function, and this diminished function can be circumvented by a lower oxygen shock suffered by the reperfused tissue at reperfusion. We proved our hypothesis with MRI based evaluation of cardiac function post IR in animal groups with different levels of hyperoxic shock. The p21 pathway was implicated as a major player in the induction of perceived hyperoxic shock and its effects.

5.2 General Discussion

The underlying connective matrix that binds this thesis together is oxygen. Molecular oxygen is relatively stable but its reactive forms (reactive oxygen

species, ROS) are known to cause lethal injury to tissue. Extensive studies have clearly shown that ROS are able to produce chemical modifications and damage to proteins, lipids, carbohydrates and nucleotides (268). Therefore, if such reactive free radicals are produced in vivo, or in cells in vitro, in amounts sufficient to overcome the normally efficient protective mechanisms, metabolic and cellular disturbances will occur in various major ways. On the other hand, ROS can also participate as benevolent molecules in cell signaling processes (269). Oxygen is thus both vital and deleterious. In all three tissue systems discussed in this thesis – brain, skin and heart – oxygen and its derivatives play a major role in tissue injury. We employed various biomedical imaging techniques to evaluate tissue injury-repair addressing the role of oxygen and its derivatives.

Within the centre or core of an ischemic territory, blood flow deficits, low ATP levels and energy stores, ionic disruption and metabolic failure are severe, and cell death progresses in minutes. However, the peripheral zone within the flow compromised territory (peri-infarct region) suffers less severe insults due to residual perfusion from collateral blood vessels, and is potentially salvageable. In the peri-infarct zone, active cell death mechanisms are recruited, and targeting these mechanisms provides promising therapeutic approaches. Within the core of the brain or cardiac infarct, salvage of rapidly dying cells might not be feasible without early reperfusion. In fact, once tissues are damaged beyond a critical point, cell death seems inevitable, despite restoration of both blood flow and ATP levels (27).

There are at least three fundamental mechanisms leading to cell death during ischemic brain injury: excitotoxicity and ionic imbalance, oxidative/nitrosative stress, and apoptotic-like cell death. They mediate injury within neurons, glia and vascular elements, and at the subcellular level, they impact the function of mitochondria, nuclei, cell membranes, endoplasmic reticula and lysosomes. Cell death proceeds by mechanisms promoting rupture, lysis, phagocytosis or involution and shrinkage. We employed MRI to monitor global brain damage after cerebral ischemia.

The mammalian heart is an aerobic organ and cannot produce enough energy under anaerobic conditions to maintain essential cellular processes; thus, a constant supply of oxygen is indispensable to sustain cardiac function and viability. In addition, oxygen is a major determinant of myocardial gene expression, and as myocardial O₂ levels decrease, either during isolated hypoxia or ischemia-associated hypoxia, gene expression patterns in the heart are significantly altered (270). Oxygen also participates in the generation of NO, which plays a critical role in determining vascular tone, cardiac contractility, and a variety of additional parameters. We developed a cardiac MRI technique to study the effect of IR on LV remodeling. In addition, we established a connection between induction of p21 gene expression with hyperoxic insult and loss of cardiac function post IR.

Oxygen and oxygen radicals play a major role in wound healing. Compromised tissue oxygenation or wound hypoxia is viewed as a major factor that limits the healing process as well as wound disinfection (62). Also, our group

have previously reported that H_2O_2 is actively generated by cells at the wound-site and that H_2O_2 -driven redox signaling support wound angiogenesis and healing (60; 61). We used EPR to prove the existence of superoxide oxygen radical at the wound site at the time of respiratory burst of inflammatory cells. We further showed that the lack of *rac2*, a Rho GTPase which regulates NADPH oxidase activation, compromises wound healing by inhibiting ROS production at the wound site.

5.3 A Philosophical Note on Oxygen

Oxygen is the source of life. Humans cannot survive without oxygen. Hypoxia has been known for a long time to be an important physiological parameter in tumor growth and response to therapy. It is also now known to be a cause of poor healing in chronic wounds. To make things more complicated too much oxygen is also damaging, causing oxygen toxicity. Priestley, who discovered oxygen, was himself amongst the first to suggest that there may be adverse affects of this 'pure air', when in 1775, he observed a candle to burn out faster in oxygen than in air, and wondered if "the animal powers too be soon exhausted in this pure kind of air". He further recorded, "...oxygen might be very useful as a medicine, [but] it might not be so useful for us in the normal healthy state of the body". What makes all this more fascinating and scary at the same time is the concept of 'perceived hyperoxia' and that 'normoxia' for cells is a variable that is dependent on the specific localization of the cell in organs and functional status of the specific tissue (271).

Nick Lane, author of 'Oxygen: The Molecule that Made the World', agrees that oxygen, the Elixir of Life – a wonder tonic, a cure for ageing, a beauty treatment, a potent medical therapy, is muddled in controversy (272). It is a fire hazard and considered a dangerous poison that will kill us in the end. Divers breathing pure oxygen at depth suffer from convulsions and lung injury. The so-called active oxygen treatments, including ozone and hydrogen peroxide, are touted as miracles in combating infection and promoting wound healing; yet it is suggested that the secret to a long and healthy life is to eat a lot of antioxidants – to protect us against these very active forms of oxygen. Oxygen, a colorless and odorless gas, one of the most toxic substances on Earth, the source of our life, is way too important for us to ignore.

BIBLIOGRAPHY

1. **Howard D.** Albert Einstein as a Philosopher of Science. *Physics Today*, 2005.
2. **Minkel CW.** Observations on the Control of Quality in Theses and Dissertations. *Council of Graduate Schools Communicator* 15, 1982.
3. **Gannon F.** What is a Ph.D? *EMBO reports* 7: 1061, 2006.
4. **Wikipedia.** Doctor of Philosophy [online]. Available at en.wikipedia.org/wiki/Doctor_of_Philosophy, 2007.
5. **Rosenberg RP.** Eugene Schuyler's Doctor of Philosophy Degree. *The Journal of Higher Education* 33, 1962.
6. **Brock WH.** How the PhD came to Britain. A century of struggle for postgraduate education. *Med Hist.* 30: 108-109, 1986.
7. **Academy B.** Review of Graduate Studies in the Humanities and Social Sciences., 2001.
8. **Trust TW.** Review of Wellcome Trust PhD Research Training: The Student Perspective: The Wellcome Trust, 2000.
9. **Trust TW.** Review of Wellcome Trust PhD Research Training: The Career Paths of a 1988-1990 Prize Student Cohort: The Wellcome Trust, 2000.
10. **University P.** Notes on the PhD degree [online]. Available at cs.purdue.edu/homes/dec/essay.phd.html.
11. **Jalote P.** Doing a PhD – Preparing for a Career in Research [online]. Accessible at cse.iitk.ac.in/users/jalote/GenArticles/DoingPhD.pdf.
12. **Lotka AJ.** The frequency distribution of scientific productivity. *Journal of the Washington Academy of Sciences* 16: 317, 1926.

13. **Kuppusamy P and Zweier JL.** Cardiac applications of EPR imaging. *NMR Biomed.* 17: 226-239., 2004.
14. **Damadian R.** Tumor detection by nuclear magnetic resonance. *Science.* 171: 1151-1153., 1971.
15. **Lauterbur PC.** Image formation by induced local interactions. Examples employing nuclear magnetic resonance. 1973. *Clin Orthop Relat Res.*: 3-6., 1989.
16. **Aue WP, Bartholdi E and Ernst RR.** Two-dimensional spectroscopy. Application to nuclear magnetic resonance. *The Journal of Chemical Physics* 64: 2229-2246, 1976.
17. **Prasad A.** Scientific Culture in the 'Other' Theater of 'Modern Science': An Analysis of the Culture of Magnetic Resonance Imaging Research in India. *Social Studies of Science* 35: 463, 2005.
18. **AHA.** Heart Disease and Stroke Statistics: American Heart Association, American Stroke Association, 2007.
19. **Carmichael ST.** Rodent models of focal stroke: size, mechanism, and purpose. *NeuroRx.* 2: 396-409., 2005.
20. **Nedergaard M.** Neuronal injury in the infarct border: a neuropathological study in the rat. *Acta Neuropathol* 73: 267-274, 1987.
21. **Osborne KA, Shigeno T, Balarsky AM, Ford I, McCulloch J, Teasdale GM and Graham DI.** Quantitative assessment of early brain damage in a rat model of focal cerebral ischaemia. *J Neurol Neurosurg Psychiatry.* 50: 402-410., 1987.
22. **Kloss CU, Thomassen N, Fesl G, Martens KH, Yousri TA and Hamann GF.** Tissue-saving infarct volumetry using histochemistry validated by MRI in rat focal ischemia. *Neurol Res.* 24: 713-718., 2002.
23. **Hatfield RH, Mendelow AD, Perry RH, Alvarez LM and Modha P.** Triphenyltetrazolium chloride (TTC) as a marker for ischaemic changes in rat brain following permanent middle cerebral artery occlusion. *Neuropathol Appl Neurobiol.* 17: 61-67., 1991.
24. **Kollmar R, Schabitz WR, Heiland S, Georgiadis D, Schellinger PD, Bardutzky J and Schwab S.** Neuroprotective effect of delayed moderate hypothermia after focal cerebral ischemia: an MRI study. *Stroke.* 33: 1899-1904., 2002.
25. **Neumann-Haefelin T, Kastrup A, de Crespigny A, Yenari MA, Ringer T, Sun GH and Moseley ME.** Serial MRI after transient focal cerebral ischemia in

rats: dynamics of tissue injury, blood-brain barrier damage, and edema formation. *Stroke*. 31: 1965-1972; discussion 1972-1963., 2000.

26. **Soltanian-Zadeh H, Pasnoor M, Hammoud R, Jacobs MA, Patel SC, Mitsias PD, Knight RA, Zheng ZG, Lu M and Chopp M.** MRI tissue characterization of experimental cerebral ischemia in rat. *J Magn Reson Imaging*. 17: 398-409., 2003.

27. **Lo EH, Dalkara T and Moskowitz MA.** Mechanisms, challenges and opportunities in stroke. *Nat Rev Neurosci*. 4: 399-415., 2003.

28. **Rink C.** The significance of vitamin E in stroke and 12-lipoxygenase: American Heart Association, 2006.

29. **Gerriets T, Stolz E, Walberer M, Muller C, Rottger C, Kluge A, Kaps M, Fisher M and Bachmann G.** Complications and pitfalls in rat stroke models for middle cerebral artery occlusion: a comparison between the suture and the macrosphere model using magnetic resonance angiography. *Stroke*. 35: 2372-2377. Epub 2004 Sep 2372., 2004.

30. **Derouesne C, Cambon H, Yelnik A, Duyckaerts C and Hauw JJ.** Infarcts in the middle cerebral artery territory. Pathological study of the mechanisms of death. *Acta Neurol Scand* 87: 361-366, 1993.

31. **Marinkovic SV, Kovacevic MS and Marinkovic JM.** Perforating branches of the middle cerebral artery. Microsurgical anatomy of their extracerebral segments. *J Neurosurg* 63: 266-271, 1985.

32. **McAuley MA.** Rodent models of focal ischemia. *Cerebrovasc Brain Metab Rev* 7: 153-180, 1995.

33. **Belayev L, Busto R, Zhao W and Ginsberg MD.** Quantitative evaluation of blood-brain barrier permeability following middle cerebral artery occlusion in rats. *Brain Res*. 739: 88-96., 1996.

34. **Longa EZ, Weinstein PR, Carlson S and Cummins R.** Reversible middle cerebral artery occlusion without craniectomy in rats. *Stroke*. 20: 84-91., 1989.

35. **Koizumi J, Yoshida Y, Nakazawa T and Ooneda G.** Experimental studies of ischemic brain edema. I: a new experimental model of cerebral embolism in rats in which recirculation can be introduced in the ischemic area. *Jpn J Stroke* 8: 1-8, 1986.

36. **Dihne M, Grommes C, Lutzenburg M, Witte OW and Block F.** Different mechanisms of secondary neuronal damage in thalamic nuclei after focal cerebral ischemia in rats. *Stroke* 33: 3006-3011, 2002.

37. **Hata R, Mies G, Wiessner C, Fritze K, Hesselbarth D, Brinker G and Hossmann KA.** A reproducible model of middle cerebral artery occlusion in mice: hemodynamic, biochemical, and magnetic resonance imaging. *J Cereb Blood Flow Metab.* 18: 367-375., 1998.
38. **Kondo T, Reaume AG, Huang TT, Carlson E, Murakami K, Chen SF, Hoffman EK, Scott RW, Epstein CJ and Chan PH.** Reduction of CuZn-superoxide dismutase activity exacerbates neuronal cell injury and edema formation after transient focal cerebral ischemia. *J Neurosci.* 17: 4180-4189., 1997.
39. **Bahn MM, Oser AB and Cross DT, 3rd.** CT and MRI of stroke. *J Magn Reson Imaging.* 6: 833-845., 1996.
40. **Li TQ, Chen ZG and Hindmarsh T.** Diffusion-weighted MR imaging of acute cerebral ischemia. *Acta Radiol.* 39: 460-473., 1998.
41. **Le Bihan D, Breton E, Lallemand D, Grenier P, Cabanis E and Laval-Jeantet M.** MR imaging of intravoxel incoherent motions: application to diffusion and perfusion in neurologic disorders. *Radiology.* 161: 401-407., 1986.
42. **Koyama T, Tamai K and Togashi K.** Current status of body MR imaging: fast MR imaging and diffusion-weighted imaging. *Int J Clin Oncol.* 11: 278-285., 2006.
43. **Lundy EF, Solik BS, Frank RS, Lacy PS, Combs DJ, Zelenock GB and D'Alecy LG.** Morphometric evaluation of brain infarcts in rats and gerbils. *J Pharmacol Methods* 16: 201-214, 1986.
44. **Loubinoux I, Volk A, Borredon J, Guirimand S, Tiffon B, Seylaz J and Meric P.** Spreading of vasogenic edema and cytotoxic edema assessed by quantitative diffusion and T2 magnetic resonance imaging. *Stroke* 28: 419-426; discussion 426-417, 1997.
45. **EI-Abhar HS, Shaalan M, Barakat M and EI-Denshary ES.** Effect of melatonin and nifedipine on some antioxidant enzymes and different energy fuels in the blood and brain of global ischemic rats. *J Pineal Res.* 33: 87-94., 2002.
46. **Farkas E, Luiten PG and Bari F.** Permanent, bilateral common carotid artery occlusion in the rat: a model for chronic cerebral hypoperfusion-related neurodegenerative diseases. *Brain Res Rev.* 54: 162-180. Epub 2007 Jan 2018., 2007.

47. **Tietjen GE, Futrell N, Garcia JH and Millikan C.** Platelet emboli in rat brain cross when the contralateral carotid artery is occluded. *Stroke*. 22: 1053-1058., 1991.
48. **Beaulieu C, de Crespigny A, Tong DC, Moseley ME, Albers GW and Marks MP.** Longitudinal magnetic resonance imaging study of perfusion and diffusion in stroke: evolution of lesion volume and correlation with clinical outcome. *Ann Neurol*. 46: 568-578., 1999.
49. **Busch E, Kruger K, Allegrini PR, Kerskens CM, Gyngell ML, Hoehn-Berlage M and Hossmann KA.** Reperfusion after thrombolytic therapy of embolic stroke in the rat: magnetic resonance and biochemical imaging. *J Cereb Blood Flow Metab*. 18: 407-418., 1998.
50. **Wang YF, Tsirka SE, Strickland S, Stieg PE, Soriano SG and Lipton SA.** Tissue plasminogen activator (tPA) increases neuronal damage after focal cerebral ischemia in wild-type and tPA-deficient mice. *Nat Med*. 4: 228-231., 1998.
51. **Davis SM, Donnan GA, Butcher KS and Parsons M.** Selection of thrombolytic therapy beyond 3 h using magnetic resonance imaging. *Curr Opin Neurol*. 18: 47-52., 2005.
52. **Donnan GA, Howells DW, Markus R, Toni D and Davis SM.** Can the time window for administration of thrombolytics in stroke be increased? *CNS Drugs* 17: 995-1011, 2003.
53. **Fisher M and Takano K.** The penumbra, therapeutic time window and acute ischaemic stroke. *Baillieres Clin Neurol*. 4: 279-295., 1995.
54. **Schellinger PD, Fiebich JB and Hacke W.** Imaging-based decision making in thrombolytic therapy for ischemic stroke: present status. *Stroke*. 34: 575-583., 2003.
55. **Baron JC, von Kummer R and del Zoppo GJ.** Treatment of acute ischemic stroke. Challenging the concept of a rigid and universal time window. *Stroke*. 26: 2219-2221., 1995.
56. **Veltkamp R, Siebing DA, Sun L, Heiland S, Bieber K, Marti HH, Nagel S, Schwab S and Schwaninger M.** Hyperbaric oxygen reduces blood-brain barrier damage and edema after transient focal cerebral ischemia. *Stroke*. 36: 1679-1683. Epub 2005 Jul 16 14., 2005.
57. **Barja G.** Mitochondrial free radical production and aging in mammals and birds. *Ann N Y Acad Sci*. 854: 224-238., 1998.

58. **Sen CK**. The general case for redox control of wound repair. *Wound Repair Regen.* 11: 431-438., 2003.
59. **Sen CK and Packer L**. Antioxidant and redox regulation of gene transcription. *Faseb J.* 10: 709-720., 1996.
60. **Sen CK, Khanna S, Babior BM, Hunt TK, Ellison EC and Roy S**. Oxidant-induced vascular endothelial growth factor expression in human keratinocytes and cutaneous wound healing. *J Biol Chem.* 277: 33284-33290. Epub 32002 Jun 33214., 2002.
61. **Roy S, Khanna S, Nallu K, Hunt TK and Sen CK**. Dermal wound healing is subject to redox control. *Mol Ther.* 13: 211-220. Epub 2005 Aug 2026., 2006.
62. **Gordillo GM and Sen CK**. Revisiting the essential role of oxygen in wound healing. *Am J Surg* 186: 259-263, 2003.
63. **Kivisaari J, Vihersaari T, Renvall S and Niinikoski J**. Energy metabolism of experimental wounds at various oxygen environments. *Ann Surg.* 181: 823-828., 1975.
64. **Grief R, Akca O, Horn E-P, Kurz A and Sessler D**. Supplemental perioperative oxygen to reduce the incidence of surgical-wound infection.Outcomes research group. *N engl J med* 342: 161-167, 2000.
65. **Sen CK, Khanna S, Gordillo G, Bagchi D, Bagchi M and Roy S**. Oxygen, oxidants, and antioxidants in wound healing: an emerging paradigm. *Ann N Y Acad Sci.* 957: 239-249., 2002.
66. **Suh YA, Arnold RS, Lassegue B, Shi J, Xu X, Sorescu D, Chung AB, Griending KK and Lambeth JD**. Cell transformation by the superoxide-generating oxidase Mox1. *Nature.* 401: 79-82., 1999.
67. **Stone JR and Yang S**. Hydrogen peroxide: a signaling messenger. *Antioxid Redox Signal* 8: 243-270, 2006.
68. **Irani K, Xia Y, Zweier JL, Sollott SJ, Der CJ, Fearon ER, Sundaresan M, Finkel T and Goldschmidt-Clermont PJ**. Mitogenic signaling mediated by oxidants in Ras-transformed fibroblasts. *Science.* 275: 1649-1652., 1997.
69. **Schafer FQ and Buettner GR**. Redox environment of the cell as viewed through the redox state of the glutathione disulfide/glutathione couple. *Free Radic Biol Med.* 30: 1191-1212., 2001.
70. **Hordijk PL**. Regulation of NADPH oxidases: the role of Rac proteins. *Circ Res.* 98: 453-462., 2006.

71. **Villamena FA and Zweier JL.** Detection of reactive oxygen and nitrogen species by EPR spin trapping. *Antioxid Redox Signal.* 6: 619-629., 2004.
72. **Liu X and Zweier JL.** A real-time electrochemical technique for measurement of cellular hydrogen peroxide generation and consumption: evaluation in human polymorphonuclear leukocytes. *Free Radic Biol Med.* 31: 894-901., 2001.
73. **Velayutham M, Villamena FA, Navamal M, Fishbein JC and Zweier JL.** Glutathione-mediated formation of oxygen free radicals by the major metabolite of oltipraz. *Chem Res Toxicol.* 18: 970-975., 2005.
74. **Underwood RA, Gibran NS, Muffley LA, Usui ML and Olerud JE.** Color subtractive-computer-assisted image analysis for quantification of cutaneous nerves in a diabetic mouse model. *J Histochem Cytochem.* 49: 1285-1291., 2001.
75. **Beanes SR, Dang C, Soo C and Ting K.** Skin repair and scar formation: the central role of TGF-beta. *Expert Rev Mol Med.* 5: 1-22., 2003.
76. **Sachse J-H and Marsh D.** Line intensities in spin-exchanged nitroxide ESR spectra. *J. Magn. Reson.* 68: 540-543, 1986.
77. **He G, Samouilov A, Kuppusamy P and Zweier JL.** In vivo EPR imaging of the distribution and metabolism of nitroxide radicals in human skin. *J Magn Reson* 148: 155-164, 2001.
78. **Dikalov SI, Vitek MP, Maples KR and Mason RP.** Amyloid beta peptides do not form peptide-derived free radicals spontaneously, but can enhance metal-catalyzed oxidation of hydroxylamines to nitroxides. *J Biol Chem.* 274: 9392-9399., 1999.
79. **Kocherginsky N and Swartz HM.** *Nitroxide Spin Labels, Reactions in Biology and Chemistry:* CRC Press, 1995.
80. **Sentjurc M and Mason RP.** Inhibition of radical adduct reduction and reoxidation of the corresponding hydroxylamines in in vivo spin trapping of carbon tetrachloride-derived radicals. *Free Radic Biol Med* 13: 151-160, 1992.
81. **Rosen GM, Pou S, Ramos CL, Cohen MS and Britigan BE.** Free radicals and phagocytic cells. *Faseb J* 9: 200-209, 1995.
82. **Yamauchi A, Kim C, Li S, Marchal CC, Towe J, Atkinson SJ and Dinauer MC.** Rac2-deficient murine macrophages have selective defects in superoxide production and phagocytosis of opsonized particles. *J Immunol* 173: 5971-5979, 2004.

83. **Ambruso DR, Knall C, Abell AN, Panepinto J, Kurkchubasche A, Thurman G, Gonzalez-Aller C, Hiester A, deBoer M, Harbeck RJ, Oyer R, Johnson GL and Roos D.** Human neutrophil immunodeficiency syndrome is associated with an inhibitory Rac2 mutation. *Proc Natl Acad Sci U S A.* 97: 4654-4659., 2000.
84. **Witte MB and Barbul A.** General principles of wound healing. *Surg Clin North Am* 77: 509-528, 1997.
85. **Esterbauer H, Schaur RJ and Zollner H.** Chemistry and biochemistry of 4-hydroxynonenal, malonaldehyde and related aldehydes. *Free Radic Biol Med* 11: 81-128, 1991.
86. **Wheeler AP, Wells CM, Smith SD, Vega FM, Henderson RB, Tybulewicz VL and Ridley AJ.** Rac1 and Rac2 regulate macrophage morphology but are not essential for migration. *J Cell Sci.* 119: 2749-2757. Epub 2006 Jun 27 13., 2006.
87. **Wessels A and Sedmera D.** Developmental anatomy of the heart: a tale of mice and man. *Physiol Genomics.* 15: 165-176., 2003.
88. **West GB, Brown JH and Enquist BJ.** The fourth dimension of life: fractal geometry and allometric scaling of organisms. *Science.* 284: 1677-1679., 1999.
89. **West GB, Brown JH and Enquist BJ.** A general model for the origin of allometric scaling laws in biology. *Science.* 276: 122-126., 1997.
90. **Hachamovitch R, Berman DS, Shaw LJ, Kiat H, Cohen I, Cabico JA, Friedman J and Diamond GA.** Incremental prognostic value of myocardial perfusion single photon emission computed tomography for the prediction of cardiac death: differential stratification for risk of cardiac death and myocardial infarction. *Circulation.* 97: 535-543., 1998.
91. **Gehrmann J, Frantz S, Maguire CT, Vargas M, Ducharme A, Wakimoto H, Lee RT and Berul CI.** Electrophysiological characterization of murine myocardial ischemia and infarction. *Basic Res Cardiol.* 96: 237-250., 2001.
92. **Berul CI, Aronovitz MJ, Wang PJ and Mendelsohn ME.** In vivo cardiac electrophysiology studies in the mouse. *Circulation.* 94: 2641-2648., 1996.
93. **Kuhn DE, Roy S, Radtke J, Gupta S and Sen CK.** Laser microdissection and pressure-catapulting technique to study gene expression in the reoxygenated myocardium. *Am J Physiol Heart Circ Physiol.* 290: H2625-2632. Epub 2006 Jan 26 27., 2006.

94. **Hu TC, Bao W, Lenhard SC, Schaeffer TR, Yue TL, Willette RN and Jucker BM.** Simultaneous assessment of left-ventricular infarction size, function and tissue viability in a murine model of myocardial infarction by cardiac manganese-enhanced magnetic resonance imaging (MEMRI). *NMR Biomed.* 17: 620-626., 2004.
95. **Fieno DS, Kim RJ, Chen EL, Lomasney JW, Klocke FJ and Judd RM.** Contrast-enhanced magnetic resonance imaging of myocardium at risk: distinction between reversible and irreversible injury throughout infarct healing. *J Am Coll Cardiol.* 36: 1985-1991., 2000.
96. **Kim RJ, Fieno DS, Parrish TB, Harris K, Chen EL, Simonetti O, Bundy J, Finn JP, Klocke FJ and Judd RM.** Relationship of MRI delayed contrast enhancement to irreversible injury, infarct age, and contractile function. *Circulation.* 100: 1992-2002., 1999.
97. **Kim RJ, Wu E, Rafael A, Chen EL, Parker MA, Simonetti O, Klocke FJ, Bonow RO and Judd RM.** The use of contrast-enhanced magnetic resonance imaging to identify reversible myocardial dysfunction. *N Engl J Med.* 343: 1445-1453., 2000.
98. **Yang Z, Berr SS, Gilson WD, Toufektsian MC and French BA.** Simultaneous evaluation of infarct size and cardiac function in intact mice by contrast-enhanced cardiac magnetic resonance imaging reveals contractile dysfunction in noninfarcted regions early after myocardial infarction. *Circulation.* 109: 1161-1167. Epub 2004 Feb 1116., 2004.
99. **Brutsaert DL.** Cardiac dysfunction in heart failure: the cardiologist's love affair with time. *Prog Cardiovasc Dis.* 49: 157-181., 2006.
100. **Chatterjee K.** Primary diastolic heart failure. *Am J Geriatr Cardiol.* 11: 178-187; quiz 188-179., 2002.
101. **Gyurko R, Kuhlencordt P, Fishman MC and Huang PL.** Modulation of mouse cardiac function in vivo by eNOS and ANP. *Am J Physiol Heart Circ Physiol.* 278: H971-981., 2000.
102. **Xu Q, Ming Z, Dart AM and Du XJ.** Optimizing dosage of ketamine and xylazine in murine echocardiography. *Clin Exp Pharmacol Physiol.* 34: 499-507., 2007.
103. **Hochhauser E, Cheporko Y, Yasovich N, Pinchas L, Offen D, Barhum Y, Pannet H, Tobar A, Vidne BA and Birk E.** Bax deficiency reduces infarct size and improves long-term function after myocardial infarction. *Cell Biochem Biophys* 47: 11-20, 2007.

104. **Young AA, French BA, Yang Z, Cowan BR, Gilson WD, Berr SS, Kramer CM and Epstein FH.** Reperfused myocardial infarction in mice: 3D mapping of late gadolinium enhancement and strain. *J Cardiovasc Magn Reson* 8: 685-692, 2006.
105. **Tanaka N, Dalton N, Mao L, Rockman HA, Peterson KL, Gottshall KR, Hunter JJ, Chien KR and Ross J, Jr.** Transthoracic echocardiography in models of cardiac disease in the mouse. *Circulation*. 94: 1109-1117., 1996.
106. **Ross AJ, Yang Z, Berr SS, Gilson WD, Petersen WC, Oshinski JN and French BA.** Serial MRI evaluation of cardiac structure and function in mice after reperfused myocardial infarction. *Magn Reson Med*. 47: 1158-1168., 2002.
107. **Maass DL, Naseem RH, Garry M and Horton JW.** Echocardiography assessment of myocardial function after burn injury. *Shock*. 25: 363-369., 2006.
108. **Smith SA, Mammen PP, Mitchell JH and Garry MG.** Role of the exercise pressor reflex in rats with dilated cardiomyopathy. *Circulation*. 108: 1126-1132. Epub 2003 Aug 11 118., 2003.
109. **Haris Naseem R, Meeson AP, Michael Dimaio J, White MD, Kallhoff J, Humphries C, Goetsch SC, De Windt LJ, Williams MA, Garry MG and Garry DJ.** Reparative myocardial mechanisms in adult C57BL/6 and MRL mice following injury. *Physiol Genomics*. 30: 44-52. Epub 2007 Feb 20 207., 2007.
110. **Mammen PP, Kanatous SB, Yuhanna IS, Shaul PW, Garry MG, Balaban RS and Garry DJ.** Hypoxia-induced left ventricular dysfunction in myoglobin-deficient mice. *Am J Physiol Heart Circ Physiol*. 285: H2132-2141. Epub 2003 Jul 21 214., 2003.
111. **Wiesmann F, Ruff J, Engelhardt S, Hein L, Dienesch C, Leupold A, Illinger R, Frydrychowicz A, Hiller KH, Rommel E, Haase A, Lohse MJ and Neubauer S.** Dobutamine-stress magnetic resonance microimaging in mice : acute changes of cardiac geometry and function in normal and failing murine hearts. *Circ Res*. 88: 563-569., 2001.
112. **Slawson SE, Roman BB, Williams DS and Koretsky AP.** Cardiac MRI of the normal and hypertrophied mouse heart. *Magn Reson Med*. 39: 980-987., 1998.
113. **Siri FM, Jelicks LA, Leinwand LA and Gardin JM.** Gated magnetic resonance imaging of normal and hypertrophied murine hearts. *Am J Physiol*. 272: H2394-2402., 1997.
114. **Franco F, Dubois SK, Peshock RM and Shohet RV.** Magnetic resonance imaging accurately estimates LV mass in a transgenic mouse model of cardiac hypertrophy. *Am J Physiol*. 274: H679-683., 1998.

115. **Ruff J, Wiesmann F, Hiller KH, Voll S, von Kienlin M, Bauer WR, Rommel E, Neubauer S and Haase A.** Magnetic resonance microimaging for noninvasive quantification of myocardial function and mass in the mouse. *Magn Reson Med.* 40: 43-48., 1998.
116. **Rose SE, Wilson SJ, Zelaya FO, Crozier S and Doddrell DM.** High resolution high field rodent cardiac imaging with flow enhancement suppression. *Magn Reson Imaging* 12: 1183-1190, 1994.
117. **Wiesmann F, Ruff J and Haase A.** High-resolution MR imaging in mice. *Magma.* 6: 186-188., 1998.
118. **Franco F, Thomas GD, Giroir B, Bryant D, Bullock MC, Chwialkowski MC, Victor RG and Peshock RM.** Magnetic resonance imaging and invasive evaluation of development of heart failure in transgenic mice with myocardial expression of tumor necrosis factor-alpha. *Circulation.* 99: 448-454., 1999.
119. **Wiesmann F, Ruff J, Hiller KH, Rommel E, Haase A and Neubauer S.** Developmental changes of cardiac function and mass assessed with MRI in neonatal, juvenile, and adult mice. *Am J Physiol Heart Circ Physiol.* 278: H652-657., 2000.
120. **Henson RE, Song SK, Pastorek JS, Ackerman JJ and Lorenz CH.** Left ventricular torsion is equal in mice and humans. *Am J Physiol Heart Circ Physiol.* 278: H1117-1123., 2000.
121. **Zhou R, Pickup S, Glickson JD, Scott CH and Ferrari VA.** Assessment of global and regional myocardial function in the mouse using cine and tagged MRI. *Magn Reson Med.* 49: 760-764., 2003.
122. **Yang Z, Bove CM, French BA, Epstein FH, Berr SS, DiMaria JM, Gibson JJ, Carey RM and Kramer CM.** Angiotensin II type 2 receptor overexpression preserves left ventricular function after myocardial infarction. *Circulation.* 106: 106-111., 2002.
123. **Yang Z, Cerniway RJ, Byford AM, Berr SS, French BA and Matherne GP.** Cardiac overexpression of A1-adenosine receptor protects intact mice against myocardial infarction. *Am J Physiol Heart Circ Physiol.* 282: H949-955., 2002.
124. **Yang Z, French BA, Gilson WD, Ross AJ, Oshinski JN and Berr SS.** Cine magnetic resonance imaging of myocardial ischemia and reperfusion in mice. *Circulation.* 103: E84., 2001.

125. **Edelman RR, Wallner B, Singer A, Atkinson DJ and Saini S.** Segmented turboFLASH: method for breath-hold MR imaging of the liver with flexible contrast. *Radiology*. 177: 515-521., 1990.
126. **Earls JP, Ho VB, Foo TK, Castillo E and Flamm SD.** Cardiac MRI: recent progress and continued challenges. *J Magn Reson Imaging*. 16: 111-127., 2002.
127. **Pettigrew RI.** Dynamic cardiac MR imaging. Techniques and applications. *Radiol Clin North Am*. 27: 1183-1203., 1989.
128. **Pettigrew RI, Oshinski JN, Chatzimavroudis G and Dixon WT.** MRI techniques for cardiovascular imaging. *J Magn Reson Imaging*. 10: 590-601., 1999.
129. **Lee VS.** *Cardiovascular MRI: physical principles to practical protocols*: LWW, 2006.
130. **Roy S, Khanna S, Wallace WA, Lappalainen J, Rink C, Cardounel AJ, Zweier JL and Sen CK.** Characterization of perceived hyperoxia in isolated primary cardiac fibroblasts and in the reoxygenated heart. *J Biol Chem*. 278: 47129-47135. Epub 42003 Sep 47122., 2003.
131. **Horiuchi K, Tsukamoto T, Saito M, Nakayama M, Fujibayashi Y and Saji H.** The development of (99m)Tc-analog of Cu-DTS as an agent for imaging hypoxia. *Nucl Med Biol*. 27: 391-399., 2000.
132. **Zhu X, Zuo L, Cardounel AJ, Zweier JL and He G.** Characterization of in vivo tissue redox status, oxygenation, and formation of reactive oxygen species in postischemic myocardium. *Antioxid Redox Signal*. 9: 447-455., 2007.
133. **Stapel H, Kim SC, Osterkamp S, Knuefermann P, Hoefft A, Meyer R, Grohe C and Baumgarten G.** Toll-like receptor 4 modulates myocardial ischaemia-reperfusion injury: Role of matrix metalloproteinases. *Eur J Heart Fail*. 8: 665-672. Epub 2006 Jul 2007., 2006.
134. **Chen Z, Chua CC, Gao J, Hamdy RC and Chua BH.** Protective effect of melatonin on myocardial infarction. *Am J Physiol Heart Circ Physiol*. 284: H1618-1624., 2003.
135. **Bove CM, Gilson WD, Scott CD, Epstein FH, Yang Z, Dimaria JM, Berr SS, French BA, Bishop SP and Kramer CM.** The angiotensin II type 2 receptor and improved adjacent region function post-MI. *J Cardiovasc Magn Reson* 7: 459-464, 2005.
136. **Nossuli TO, Lakshminarayanan V, Baumgarten G, Taffet GE, Ballantyne CM, Michael LH and Entman ML.** A chronic mouse model of

myocardial ischemia-reperfusion: essential in cytokine studies. *Am J Physiol Heart Circ Physiol.* 278: H1049-1055., 2000.

137. **Li RA, Leppo M, Miki T, Seino S and Marban E.** Molecular basis of electrocardiographic ST-segment elevation. *Circ Res.* 87: 837-839., 2000.

138. **Wagner A, Mahrholdt H, Thomson L, Hager S, Meinhardt G, Rehwald W, Parker M, Shah D, Sechtem U, Kim RJ and Judd RM.** Effects of time, dose, and inversion time for acute myocardial infarct size measurements based on magnetic resonance imaging-delayed contrast enhancement. *J Am Coll Cardiol.* 47: 2027-2033. Epub 2006 Apr 2027., 2006.

139. **Baert AL.** *Clinical Cardiac MRI:* Springer Berlin Heidelberg, 2005.

140. **Ni Y, Cresens E, Adriaens P, Dymarkowski S, Bogaert J, Zhang H, Bosmans H, Verbruggen A and Marchal G.** Exploring multifunctional features of necrosis avid contrast agents. *Acad Radiol.* 9 Suppl 2: S488-490., 2002.

141. **Ni Y, Cresens E, Adriaens P, Miao Y, Verbeke K, Dymarkowski S, Verbruggen A and Marchal G.** Necrosis-avid contrast agents: introducing nonporphyrin species. *Acad Radiol.* 9 Suppl 1: S98-101., 2002.

142. **Weinmann HJ, Brasch RC, Press WR and Wesbey GE.** Characteristics of gadolinium-DTPA complex: a potential NMR contrast agent. *AJR Am J Roentgenol.* 142: 619-624., 1984.

143. **Weinmann HJ, Laniado M and Mutzel W.** Pharmacokinetics of GdDTPA/dimeglumine after intravenous injection into healthy volunteers. *Physiol Chem Phys Med NMR* 16: 167-172, 1984.

144. **Sarka L, Burai L and Brucher E.** The rates of the exchange reactions between $[\text{Gd}(\text{DTPA})]^{2-}$ and the endogenous ions Cu^{2+} and Zn^{2+} : a kinetic model for the prediction of the in vivo stability of $[\text{Gd}(\text{DTPA})]^{2-}$, used as a contrast agent in magnetic resonance imaging. *Chemistry.* 6: 719-724., 2000.

145. **Cacheris WP, Quay SC and Rocklage SM.** The relationship between thermodynamics and the toxicity of gadolinium complexes. *Magn Reson Imaging* 8: 467-481, 1990.

146. **Boyd AS, Zic JA and Abraham JL.** Gadolinium deposition in nephrogenic fibrosing dermopathy. *J Am Acad Dermatol.* 56: 27-30. Epub 2006 Nov 2015., 2007.

147. **Ortonne N, Lipsker D, Chantrel F, Boehm N, Grosshans E and Cribier B.** Presence of CD45RO+ CD34+ cells with collagen synthesis activity in

nephrogenic fibrosing dermopathy: a new pathogenic hypothesis. *Br J Dermatol.* 150: 1050-1052., 2004.

148. **Marckmann P, Skov L, Rossen K, Dupont A, Damholt MB, Heaf JG and Thomsen HS.** Nephrogenic systemic fibrosis: suspected causative role of gadodiamide used for contrast-enhanced magnetic resonance imaging. *J Am Soc Nephrol.* 17: 2359-2362. Epub 2006 Aug 2352., 2006.

149. **Spencer AJ, Wilson SA, Batchelor J, Reid A, Rees J and Harpur E.** Gadolinium chloride toxicity in the rat. *Toxicol Pathol.* 25: 245-255., 1997.

150. **USFDA.** Information for Healthcare Professionals

Gadolinium-Based Contrast Agents for Magnetic Resonance Imaging (marketed as Magnevist, MultiHance, Omniscan, OptiMARK, ProHance): Center for Drug Evaluation and Research, 2007.

151. **Sandstede JJ.** Assessment of myocardial viability by MR imaging. *Eur Radiol* 13: 52-61, 2003.

152. **Kim RJ, Wu E, Rafael A, Chen EL, Parker MA, Simonetti O, Klocke FJ, Bonow RO and Judd RM.** The use of contrast-enhanced magnetic resonance imaging to identify reversible myocardial dysfunction. *N Engl J Med* 343: 1445-1453, 2000.

153. **Fieno DS, Hillenbrand HB, Rehwald WG, Harris KR, Decker RS, Parker MA, Klocke FJ, Kim RJ and Judd RM.** Infarct resorption, compensatory hypertrophy, and differing patterns of ventricular remodeling following myocardial infarctions of varying size. *J Am Coll Cardiol.* 43: 2124-2131., 2004.

154. **Oshinski JN, Yang Z, Jones JR, Mata JF and French BA.** Imaging time after Gd-DTPA injection is critical in using delayed enhancement to determine infarct size accurately with magnetic resonance imaging. *Circulation.* 104: 2838-2842., 2001.

155. **Tyler DJ, Hudsmith LE, Petersen SE, Francis JM, Weale P, Neubauer S, Clarke K and Robson MD.** Cardiac cine MR-imaging at 3T: FLASH vs SSFP. *J Cardiovasc Magn Reson* 8: 709-715, 2006.

156. **Simonetti OP, Kim RJ, Fieno DS, Hillenbrand HB, Wu E, Bundy JM, Finn JP and Judd RM.** An improved MR imaging technique for the visualization of myocardial infarction. *Radiology.* 218: 215-223., 2001.

157. **Kim RJ, Shah DJ and Judd RM.** How we perform delayed enhancement imaging. *J Cardiovasc Magn Reson* 5: 505-514, 2003.

158. **Kim RJ, Chen EL, Lima JA and Judd RM.** Myocardial Gd-DTPA kinetics determine MRI contrast enhancement and reflect the extent and severity of myocardial injury after acute reperfused infarction. *Circulation*. 94: 3318-3326., 1996.
159. **Klein HH.** The Mechanism of the Tetrazolium Reaction in Identifying Experimental Myocardial Infarction. *Virchows Arch [Pathol Anat]* 393: 297-297, 1981.
160. **Miyatake K, Yamagishi M, Tanaka N, Uematsu M, Yamazaki N, Mine Y, Sano A and Hiram M.** New method for evaluating left ventricular wall motion by color-coded tissue Doppler imaging: in vitro and in vivo studies. *J Am Coll Cardiol*. 25: 717-724., 1995.
161. **Edvardsen T, Urheim S, Skulstad H, Steine K, Ihlen H and Smiseth OA.** Quantification of left ventricular systolic function by tissue Doppler echocardiography: added value of measuring pre- and postejction velocities in ischemic myocardium. *Circulation*. 105: 2071-2077., 2002.
162. **Bach DS, Armstrong WF, Donovan CL and Muller DW.** Quantitative Doppler tissue imaging for assessment of regional myocardial velocities during transient ischemia and reperfusion. *Am Heart J*. 132: 721-725., 1996.
163. **Schaefer A, Klein G, Brand B, Lippolt P, Drexler H and Meyer GP.** Evaluation of left ventricular diastolic function by pulsed Doppler tissue imaging in mice. *J Am Soc Echocardiogr*. 16: 1144-1149., 2003.
164. **Royer A, van Veen TA, Le Bouter S, Marionneau C, Griol-Charhbili V, Leoni AL, Steenman M, van Rijen HV, Demolombe S, Goddard CA, Richer C, Escoubet B, Jarry-Guichard T, Colledge WH, Gros D, de Bakker JM, Grace AA, Escande D and Charpentier F.** Mouse model of SCN5A-linked hereditary Lenegre's disease: age-related conduction slowing and myocardial fibrosis. *Circulation*. 111: 1738-1746. Epub 2005 Apr 1734., 2005.
165. **Liang J, McInerney T and Terzopoulos D.** United snakes. *Med Image Anal*. 10: 215-233. Epub 2005 Nov 2028., 2006.
166. **Iyengar S.** *A processing workflow for small animal cardiac MR images*: The Ohio State University, 2007.
167. **Arheden H, Saeed M, Higgins CB, Gao DW, Bremerich J, Wyttenbach R, Dae MW and Wendland MF.** Measurement of the distribution volume of gadopentetate dimeglumine at echo-planar MR imaging to quantify myocardial infarction: comparison with 99mTc-DTPA autoradiography in rats. *Radiology*. 211: 698-708., 1999.

168. **Piper HM, Abdallah Y and Schafer C.** The first minutes of reperfusion: a window of opportunity for cardioprotection. *Cardiovasc Res.* 61: 365-371., 2004.
169. **Piper HM, Garcia-Dorado D and Ovize M.** A fresh look at reperfusion injury. *Cardiovasc Res.* 38: 291-300., 1998.
170. **Zeltcer G, Berenshtein E, Kitrossky N, Chevion M and Samuni A.** Time window of nitroxide effect on myocardial ischemic-reperfusion injury potentiated by iron. *Free Radic Biol Med.* 32: 912-919., 2002.
171. **Durot I, Maupoil V, Ponsard B, Cordelet C, Vergely-Vandriessse C, Rochette L and Athias P.** Oxidative injury of isolated cardiomyocytes: dependence on free radical species. *Free Radic Biol Med.* 29: 846-857., 2000.
172. **Zweier JL, Rayburn BK, Flaherty JT and Weisfeldt ML.** Recombinant superoxide dismutase reduces oxygen free radical concentrations in reperfused myocardium. *J Clin Invest.* 80: 1728-1734., 1987.
173. **Zweier JL and Talukder MA.** The role of oxidants and free radicals in reperfusion injury. *Cardiovasc Res.* 70: 181-190. Epub 2006 Mar 2003., 2006.
174. **Kutala VK, Khan M, Angelos MG and Kuppusamy P.** Role of oxygen in postischemic myocardial injury. *Antioxid Redox Signal.* 9: 1193-1206., 2007.
175. **Henry TD, Archer SL, Nelson D, Weir EK and From AH.** Postischemic oxygen radical production varies with duration of ischemia. *Am J Physiol.* 264: H1478-1484., 1993.
176. **Henry TD, Archer SL, Nelson D, Weir EK and From AH.** Enhanced chemiluminescence as a measure of oxygen-derived free radical generation during ischemia and reperfusion. *Circ Res.* 67: 1453-1461., 1990.
177. **Gupta M and Singal PK.** Time course of structure, function, and metabolic changes due to an exogenous source of oxygen metabolites in rat heart. *Can J Physiol Pharmacol.* 67: 1549-1559., 1989.
178. **Khan M, Mohan IK, Kutala VK, Kumbala D and Kuppusamy P.** Cardioprotection by Sulfaphenazole, a Cytochrome P450 Inhibitor: Mitigation of Ischemia-reperfusion Injury by Scavenging of Reactive Oxygen Species. *J Pharmacol Exp Ther* 14: 14, 2007.
179. **Ambrosio G and Tritto I.** Reperfusion injury: experimental evidence and clinical implications. *Am Heart J.* 138: S69-75., 1999.
180. **Ferrari R and Hearse DJ.** Reperfusion Injury: Does It Exist and Does It Have Clinical Relevance? *J Thromb Thrombolysis.* 4: 25-34., 1997.

181. **Kloner RA.** Does reperfusion injury exist in humans? *J Am Coll Cardiol.* 21: 537-545., 1993.
182. **Bardales RH, Hailey LS, Xie SS, Schaefer RF and Hsu SM.** In situ apoptosis assay for the detection of early acute myocardial infarction. *Am J Pathol.* 149: 821-829., 1996.
183. **Veinot JP, Gattinger DA and Fliss H.** Early apoptosis in human myocardial infarcts. *Hum Pathol.* 28: 485-492., 1997.
184. **Fliss H and Gattinger D.** Apoptosis in ischemic and reperfused rat myocardium. *Circ Res.* 79: 949-956., 1996.
185. **Suzuki H, Wildhirt SM, Dudek RR, Narayan KS, Bailey AH and Bing RJ.** Induction of apoptosis in myocardial infarction and its possible relationship to nitric oxide synthase in macrophages. *Tissue Cell.* 28: 89-97., 1996.
186. **Saraste A, Pulkki K, Kallajoki M, Heikkila P, Laine P, Mattila S, Nieminen MS, Parvinen M and Voipio-Pulkki LM.** Cardiomyocyte apoptosis and progression of heart failure to transplantation. *Eur J Clin Invest.* 29: 380-386., 1999.
187. **Saraste A, Voipio-Pulkki LM, Parvinen M and Pulkki K.** Apoptosis in the heart. *N Engl J Med.* 336: 1025-1026; author reply 1026., 1997.
188. **Saraste A, Pulkki K, Kallajoki M, Henriksen K, Parvinen M and Voipio-Pulkki LM.** Apoptosis in human acute myocardial infarction. *Circulation.* 95: 320-323., 1997.
189. **Kajstura J, Cheng W, Reiss K, Clark WA, Sonnenblick EH, Krajewski S, Reed JC, Olivetti G and Anversa P.** Apoptotic and necrotic myocyte cell deaths are independent contributing variables of infarct size in rats. *Lab Invest.* 74: 86-107., 1996.
190. **Klem I, Heitner JF, Shah DJ, Sketch MH, Jr., Behar V, Weinsaft J, Cawley P, Parker M, Elliott M, Judd RM and Kim RJ.** Improved detection of coronary artery disease by stress perfusion cardiovascular magnetic resonance with the use of delayed enhancement infarction imaging. *J Am Coll Cardiol.* 47: 1630-1638. Epub 2006 Mar 1627., 2006.
191. **Shah DJ, Judd RM and Kim RJ.** Technology insight: MRI of the myocardium. *Nat Clin Pract Cardiovasc Med.* 2: 597-605; quiz 606., 2005.
192. **Bello D, Shah DJ, Farah GM, Di Luzio S, Parker M, Johnson MR, Cotts WG, Klocke FJ, Bonow RO, Judd RM, Gheorghide M and Kim RJ.** Gadolinium cardiovascular magnetic resonance predicts reversible myocardial

dysfunction and remodeling in patients with heart failure undergoing beta-blocker therapy. *Circulation*. 108: 1945-1953. Epub 2003 Oct 19 13., 2003.

193. **Kim RJ, Shah DJ and Judd RM**. How we perform delayed enhancement imaging. *J Cardiovasc Magn Reson*. 5: 505-514., 2003.

194. **Mahrholdt H, Goedecke C, Wagner A, Meinhardt G, Athanasiadis A, Vogelsberg H, Fritz P, Klingel K, Kandolf R and Sechtem U**. Cardiovascular magnetic resonance assessment of human myocarditis: a comparison to histology and molecular pathology. *Circulation*. 109: 1250-1258. Epub 2004 Mar 12 51., 2004.

195. **Schindlbeck NE, Wiebecke B, Klauser AG, Voderholzer WA and Muller-Lissner SA**. Diagnostic value of histology in non-erosive gastro-oesophageal reflux disease. *Gut*. 39: 151-154., 1996.

196. **Knodell RG, Ishak KG, Black WC, Chen TS, Craig R, Kaplowitz N, Kiernan TW and Wollman J**. Formulation and application of a numerical scoring system for assessing histological activity in asymptomatic chronic active hepatitis. *Hepatology*. 1: 431-435., 1981.

197. **Statlab Medical Products I**. Fixation. Lewisville.

198. **Yu X, Patterson E, Huang S, Garrett MW and Kem DC**. Tumor necrosis factor alpha, rapid ventricular tachyarrhythmias, and infarct size in canine models of myocardial infarction. *J Cardiovasc Pharmacol*. 45: 153-159., 2005.

199. **Nash MP, Bradley CP and Paterson DJ**. Imaging electrocardiographic dispersion of depolarization and repolarization during ischemia: simultaneous body surface and epicardial mapping. *Circulation*. 107: 2257-2263. Epub 2003 Apr 22 21., 2003.

200. **Sugiyama S and Ozawa T**. Biochemical basis for reperfusion arrhythmias. *J Mol Cell Cardiol*. 19 Suppl 5: 67-75., 1987.

201. **Lai ZF, Shao Z, Chen YZ, He M, Huang Q and Nishi K**. Effects of sasanquasaponin on ischemia and reperfusion injury in mouse hearts. *J Pharmacol Sci*. 94: 313-324., 2004.

202. **Braunwald E**. *Heart Disease: A Textbook of Cardiovascular Medicine*: W.B. Saunders Co., 1997.

203. **Wehrens XH, Kirchhoff S and Doevendans PA**. Mouse electrocardiography: an interval of thirty years. *Cardiovasc Res*. 45: 231-237., 2000.

204. **Kleber AG**. ST-segment elevation in the electrocardiogram: a sign of myocardial ischemia. *Cardiovasc Res*. 45: 111-118., 2000.
205. **Pascale P, Quartenoud B and Stauffer JC**. Isolated large inverted T wave in pulmonary edema due to hypertensive crisis: a novel electrocardiographic phenomenon mimicking ischemia? *Clin Res Cardiol*. 96: 288-294. Epub 2007 Feb 2026., 2007.
206. **Drew BJ, Califf RM, Funk M, Kaufman ES, Krucoff MW, Laks MM, Macfarlane PW, Som margren C, Swiryn S and Van Hare GF**. Practice standards for electrocardiographic monitoring in hospital settings: an American Heart Association scientific statement from the Councils on Cardiovascular Nursing, Clinical Cardiology, and Cardiovascular Disease in the Young: endorsed by the International Society of Computerized Electrocardiology and the American Association of Critical-Care Nurses. *Circulation*. 110: 2721-2746., 2004.
207. **Kuhn DE, Roy S, Radtke J, Khanna S and Sen CK**. Laser microdissection and capture of pure cardiomyocytes and fibroblasts from infarcted heart regions: perceived hyperoxia induces p21 in peri-infarct myocytes. *Am J Physiol Heart Circ Physiol*. 292: H1245-1253. Epub 2006 Dec 1248., 2007.
208. **Roy S, Khanna S, Kuhn DE, Rink C, Williams WT, Zweier JL and Sen CK**. Transcriptome analysis of the ischemia-reperfused remodeling myocardium: temporal changes in inflammation and extracellular matrix. *Physiol Genomics*. 25: 364-374. Epub 2006 Mar 2022., 2006.
209. **Medicine YUSo**.
med.yale.edu/intmed/cardio/imaging/anatomy/short_axis_views/index.html, 1999.
210. **Olivetti G, Quaini F, Sala R, Lagrasta C, Corradi D, Bonacina E, Gambert SR, Cigola E and Anversa P**. Acute myocardial infarction in humans is associated with activation of programmed myocyte cell death in the surviving portion of the heart. *J Mol Cell Cardiol*. 28: 2005-2016., 1996.
211. **Itoh G, Tamura J, Suzuki M, Suzuki Y, Ikeda H, Koike M, Nomura M, Jie T and Ito K**. DNA fragmentation of human infarcted myocardial cells demonstrated by the nick end labeling method and DNA agarose gel electrophoresis. *Am J Pathol*. 146: 1325-1331., 1995.
212. **Gottlieb RA, Burleson KO, Kloner RA, Babior BM and Engler RL**. Reperfusion injury induces apoptosis in rabbit cardiomyocytes. *J Clin Invest*. 94: 1621-1628., 1994.
213. **Tanaka M, Ito H, Adachi S, Akimoto H, Nishikawa T, Kasajima T, Marumo F and Hiroe M**. Hypoxia induces apoptosis with enhanced expression

of Fas antigen messenger RNA in cultured neonatal rat cardiomyocytes. *Circ Res.* 75: 426-433., 1994.

214. **Hazarika S, Van Scott MR and Lust RM.** Severity of myocardial injury following ischemia-reperfusion is increased in a mouse model of allergic asthma. *Am J Physiol Heart Circ Physiol.* 292: H572-579. Epub 2006 Aug 2011., 2007.

215. **Jordan JE, Zhao ZQ and Vinten-Johansen J.** The role of neutrophils in myocardial ischemia-reperfusion injury. *Cardiovasc Res.* 43: 860-878., 1999.

216. **Berr SS, Xu Y, Roy RJ, Kundu B, Williams MB and French BA.** Images in cardiovascular medicine. Serial multimodality assessment of myocardial infarction in mice using magnetic resonance imaging and micro-positron emission tomography provides complementary information on the progression of scar formation. *Circulation.* 115: e428-429., 2007.

217. **Taatjes DJ, Wadsworth MP, Zaman AK, Schneider DJ and Sobel BE.** A novel dual staining method for identification of apoptotic cells reveals a modest apoptotic response in infarcted mouse myocardium. *Histochem Cell Biol.* 128: 275-283. Epub 2007 Aug 2008., 2007.

218. **Acton PD, Thomas D and Zhou R.** Quantitative imaging of myocardial infarct in rats with high resolution pinhole SPECT. *Int J Cardiovasc Imaging.* 22: 429-434. Epub 2006 Mar 2004., 2006.

219. **Fryer RM, Hsu AK, Eells JT, Nagase H and Gross GJ.** Opioid-induced second window of cardioprotection: potential role of mitochondrial KATP channels. *Circ Res.* 84: 846-851., 1999.

220. **Kurrelmeyer KM, Michael LH, Baumgarten G, Taffet GE, Peschon JJ, Sivasubramanian N, Entman ML and Mann DL.** Endogenous tumor necrosis factor protects the adult cardiac myocyte against ischemic-induced apoptosis in a murine model of acute myocardial infarction. *Proc Natl Acad Sci U S A.* 97: 5456-5461., 2000.

221. **Matsui T, Tao J, del Monte F, Lee KH, Li L, Picard M, Force TL, Franke TF, Hajjar RJ and Rosenzweig A.** Akt activation preserves cardiac function and prevents injury after transient cardiac ischemia in vivo. *Circulation.* 104: 330-335., 2001.

222. **Xiao CY, Hara A, Yuhki K, Fujino T, Ma H, Okada Y, Takahata O, Yamada T, Murata T, Narumiya S and Ushikubi F.** Roles of prostaglandin I(2) and thromboxane A(2) in cardiac ischemia-reperfusion injury: a study using mice lacking their respective receptors. *Circulation.* 104: 2210-2215., 2001.

223. **Yet SF, Tian R, Layne MD, Wang ZY, Maemura K, Solovyeva M, Ith B, Melo LG, Zhang L, Ingwall JS, Dzau VJ, Lee ME and Perrella MA.** Cardiac-

specific expression of heme oxygenase-1 protects against ischemia and reperfusion injury in transgenic mice. *Circ Res.* 89: 168-173., 2001.

224. **Parsa CJ, Matsumoto A, Kim J, Riel RU, Pascal LS, Walton GB, Thompson RB, Petrofski JA, Annex BH, Stamler JS and Koch WJ.** A novel protective effect of erythropoietin in the infarcted heart. *J Clin Invest.* 112: 999-1007., 2003.

225. **Jong WM, Reitsma PH, ten Cate H and de Winter RJ.** Modified two-step model for studying the inflammatory response during myocardial ischemia and reperfusion in mice. *Comp Med.* 53: 522-526., 2003.

226. **Nishimura T, Yamada Y, Hayashi M, Kozuka T, Nakatani T, Noda H and Takano H.** Determination of infarct size of acute myocardial infarction in dogs by magnetic resonance imaging and gadolinium-DTPA: comparison with indium-111 antimyosin imaging. *Am J Physiol Imaging* 4: 83-88, 1989.

227. **Jennings RB, Schaper J, Hill ML, Steenbergen C, Jr. and Reimer KA.** Effect of reperfusion late in the phase of reversible ischemic injury. Changes in cell volume, electrolytes, metabolites, and ultrastructure. *Circ Res.* 56: 262-278., 1985.

228. **Schaefer S, Malloy CR, Katz J, Parkey RW, Buja LM, Willerson JT and Peshock RM.** Gadolinium-DTPA-enhanced nuclear magnetic resonance imaging of reperfused myocardium: identification of the myocardial bed at risk. *J Am Coll Cardiol.* 12: 1064-1072., 1988.

229. **McNamara MT, Tscholakoff D, Revel D, Soulen R, Schechtmann N, Botvinick E and Higgins CB.** Differentiation of reversible and irreversible myocardial injury by MR imaging with and without gadolinium-DTPA. *Radiology.* 158: 765-769., 1986.

230. **Reimer KA and Jennings RB.** The changing anatomic reference base of evolving myocardial infarction. Underestimation of myocardial collateral blood flow and overestimation of experimental anatomic infarct size due to tissue edema, hemorrhage and acute inflammation. *Circulation.* 60: 866-876., 1979.

231. **Hallstrom A, Pratt CM, Greene HL, Huther M, Gottlieb S, DeMaria A and Young JB.** Relations between heart failure, ejection fraction, arrhythmia suppression and mortality: analysis of the Cardiac Arrhythmia Suppression Trial. *J Am Coll Cardiol.* 25: 1250-1257., 1995.

232. **Bigger JT, Jr., Fleiss JL, Kleiger R, Miller JP and Rolnitzky LM.** The relationships among ventricular arrhythmias, left ventricular dysfunction, and mortality in the 2 years after myocardial infarction. *Circulation.* 69: 250-258., 1984.

233. **Ruberman W, Weinblatt E, Goldberg JD, Frank CW, Chaudhary BS and Shapiro S.** Ventricular premature complexes and sudden death after myocardial infarction. *Circulation*. 64: 297-305., 1981.
234. **Ruberman W, Weinblatt E, Goldberg JD, Frank CW, Shapiro S and Chaudhary BS.** Ventricular premature complexes in prognosis of angina. *Circulation*. 61: 1172-1182., 1980.
235. **Minatoguchi S, Takemura G, Chen XH, Wang N, Uno Y, Koda M, Arai M, Misao Y, Lu C, Suzuki K, Goto K, Komada A, Takahashi T, Kosai K, Fujiwara T and Fujiwara H.** Acceleration of the healing process and myocardial regeneration may be important as a mechanism of improvement of cardiac function and remodeling by postinfarction granulocyte colony-stimulating factor treatment. *Circulation*. 109: 2572-2580. Epub 2004 May 2573., 2004.
236. **Naumova AV, Chacko VP, Ouwerkerk R, Stull L, Marban E and Weiss RG.** Xanthine oxidase inhibitors improve energetics and function after infarction in failing mouse hearts. *Am J Physiol Heart Circ Physiol*. 290: H837-843. Epub 2005 Sep 2023., 2006.
237. **Ikonomidis JS, Hendrick JW, Parkhurst AM, Herron AR, Escobar PG, Dowdy KB, Stroud RE, Hapke E, Zile MR and Spinale FG.** Accelerated LV remodeling after myocardial infarction in TIMP-1-deficient mice: effects of exogenous MMP inhibition. *Am J Physiol Heart Circ Physiol*. 288: H149-158., 2005.
238. **Patterson JH and Adams KF, Jr.** Pathophysiology of heart failure: changing perceptions. *Pharmacotherapy*. 16: 27S-36S., 1996.
239. **Paulus WJ, Tschope C, Sanderson JE, Rusconi C, Flachskampf FA, Rademakers FE, Marino P, Smiseth OA, De Keulenaer G, Leite-Moreira AF, Borbely A, Edes I, Handoko ML, Heymans S, Pezzali N, Pieske B, Dickstein K, Fraser AG and Brutsaert DL.** How to diagnose diastolic heart failure: a consensus statement on the diagnosis of heart failure with normal left ventricular ejection fraction by the Heart Failure and Echocardiography Associations of the European Society of Cardiology. *Eur Heart J* 11: 11, 2007.
240. **Carson P, Johnson G, Fletcher R and Cohn J.** Mild systolic dysfunction in heart failure (left ventricular ejection fraction >35%): baseline characteristics, prognosis and response to therapy in the Vasodilator in Heart Failure Trials (V-HeFT). *J Am Coll Cardiol*. 27: 642-649., 1996.
241. **Adamopoulos C, Zannad F, Fay R, Mebazaa A, Cohen-Solal A, Guize L, Juilliere Y and Alla F.** Ejection fraction and blood pressure are important and interactive predictors of 4-week mortality in severe acute heart failure. *Eur J Heart Fail*. 9: 935-941. Epub 2007 Jul 2012., 2007.

242. **Buckberg GD.** Defining the relationship between akinesia and dyskinesia and the cause of left ventricular failure after anterior infarction and reversal of remodeling to restoration. *J Thorac Cardiovasc Surg.* 116: 47-49., 1998.
243. **Vartdal T, Brunvand H, Pettersen E, Smith HJ, Lyseggen E, Helle-Valle T, Skulstad H, Ihlen H and Edvardsen T.** Early prediction of infarct size by strain Doppler echocardiography after coronary reperfusion. *J Am Coll Cardiol.* 49: 1715-1721. Epub 2007 Apr 1715., 2007.
244. **Gotte MJ, van Rossum AC, Twisk JWR, Kuijer JPA, Marcus JT and Visser CA.** Quantification of regional contractile function after infarction: strain analysis superior to wall thickening analysis in discriminating infarct from remote myocardium. *J Am Coll Cardiol.* 37: 808-817., 2001.
245. **De Celle T, Cleutjens JP, Blankesteyn WM, Debets JJ, Smits JF and Janssen BJ.** Long-term structural and functional consequences of cardiac ischaemia-reperfusion injury in vivo in mice. *Exp Physiol.* 89: 605-615. Epub 2004 Jul 2015., 2004.
246. **Semenza GL.** HIF-1, O(2), and the 3 PHDs: how animal cells signal hypoxia to the nucleus. *Cell.* 107: 1-3., 2001.
247. **Webster KA.** Hypoxia: life on the edge. *Antioxid Redox Signal.* 9: 1303-1307., 2007.
248. **Packer L and Fuehr K.** Low oxygen concentration extends the lifespan of cultured human diploid cells. *Nature.* 267: 423-425., 1977.
249. **Graham RM, Frazier DP, Thompson JW, Haliko S, Li H, Wasserlauf BJ, Spiga MG, Bishopric NH and Webster KA.** A unique pathway of cardiac myocyte death caused by hypoxia-acidosis. *J Exp Biol.* 207: 3189-3200., 2004.
250. **Ohnishi S, Yasuda T, Kitamura S and Nagaya N.** Effect of hypoxia on gene expression of bone marrow-derived mesenchymal stem cells and mononuclear cells. *Stem Cells.* 25: 1166-1177. Epub 2007 Feb 1168., 2007.
251. **Ke Q and Costa M.** Hypoxia-inducible factor-1 (HIF-1). *Mol Pharmacol.* 70: 1469-1480. Epub 2006 Aug 1463., 2006.
252. **Krishnamachary B, Zagzag D, Nagasawa H, Rainey K, Okuyama H, Baek JH and Semenza GL.** Hypoxia-inducible factor-1-dependent repression of E-cadherin in von Hippel-Lindau tumor suppressor-null renal cell carcinoma mediated by TCF3, ZFH1A, and ZFH1B. *Cancer Res.* 66: 2725-2731., 2006.

253. **Volm M and Koomagi R.** Hypoxia-inducible factor (HIF-1) and its relationship to apoptosis and proliferation in lung cancer. *Anticancer Res.* 20: 1527-1533., 2000.
254. **Roy S, Khanna S, Bickerstaff AA, Subramanian SV, Atalay M, Bierl M, Pendyala S, Levy D, Sharma N, Venojarvi M, Strauch A, Orosz CG and Sen CK.** Oxygen sensing by primary cardiac fibroblasts: a key role of p21(Waf1/Cip1/Sdi1). *Circ Res.* 92: 264-271., 2003.
255. **Rumsey WL, Pawlowski M, Lejavardi N and Wilson DF.** Oxygen pressure distribution in the heart in vivo and evaluation of the ischemic "border zone". *Am J Physiol.* 266: H1676-1680., 1994.
256. **Siaghy EM, Devaux Y, Sfaksi N, Carteaux JP, Ungureanu-Longrois D, Zannad F, Villemot JP, Burlet C and Mertes PM.** Consequences of inspired oxygen fraction manipulation on myocardial oxygen pressure, adenosine and lactate concentrations: a combined myocardial microdialysis and sensitive oxygen electrode study in pigs. *J Mol Cell Cardiol.* 32: 493-504., 2000.
257. **Novotna J, Bibova J, Hampl V, Deyl Z and Herget J.** Hyperoxia and recovery from hypoxia alter collagen in peripheral pulmonary arteries similarly. *Physiol Res* 50: 153-163, 2001.
258. **Elsasser A, Schlepper M, Klovekorn WP, Cai WJ, Zimmermann R, Muller KD, Strasser R, Kostin S, Gagel C, Munkel B, Schaper W and Schaper J.** Hibernating myocardium: an incomplete adaptation to ischemia. *Circulation.* 96: 2920-2931., 1997.
259. **Roy S, Khanna S, Rink T, Radtke J, Williams WT, Biswas S, Schnitt R, Strauch AR and Sen CK.** p21waf1/cip1/sdi1 as a Central Regulator of Inducible Smooth Muscle Actin Expression and Differentiation of Cardiac Fibroblasts to Myofibroblasts. *Mol Biol Cell* 19: 19, 2007.
260. **Angelos MG, Kutala VK, Torres CA, He G, Stoner JD, Mohammad M and Kuppusamy P.** Hypoxic reperfusion of the ischemic heart and oxygen radical generation. *Am J Physiol Heart Circ Physiol.* 290: H341-347. Epub 2005 Aug 2026., 2006.
261. **Zhao X, He G, Chen YR, Pandian RP, Kuppusamy P and Zweier JL.** Endothelium-derived nitric oxide regulates postischemic myocardial oxygenation and oxygen consumption by modulation of mitochondrial electron transport. *Circulation.* 111: 2966-2972., 2005.
262. **Roy S, Khanna S and Sen CK.** Perceived hyperoxia: oxygen-regulated signal transduction pathways in the heart. *Methods Enzymol* 381: 133-139, 2004.
263. **Burgemeister R.** New aspects of laser microdissection in research and routine. *J Histochem Cytochem.* 53: 409-412., 2005.

264. **Burgemeister R, Gangnus R, Haar B, Schutze K and Sauer U.** High quality RNA retrieved from samples obtained by using LMPC (laser microdissection and pressure catapulting) technology. *Pathol Res Pract* 199: 431-436, 2003.
265. **Nafe R, Gangnus R, Glienke W, Burgemeister R, Haar B, Pries A and Schlote W.** Laser microdissection and pressure catapulting (LMPC) in paraffin sections mounted on glass slides. A methodological report. *Pathol Res Pract* 199: 411-414, 2003.
266. **Suarez-Quian CA, Goldstein SR, Pohida T, Smith PD, Peterson JI, Wellner E, Ghany M and Bonner RF.** Laser capture microdissection of single cells from complex tissues. *Biotechniques*. 26: 328-335., 1999.
267. **Bonner RF, Emmert-Buck M, Cole K, Pohida T, Chuaqui R, Goldstein S and Liotta LA.** Laser capture microdissection: molecular analysis of tissue. *Science*. 278: 1481,1483., 1997.
268. **Slater TF.** Free-radical mechanisms in tissue injury. *Biochem J*. 222: 1-15., 1984.
269. **Davies KJ.** Oxidative stress: the paradox of aerobic life. *Biochem Soc Symp* 61: 1-31, 1995.
270. **Huang Y, Hickey RP, Yeh JL, Liu D, Dadak A, Young LH, Johnson RS and Giordano FJ.** Cardiac myocyte-specific HIF-1alpha deletion alters vascularization, energy availability, calcium flux, and contractility in the normoxic heart. *Faseb J*. 18: 1138-1140. Epub 2004 May 1137., 2004.
271. **Sen CK, Roy S.** Perceived hyperoxia: Oxygen-induced remodeling of the reoxygenated heart. . *Cardiovascular Research* 71: 280-288, 2006.
272. **Lane N.** *Oxygen: The Elixir of Life*: Oxford University Press, 2002.